The Dissertation Committee for Ren-Tsung Wu Certifies that this is the approved version of the following Dissertation:

Supramolecular Chemistry of Functionalized "Texas-Sized" Molecular Boxes and Their Applications in Hydrogel Materials

Committee:

Jonathan L. Sessler, Supervisor

Jennifer S. Brodbelt

Hung-Wen Liu

Eric V. Anslyn

Adrian T. Keatinge-Clay

Supramolecular Chemistry of Functionalized "Texas-Sized" Molecular Boxes and Their Applications in Hydrogel Materials

by

Ren-Tsung Wu

Dissertation

Presented to the Faculty of the Graduate School of

The University of Texas at Austin

in Partial Fulfillment

of the Requirements

for the Degree of

Doctor of Philosophy

The University of Texas at Austin

May 2018

Dedication

To my father, Ming-Guei Wu

To my mother, Hsin-Hua Chen

To my sister, Hui-Chen Wu

Acknowledgements

First and foremost, I would like to thank my advisor Professor Jonathan Sessler for giving me the chance to work in his group. It has been a great honor to be his student and lab member in my pursuit of a Ph.D. He has always taught me and the group members how to achieve good chemical research by showing us a plenty of fascinating proposals and projects, as well as numerous feasible ways to solve our puzzles and difficulties in research. I truly appreciate all his contributions of time, ideas, and funding to make my Ph.D. experience so meaningful and memorable.

All the members of my family in Taiwan have always supported me in the course of my overseas study and research at UT-Austin over the past seven years. Most importantly, I am deeply thankful to my parents, whose love and care are always with me in whatever I pursue. I am forever indebted to them.

The members of the Sessler group have contributed enormously to my personal and professional time at UT-Austin. Our group has served as a source of friendships, as well as good advice and collaboration. I am especially grateful to Dr. Gabriela Vargas-Zúñiga, Dr. Takehiro Hirao, Dr. Murat Deliomeroglu, Dr. Xiaofan Ji, Dr. Xiaodong Chi, Dr. Hao Li, Dr. Gregory Thiabaud, Dr. Juhoon Lee, Dr. Eric Silver, Dr. Aaron Lammer, etc. Without their collaboration, advice, and help, I might not be able to overcome some challenges in those stressful moments and accomplish our research objectives. Moreover, I would like to acknowledge many past and present group members for their friendships and assistance in all aspects of my life and research.

My special thanks go to Mr. Steven Sorey, Dr. Vincent Lynch, and Dr. Ian Riddington in the Department of Chemistry. Their efforts to analyze and characterize the major products greatly facilitated us to make progress on our research.

Furthermore, I owe an immense debt of gratitude to our Graduate Program Coordinator, Ms. Betsy Hamblen, who has helped me address countless difficulties throughout my years in the Ph.D. program. Also, I am honored to become a true friend with Dr. Andrew T. Nelson whom I have learned a lot from in regard to American cultures, medical knowledge, English language proficiency, and a great sense of humor.

I am very grateful to both of my former advisors whom I had a privilege to work with during my time as an undergraduate and a graduate student in Taiwan. I would like to thank Professor Teh-Chang Chou for accepting me into his group when I was a sophomore at National Chung-Cheng University. With his guidance, I have been taught how to survive in a synthetic organic chemistry lab and inspired to discover the beauty of organic chemistry in a more advanced way. I also appreciate Professor Wen-Sheng Chung for offering me an opportunity to work with him at National Chiao-Tung University. Under his supervision, I have developed a strong interest in supramolecular chemistry and become versed in many key analytical techniques to carry out significant experiments. He also kindly introduced me to Professor Sessler, thus allowing me to pursue my Ph.D. in the world-renowned Sessler group.

Last but not least, I am appreciative of each member of my Dissertation Committee, Professor Eric Anslyn, Professor Jennifer Brodbelt, Professor Keatinge-Clay, and Professor Hung-Wen Liu, for taking their time to serve on my committee and providing me some valuable professional advice.

Abstract

Supramolecular Chemistry of Functionalized "Texas-Sized" Molecular Boxes and Their Applications in Hydrogel Materials

Ren-Tsung Wu, Ph.D.

The University of Texas at Austin, 2018

Supervisor: Jonathan L. Sessler

Positively charged, electron-deficient, and box-like macrocyclic receptors, such as "the blue box" (**CBPQT**$^{4+}$) and its diversiform congeners, have been widely recognized for their roles in the construction of mechanically interlocked molecules (MIMs). These receptors display a high affinity for various π-donor guests, allowing researchers to use them to create a wide range of molecular and supramolecular ensembles, including rotaxanes, catenanes, polypseudorotaxanes, and electrochemically switchable molecules. To explore novel supramolecular architectures that are not accessible using the classic **CBPQT**$^{4+}$ motif, our group developed a more flexible tetracationic imidazolium-based "Texas-sized" molecular box and several synthetic analogues since 2010. This system has been found to afford a number of stimuli-responsive self-associated ensembles. On the basis of the prior work, we synthesized the functionalized Texas-sized molecular boxes, leading us to investigate their self-assembling properties and to incorporate them into gel-forming copolymeric materials. This dissertation details the author's work focused on the preparation, analyses, and applications of three Texas-sized macrocycles appended with the monocarboxylic acid, dicarboxylic acid, and methacrylate functionalities, respectively.

Chapter 1 provides a brief review regarding our current understanding of the solution-based and solid-state host-guest assembly of the unfunctionalized Texas-sized macrocycle with a diversity of anionic guests. Chapter 2 depicts our studies on the self-complementary dimerization of a monocarboxylic acid-functionalized Texas-sized molecular box in the solid state and the head-to-tail polymerization of its conjugate base in solution and the solid state. Chapter 3 describes our work incorporating a dicarboxylic acid-substituted Texas-sized macrocycle into a covalently cross-linked copolymeric network. Such a copolymer is found to form a hydrogel capable of absorbing inorganic and organic anions from aqueous media. Chapter 4 details the multicolor hydrogels containing both anion-binding tetracationic receptor motifs and gel-specific fluorophores, which may be used as building blocks to produce multifluorescent color 3D codes through physical adhesion. The encoded information produced by patterns of such hydrogels may be further transformed through either physical action or by exposure to a chemical stimulus. Chapter 5 includes all the syntheses and characterization data of the compounds prepared by the author, as well as the single crystal X-ray diffraction data of four functionalized Texas-sized molecular boxes.

Table of Contents

List of Tables

List of Figures

List of Schemes

Chapter 1: Introduction to Tetracationic Macrocyclic Receptors

1.1 "The Blue Box" and "The Texas-Sized Molecular Box"

Macrocyclic receptors and hosts that demonstrate a combination of molecular recognition and complexation properties have played a time-honored role in the development of supramolecular chemistry.[1–5] Within the subset of positively charged macrocycles, the tetracationic cyclobis(paraquat-*p*-phenylene) (**CBPQT**$^{4+}$), also known as the "blue box," and structurally related macrocycles, developed by Stoddart and co-workers, are arguably the most iconic.[5–9] The box-like geometry of **CBPQT**$^{4+}$ and the strong donor-acceptor interactions it and its congeners support have allowed a wide range of mechanically interlocked molecular architectures to be prepared (*cf*. Figure 1.1); many have emerged as promising materials for use in applications as diverse as *inter alia*: (i) host-guest recognition and assembly,[9–11] (ii) artificial photosynthesis,[12,13] (iii) molecular electronics,[14,15] and (iv) molecular machines.[16,17]

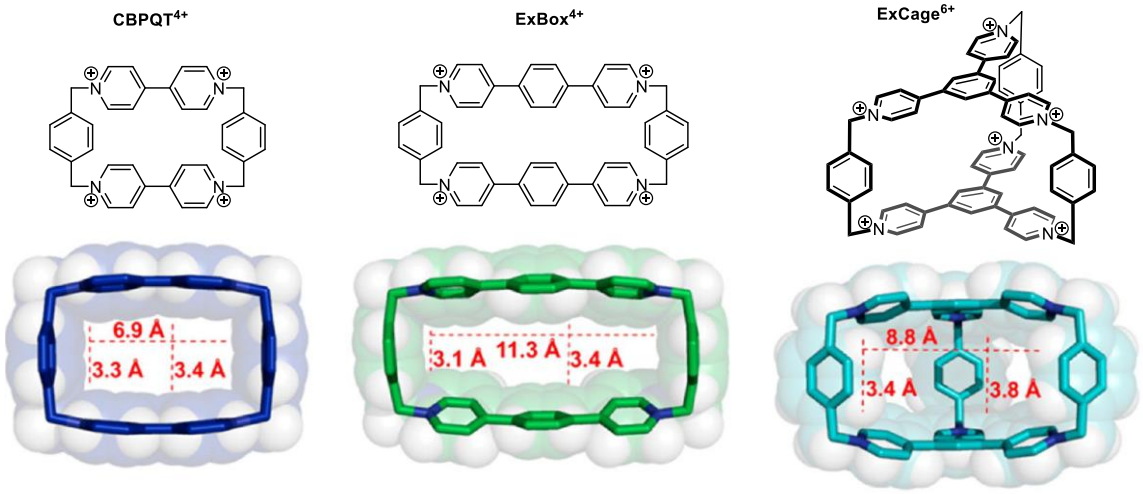

Figure 1.1 Structures of **CBPQT**$^{4+}$ and its congeners developed by the Stoddart group. Key metric parameters are also shown. Reproduced with permission from *Acc. Chem. Res*. **2016**, *49*, 262. Copyright 2016 American Chemical Society.[9]

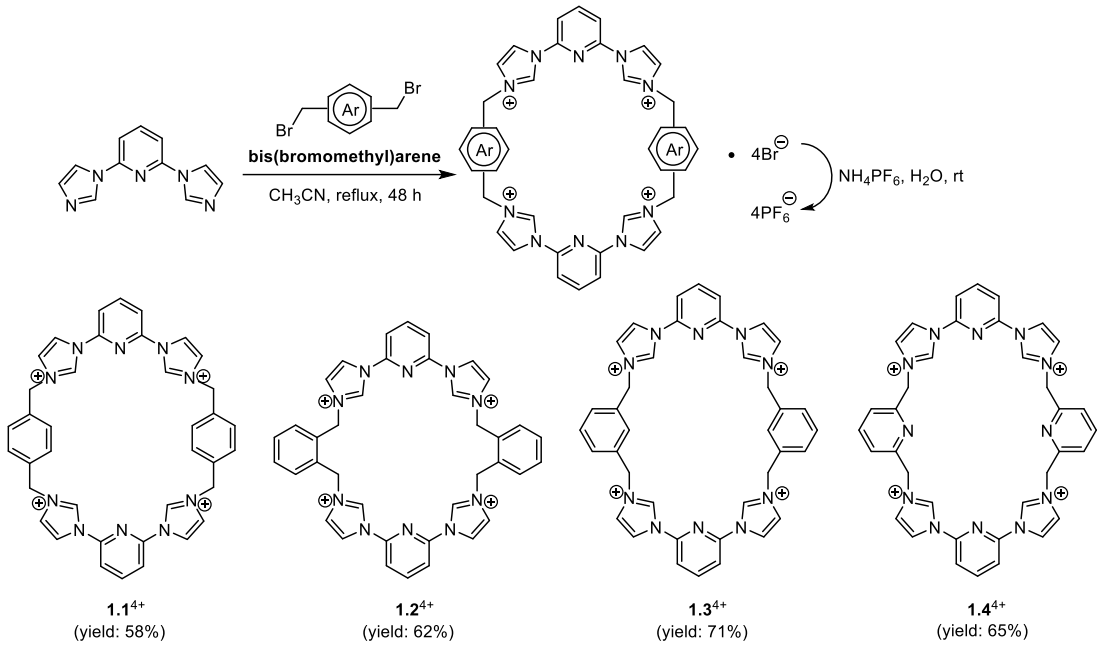

Scheme 1.1 Syntheses of the tetracationic "Texas-sized" molecular box $\mathbf{1.1}^{4+}$ and its analogous macrocycles $\mathbf{1.2}^{4+}$–$\mathbf{1.4}^{4+}$ developed by the Sessler group.[13]

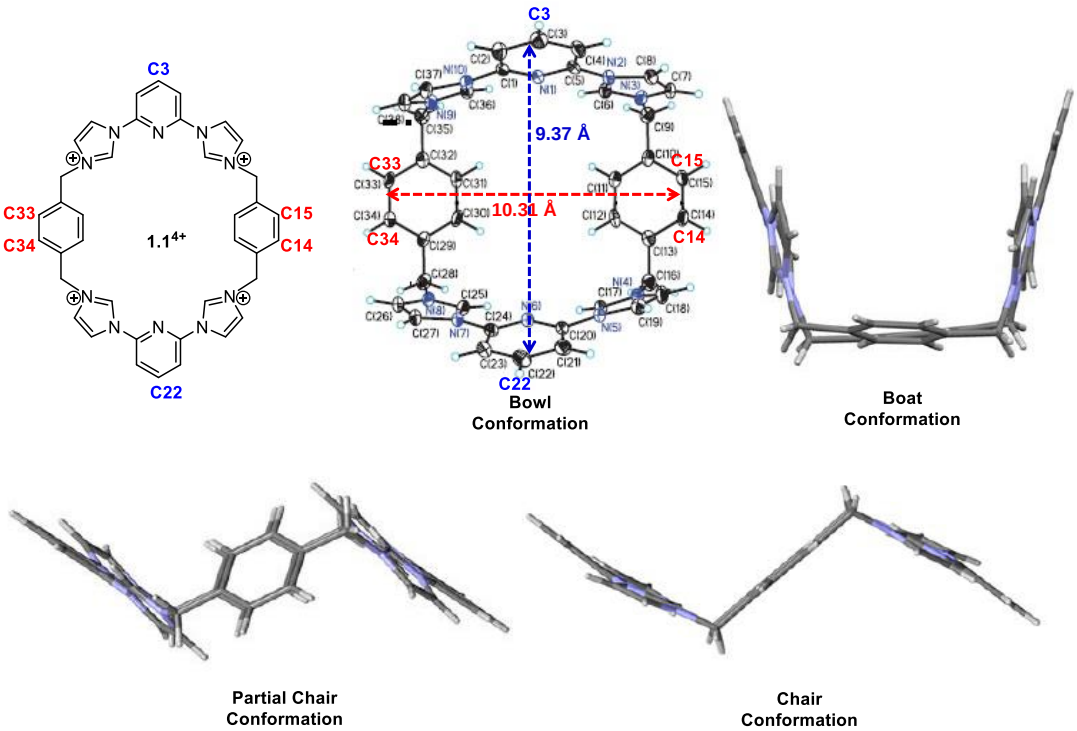

Figure 1.2 Various conformations of $\mathbf{1.1}^{4+}$ observed in the solid state. Reproduced with permission from *J. Am. Chem. Soc.* **2011**, *133*, 1526. Copyright 2011 American Chemical Society.[22]

Inspired by the chemistry of **CBPQT**$^{4+}$, in 2010 our group designed and prepared a tetracationic imidazolium-based macrocycle **1.1**$^{4+}$ and, subsequently, several related systems, *e.g.*, **1.2**$^{4+}$–**1.4**$^{4+}$ (Scheme 1.1).[18–20] Since our first-generation molecular box **1.1**$^{4+}$ was found to display greater conformational flexibility and a larger central cavity than the original blue box **CBPQT**$^{4+}$ (*cf.* Figure 1.2),[5] it was referred to as a "Texas-Sized" molecular box in order to highlight its distinctive structural features.[18]

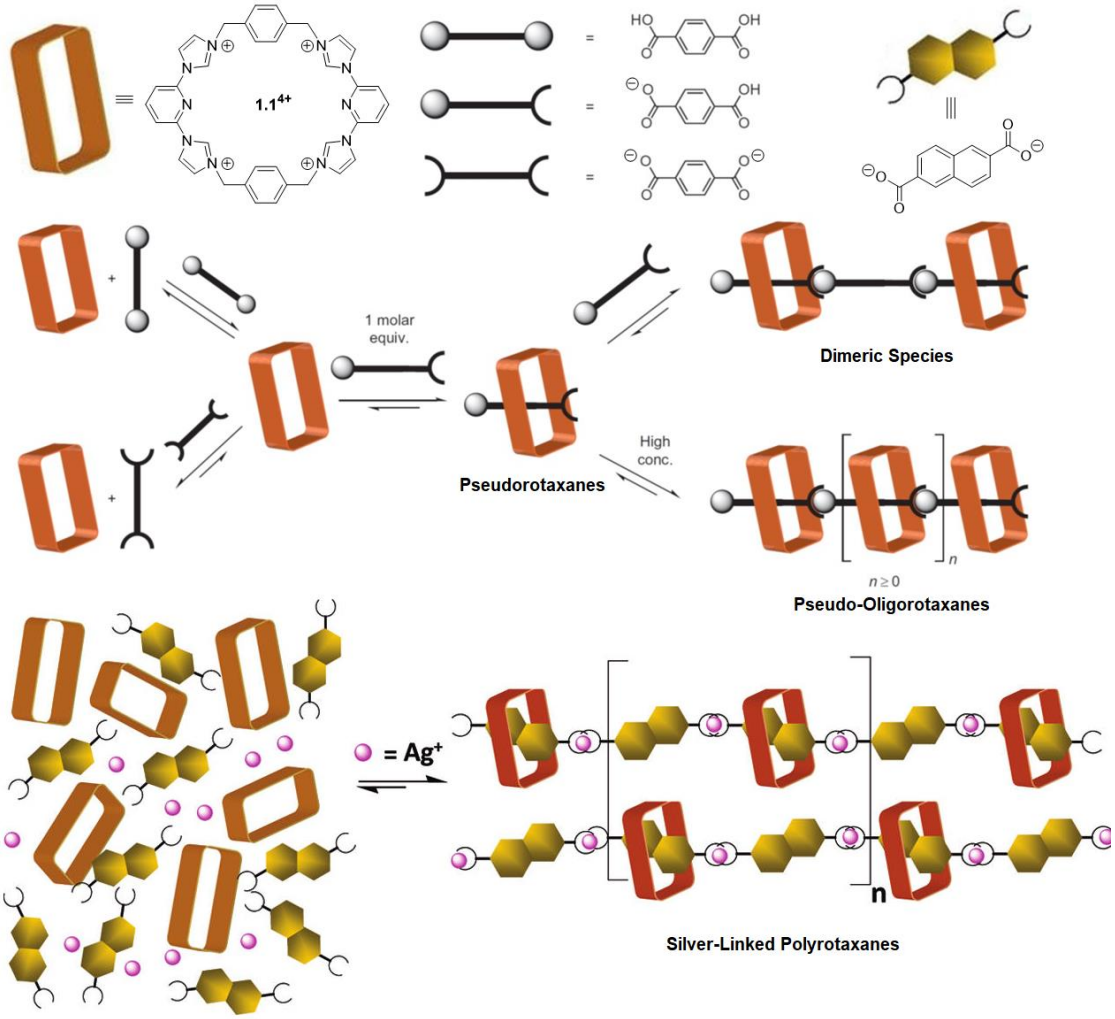

Figure 1.3 Cartoon representations of self-assembled complexes stabilized by the Texas-sized molecular box **1.1**$^{4+}$ with selected electron-rich guests observed in solution and in the solid state. Reproduced with permission from *J. Am. Chem. Soc.* **2011**, *133*, 1526. Copyright 2011 American Chemical Society.[22]

Based on the investigations carried out by our group between 2010 and 2013, **1.1**$^{4+}$ was found capable of attracting and enclosing a variety of electron-rich neutral and anionic guests. This was ascribed to its structural merits including a guest-dependent macrocyclic geometry and the presence of both imidazolium and neutral aromatic subunits within the ring. Therefore, a number of notable threaded or interpenetrated pseudorotaxane complexes of **1.1**$^{4+}$ with selected aromatic carboxylate anions could be formed and stabilized through what were apparently strong host-guest $(C–H)^{+}\cdots X^{-}$ hydrogen bonding and π-π donor-acceptor interactions in solution and in the solid state.[18–23] Further studies have also corroborated that pseudorotaxane monomers of [**1.1**$^{4+}$·mono-terephthalate anion] could self-associate and support the formation of pseudo-oligorotaxane superarchitectures at high concentrations in solution.[22,23] In the case of pseudorotaxane monomers of [**1.1**$^{4+}$·2,6-naphthalenedicarboxylate dianion], self-assembly into higher order polyrotaxane chains in the solid state could be achieved by introducing silver cation into the self-assembly process (*cf*. Figure 1.3).[22,23]

In 2015 and 2016, Gong and co-workers detailed the solution-based host-guest binding properties of **1.1**$^{4+}$. They tested a broad spectrum of aromatic and aliphatic mono- and dicarboxylate anions and employed one- and two-dimensional ^{1}H NMR spectroscopy to measure separate samples in DMSO-d_6. Notable analytical results are summarized in Table 1.1. From their findings, strong support it was inferred that **1.1**$^{4+}$ can act as a versatile macrocyclic host to bind a diversity of electron-rich guests in solution. Such self-organizational behavior is ascribed to the relatively high conformational flexibility of **1.1**$^{4+}$ and the stabilizing interactions provided by the various functional motifs of **1.1**$^{4+}$, the surrounding solvent molecules, the peripheral PF_6^{-} counterions, and the carboxylate guests in the solution state.[24,25]

Guest	Binding Site	H:G Binding Ratio	Equilibrium	Association Constant
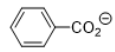	Outside Cavity	2:3	$[H] + [G] \overset{K_1}{\rightleftharpoons} [H \cdot G]$ $2[H \cdot G] + [G] \overset{K_2}{\rightleftharpoons} [H_2 \cdot G_3]$	K_1 = (8.3 ± 0.4) X 10^3 M^{-1} K_2 = (2.3 ± 0.1) X 10^6 M^{-2}
	Threaded through Cavity	1:2	$[H] + [G] \overset{K_1}{\rightleftharpoons} [H \cdot G]$ $[H \cdot G] + [G] \overset{K_2}{\rightleftharpoons} [H \cdot G_2]$	K_1 = (1.0 ± 0.1) X 10^4 M^{-1} K_2 = (3.5 ± 0.2) X 10^3 M^{-1}
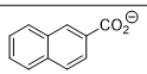	Threaded through Cavity	1:2	$[H] + [G] \overset{K_1}{\rightleftharpoons} [H \cdot G]$ $[H \cdot G] + [G] \overset{K_2}{\rightleftharpoons} [H \cdot G_2]$	K_1 = (8.3 ± 0.4) X 10^3 M^{-1} K_2 = (2.3 ± 0.2) X 10^3 M^{-1}
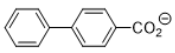	Threaded through Cavity	2:3	$[H] + [G] \overset{K_1}{\rightleftharpoons} [H \cdot G]$ $2[H \cdot G] + [G] \overset{K_2}{\rightleftharpoons} [H_2 \cdot G_3]$	K_1 = (9.1 ± 0.5) X 10^3 M^{-1} K_2 = (8.1 ± 0.4) X 10^5 M^{-2}
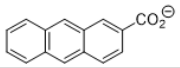	Threaded through Cavity	1:2	$[H] + [G] \overset{K_1}{\rightleftharpoons} [H \cdot G]$ $[H \cdot G] + [G] \overset{K_2}{\rightleftharpoons} [H \cdot G_2]$	K_1 = (6.1 ± 0.3) X 10^2 M^{-1} K_2 = (7.2 ± 0.4) X 10^2 M^{-1}
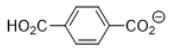	Threaded through Cavity	2:3	$[H] + [G] \overset{K_1}{\rightleftharpoons} [H \cdot G]$ $2[H \cdot G] + [G] \overset{K_2}{\rightleftharpoons} [H_2 \cdot G_3]$	K_1 = (2.1 ± 0.1) X 10^3 M^{-1} K_2 = (2.4 ± 0.2) X 10^5 M^{-2}
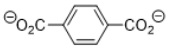	Outside Cavity	1:1	$[H] + [G] \overset{K_a}{\rightleftharpoons} [H \cdot G]$	K_a = (3.3 ± 0.1) X 10^3 M^{-1}
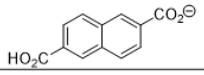	Threaded through Cavity	1:1	$[H] + [G] \overset{K_a}{\rightleftharpoons} [H \cdot G]$	K_a = (2.1 ± 0.1) X 10^3 M^{-1}
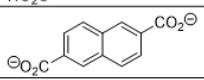	Threaded through Cavity	1:1	$[H] + [G] \overset{K_a}{\rightleftharpoons} [H \cdot G]$	K_a = (3.5 ± 0.2) X 10^3 M^{-1}
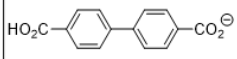	Threaded through Cavity	2:3	$[H] + [G] \overset{K_1}{\rightleftharpoons} [H \cdot G]$ $2[H \cdot G] + [G] \overset{K_2}{\rightleftharpoons} [H_2 \cdot G_3]$	K_1 = (1.5 ± 0.1) X 10^3 M^{-1} K_2 = (1.8 ± 0.2) X 10^7 M^{-2}
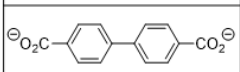	Threaded through Cavity	2:3	$[H] + [G] \overset{K_1}{\rightleftharpoons} [H \cdot G]$ $2[H \cdot G] + [G] \overset{K_2}{\rightleftharpoons} [H_2 \cdot G_3]$	K_1 = (1.8 ± 0.2) X 10^3 M^{-1} K_2 = (1.1 ± 0.1) X 10^7 M^{-2}
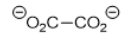	Outside Cavity	1:1	$[H] + [G] \overset{K_a}{\rightleftharpoons} [H \cdot G]$	K_a = (1.7 ± 0.1) X 10^3 M^{-1}
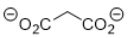	Outside Cavity	1:1	$[H] + [G] \overset{K_a}{\rightleftharpoons} [H \cdot G]$	K_a = (3.6 ± 0.2) X 10^3 M^{-1}
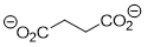	Outside Cavity	1:1	$[H] + [G] \overset{K_a}{\rightleftharpoons} [H \cdot G]$	K_a = (4.8 ± 0.2) X 10^3 M^{-1}
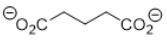	Outside Cavity	1:1	$[H] + [G] \overset{K_a}{\rightleftharpoons} [H \cdot G]$	K_a = (7.1 ± 0.4) X 10^3 M^{-1}
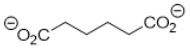	Outside Cavity	1:1	$[H] + [G] \overset{K_a}{\rightleftharpoons} [H \cdot G]$	K_a = (1.0 ± 0.1) X 10^4 M^{-1}
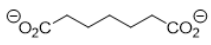	Outside Cavity	1:1	$[H] + [G] \overset{K_a}{\rightleftharpoons} [H \cdot G]$	K_a = (2.6 ± 0.1) X 10^4 M^{-1}
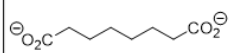	Outside Cavity	1:1	$[H] + [G] \overset{K_a}{\rightleftharpoons} [H \cdot G]$	K_a = (4.9 ± 0.2) X 10^3 M^{-1}
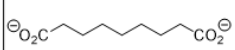	Outside Cavity	1:1	$[H] + [G] \overset{K_a}{\rightleftharpoons} [H \cdot G]$	K_a = (4.6 ± 0.2) X 10^3 M^{-1}
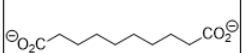	Outside Cavity	1:1	$[H] + [G] \overset{K_a}{\rightleftharpoons} [H \cdot G]$	K_a = (6.9 ± 0.4) X 10^3 M^{-1}

Table 1.1 Summary of host-guest binding properties of **1.1**$^{4+}$ with a wide range of guests in DMSO-d_6 solution.[24,25]

The congeneric macrocycles **1.2**$^{4+}$–**1.4**$^{4+}$ are found to afford dramatically different self-associated ensembles when treated with 2,6-naphthalenedicarboxylate dianion under analogous conditions. Such observations led to the conclusion that the bridges (derived from the bis(bromomethyl)arenes) between two imidazolium moieties in these macrocyclic receptors plays an important role in defining the host-guest interactions (*cf*. Figure 1.4).[19]

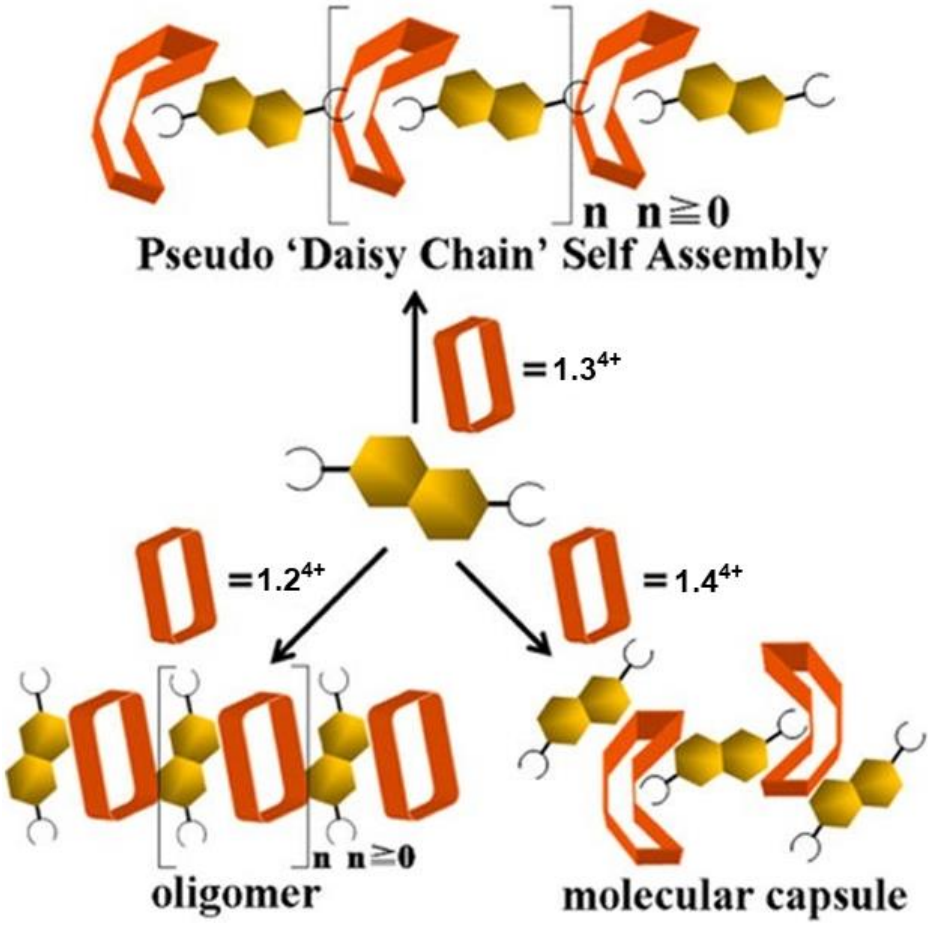

Figure 1.4 Cartoon representations of interlocked ensembles supported by congeneric macrocycles **1.2**$^{4+}$–**1.4**$^{4+}$ with 2,6-naphthalenedicarboxylate dianion as observed in solution and in the solid state. Reproduced with permission from *J*. *Am*. *Chem*. *Soc*. **2013**, *135*, 6330. Copyright 2013 American Chemical Society.[19]

1.2 Self-Assembly of Texas-Sized Box And Amphiphilic Copolymer in Water

Amphiphilic copolymers, polymeric systems containing hydrophilic/hydrophobic domains, have attracted attention across a diversity of fields, including polymer science, supramolecular chemistry, and biomedicine, because of their well-defined capacity to self-organize into diversiform structures in aqueous solutions, including vesicles, lamellae, bicontinuous structures, cylindrical micelles, disk-like micelles, spherical micelles and other complex or hierarchical aggregates.[26] Thanks to the good mechanical and physical properties resulting from the use of covalent polymeric backbones, polymer aggregates derived from amphiphilic copolymers generally display higher stability and durability than most small molecule aggregates.[27] This has made amphiphilic copolymers promising candidates for exploring the determinants that underlie the shape transformations found in the case of naturally occurring vesicles and organelles. Traditionally, the morphologies of amphiphilic polymer aggregates can be modulated by tuning the ratio of the hydrophilic/hydrophobic portions within the copolymer. However, such modifications require sophisticated polymer design, elaborate polymer syntheses, and precise control over processing.[28] Recently, dynamic and reversible host-guest interactions have been proposed as a means of adjusting the hydrophilic/hydrophobic balance within amphiphilic copolymers and hence controlling the morphologies produced via polymer self-assembly. To date, these efforts have for the most part relied on macrocycle-based host-guest interactions involving cationic or neutral guests. Macrocycle-anion recognition has rarely been employed as a means of dictating polymer structures and behaviors.

Since anions are ubiquitous and critical to many biological processes, we considered it important to explore new approaches wherein the host-guest interactions between macrocycles and anions in water are employed to dictate amphiphilic polymer

self-assembly and the associated morphologies. In 2016, the Sessler and Huang groups detailed a supramolecular system, wherein macrocycle-anion recognition was exploited to control the morphologies of self-aggregates stabilized by copolymer **1.5** and water-soluble chloride salt of Texas-sized molecular box **1.1**·4Cl in aqueous media (*cf*. Figure 1.5).[29] Copolymer **1.5** is characterized as amphiphilic owing to the fact that it contains three types of repeating units: Hydrophobic styrene, a hydrophilic oligo(ethylene glycol) methacrylate (OEGMA), and a styrene derivative bearing the salt form of a long chain carboxylic acid. In water, **1.5** alone self-assembles into tube structures. When water-soluble **1.1**·4Cl is added into an aqueous solution of **1.5** binding to the carboxylate-containing side chains occurs, thus altering in a monotonic manner the hydrophilic-hydrophobic balance of the overall macrocycle-copolymer complex.

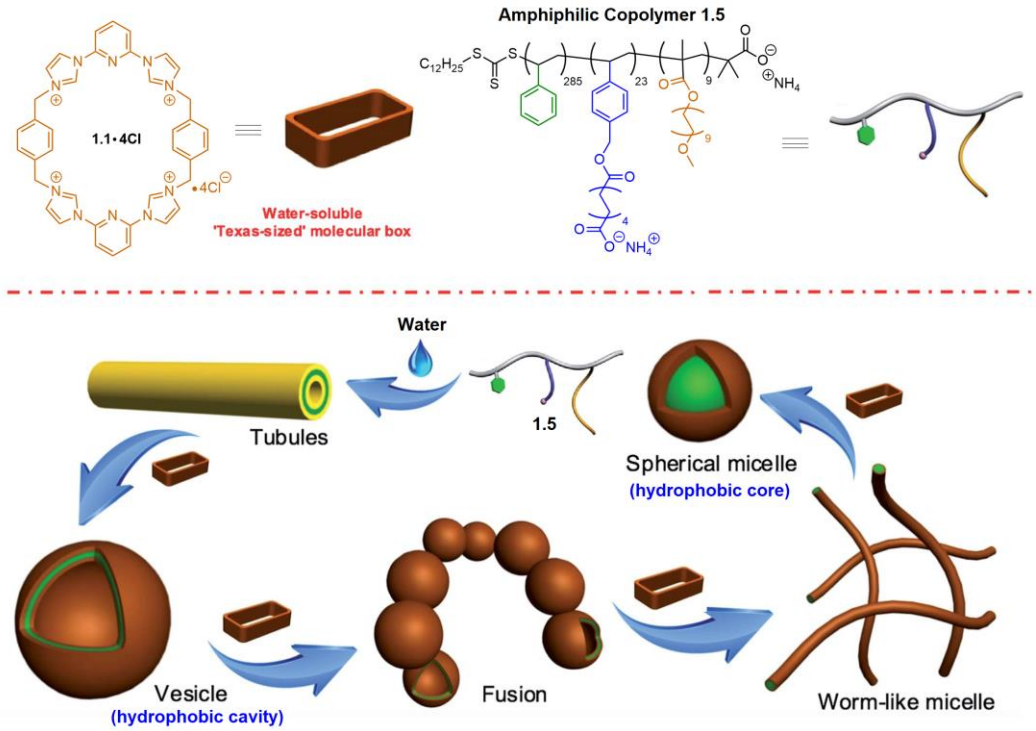

Figure 1.5 Chemical structures of water-soluble macrocyclic receptor **1.1**·4Cl and copolymer **1.5**; schematic views of the diverse assemblies formed and stabilized by **1.5** and **1.1**·4Cl as the result of target molecular recognition. Reproduced with permission from *Chem*. *Sci*. **2016**, *7*, 6006. Copyright 2016 The Royal Society of Chemistry.[29]

To probe further the morphological changes in the polymer aggregates induced via the addition of **1.1**·Cl_4, transmission electron microscopy (TEM) was utilized to analyze a series of samples under different conditions. As summarized in Figure 1.5, tube-like structures (length: several micrometers; diameter: ~400 nm) are observed when copolymer **1.5** (0.100 mM) is added into water in the absence of any other additive. Addition of a relatively small amount of **1.1**·4Cl (0.500 mM final concentration) to an initial aqueous solution of **1.5** causes these tubules to vanish completely with the concomitant formation of large vesicular nanostructures (wall thickness: ~50 nm; diameter: 200–400 nm). When the concentration of **1.1**·4Cl is increased to 1.00 mM while that of **1.5** is held constant, evidence of fusion through membrane adhesion is seen; this leads to the formation of strings of beads. As the concentration of **1.1**·4Cl is further increased to 1.50 mM, these beads constrict themselves resulting in the formation of wormlike micelles. These latter nanofibers have an average diameter of 80 nm and are several micrometers in length. Finally, when the concentration of **1.1**·4Cl is increased to 2.30 mM, the worm-like micelles are replaced by spherical micelles with typical coronacore nanostructures. These spherical micelles are between 50 and 120 nm in diameter. These results revealed that the nature of the aggregates formed from the amphiphilic copolymer **1.5** and their evolution can be controlled by varying the relative concentration of **1.1**·4Cl. This control is ascribed to the macrocycle-anion host-guest recognition between the receptor $\mathbf{1.1}^{4+}$ and the carboxylate anion-appended copolymer **1.5**.

The vesicles and micelles produced from **1.1**·4Cl and **1.5** contain hydrophilic cavities and hydrophobic cores, respectively. They could be used to encapsulate hydrophilic fluorescein isothiocyanate (FITC) and hydrophobic chemotherapeutic agent doxorubicin (DOX), respectively. Both vesicles and micelles are observed to undergo

controlled dissociation in the presence of adenosine-5'-triphosphate (ATP), adenosine-5'-diphosphate (ADP), and adenosine-5'-monophosphate (AMP). These nucleotides compete with the key host-guest binding interactions that stabilize these polymer ensembles. Further analyses revealed that ATP was the most efficient of the nucleotides tested in inducing the release of the enclosed FITC and DOX from the corresponding cavities and cores. Such findings were taken as support for the notion that diversiform aggregates made up from **1.1**·4Cl and **1.5** could be designed to function as small molecule carriers and transport agents. This work was touted as being a first step towards the study of the Texas-sized box in the fields of stimuli-responsive drug delivery and photoelectric materials.[30]

1.3 ANION-RESPONSIVE COPOLYMERS CONTAINING MACROCYCLIC MOIETIES

In an effort to achieve a macromolecular system capable of affording gel materials via anion-induced supramolecular cross-linking, the Sessler group developed a copolymer **1.6** by incorporating a calix[4]pyrrole macrocyclic receptor into a methyl methacrylate-derived polymer backbone in 2014 (*cf.* Scheme 1.2).[31]

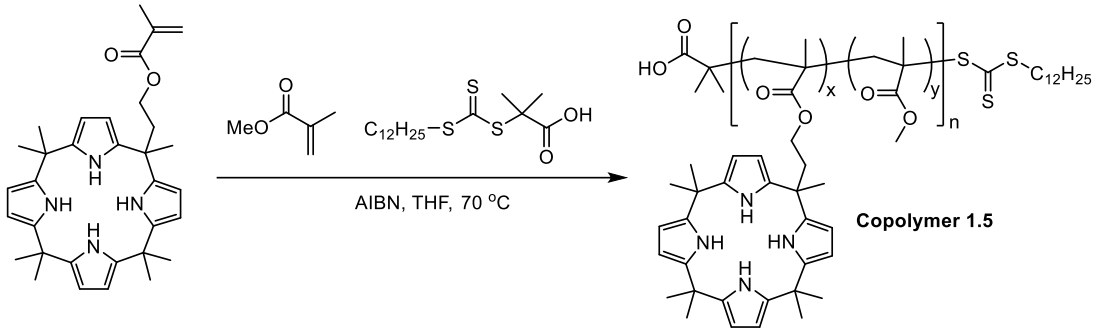

Scheme 1.2 Synthesis of copolymer **1.6** (poly(calix[4]pyrrole ethyl methacrylate-*co*-methyl methacrylate)).[31]

Copolymer **1.6** was found to undergo supramolecular cross-linking upon exposure to selected dianionic species. The resulting supramolecular cross-linking induces reversible changes in the viscoeleastic properties of the polymeric system, as inferred from viscosity measurements, ^{1}H NMR spectroscopy, and dynamic mechanical analysis (DMA). Moreover, gel-like materials were obtained by dissolving copolymer **1.6** in a minimum amount of CH_2Cl_2 and then adding $(TBA)_2TPA$ (tetrabutylammonium terephthalate). Gel formation is reversed through the addition of TBAF (tetrabutylammonium fluoride) as a source of a competitive monoanion and/or by raising temperature. The effects of anion addition to copolymer **1.6** are also clearly observed under conditions of bulk analysis. For instance, when copolymer **1.6** (40 mg) is dissolved in a minimum amount of CH_2Cl_2, the free-flowing solution becomes subject to gelation upon the addition of $(TBA)_2TPA$ (15 mg). This is a reversible process. For example, the addition of a competitive monoanion (TBAF) to the gel leads to its breakup (*cf.* Figure

1.6a). Similarly, heating the gel system also leads to a disruption in gelation (*cf.* Figure 1.6b). The de-gelling phenomenon is ascribed to the competitive binding of the fluoride anion to the calix[4]pyrrole sites and hence a severing of the dianion-induced supramolecular polymer cross-linking process.

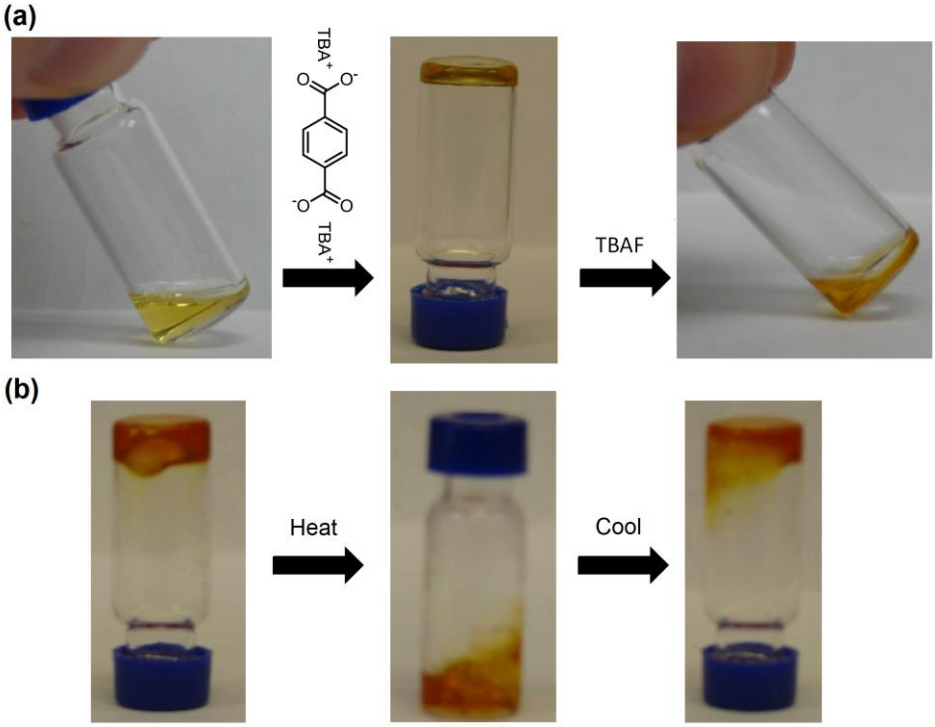

Figure 1.6 (a) Photographs of (left to right) 40 mg of **1.6** dissolved in CH_2Cl_2 (0.15 mL), gel formed after addition of $(TBA)_2TPA$ (15 mg), and breakup of the gel after addition of excess TBAF. (b) The gel formed between copolymer **1.6** and $(TBA)_2TPA$: Left, at room temperature after allowing to set overnight; center, after heating and; right, after cooling to room temperature, gelation appeared to be restored according to an inversion test. Reproduced with permission from *J. Am. Chem. Soc.* **2014**, *136*, 2252. Copyright 2014 American Chemical Society.[31]

More importantly, it was demonstrated that copolymer **1.6** could be used to extract the terephthalate dianion (as the TBA salt) from aqueous environments with concurrent formation of an organic gel. These findings lead to the suggestion that systems such as **1.6** could be employed in the extraction and separation of dianions from aqueous media. It also led to the proposal that anion-induced cross-linking may be used to

influence the physical and material properties of polymeric species and to produce materials that have potential utility in the recognition and selective separation of a broad range of dianions.[32]

Encouraged by the above studies, we sought to devise and synthesize novel copolymers, such as **1.7**, **1.8**, and analogous systems, wherein Texas-sized molecular boxes are covalently appended to polymeric backbones and able to serve as anion receptors for the extraction of specific anionic guests from various media (*cf.* Figure 1.7). We were keen to test whether these new putative materials could achieve supramolecular cross-linking and gel formation upon exposure to selective anions under diverse conditions.

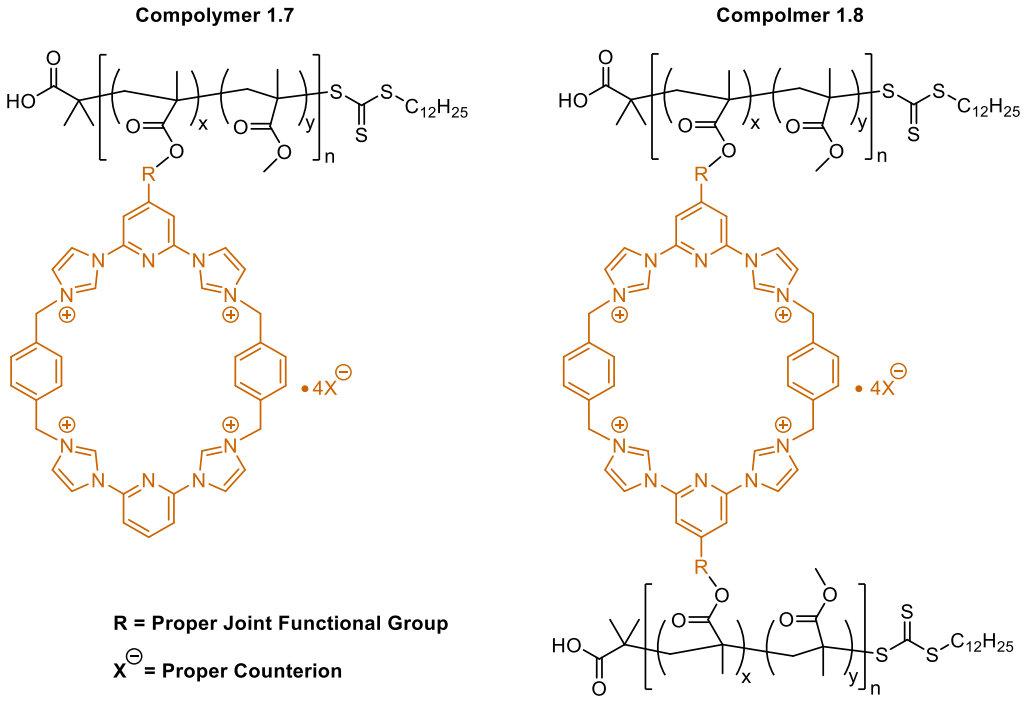

Figure 1.7 Proposed prototypes of copolymers functionalized with tetracationic Texas-sized molecular boxes as pendant or cross-linked anion receptors.

1.4 SUMMARY AND OUTLINE

This chapter provides an overview of our current understanding of the solution-based and solid-state supramolecular properties of the Texas-sized molecular box $\mathbf{1.1}^{4+}$, as well as its analogues $\mathbf{1.2}^{4+}$–$\mathbf{1.4}^{4+}$. The water-soluble chloride salt **1.1**·4Cl can serve as an additive to induce disparate morphological changes when used in conjunction with the self-assembled amphiphilic copolymer complexes **1.5**. Triggered drug release from the resulting self-aggregated systems is a potentially important application. Separately, as described above, copolymer **1.6** proved capable of forming a gel-type material through supramolecular cross-linking resulting from effective complexation between the pendant calix[4]pyrroles and terephthalate dianions. The capability of anion-selective gelation is of particular interest and further exploited because it may allow for the liquid-liquid extraction and facile separation of certain anions from aqueous media. These prior results provided the author with a desire to design and prepare a series of functionalized Texas-sized molecular boxes that might allow the further creation of versatile stimuli-responsive supramolecular systems and self-healing macromolecular materials. Efforts along these lines are described in this dissertation.

Chapter 2 details the synthesis of a monocarboxylic acid-functionalized Texas-sized molecular box (**TxSB-CO_2H**) by combining two separate building blocks via an iodide-catalyzed macrocyclization reaction. As-prepared **TxSB-CO_2H** and its conjugate base **TxSB-CO_2^-** act as self-complementary monomers that undergo disparate assembly processes in organic media to stabilize drastically different interlocked superstructures $\{[\mathbf{TxSB\text{-}CO_2H}]_2\}_n$ and $[\mathbf{TxSB\text{-}CO_2^-}]_n$. The dimerization and further aggregation of **TxSB-CO_2H**, as well as polymerization of **TxSB-CO_2^-**, have been studied in solution and in the solid state by means of one- and two-dimensional ^{1}H NMR spectroscopy, X-ray crystallography, dynamic light scattering, and scanning electron microscopy. A series

of solution-based analyses carried out provided support for the notion that the self-assembled constructs produced from these molecular box monomers are responsive to environmental stimuli, including exposure to the acetate anion, changes in overall concentration, temperature, and pH. The reversible nature of the underlying noncovalent interactions allow the interconversion between [**TxSB-CO_2H**]$_2$ and [**TxSB-CO_2^-**]$_n$ to be controlled in a directional manner by altering the solution pH. The majority of this work has been accepted and will be published as an article by the Journal of the American Chemical Society. The candidate is the first author on this publication and was responsible for the syntheses, characterization, and ensuing self-assembly studies both in solution and in the solid state.

Chapter 3 describes the preparation of a hydrogel-forming polymer network incorporating a covalently cross-linked diester-substituted Texas-sized molecular box moiety. Upon immersion of this polymer network in aqueous solution containing various inorganic and organic salts, supramolecular hydrogelation and absorption of anions into the network were observed. Such anion absorption is ascribed to host-guest interactions involving the tetracationic macrocyclic receptor. Removal of the anions was achieved by lifting the resulting hydrogels out of the aqueous phase. Treating the anion-containing hydrogels with dilute HCl led to the release of the bound anions, allowing the hydrogels to be recycled for reuse. The majority of this work was published as a communication in the Journal of the American Chemical Society.[33] The candidate is the second author on this publication and was responsible for the syntheses and characterization of the nonfunctionalized and dicarboxylic acid-substituted Texas-sized molecular boxes. This project was performed in collaboration with Dr. Xiaofan Ji in the Sessler group, Prof. Lingliang Long of Jiangsu University, Prof. Niveen M. Khashab of King Abdullah University of Science and Technology, and Prof. Feihe Huang of Zhejiang University.

Dr. Ji is the first author on this publication and was responsible for the preparation and characterization of the corresponding hydrogels, as well as the studies of anion removal from aqueous media.

Chapter 4 depicts the preparation of three fluorescent (blue, green, and red) hydrogels containing both tetracationic receptor–anion recognition motifs and gel-specific fluorophores, which may be used as building blocks to construct through physical adhesion fluorescent color 3D codes (**Code A**, **Code B**, and **Code C**) that may be read out by a smartphone. As a result, parts of the individual gel components that make up **Code B** can be replaced with other gel building blocks to form **Code A** via a cut and adhesion approach. A fluorophore responsive to ammonia is further incorporated into one of the hydrogels. This allows the gel block-derived pattern that makes up **Code C** to be converted to **Code A** by chemical means. Therefore, the encoded information produced by patterns of the present hydrogels may be transformed through either physical action or by exposure to a chemical stimulus. The majority of this work was published as a communication in Advanced Materials.[34] The candidate is the second author on this publication and was responsible the syntheses and characterization of the nonfunctionalized and methacrylate-appended Texas-sized molecular boxes. This project was performed in collaboration with Dr. Xiaofan Ji in the Sessler group, Prof. Lingliang Long of Jiangsu University, and Prof. Feihe Huang of Zhejiang University. Dr. Ji is the first author on this publication and was responsible for the key physical and chemical analyses of the multicolor hydrogels and the resulting 3D code arrays.

Chapter 5 details the synthetic procedures and characterization of all the compounds discussed in this dissertation. This includes ^{1}H NMR and ^{13}C NMR spectroscopic data, single crystal X-ray diffraction data, mass spectrometry data, and melting points.

1.5 References

1) Schmidtchen, F. P.; Berger, M. *Chem*. *Rev*. **1997**, *97*, 1609–1646.
2) Beer, P. D.; Gale, P. A. *Angew. Chem*. *Int*. *Ed*. **2001**, *40*, 486–516.
3) Steed, J. W.; Atwood, J. L. *Supramolecular Chemistry*, 2nd ed.; Wiley & Sons: Chichester, UK, 2009; pp. 308–382.
4) Kim, S. K.; Sessler, J. L. *Acc*. *Chem*. *Res*. **2014**, *47*, 2525–2536.
5) Liu, Z.; Nalluri, S. K. M.; Stoddart, J. F. *Chem. Soc. Rev.* **2017**, *46*, 2459–2478.
6) Odell, B.; Reddington, M. V.; Slawin, A. M. Z.; Spencer, N.; Stoddart, J. F.; Williams, D. J. *Angew*. *Chem. Int. Ed.* **1988**, *27*, 1547–1550.
7) Amabilino, D. B.; Stoddart, J. F. *Pure Appl. Chem*. **1996**, *68*, 2351–2359.
8) Langford, S. J.; Stoddart, J. F. *Pure Appl. Chem*. **1996**, *68*, 1255–1260.
9) Dale, E. J.; Vermeulen, N. A.; Juríček, M.; Barnes, J. C.; Young, R. M.; Wasielewski, M. R.; Stoddart, J. F. *Acc. Chem. Res.* **2016**, *49*, 262–273.
10) Raymo, F. M.; Stoddart, J. F. *Chem. Rev.* **1999,** *99,* 1643–1664.
11) Barin, G.; Coskun, A.; Fouda, M. M. G.; Stoddart, J. F. *ChemPlusChem* **2012**, *77*, 159–185.
12) Young, R. M.; Dyar, S. M.; Barnes, J. C.; Juríček, M.; Stoddart, J. F.; Co, D. T.; Wasielewski, M. R. *J. Phys. Chem. A* **2013**, *117*, 12438–12448.
13) Dyar, S. M.; Barnes, J. C.; Juríček, M.; Stoddart, J. F.; Co, D. T.; Young, R. M.; Wasielewski, M. R. *Angew. Chem. Int. Ed.* **2014**, *53*, 5371–5375.
14) Flood, A. H.; Stoddart, J. F.; Steuerman, D. W.; Heath, J. R. *Science* **2004**, *306*, 2055–2056.
15) Stoddart, J. F. *Chem. Soc. Rev.* **2009**, *38*, 1802–1820.
16) Balzani, V.; Gómez-López, M.; Stoddart, J. F. *Acc. Chem. Res.* **1998**, *31*, 405–414.
17) Erbas-Cakmak, S.; Leigh, D. A.; McTernan, C. T.; Nussbaumer, A. L. *Chem*. *Rev*. **2015**, *115*, 10081–10206.
18) Gong, H. -Y.; Rambo, B. M.; Karnas, E.; Lynch, V. M.; Sessler, J. L. *Nat. Chem.* **2010**, *2*, 406–409.
19) Gong, H. -Y.; Rambo, B. M.; Lynch, V. M.; Keller, K. M.; Sessler, J. L. *J. Am. Chem. Soc*. **2013**, *135*, 6330–6337.
20) Yang, Y. -D.; Sessler. J. L.; Gong, H. -Y. *Chem. Commun.* **2017**, *53*, 9684–9696.
21) Gong, H. -Y.; Rambo, B. M.; Lynch, V. M.; Keller, K. M.; Sessler, J. L. *Chem. –Eur. J.* **2012**, *18*, 7803–7809.
22) Gong, H. -Y.; Rambo, B. M.; Karnas, E.; Lynch, V. M.; Keller, K. M.; Sessler, J. L. *J. Am*. *Chem*. *Soc*. **2011**, *133*, 1526–1533.
23) Rambo, B. M.; Gong, H. -Y.; Oh, M.; Sessler, J. L. *Acc*. *Chem*. *Res*. **2012**, *45*, 1390–1401.
24) Tang, F.; Cao, R.; Gong, H. -Y.; *Tetrahedron Lett*. **2015**, *56*, 820–823.
25) Ding, C. -J.; Shen, M. -J.; Xu, L. -J.; Gong, H. -Y. *Tetrahedron* **2016**, *72*, 431–435.
26) (a) Li, C.; Wu, T.; Hong, C.; Zhang, G.; Liu, S. *Angew*. *Chem*. *Int*. *Ed*. **2012**, *51*, 455–459. (b) Dong, R.; Zhu, B.; Zhou, Y.; Yan, D.; Zhu, X. *Angew*. *Chem. Int. Ed*. **2012**, *51*, 11633–11637. (c) Hu, X.; Hu, J.; Tian, J.; Ge, Z.; Zhang, G.; Luo, K.; Liu, S. *J. Am*. *Chem*. *Soc*. **2013**, *135*, 17617–17629.

27) (a) Yan, Q.; Wang, J.; Yin, Y.; Yuan, J. *Angew*. *Chem*. *Int*. *Ed*. **2013**, *52*, 5070–5073. (b) Raghupathi, K. R.; Guo, J.; Munkhbat, O.; Rangadurai, P.; Thayumanavan, S. *Acc*. *Chem*. *Res*. **2014**, 47, 2200–2211.
28) (a) Blanazs, A.; Madsen, J.; Battaglia, G.; Ryan, A. J.; Armes, S. P. *J*. *Am*. *Chem*. *Soc*. **2011**, *133*, 16581–16587. (b) Mai, Y.; Eisenberg, A. *Chem*. *Soc*. *Rev*. **2012**, *41*, 5969–5985. (c) Warren, N. J.; Armes, S. P. *J*. *Am*. *Chem*. *Soc*. **2014**, *136*, 10174–10185.
29) Ji, X.; Wang, H.; Li, Y.; Xia, D.; Li, H.; Tang, G.; Sessler, J. L.; Huang, F. *Chem*. *Sci*. **2016**, *7*, 6006–6014.
30) Qiao, Z. -Y.; Ji. R.; Huang, X. -N.; Du, F. -S.; Zhang, R.; Liang, D. -H.; Li, Z. -C.; *Biomacromolecules* **2013**, *14*, 1555–1563.
31) Silver, E. S.; Rambo, B. M.; Bielawski, C. W.; Sessler, J. L. *J*. *Am*. *Chem*. *Soc*. **2014**, *136*, 2252–2255.
32) (a) Pressly, E. D.; Rossin, R.; Hagooly, A.; Fukukawa, K.; Messmore, B. W.; Welch, M. J.; Wooley, K. L.; Lamm, M. S.; Hule, R. A.; Pochan, D. J.; Hawker, C. J. *Biomacromolecules* **2007**, *8*, 3126–3134. (b) Fukukawa, K.; Rossin, R.; Hagooly, A.; Pressly, E. D.; Hunt, J. N.; Messmore, B. W.; Wooley, K. L.; Welch, M. J.; Hawker, C. J. *Biomacromolecules* **2008**, *9*, 1329–1339.
33) Ji, X.; Wu, R. -T.; Long, L.; Guo, C.; Khashab, N. M.; Huang, F.; Sessler, J. L. *J. Am. Chem. Soc*. **2018**, *140*, 2777–2780.
34) Ji, X.; Wu, R. -T.; Long, L.; Ke, X. -S.; Guo, C.; Ghang, Y. -J.; Lynch, V. M.; Huang, F.; Sessler, J. L. *Adv. Mater*. **2018**, *30*, 1705480.

Chapter 2: Supramolecular Properties of a Monocarboxylic Acid-Functionalized "Texas-Sized" Molecular Box

2.1 INTRODUCTION

Supramolecular oligomers and polymers are receiving considerable attention due to their potential in developing stimuli-responsive, self-healing, and shape-memory materials.[1–4] To date, a number of macrocyclic receptors have been exploited as self-complementary monomers capable of affording desirable oligomeric and polymeric superstructures via "head-to-tail" self-assembly.[5–8] Such macrocycle-based monomers are commonly obtained by incorporating a macrocyclic host (head) with a guest unit (tail) tethered to the core. When designed appropriately, the head of one macrocycle may be used to bind a tail of another monomer via intermolecular host-guest interactions, thus supporting self-assembly.

For instance, our group noted early on that monocarboxylate-functionalized sapphyrins self-associate to produce head-to-tail supramolecular dimers in organic media and in the solid state.[29] Fluoride anions act as inhibitors of the dimerization process by competing for the sapphyrin cavity in preference over the pendant carboxylate arm (*cf.* Figure 2.1). More recently, Stoddart *et al.*[7] reported a self-complementary monomer comprising a π electron-rich tetrathiafulvalene guest chromophore linked to a **CBPQT**$^{4+}$ ring. This system was shown to dimerize into a [*c2*]daisy chain system and undergo rapid dissociation and recombination in solution in a manner that was found to depend on the concentration, temperature, and the nature of the linker (Figure 2.2).[7,8]

---

§ The majority of this work will be published on the Journal of the American Chemical Society:
Wu, **R**. **-T**.; Chi, X.; Hirao, T.; Lynch, V. M.; Sessler, J. L. Supramolecular Properties of a Monocarboxylic Acid-Functionalized "Texas-Sized" Molecular Box (DOI: 10.1021/jacs.7b12957).
The candidate is the first author on this publication and was responsible for synthesizing all products, growing key single crystals, and carrying out the major NMR analyses.

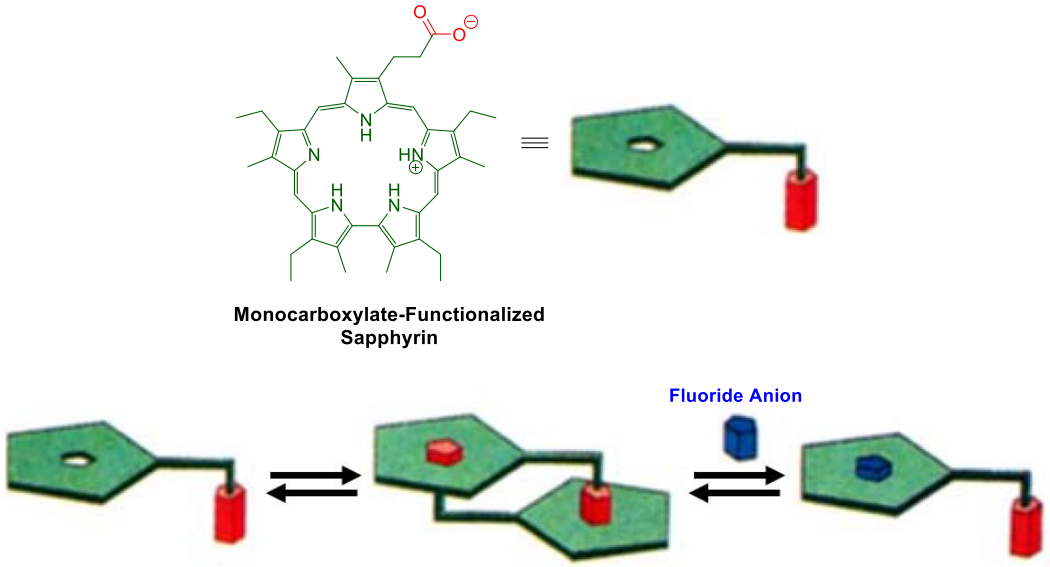

Figure 2.1 Schematic views of a selected monocarboxylate-functionalized sapphyrin, supramolecular dimerization, and fluoride-induced inhibition thereof. This figure, which originally appeared in *Angew. Chem. Int. Ed.* **1996**, *35*, 2782 (Copyright John Wiley and Sons), is reproduced with permission.[5]

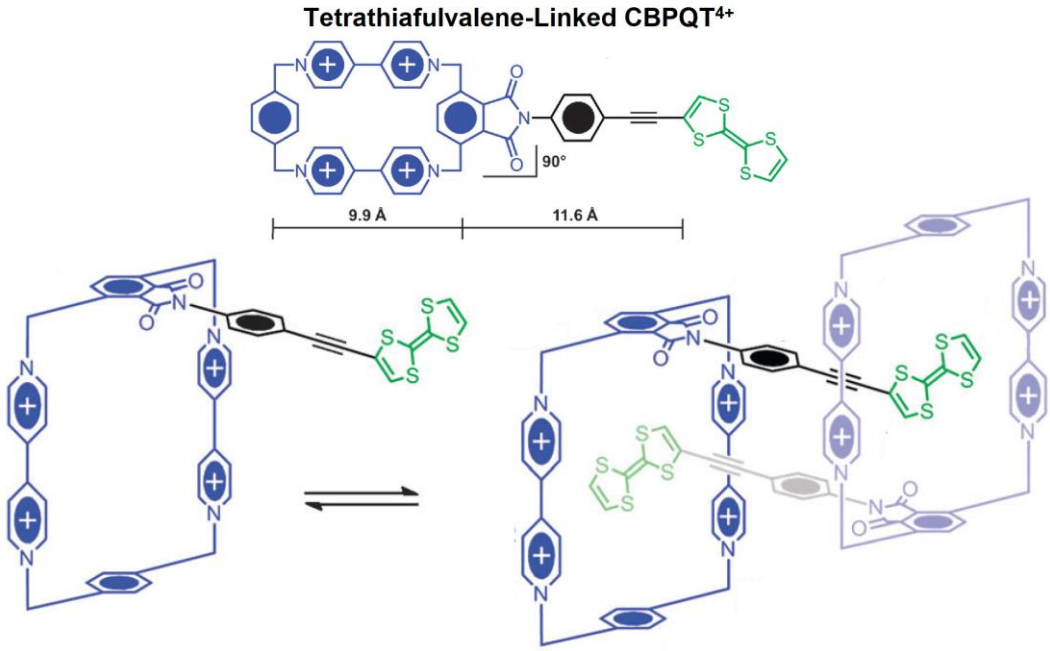

Figure 2.2 Chemical structure of a self-complementary tetrathiafulvalene-linked **CBPQT**$^{4+}$ and the proposed equilibrium between the monomer and dimer. Reproduced with permission from *Chem. Commun.* **2012**, *48*, 6791. Copyright 2012 The Royal Society of Chemistry.[7]

In order to explore further the self-assembly chemistry of the Texas-sized molecular box, we prepared a carboxyl-functionalized derivative termed "**TxSB-CO_2H**", as well as its conjugate base "**TxSB-CO_2^-**" (Scheme 2.1). **TxSB-CO_2H** and **TxSB-CO_2^-** are expected to produce dramatically different superarchitectures in solution and in the solid state.

This system was chosen for study because carboxylate anions are known to bind well to **2.1**$^{4+}$. In addition, switching between the acid (**TxSB-CO_2H**) and base (**TxSB-CO_2^-**) forms might result in the formation of two separate interlocked species exhibiting distinct molecular topologies. Finally, the short distance between the macrocyclic moiety (head) and the carboxylic acid (tail) was expected to preclude direct intramolecular self-association since the head cannot "bite" its own tail.[4] In fact, as discussed below, noncovalent dimerization of **TxSB-CO_2H** takes place in the solid state, albeit not in the competitive solvent, dimethyl sulfoxide (DMSO). In contrast, evidence for the stabilization of self-assembled oligomers of **TxSB-CO_2^-** is seen both in DMSO and in the solid state. The formation of disparate architectures from ostensibly similar building blocks is expected to advance our understanding of molecular self-assembly and provide insights into the design features needed to produce environmentally responsive supramolecular polymers.[2,9–12] As detailed below, interconversion between the monomeric form and the self-assembled oligomer can be effected via the sequential addition of triethylamine (TEA) and deuterated trifluoracetic acid (TFA-d_1).

2.1 RESULTS AND DISCUSSION

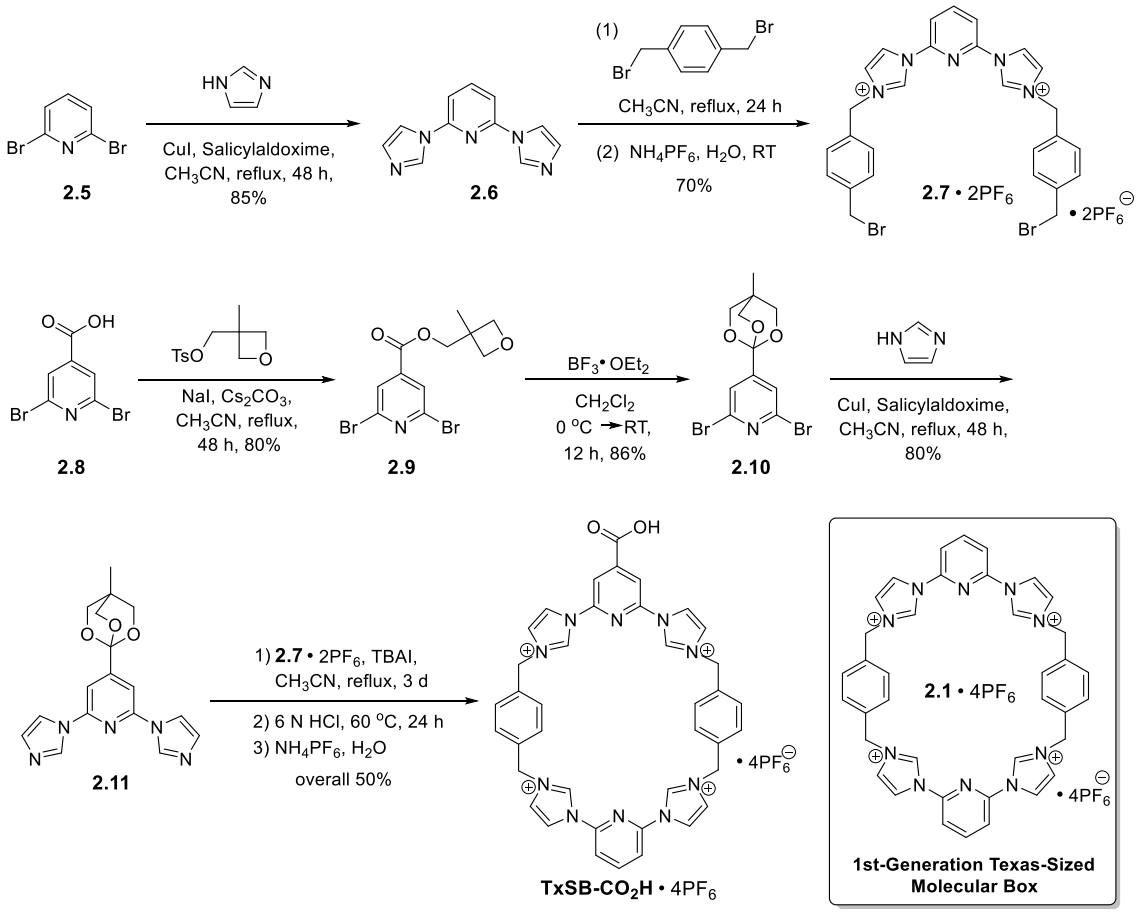

Scheme 2.1 Synthetic route used to prepare **TxSBCO₂H**·4PF_6 and chemical structure of the first-generation Texas-sized molecular box **2.1**·4PF_6

The synthesis of **TxSB-CO₂H** is summarized in Scheme 2.1. It relies on the coupling between two separate building blocks, namely **2.7**·2PF_6 and **2.11**. The acyclic dibromide **7**·2PF_6 was generated via an Ullmann-type coupling of the dibromopyridine **2.5** with imidazole to give diimidazolyl pyridine **2.6**.[13] Subsequent dialkylation of **6** with excess *p*-xylene dibromide gave **2.7**·2PF_6 after counter anion exchange.[14] The preparation of the diimidazolyl orthoester **2.11** began with an esterification of the carboxylic acid **2.8** to produce oxetane ester **2.9**.[15] This was followed by a BF_3-catalyzed isomerization to yield orthoester **2.10**,[16] which was further transformed into **2.11** via an Ullmann-type

coupling with imidazole. The reaction between **2.7**·2PF_6 and **2.11** was carried out under Finkelstein-like conditions in the presence of tetrabutylammonium iodide (TBAI).[17] The resulting crude orthoester-appended macrocyclic precursor was then subject to hydrolysis in 6 N HCl[18] before being treated with excess NH_4PF_6. This afforded the desired monocarboxylic acid-functionalized molecular box **TxSB-CO_2H**·4PF_6 in an overall yield of 50%.

Previous work with **2.1**$^{4+}$ revealed that treatment with hydroxide anion could lead to irreversible imidazolium ring opening and destruction of the macrocycle.[19] Decomposition of [**TxSB-CO_2H**]$^{4+}$ was seen when it was treated with tetrabutylammonium hydroxide (TBAOH) in DMSO-d_6 or with triethylamine (TEA) in D_2O (Figures 2.3 and 2.4). Fortunately, the fully deprotonated form, **TxSB-CO_2^-**, could be prepared by adding two or more equivalents of TEA[20] in DMSO-d_6, as inferred from ^{1}H NMR spectroscopic titrations (Figure 2.5). Precipitation of the resulting $HTEA^+$ salt was seen in most common organic solvents and in aqueous media. Therefore, DMSO and DMSO-d_6 were chosen as the primary solvents for studies involving **TxSB-CO_2^-**.

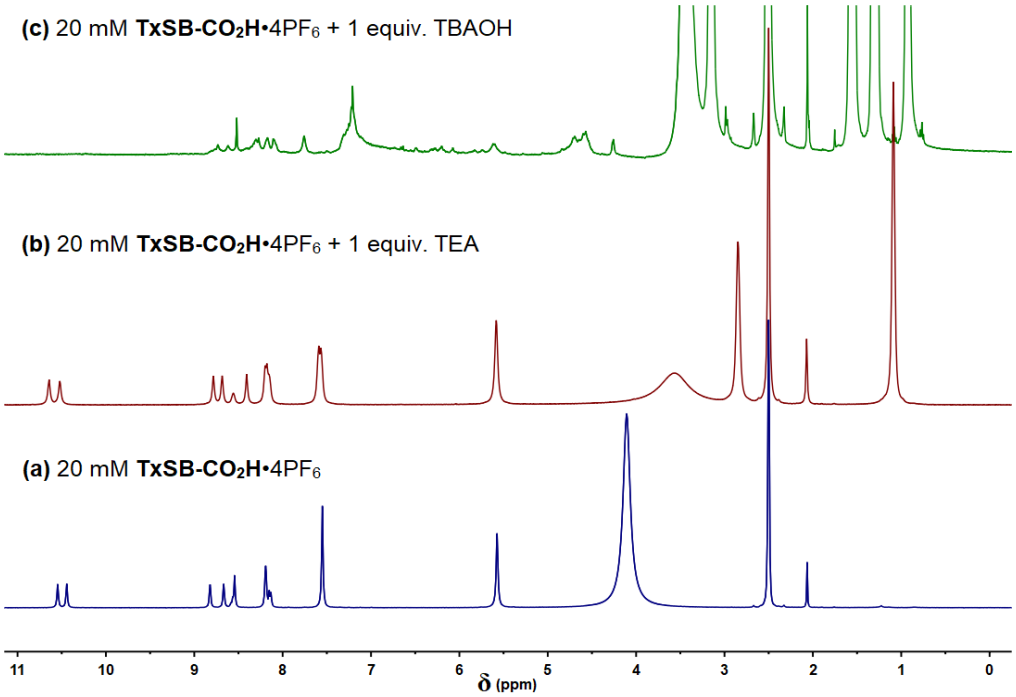

Figure 2.3 ^{1}H NMR spectroscopic comparisons among (a) **TxSB-CO$_2$H**·4PF$_6$, (b) an equimolar mixture of **TxSB-CO$_2$H**·4PF$_6$ and TEA, and (c) an equimolar mixture of **TxSB-CO$_2$H**·4PF$_6$ and TBAOH in DMSO-d_6 at 298K.

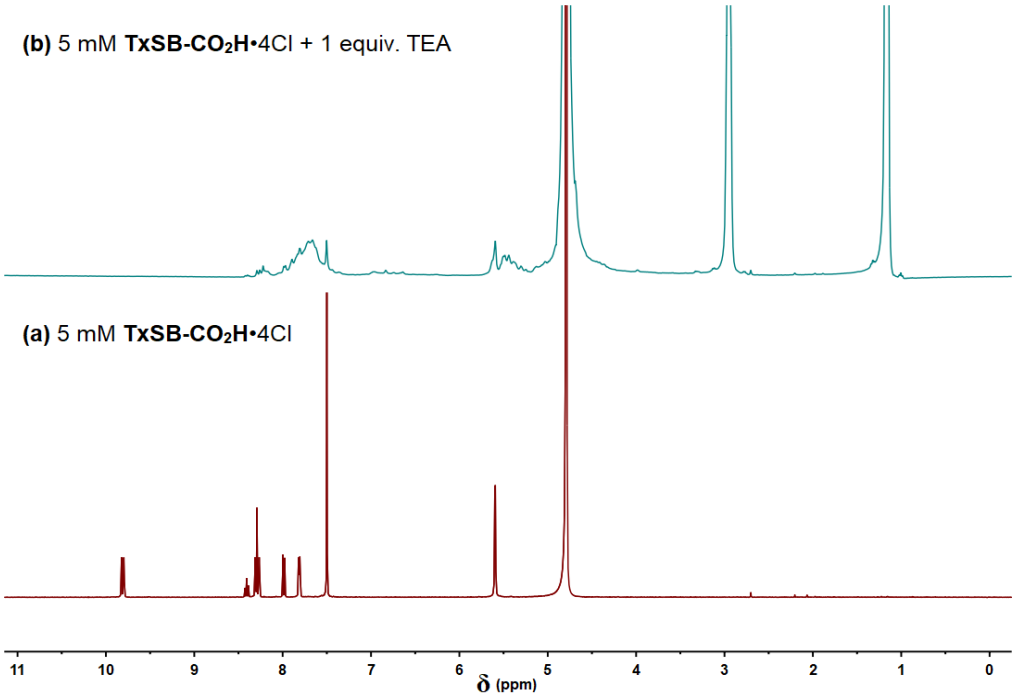

Figure 2.4 ^{1}H NMR spectroscopic comparisons between (a) **TxSB-CO$_2$H**·4Cl and (b) an equimolar mixture of **TxSB-CO$_2$H**·4Cl and TEA in D$_2$O at 298K.

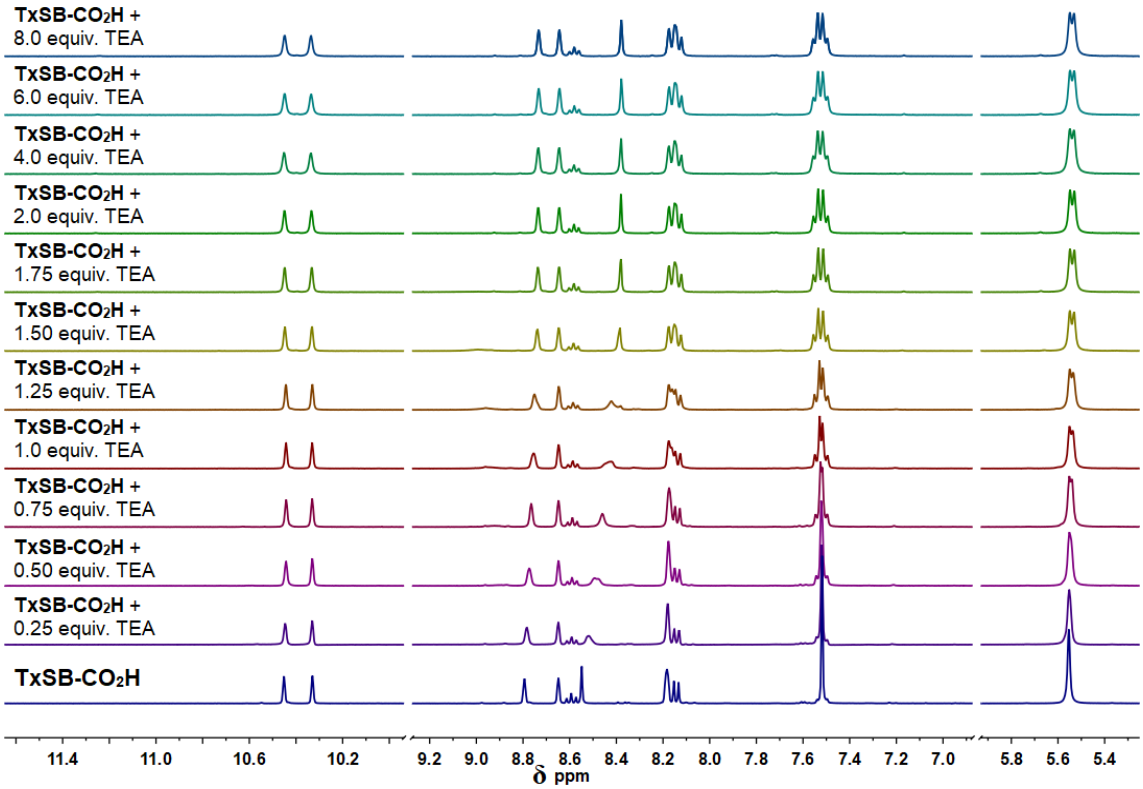

Figure 2.5 ^{1}H NMR spectroscopic titration of a 5 mM solution of **TxSB-CO$_2$H**·4PF$_6$ with increasing concentrations of TEA in DMSO-d_6 at 298K.

Single crystals of **TxSB-CO$_2$H** suitable for X-ray diffraction analysis were grown by slow diffusion of 2-propanol into a solution of **TxSB-CO$_2$H**·4PF$_6$ in DMSO containing a trace amount of trifluoroacetic acid (TFA). Inspection of the crystallographic data revealed that each single crystal includes five DMSO solvent molecules and four PF_6^- counter anions per **TxSB-CO$_2$H** unit (*i.e.*, [**TxSB-CO$_2$H**·4PF$_6$·5DMSO]), wherein two DMSO molecules are bound to the upper and lower rims, respectively, of the macrocycle and within the cavity formed as the result of the "clip-like" conformation adopted in the solid state (Figures 1a and 1b). Two clip-like monomers pair to form a head-to-tail dimer (*i.e.*, [**TxSB-CO$_2$H**]$_2$), in which the two carboxylic acid-bearing pyridine rings, as well as the two carboxylic acid groups, are paired in an antiparallel fashion (Figures 2.6 and 2.7). These dimers are further aggregated in the solid state to

form what can be considered as dimer-based constructs of net formula {[**TxSB-CO$_2$H**]$_2$}$_n$. Presumably, this oligomeric solid state architecture is produced via a nucleation-elongation mechanism that is operative during the course of crystallization (*cf.* Figure 2.8). Based on considerations of stoichiometry and literature precedence involving other self-associating systems, dimerization of **TxSB-CO$_2$H** to form [**TxSB-CO$_2$H**]$_2$ is thought to constitute the first step in this nucleation and crystallization process.[21,22]

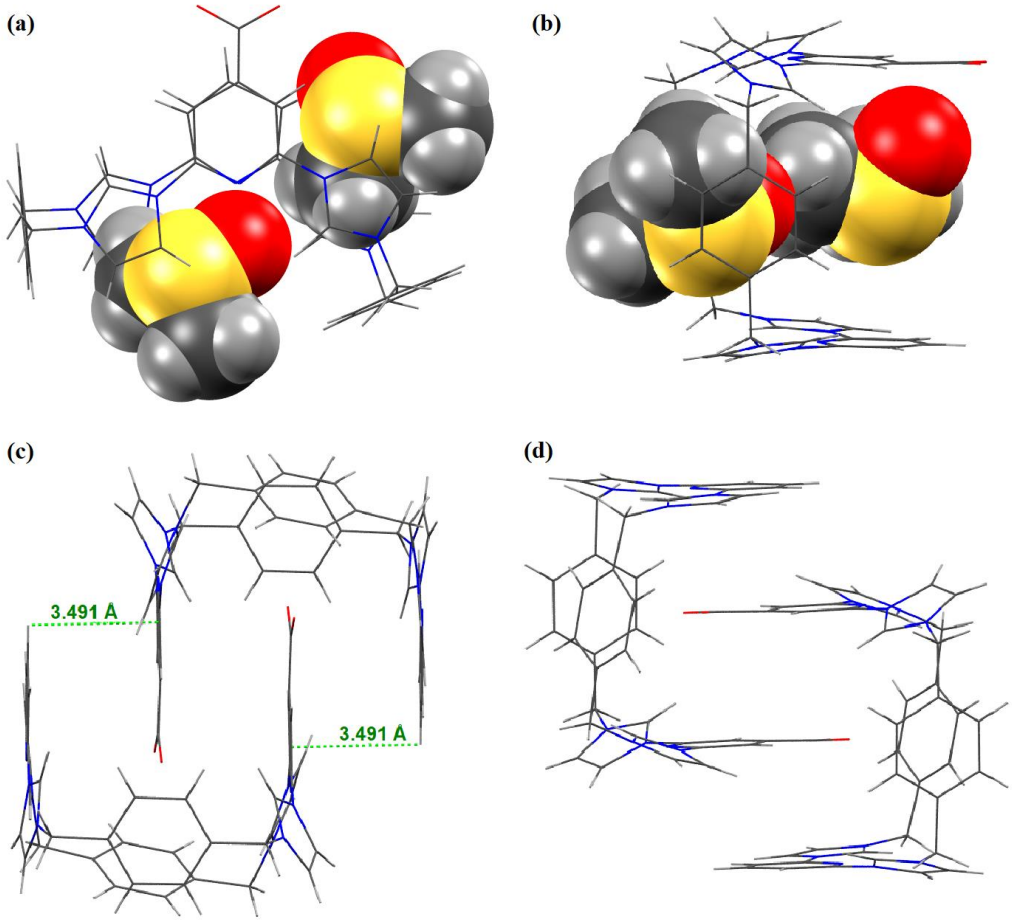

Figure 2.6 (a) Front and (b) side views of a single crystal X-ray diffraction structure of [**TxSB-CO$_2$H**·4PF$_6$·5DMSO] revealing a clip-like conformation for the macrocycle. Two DMSO molecules are bound within the cavity. Front (c) and side (d) views of the individual head-to-tail dimeric ensemble seen in the solid state. Some or all of the counter anions and solvent molecules have been omitted for clarity.

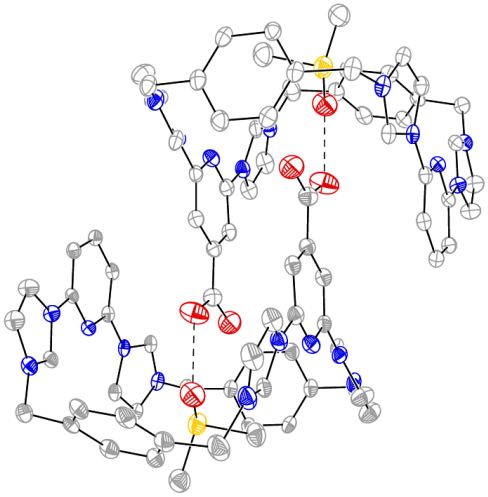

Figure 2.7 View of a noncovalent dimer formed in [**TxSB-CO$_2$H**·4PF$_6$·5DMSO]. Displacement ellipsoids are scaled to the 30% probability level. All hydrogen atoms, all counter anions, and some solvent molecules were omitted for clarity. The molecules are situated around a crystallographic inversion center at ½, ½, ½. Two sets of H-bonding formed between each in-cavity lower-rim-bound DMSO molecule and the carboxylic acid present in the complementary **TxSB-CO$_2$H** monomer are seen that presumably facilitate the mutual head-to-tail inclusion, thus supporting the formation of the resulting dimeric superstructure.

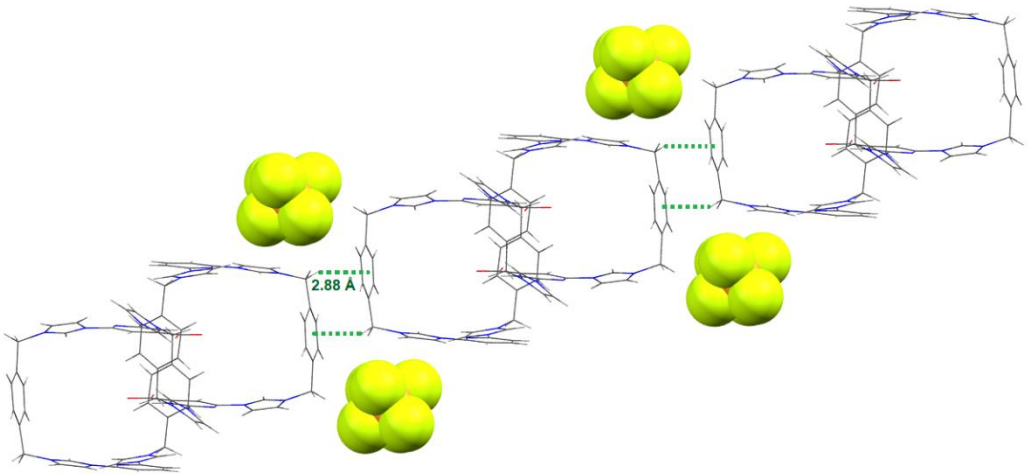

Figure 2.8 Truncated view of a dimer-based higher-order construct {[**TxSB-CO$_2$H**]$_2$}$_n$ seen in the solid state displaying the further association of discrete dimers through a cooperative nucleation-elongation mechanism in the solid state. Highlighted with green dashed lines are the intermolecular C–H···π interactions presumed to connect individual dimer complex moieties, as well as stabilize the formation of such higher-order self-assemblies. Multiple PF_6^- counterions are found to bridge the respective dimers, thus further strengthening the resulting self-assembled aggregates in the crystal structure. Some counterions and all solvent molecules are omitted for clarity.

As inferred from the X-ray single crystal analysis, a combination of noncovalent interactions serve to stabilize the solid-state interlocked dimer and higher order aggregates in the solid state; these consist of: (i) hydrogen-bonding interactions between each in-cavity lower-rim-bound DMSO molecule and the carboxylic acid of a complementary **TxSB-CO_2H** monomer (Figure 2.7); (ii) a pair of π-π donor–acceptor interactions between the substituted and non-substituted pyridine rings present within each pair of macrocycles; (iii) (C–H)···O interactions between the upper-rim-bound DMSO inside each cavity and the proximal aromatic rings present in the other member of the pair (Figure 2.9); (iv) multiple electrostatic and (C–H)···X^- interactions involving the associated PF_6^- counter anions (Figure 2.10).

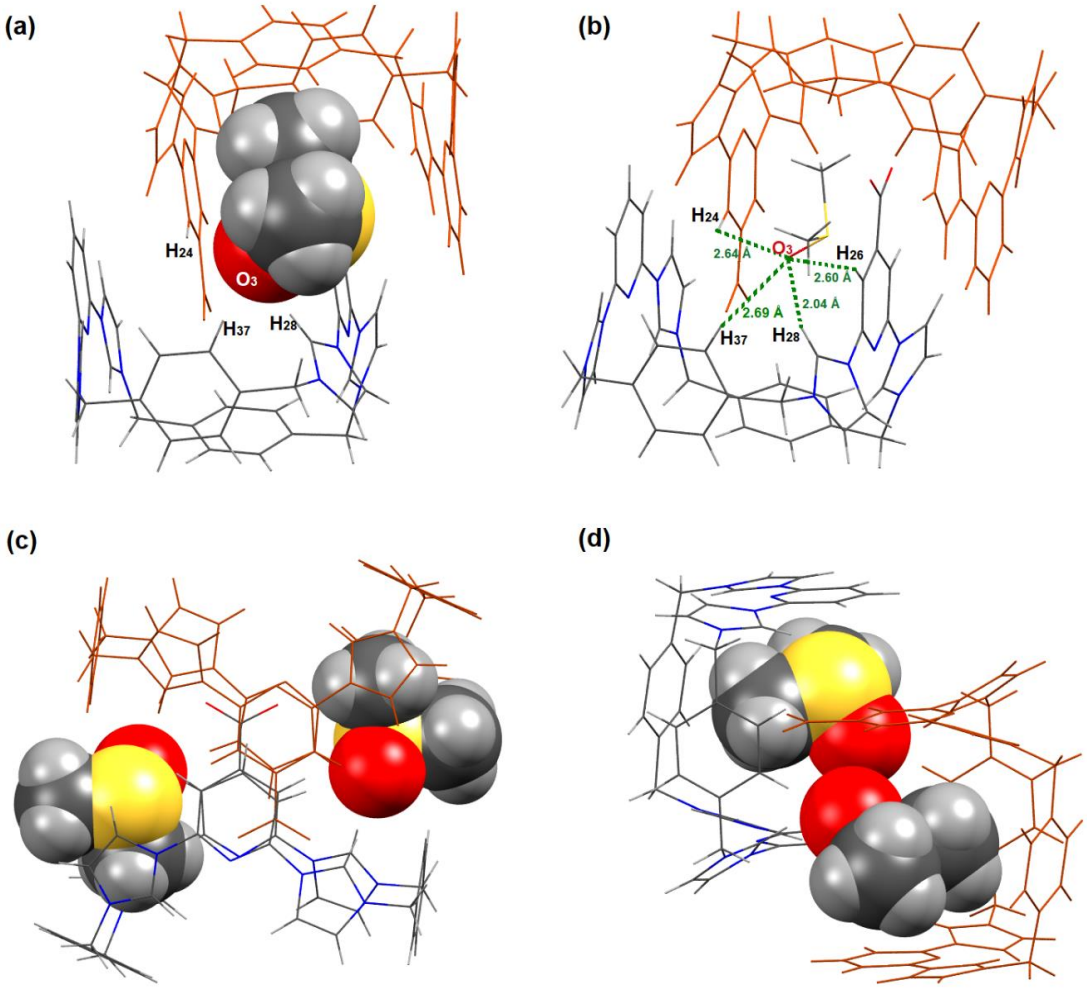

Figure 2.9 Different views of the single crystal X-ray diffraction structure of [**TxSB-CO$_2$H**·4PF$_6$·5DMSO]. Selected (C–H)···O interactions between a highlighted upper-rim-bound DMSO with the proximal aromatic rings are shown in (a) space-filling and (b) stick representations. The values shown in (b) are the interatomic distances between the designated hydrogen atom and the oxygen atom of the highlighted DMSO molecule. Shown in (c) and (d) are the complexation geometries and bridging environment of two upper-rim-bound DMSO molecules and two macrocyclic hosts inferred from the crystal structure of [**TxSB-CO$_2$H**·4PF$_6$·5DMSO]. Inspection of this structure leads us to propose that two sets of such (C–H)···O interactions play a significant role in stabilizing the dimeric architecture.

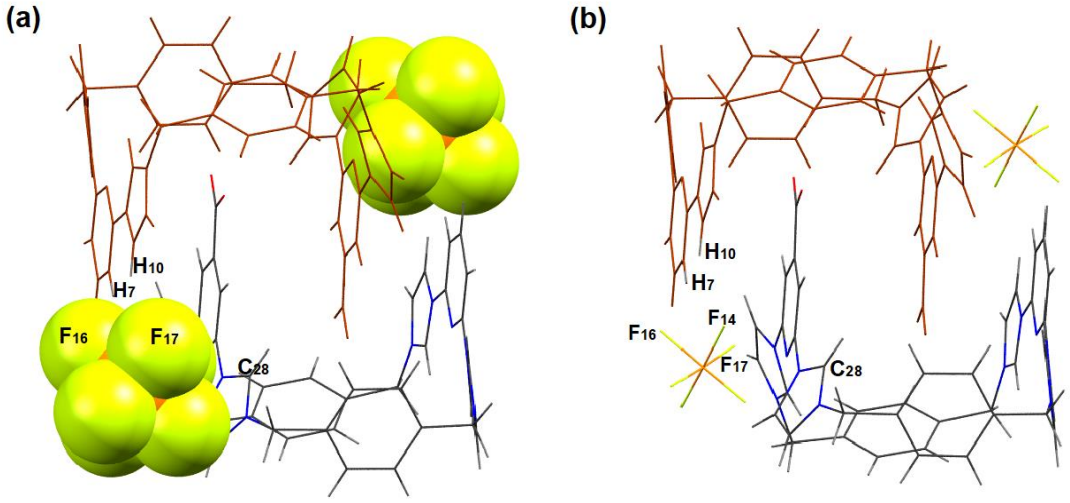

Figure 2.10 Complexation geometries and bridging environment of two selected surrounding PF_6^- anions and two macrocyclic monomers inferred from the crystal structure of [**TxSB-CO$_2$H**·4PF_6·5DMSO] are shown in (a) space-filling and (b) stick representations. These two PF_6^- anions are symmetric to one another with respect to the inversion center. From this structure it is presumed that the stabilizing interactions for this supramolecular dimer include a series of electrostatic ($C_{28}\cdots F_{14}$) and (C–H)$\cdots X^-$ interactions as determined using the selected interatomic distances [Å]: H(7)···F(14) 2.496, H(7)···F(16) 2.457, H(10)···F(16) 2.373, H(10)···F(17) 2.396, C(28)···F(14) 3.057. Identical noncovalent interactions are also observed between the diagonally opposite PF_6^- anion and the same two macrocyclic monomers. Inspection of this crystallographic analysis provides evidence for the conclusion that more than two peripheral PF_6^- anions serve to support the formation of the observed dimeric ensemble through a combination of electrostatic and (C–H)$\cdots X^-$ interactions.

In the case of **TxSB-CO$_2^-$**, diffraction grade single crystals were obtained via the slow vapor diffusion of 2-propanol into a DMSO solution containing **TxSB-CO$_2$H**·4PF_6 and excess TEA. The resulting X-ray analysis revealed a structure wherein **TxSB-CO$_2^-$** adopts a "boat-like" conformation in the solid state. Two DMSO molecules and three PF_6^- counter anions are found per **TxSB-CO$_2^-$** unit (*i.e.*, [**TxSB-CO$_2$**·3PF_6·2DMSO]). A single PF_6^- anion is enclosed within the cavity of **TxSB-CO$_2^-$** (Figures 2.11a and 2.11b).

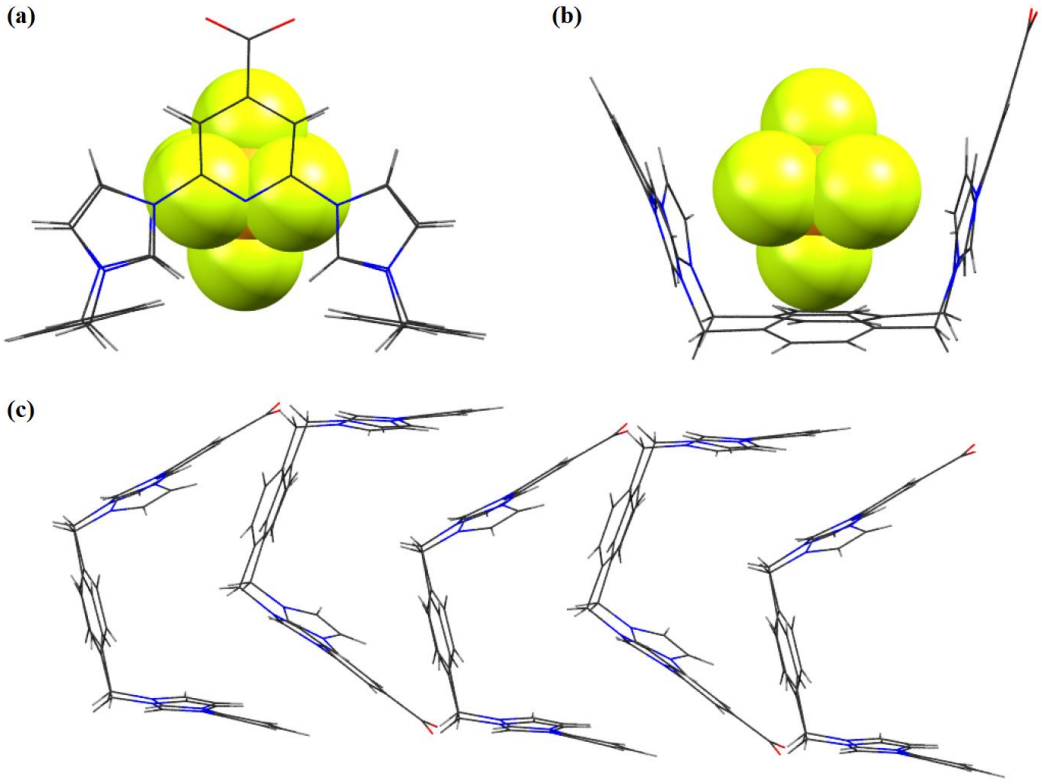

Figure 2.11 (a) Front and (b) side views of a single crystal X-ray structure of [**TxSB-CO$_2$**·3PF$_6$·2DMSO]$^-$ showing the boat-like conformation of the carboxylate anion-functionalized macrocycle. One PF$_6^-$ counter anion is held within the macrocycle cavity and between two opposing aromatic faces. Shown in (c) is a truncated view of the head-to-tail polymeric chain structure of **TxSB-CO$_2^-$** seen in the solid state. Some or all of the counter anions and solvent molecules have been omitted for clarity.

In the solid state, individual **TxSB-CO$_2^-$** subunits self-associate in a head-to-tail orientation to give a polymeric superstructure (*i.e.*, [**TxSB-CO$_2^-$**]$_n$). Both the cavity-bound PF$_6^-$ anion and the anionic carboxylate motifs are involved in numerous (C–H)$\cdots$ X$^-$ bonding interactions, which presumably play a significant role in directing the self-assembly process (Figures 2.11c and 2.12–2.14).

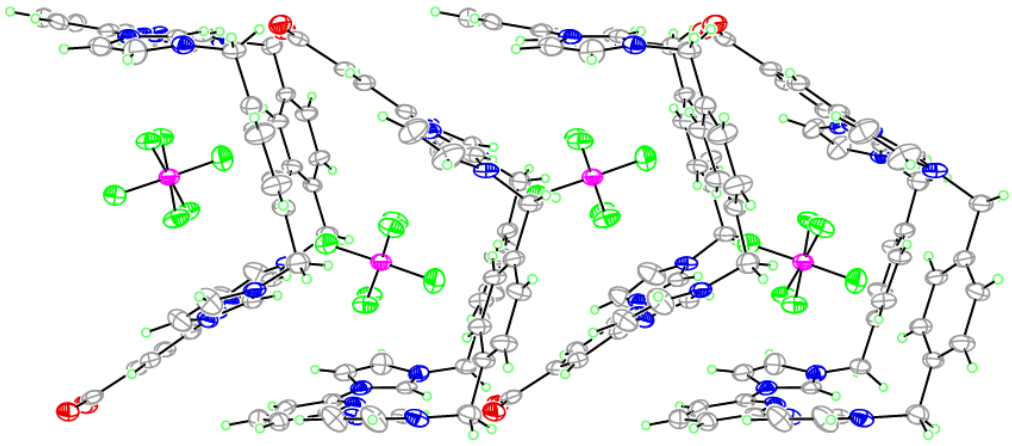

Figure 2.12. View of the macrocycle and an encapsulated hexafluorophosphate anion seen in this solid state structure of [**TxSB-CO$_2$**·3PF$_6$·2DMSO] showing the stacking of the complex along the c-axis. Displacement ellipsoids are scaled to the 50% probability level.

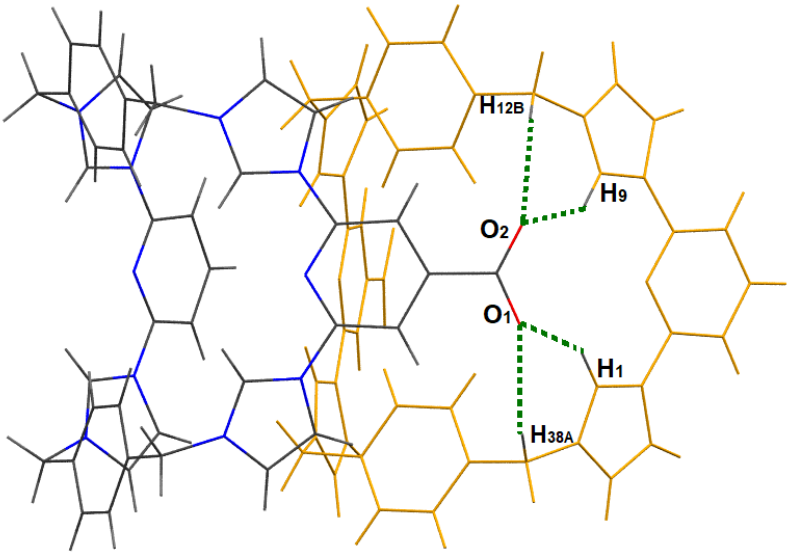

Figure 2.13 Truncated stick structure view of the polymer, [**TxSB-CO$_2$**$^-$]$_n$, seen in the solid state, showing stacking between two selected repeating units is inferred from the crystal structure of [**TxSB-CO$_2$**·3PF$_6$·2DMSO]. All the solvent molecules and counter anions are omitted for clarity. The presence of possible (C–H)$\cdots$X$^-$ interactions stabilizing the resulting polymeric ensemble was inferred from the following interatomic distances [Å]: H(1)$\cdots$O(1) 2.027, H(9)$\cdots$O(2) 2.095, H(38A)$\cdots$O(1) 2.455, H(12B)$\cdots$O(2) 2.380.

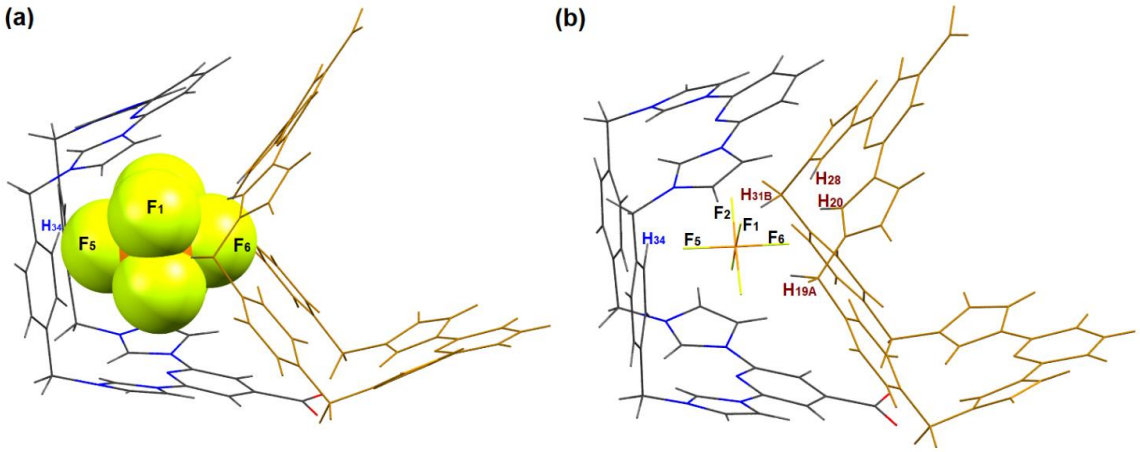

Figure 2.14 Complexation geometries and bridging environment of an in-cavity PF_6^- anion and two proximal **TxSB-CO₂**$^-$ monomers as inferred from the crystal structure of [**TxSB-CO₂**·3PF_6·2DMSO]. The structures are shown in (a) space-filling and (b) stick representations. This crystallographic analysis provides support for the suggestion that the polymeric superstructure is stabilized by numerous (C–H)···X^- interactions as determined from the selected interatomic distances [Å]: H(19A)···F(1) 2.656, H(20)··· F(1) 2.449, H(20)···F(6) 2.353, H(28)···F(2) 2.552, H(28)···F(6) 2.326, H(31B)···F(2) 2.639, H(34)···F(5) 2.644. Multiple "outside-cavity" PF_6^- anions may also support the formation of this polymeric construct through electrostatic and (C–H)···X^- interactions with the adjacent macrocyclic repeating units.

In an initial effort to determine whether the self-associated structure of **TxSB-CO_2H**, namely $\{[\mathbf{TxSB\text{-}CO_2H}]_2\}_n$, or the constituent dimer, $[\mathbf{TxSB\text{-}CO_2H}]_2$, observed in the solid state would be retained in solution, the sample as prepared (**TxSB-CO_2H**·$4PF_6$) was studied DMSO-d_6 by means of ^{1}H NMR spectroscopy. One-dimensional ^{1}H NMR spectra recorded as the concentration was increased from 5 to 70 mM (Figure 2.15a) revealed signal broadening and concentration-induced downfield shifts in the imidazolium C–H resonance H_3. The associated changes were plotted versus concentration and used to construct a binding isotherm. Assuming a cooperative nucleation-elongation model, an effective association constant K_a of 2300 ± 400 M^{-1} could be calculated via standard curve fitting (Equation 1). This allows use of an iterative algorithm to determine the association constant K_a, as well as δ_m and δ_e, from the dilution chemical shift data corresponding to a mechanism involving formation of a dimer and then further aggregation as shown below:[23]

$$\delta_{obs} = \delta_e + (\delta_e - \delta_m)\left(\frac{1+(1-\sqrt{4K_aC+1})}{2K_aC}\right) \quad \text{(Equation 1)}$$

where δ_{obs} is the observed chemical shift at a given concentration of C, δ_m is the monomer chemical shift, and δ_e is the chemical shift of the cooperative self-assembled complex. All chemical shifts are in ppm.[23]

DOSY spectral analysis of as-prepared **TxSB-CO_2H** revealed a decrease in the diffusion coefficient corresponding to the H_3 resonance from 1.97×10^{-10} m^2/sec to 1.30×10^{-10} m^2/sec as the sample concentration was increased from 0.5 to 70 mM (Figures 2.17a and 2.18).

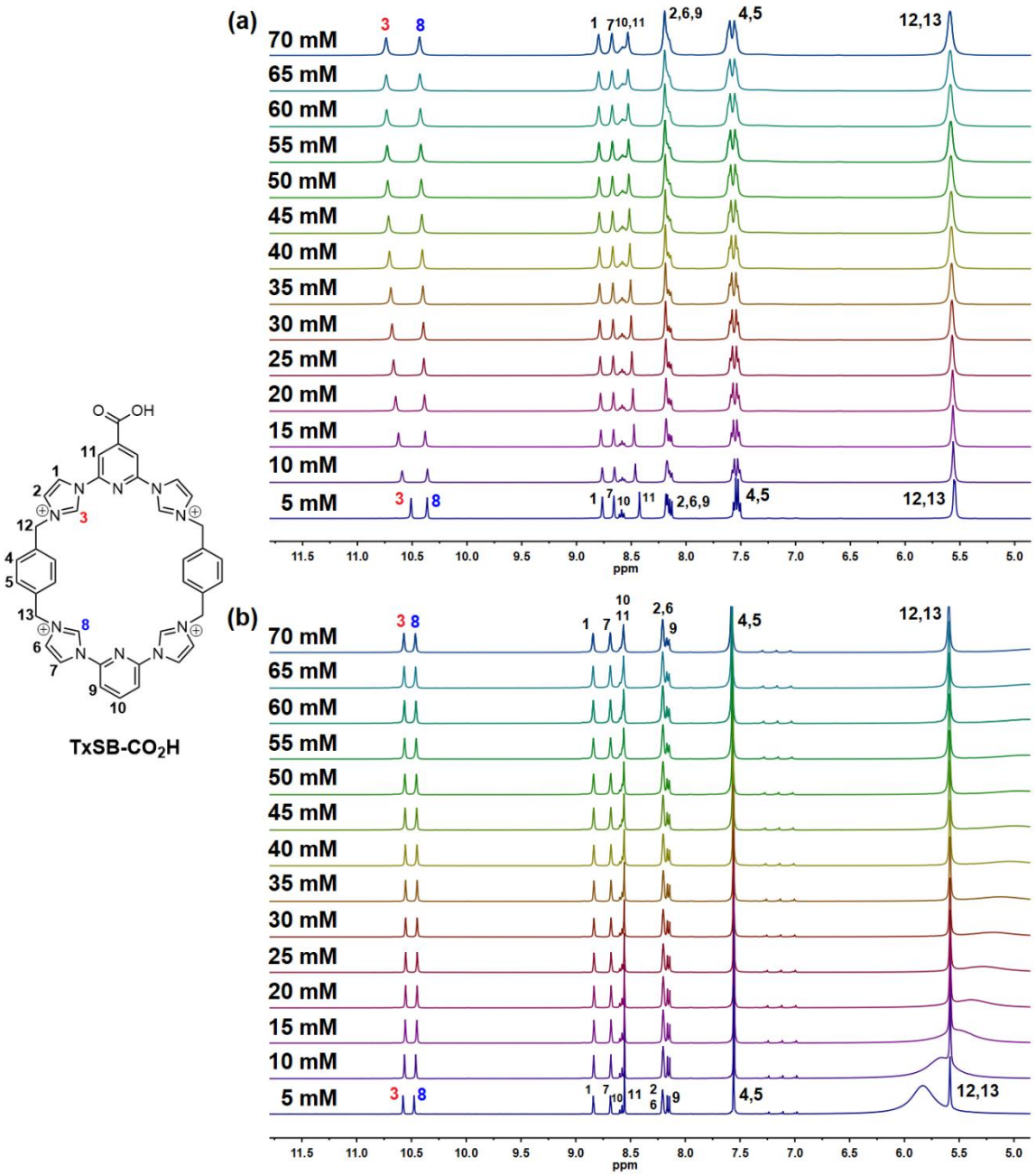

Figure 2.15 Concentration-dependent 400 MHz ^{1}H NMR spectra of **TxSB-CO$_2$H**·4PF$_6$ as recorded in DMSO-d_6 in the absence (a) and presence of 1% TFA-d_1 by weight (b) at 298K (using TMS as an internal reference).

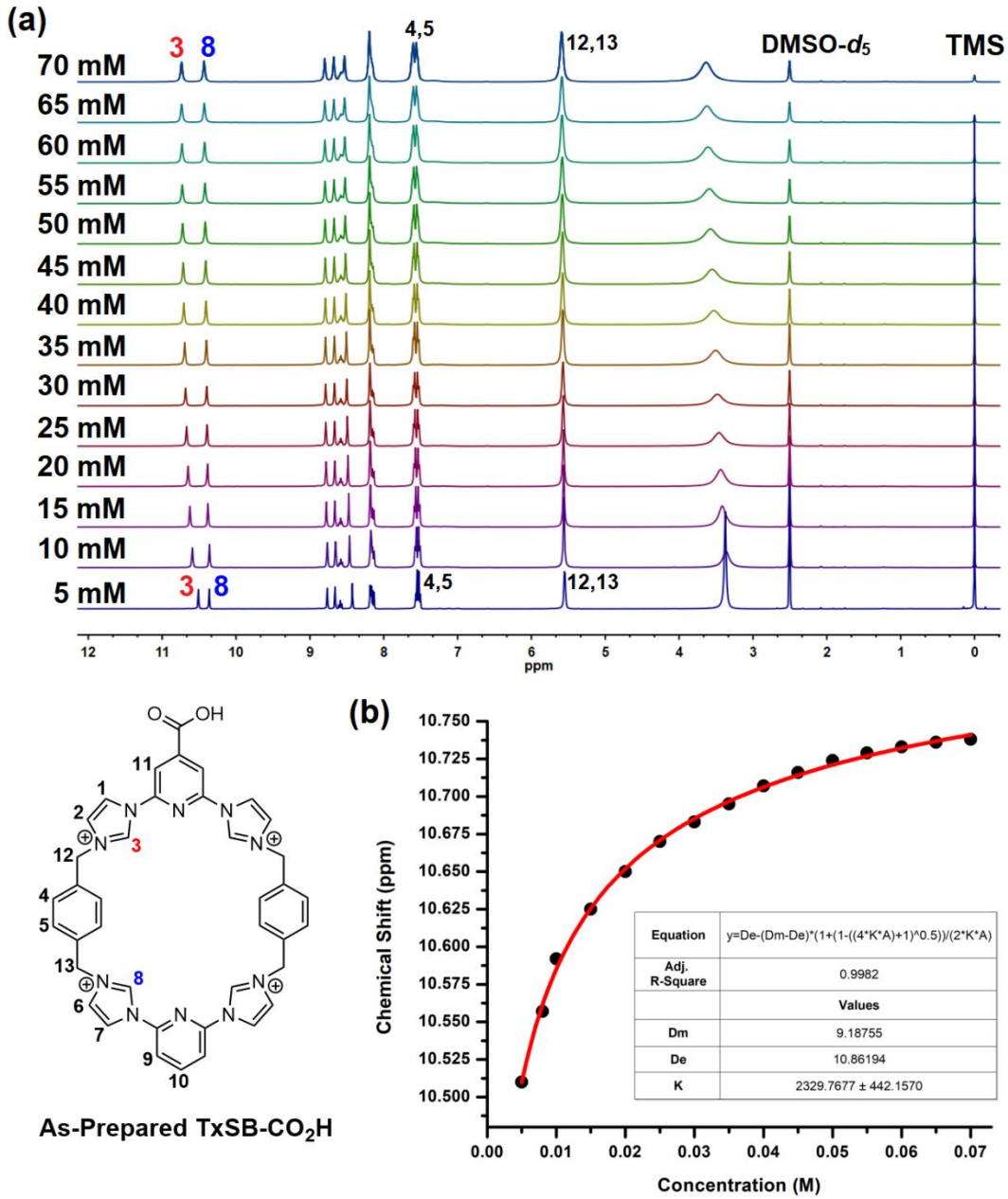

Figure 2.16 (a) Concentration-dependent 400 MHz ^{1}H NMR spectra of as-prepared **TxSB-CO$_2$H**·4PF$_6$ in DMSO-d_6 at 298K (TMS was used as an inert internal reference). The lowest field proton, H$_3$, undergoes the greatest downfield shift in response to variations in the concentration. The binding isotherm shown in (b) was obtained by plotting the resonance frequency of H$_3$ as a function of concentration. Fitting the curve to a cooperative self-association profile corresponding to a cooperative assembling process (Equation 1) allowed an effective association constant, K_a, of 2300 ± 400 M^{-1} to be calculated. Curve fitting was performed using Origin Pro 8.5 (OriginLab, Northampton, MA).

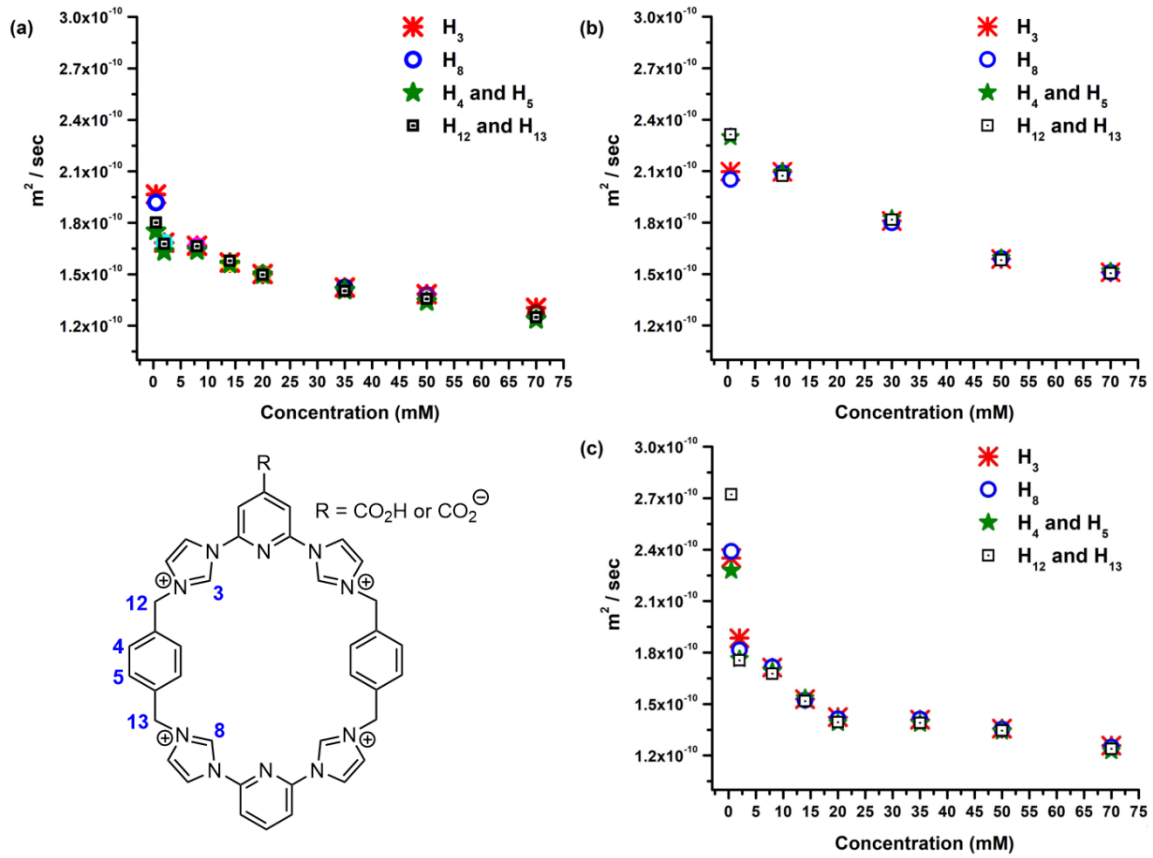

Figure 2.17 Diffusion coefficients (*D*) calculated for selected protons signals seen in the DOSY NMR spectra of (a) as-prepared **TxSB-CO_2H**, (b) **TxSB-CO_2H** in the presence of 1% TFA-d_1, and (c) **TxSB-CO_2^-** recorded at varying concentrations (0.5–70 mM) in DMSO-d_6 at 298 K. Values were obtained using the mono-exponential fitting approach and the MestReNova software (Mesterlab Research SL, Santiago, Spain), Version 6.1.0-6224.

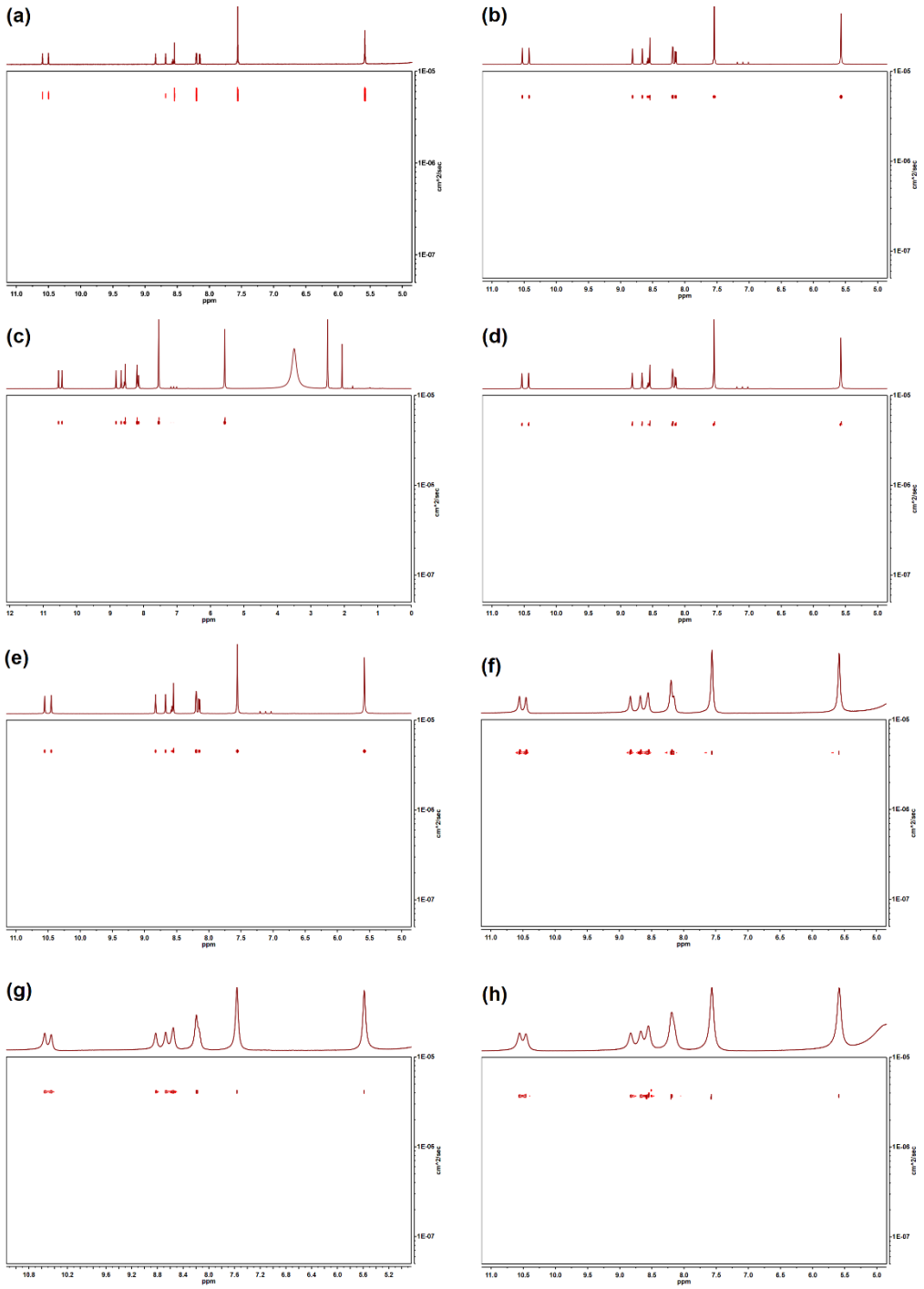

Figure 2.18 Expanded 600 MHz DOSY NMR spectra of as-prepared **TxSB-CO_2H** recorded at concentrations of (a) 0.5, (b) 2.0, (c) 8.0, (d) 14, (e) 20, (f) 35, (g) 50, and (h) 70 mM in DMSO-d_6 at 298 K

Left undetermined by the above study was the specific nature of the interactions leading to the concentration-dependent spectral shifts and hence the determinants of the inferred self-association. Initially, they were thought to mirror the weak non-covalent effects seen in the solid state crystal structure of **TxSB-CO_2H** (as deduced from the metric parameters; vide supra). However, in the context of peer review, a referee noted that aggregation could arise from the presence of the basic form (**TxSB-CO_2^-**) produced via deprotonation in the relatively polar DMSO-d_6 medium. To test this possibility, a concentration dependence study analogous to that discussed above was carried out in the presence of 1% TFA-d_1 by weight. Now, little in the way of concentration-dependent spectral changes were observed (Figure 2.15b). However, a concentration-dependent DOSY analysis revealed a slight decrease in the diffusion coefficient associated with the H_3 resonance from 2.10×10^{-10} m^2/sec at 0.5 mM to 1.51×10^{-10} m^2/sec at 70 mM (Figures 2.17b and 2.19). We thus conclude that when **TxSB-CO_2H** is present in its fully protonated form little if any self-association occurs except possibly at the highest accessible concentrations in DMSO-d_6. This may reflect a lack of electrostatic interaction between the individual **TxSB-CO_2H** subunits. However, it is also possible that competition with the trifluoroacetate anion (produced as the result of solvent-induced deprotonation) limits the self-aggregation of **TxSB-CO_2H**. The solution phase behavior of **TxSB-CO_2H** thus stands in contrast to what might be inferred from the solid state structure or from an analysis of the as-prepared material in the absence of added acid.

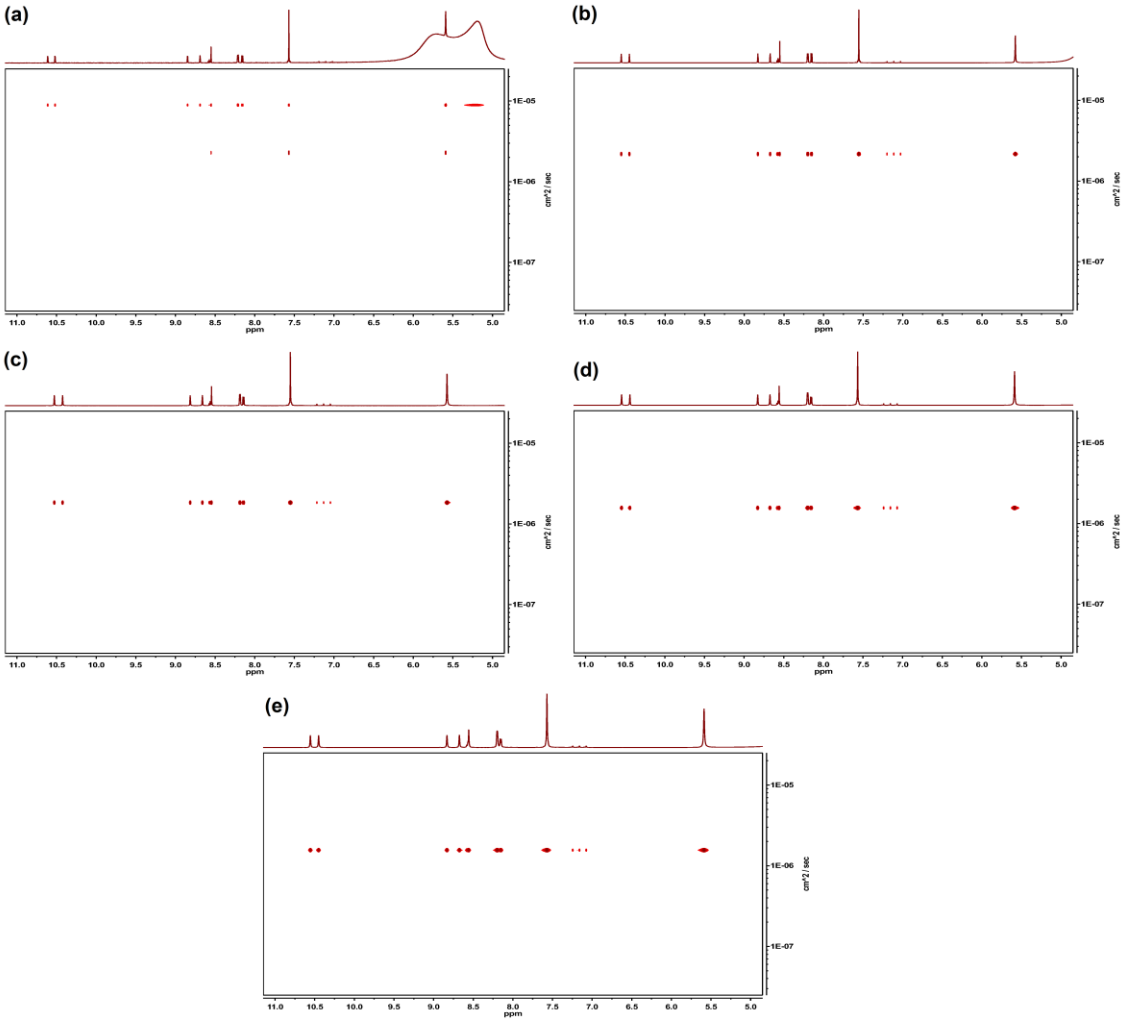

Figure 2.19 Expanded 600 MHz DOSY NMR spectra of **TxSB-CO_2H** recorded at concentrations of (a) 0.5, (b) 10, (c) 30, (d) 50, and (e) 70 mM in DMSO-d_6 containing 1% TFA-d_1 by weight at 298 K.

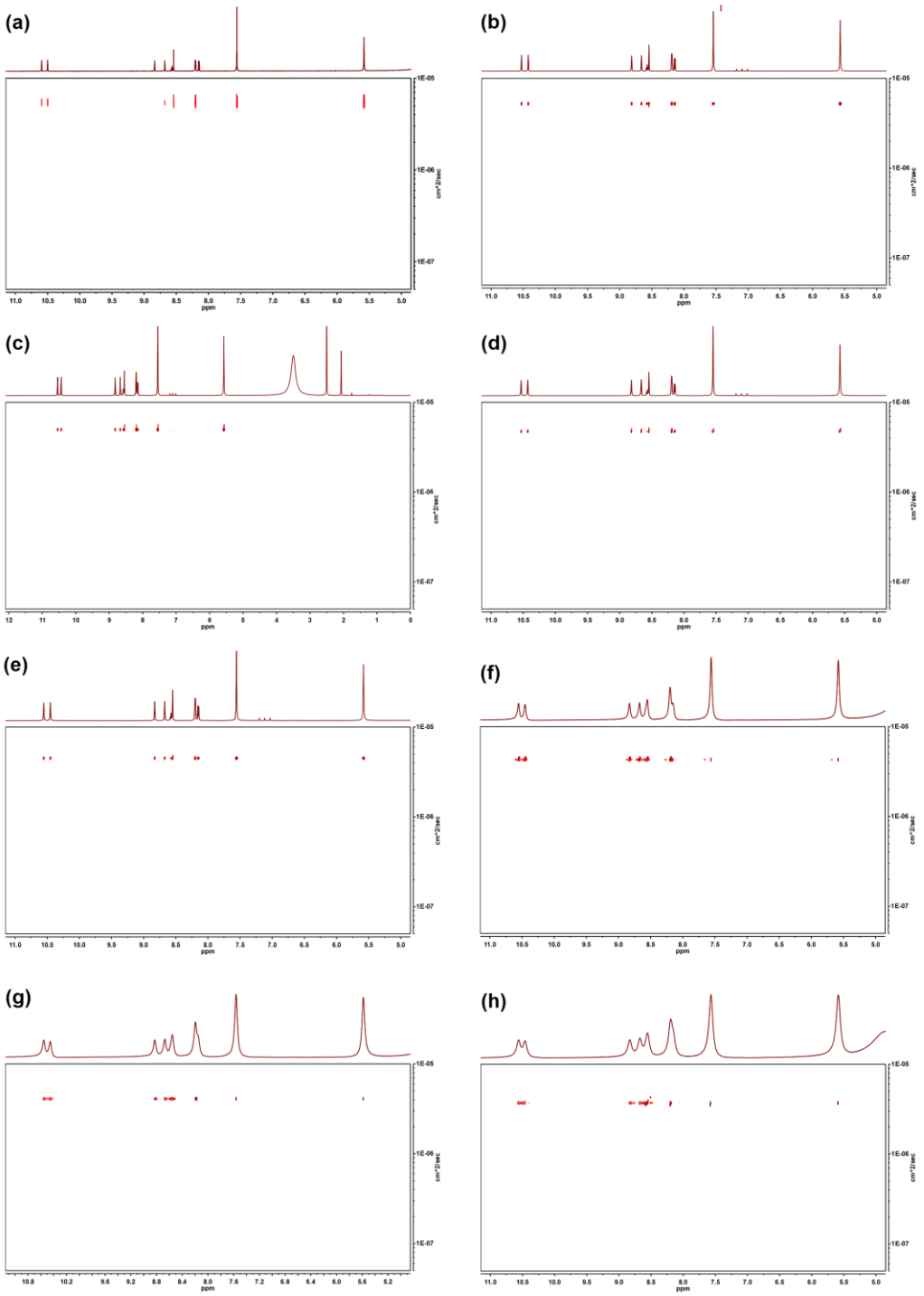

Figure 2.20 Expanded 600 MHz DOSY NMR spectra of **TxSB-CO_2^-** recorded at concentrations of (a) 0.5, (b) 2.0, (c) 8.0, (d) 14, (e) 20, (f) 35, (g) 50, and (h) 70 mM in DMSO-d_6 at 298 K.

Concentration-dependent ^{1}H NMR spectroscopic analyses were also used to probe the self-association chemistry of the deprotonated form of **TxSB-CO$_2$H** (*i.e.*, **TxSB-CO$_2^-$**) produced from a 1:2.5 mixture of **TxSB-CO$_2$H** and TEA in DMSO-d_6. For instance, the ^{1}H–^{1}H NOESY spectrum of the **TxSB-CO$_2^-$** anion recorded at a concentration of 20 mM revealed a through-space coupling between H_{11} and H_{13}. Analogous features were observed for an otherwise identical 2 mM solution (Figure 2.21). The correlations observed at both concentrations were fully consistent with what was inferred from the solid-state head-to-tail polymeric ensemble [**TxSB-CO$_2^-$**]$_n$ as shown in Figure 2.21a.

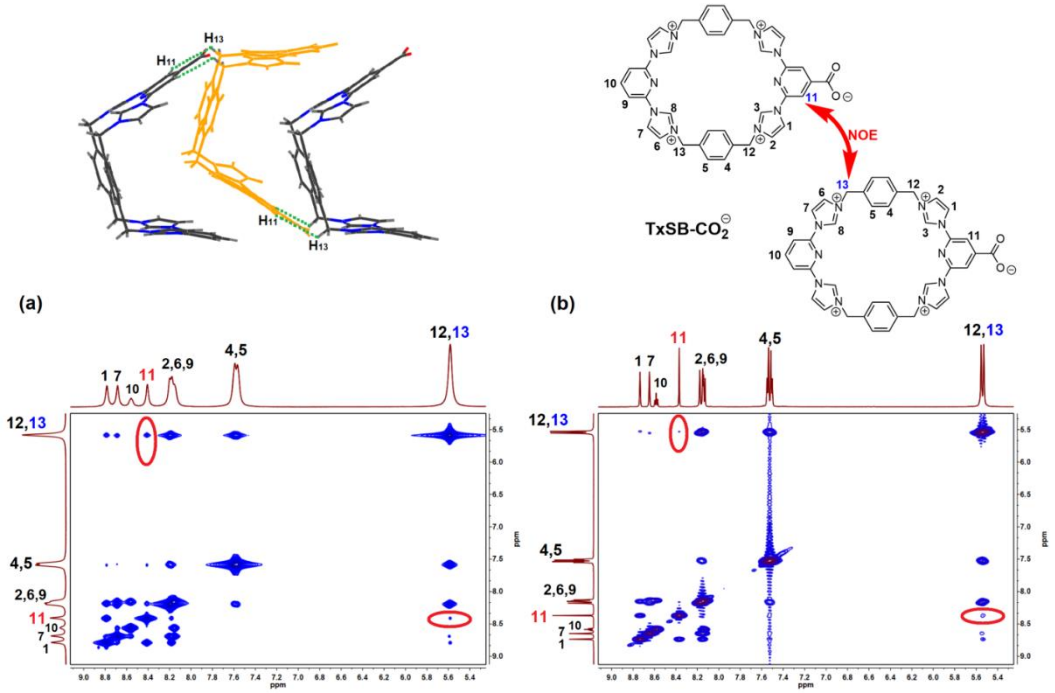

Figure 2.21 Truncated view (a) of the solid-state structure of [**TxSB-CO$_2^-$**]$_n$ showing the short separation (less than 3.0 Å) between the indicated protons. (b) Expanded regions of interest of the 600 MHz ^{1}H–^{1}H NOESY NMR spectrum of a 20 mM solution of **TxSB-CO$_2^-$** recorded in DMSO-d_6 at 298 K at the mixing time of 800 ms. Shown in (c) is an expanded view of a portion of the NOESY spectrum for a 2 mM sample measured using the same analytical method. The red circles in (b) and (c) highlight the symmetrical off-diagonal cross-peaks that are found in the NOESY NMR spectra recorded for both 20 mM and 2.0 mM solutions of **TxSB-CO$_2^-$**. Such a finding provides evidence for the proposed supramolecular polymerization of **TxSB-CO$_2^-$**, an inferred aggregation process that is dependent on the overall monomer concentration in the solution state.

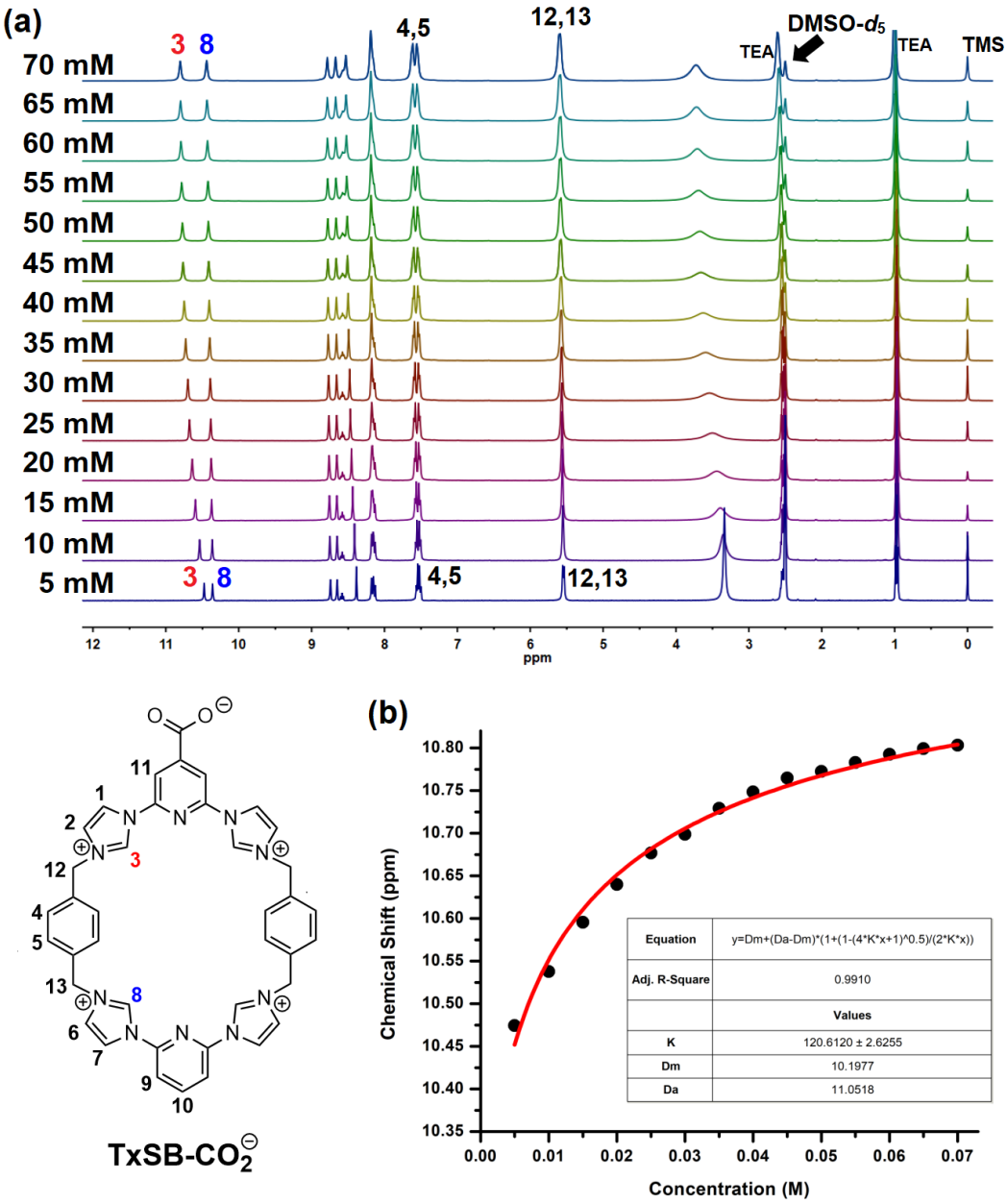

Figure 2.22 (a) Concentration-dependent 400 MHz ^{1}H NMR spectra recorded for **TxSB-CO_2^-** in DMSO-d_6 at 298K (TMS was added as an inert internal reference). The lowest field proton, H_3, undergoes the largest downfield shifts in response to an increase in concentration. The ^{1}H NMR isotherm shown in (b) was obtained by plotting the chemical shift of H_3 as a function of concentration. Fitting the curve to a reversible polymerization model allowed an estimated equilibrium constant, K_{eq}, of 120 ± 2 M^{-1} to be calculated. Curve fitting was performed using Origin Pro 8.5 (OriginLab, Northampton, MA).

Further support for the conclusion that higher monomer concentrations favored the self-association of **TxSB-CO_2^-** came from concentration-dependent ^{1}H NMR spectroscopic studies of **TxSB-CO_2^-** in DMSO-d_6 (5−70 mM) as shown in Figure 2.22. In analogy to what was seen in the case of **TxSB-CO_2H**, less-well resolved and broader peaks were seen over the full spectral region with apparent downfield shifts being observed for both imidazolium C−H resonances, of which the most downfield-shifted signal was that for H_3. These findings mirror what was seen previously in the case of the complex formed between **2.1**$^{4+}$ and the mono-terephthalate anion, a discrete monomer that self-assembles into polyrotaxane chains.[25]

By observing the concentration-dependent chemical shift changes of H_3 in **TxSB-CO_2^-**, a titration isotherm curve could be plotted and fitted using Equation 3, where δ_{obs} is the observed chemical shift at a given concentration of C, δ_m is the monomer chemical shift, and δ_p is the polymer chemical shift. All chemical shifts are specified in ppm.[26]

$$\delta_{obs} = \delta_m + (\delta_p - \delta_m)\left(1 + \frac{1-\sqrt{4K_{eq}C+1}}{2K_{eq}C}\right) \quad \text{(Equation 3)}$$

By using this non-linear fitting approach, the polymerization constant K_{eq}, as well as δ_m and δ_p, were determined from the dilution chemical shift data corresponding to a reversible monomer-polymer interconversion.[26]

Using the estimated equilibrium constant K_{eq} (120 M^{-1}) and a particular concentration (C value) in conjunction with Equation 4, allowed an average degree of polymerization (DP) of ~5 to be calculated for **TxSB-CO_2^-** at a concentration of 70 mM.[27]

$$DP = \frac{4K_{eq}C}{-1+\sqrt{1+8K_{eq}C}} \quad \text{(Equation 4)}$$

As detailed above, the chemical shift changes occurring to H_3 observed in the concentration-dependent ^{1}H NMR spectroscopic studies were monitored and plotted versus concentration to determine the polymerization equilibrium constant and the average degree of polymerization (*DP*) at 70 mM (using Equation 4). The *DP* was also calculated from the DOSY data (Figures 2.17c and 2.20) obtained at 70 mM using the diffusion coefficients corresponding to H_3 as obtained from Equation 2.[24]

$$DP(DOSY) \approx \left(\frac{D(0.5\ mM)}{D(70\ mM)}\right)^3 \quad \text{(Equation 2)}$$

where D(0.5 mM) = 2.35 × 10^{-10} m^2/sec and D(70 mM) = 1.26 × 10^{-10} m^2/sec.

The average degree of polymerization for **TxSB-CO$_2^-$** at 70 mM could therefore be estimated as *DP*(DOSY) ≈ 6. This value matches well the average *DP* value of 5 estimated from the concentration-dependent ^{1}H NMR spectroscopic analysis. The good concordance between the *DP* values obtained from the curve fits and the DOSY measurements leads to the conclusion that at relatively high, but still accessible, concentrations **TxSB-CO$_2^-$** exists in the form of short self-associated oligomers in DMSO solution.

A similar concentration-dependent ^{1}H NMR spectral analysis of the non-functionalized Texas-sized box (**1**·4PF_6) was also carried out in DMSO-d_6 (5−70 mM). This was done as a control experiment for the above studies. In contrast to what was seen for **TxSB-CO$_2$H** and **TxSB-CO$_2^-$**, no significant signal broadening and concentration-induced downfield shifts were observed in the case of **2.1**·4PF_6 (Figures 2.23). The difference between the parent system and the carboxyl and carboxylate derivatives provides support for the conclusion that the presence of a carboxylic acid or anionic carboxylate functionality endows novel stimuli-responsive supramolecular properties.

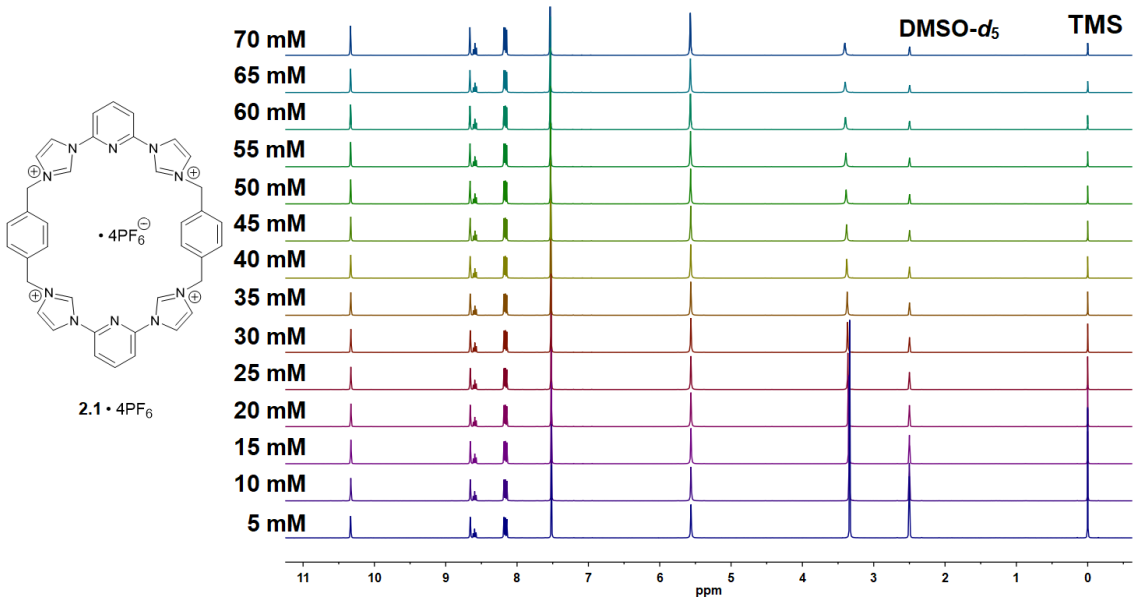

Figure 2.23 Concentration-dependent 400 MHz ^{1}H NMR spectra recorded for the non-functionalized 'Texas-sized' box **2.1**·4PF$_6$ in DMSO-d_6 at 298K (TMS was used as an inert internal reference). No significant signal broadening or concentration-induced downfield shifts were observed in the case of **2.1**·4PF$_6$.

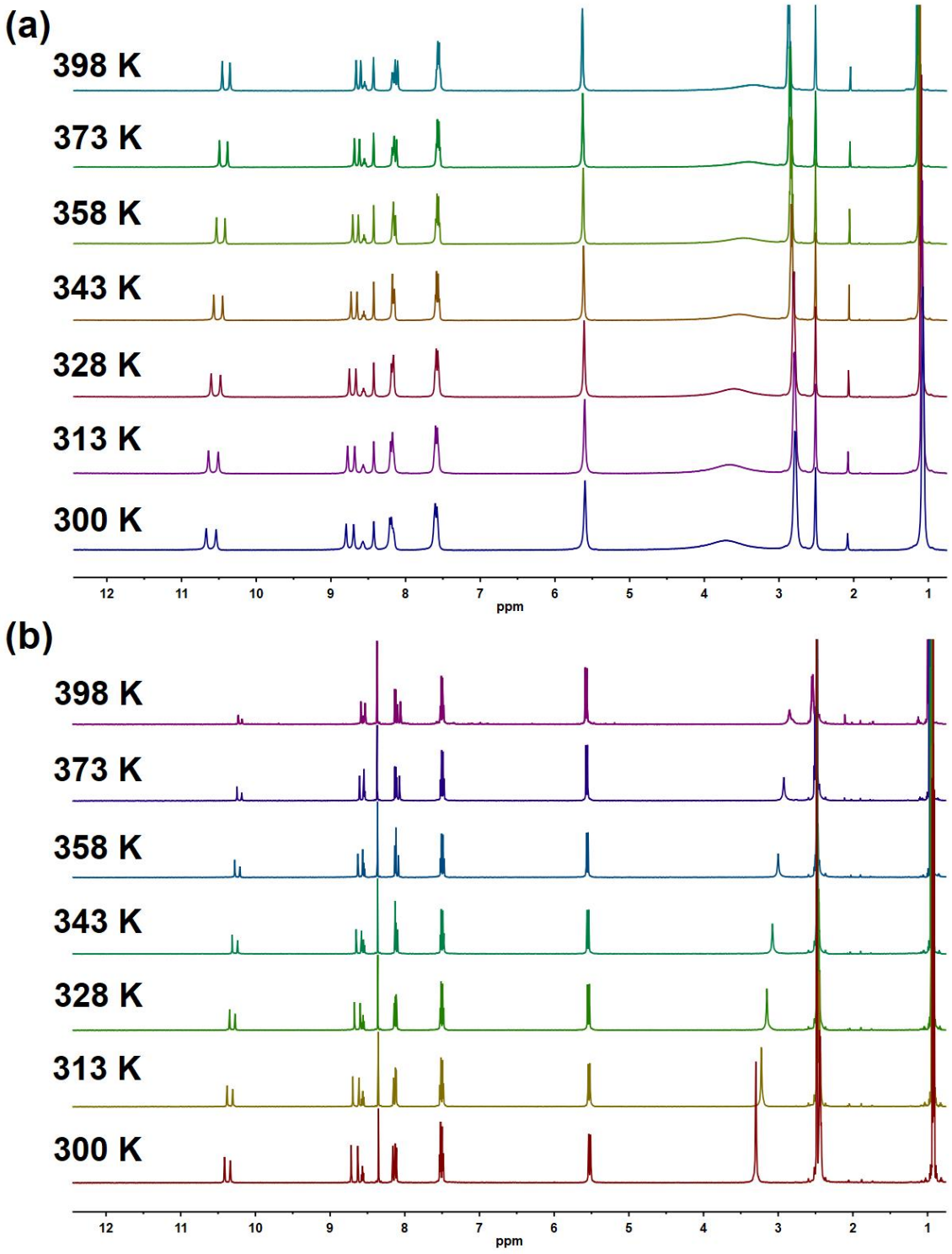

Figure 2.24 Variable-temperature 600 MHz ^{1}H NMR spectroscopic analyses of **TxSB-CO_2^-** recorded at concentrations of (a) 20 mM and (b) 2 mM in DMSO-d_6.

To gain further insights into the reversible nature of the self-associated oligomers formed from **TxSB-CO$_2^-$**, variable-temperature (VT) ^{1}H NMR spectroscopic studies were carried out. For a 20 mM (DMSO-d_6) solution of **TxSB-CO$_2^-$**, the peaks became sharper and appear well-resolved across the full spectrum as the temperature was raised. Upfield shifts were seen for many of the resonances, with the effect being greatest for the imidazolium C–H protons (Figure 2.24). Such findings are consistent with a system that undergoes thermal-based disaggregation. This is as expected for a **TxSB-CO$_2^-$**-based oligomer stabilized at room temperature via noncovalent (C−H)$\cdots$X$^-$ interactions.[20] Additional VT NMR spectra were recorded at 2 mM under the same analytical conditions. Similar spectral changes were observed at this lower concentration (Figures 2.24b). This latter finding provides further support for the contention that multiple oligomer-stabilizing intermolecular interactions are retained at lower concentrations at room temperature and that the resulting self-associated species (*i.e.*, [**TxSB-CO$_2^-$**]$_n$) dissociate as the temperature is raised.

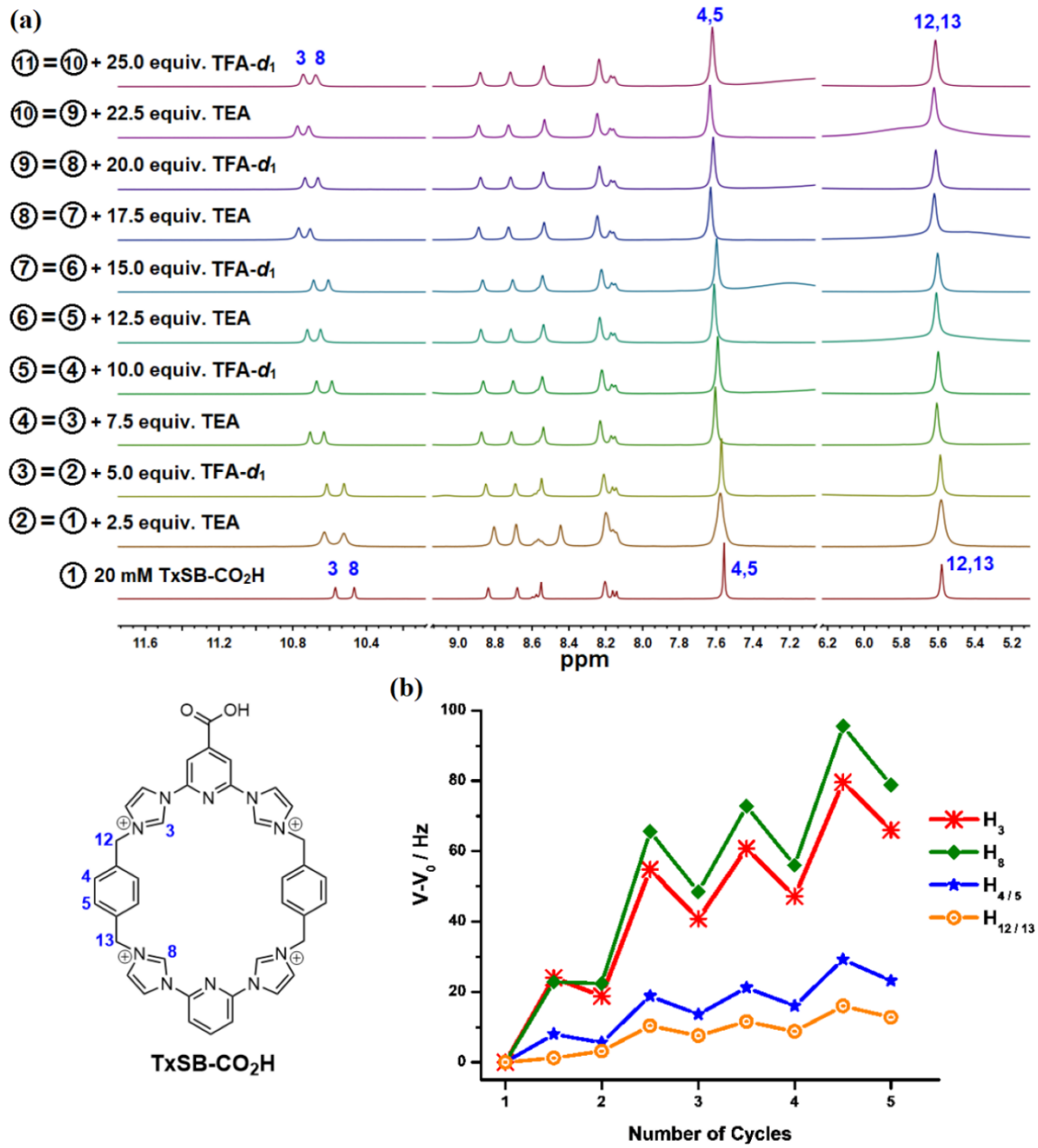

Figure 2.25 (a) pH-dependent 400 MHz ^{1}H NMR spectroscopic studies of **TxSB-CO$_2$H** carried out at a receptor concentration of 20 mM in DMSO-d_6 at 298 K. (b) Changes in resonance frequencies of selected macrocycle protons were used to monitor the pH-switchable interconversion between [**TxSB-CO$_2$H**]$_2$ and [**TxSB-CO$_2^-$**]$_n$.

Further support for the reversible nature of these self-assembly systems came from pH-dependent ^{1}H NMR spectroscopic analyses. Here, it was found that, upon addition of 2.5 equivalents of TEA to a DMSO-d_6 solution containing **TxSB-CO$_2$H** at a concentration of 20 mM, the resonances assigned to H_3, H_8, and $H_{4/5}$ (where $H_{4/5}$ refers to an overlapping signal ascribed to H_4 and H_5) within the macrocycle shift to lower field. Based on these observations, we surmise that, under these conditions, **TxSB-CO$_2$H** undergoes deprotonation to form **TxSB-CO$_2^-$**, a transformation that results initially in the dissociation of {[**TxSB-CO$_2$H**]$_2$}$_n$, followed by self-association to form [**TxSB-CO$_2^-$**]$_n$. Increasing the acidity of the resulting solution (containing [**TxSB-CO$_2^-$**]$_n$), via the addition of 5.0 equivalents of deuterated trifluoracetic acid (TFA-d_1), was found to protonate **TxSB-CO$_2^-$** and thus disassemble [**TxSB-CO$_2^-$**]$_n$ to regenerate [**TxSB-CO$_2$H**]$_2$. Evidence for this transformation came from the observation that the chemical shifts of the H_3, H_8, and $H_{4/5}$ signals reverted to their original positions upon protonation. The subsequent addition of TEA and led to restoration of spectral features ascribable to [**TxSB-CO$_2^-$**]$_n$. The process could be repeated via the subsequent additions of acid and base, thus allowing interconversion between the two sets of self-associated complexes, namely {[**TxSB-CO$_2$H**]$_2$}$_n$ and [**TxSB-CO$_2$H**]$_2$. However, with each addition of acid or base, the background salt concentration also increased. This led to a "dampening" of the interconversion effect with each cycle. Nevertheless, it proved possible to repeat the interconversion between [**TxSB-CO$_2^-$**]$_n$ and {[**TxSB-CO$_2$H**]$_2$}$_n$ a number of times (*cf.* Figure 2.25).[20]

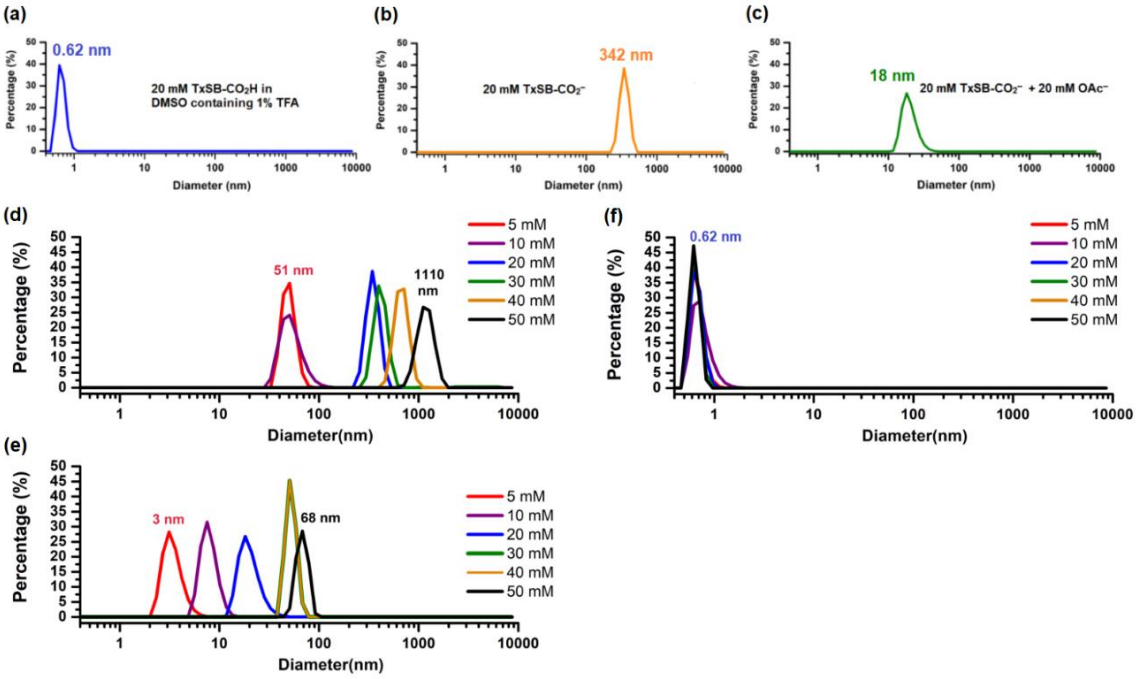

Figure 2.26 DLS size distributions of 20 mM DMSO solutions of (a) 20 mM **TxSB-CO₂H** in the presence of 1 weight % TFA, (b) 20 mM **TxSB-CO₂⁻**, and (c) an equimolar mixture of **TxSB-CO₂⁻** and TBAOAc. DLS size distributions of (d) **TxSB-CO₂⁻**, (e) an equimolar mixture of TBAOAc and **TxSB-CO₂⁻**, and (f) **TxSB-CO₂H** in the presence of 1 weight % TFA in DMSO solutions at varying concentrations. All analyses were carried out at room temperature.

As a complement to the ^{1}H NMR spectroscopic analyses, dynamic light scattering (DLS) experiments were carried out using samples of **TxSB-CO₂⁻**. At 20 mM an average particle size of ca. 342 nm was seen. This is a much larger value than that recorded for samples of **TxSB-CO₂H** containing 1% TFA at a similar concentration (particle size < 1 nm) (Figure 2.26a). Studies of **TxSB-CO₂⁻** were also carried out over various concentrations from 2 to 50 mM in DMSO. On the basis of these studies, two conclusions were reached. First, **TxSB-CO₂⁻** (but not **TxSB-CO₂H**) is able to form and stabilize oligomeric ensembles at higher concentrations. Second, in the case of **TxSB-CO₂⁻** (but not **TxSB-CO₂H**), the particle sizes were found to depend on the overall solution concentration (*cf.* Figure 2.26d). This is in a good agreement with our findings from the one- and two-dimensional ^{1}H NMR spectroscopic studies discussed above.

In addition to modulating the aggregation behavior of **TxSB-CO_2^-** through changes in temperature, pH, and concentration, we considered it likely that disassociation could be promoted via the addition of a competitive anion. Support for this postulate came from recent studies by Gong *et al*.,[28] wherein it was found that the formate and benzoate anions formed complexes with the parent (unfunctionalized) macrocycle $\mathbf{1}^{4+}$. In the present instance, it was found that addition of 1 molar equiv of tetrabutylammonium acetate (TBAOAc) to a 20 mM solution of the anionic forms of **TxSB-CO_2^-** in DMSO-d_6 led to discernible changes in the ^{1}H and ^{1}H–^{1}H NOESY NMR spectra (Figure 2.27a). A similar addition led to changes in the ^{1}H–^{1}H NOESY NMR spectrum of as-prepared samples of **TxSB-CO_2H**, as would be expected given the weakly basic nature of the OAc^- anion (Figure 2.27b). No such spectral changes were seen when acetic acid was added to a 20 mM DMSO-d_6 solution of **TxSB-CO_2H**.

In the case of **TxSB-CO_2^-** and the acetate anion, a ^{1}H NMR spectroscopic Job plot was constructed. On this basis, a 1:3 (host-guest) complex stoichiometry was inferred (Figure 2.28).[49] This stoichiometry is consistent with the presence of multiple interactions between the acetate anions and the Texas box receptor. Support for this latter inferences came from the observation of ^{1}H–^{1}H couplings between the acetate anion and various **TxSB-CO_2^-** protons in the NOESY spectrum (*cf*. Figure 2.27a).

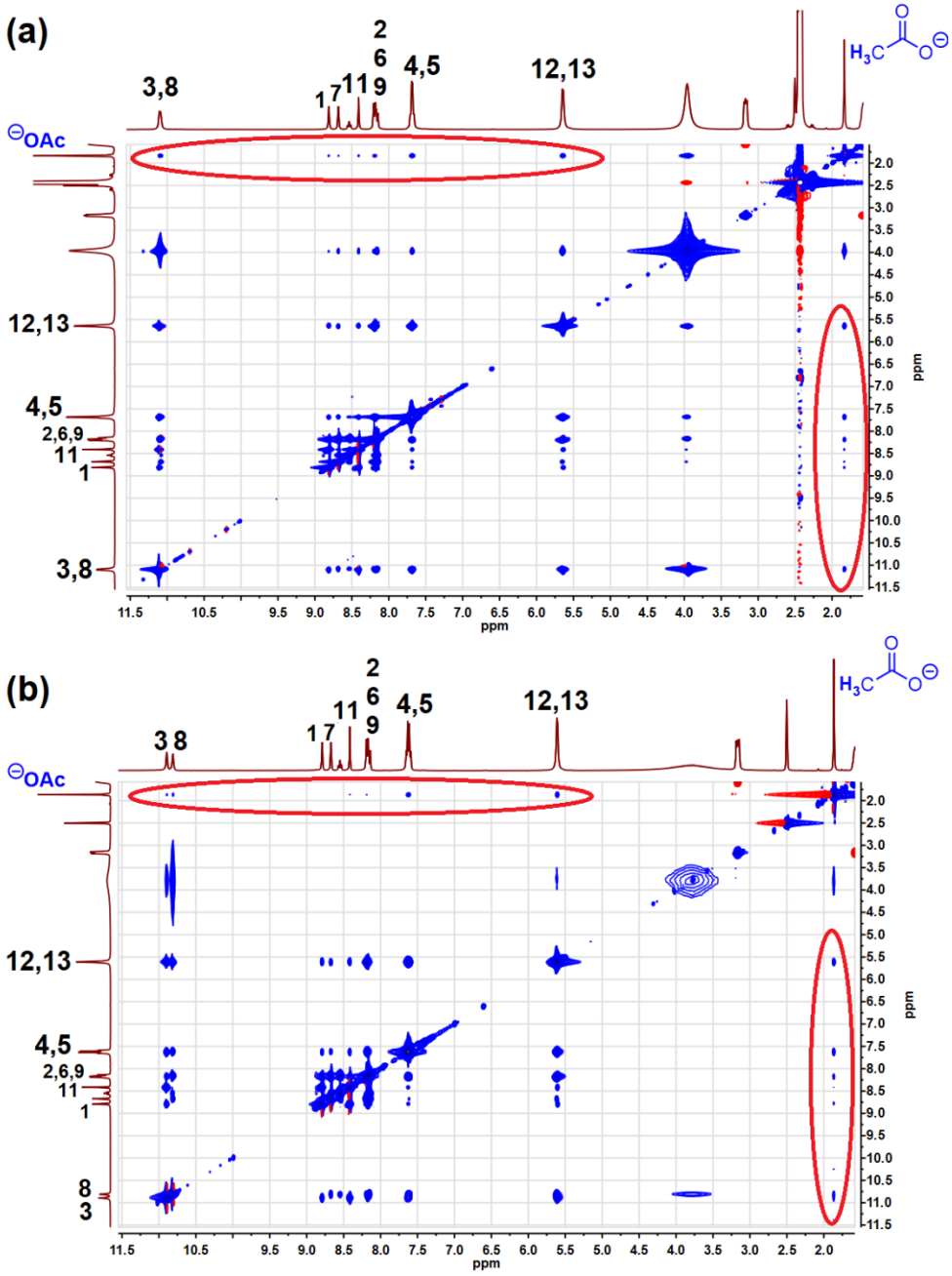

Figure 2.27 (a) Expanded view of a portion of the 600 MHz ^{1}H–^{1}H NOESY NMR spectrum of an equimolar mixture of TBAOAc and **TxSB-CO$_2^-$** recorded at 20 mM in DMSO-d_6. (b) Expanded view of the 600 MHz ^{1}H–^{1}H NOESY NMR spectrum of an equimolar mixture of TBAOAc and as-prepared **TxSB-CO$_2$H** recorded at 20 mM in DMSO-d_6. Both spectroscopic measurements were carried out at 298 K with 8 scans using a mixing time of 800 ms. Intermolecular NOESY correlations highlighted with red circles in (a) and (b) are considered indicative of a close spatial proximity between the respective macrocyclic hosts and the acetate anion under these solution state conditions.

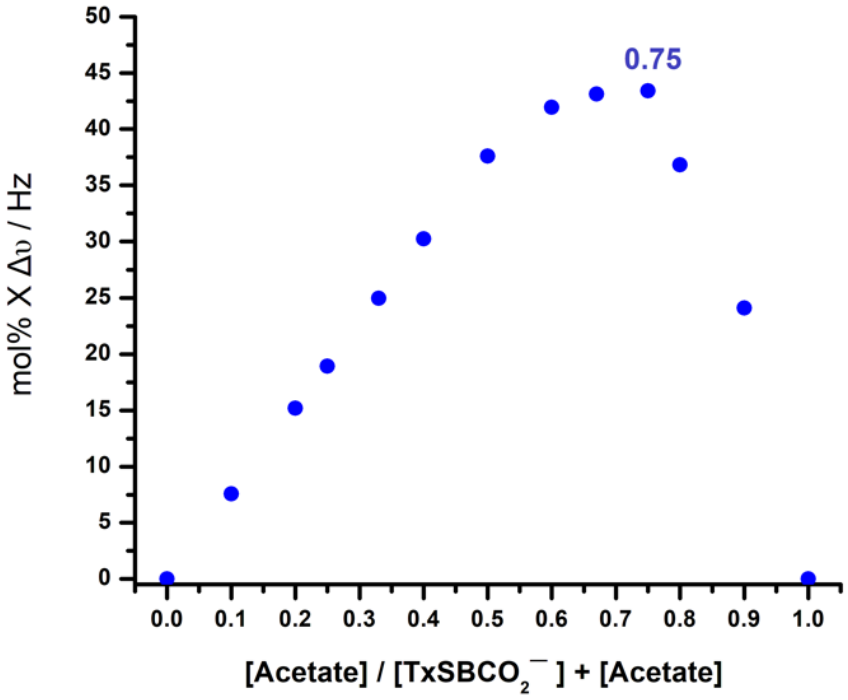

Figure 2.28 ^{1}H NMR Job plot corresponding to the complexation between **TxSB-CO_2^-** and the acetate anion ([host] + [guest] = 20 mM for this plot). The maximum values are determined to be 0.75 at such an overall concentration. This finding is consistent a 1:3 (host : guest) binding stoichiometry.

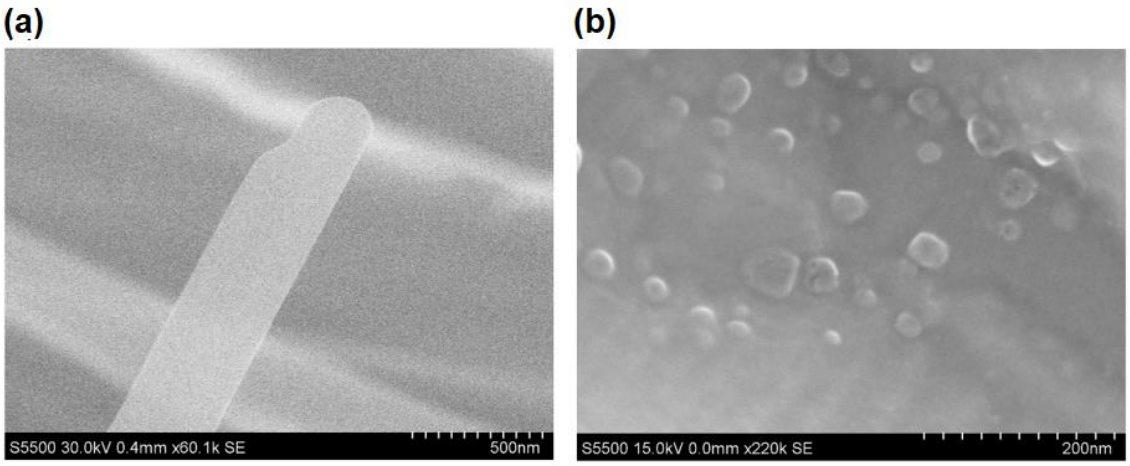

Figure 2.29 SEM images of the rod-like and grannular assemblies obtained from separate solution samples prepared from (a) **TxSB-CO_2^-** and (b) an equimolar mixture of **TxSB-CO_2^-** and TBAOAc (scale bars = 500 or 200 nm).

Further support for the suggestion that the acetate anion can be used to dissemble the self-associated form of **TxSB-CO_2^-** came from DLS analyses. As can be seen from an inspection of Figure 2.26b, a mean particle diameter of ca. 342 nm was deduced for DMSO solutions of **TxSB-CO_2^-** at a concentration of 20 mM on the basis of DLS analyses. In contrast, mixed solutions containing 1:1 TBAOAc−**TxSB-CO_2^-** at 20 mM in both species produced particles with a relatively small average diameter of 18 nm as judged from analogous DLS studies (*cf*. Figure 2.26c).

The ability of the acetate anion to induce deaggregation was also probed by means of scanning electron microscopy (SEM).[29] Consistent with the crystallographic analyses and what was inferred from the DLS studies, rod-like nanostructures were seen for the solid-phase aggregates obtained from **TxSB-CO_2^-** (*cf.* Figure 2.29a). In contrast, relatively small sized granular assemblies were found in the SEM samples made up from a 1:1 mixture of TBAOAc and **TxSB-CO_2^-** (*cf*. Figure 2.29b). On the basis, we propose that the acetate anion provides an external stimulus that can be used to control the self-association features of **TxSB-CO_2^-**. The acetate anion could thus provide a potential complement to other modulators, such as temperature, pH, and concentration.

2.3 CONCLUSIONS

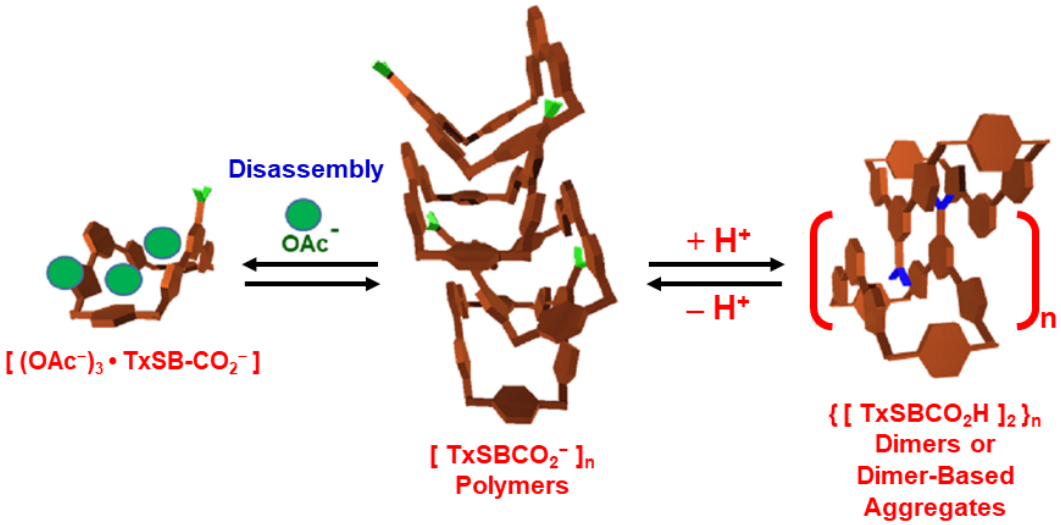

Scheme 2.2 Cartoon representation of important stimuli-responsive supramolecular association found in our present studies of **TxSB-CO$_2$H** and **TxSB-CO$_2^-$** in DMSO.

In summary, a carboxylic acid-functionalized Texas-sized molecular box **TxSB-CO$_2$H** was designed and synthesized. While this new derivative was seen to self-associate to produce an extended array of dimers in the solid state, concentration-dependent ^{1}H NMR spectroscopic studies revealed little evidence of aggregation except possibly at the highest concentrations accessible in DMSO-d_6 as long as the acid moiety was in its fully protonated form. The appended carboxylic acid group (tail unit) present in **TxSB-CO$_2$H** can be effectively converted into its conjugate base, **TxSB-CO$_2^-$**, by treatment with TEA in DMSO or DMSO-d_6. Such an alteration in the tail functionality leads to the production of self-complementary monomers, **TxSB-CO$_2^-$**. These anion-containing monomers associate into a higher-order head-to-tail oligomers [**TxSB-CO$_2^-$**]$_n$ in solution and in the solid state. These self-assembled structures were characterized on the basis of one- and two-dimensional ^{1}H NMR spectroscopic studies carried out in DMSO-d_6, single crystal X-ray diffraction analyses, DLS measurements, and SEM imaging. The ensembles produced from **TxSB-CO$_2^-$** proved to be environmentally responsive, with the extent of assembly being readily modulated via changes in

temperature, pH, and concentration, as well as via the addition of the acetate anion as a competitive guest (Scheme 2.2). The present work shows how ostensibly similar receptors can be used to create very different kinds of solution phase and solid state structures. As such, it could set the stage for the design and synthesis of more sophisticated supramolecular systems, such as so-called smart materials[2,10] and molecular level switches,[9,30] that would benefit from the availability of large cationic macrocyclic building blocks. The present work also serves to underscore how structures inferred from solid state structural analyses are not necessarily reflective of the forms that dominate in competitive solution phase media.

2.4 REFERENCES

1) Silver, E. S.; Rambo, B. M.; Bielawski, C. W.; Sessler, J. L. *J. Am. Chem. Soc*. **2014**, *136*, 2252–2255.
2) Yang, L.; Tan, X.; Wang, Z.; Zhang, X. *Chem. Rev.* **2015**, *115*, 7196−7239.
3) Takashima, Y.; Harada, A. *J. Incl. Phenom. Macrocycl. Chem*. **2017**, *88*, 85–104.
4) Gyarmati, B.; Szilágyi, B. Á.; Szilágyi, A. *Eur. Polym. J.* **2017**, *93*, 642–669.
5) Sessler, J. L.; Andrievsky, A.; Gale, P. A.; Lynch, V. M. *Angew. Chem. Int. Ed.* **1996**, *35*, 2782–2785.
6) Ashton, P. P.; Parsons, I. W.; Raymo, F. M.; Stoddart, J. F.; White, A. J. P.; Williams, D. J.; Wolf, R. *Angew. Chem. Int. Ed.* **1998**, *37*, 1913–1916.
7) Cao, D.; Wang, C.; Giesener, M. A.; Liu, Z.; Stoddart, J. F. *Chem. Commun.* **2012**, *48*, 6791−6793.
8) Rotzler J.; Mayor, M. *Chem. Soc. Rev.* **2013**, *42*, 44−62.
9) Erbas-Cakmak, S.; Leigh, D. A.; McTernan, C. T.; Nussbaumer, A. L. *Chem. Rev*. **2015**, *115*, 10081–10206.
10) Bruns, C. J.; Stoddart, J. F. *Acc. Chem. Res.* **2014**, *47*, 2186–2199.
11) Kim, D. S.; Chang, J.; Leem, S.; Park, J. S.; Thordarson, P.; Sessler, J. L. *J. Am. Chem. Soc.*, **2015**, *137*, 16038–16042.
12) Ji, X.; Wang, H.; Li, Y.; Xia, D.; Li, H.; Tang, G.; Sessler, J. L.; Huang, F. *Chem. Sci*. **2016**, *7*, 6006–6014.
13) Walter, S. M.; Kniep, F.; Herdtweck, E.; Huber S. M. *Angew. Chem. Int. Ed.* **2011**, *50*, 7187–7191.
14) Ashton, P. R.; Ballardini, R.; Balzani, V.; Bělohradský, M.; Gandolfi, M. T.; Philp, D.; Prodi, L.; Raymo, F. M.; Reddington, M. V.; Spencer, N.; Stoddart, J. F.; Venturi, M.; Williams, D. J. *J. Am. Chem. Soc.* **1996**, *118*, 4931–4951.
15) Rose, N. G. W.; Blaskovich, M. A.; Wong, A.; Lajoie, G. A. *Tetrahedron* **2001**, *57*, 1497–1507.
16) Choony, N.; James, L.; Rabun, C. *Synthetic Commun.* **2001**, *41*, 2539–2543.
17) Barnes, J. C.; Juríček, M.; Vermeulen, N. A.; Dale, E. J.; Stoddart, J. F. *J. Org. Chem*. **2013**, *78*, 11962–11969.
18) Luo, Y.; Blaskovich, M. A.; Lajoie, G. A *J. Org. Chem*. **1999**, *64*, 6106–6111.
19) Shang, J.; Rambo, B. M.; Hao, X.; Xiang, J.-F.; Gong, H.-Y.; Sessler, J. L. *Chem. Sci*. **2016**, *7*, 4148–4157.
20) Gong, H. -Y.; Rambo, B. M.; Karnas, E.; Lynch, V. M.; Keller, K. M.; Sessler, J. L. *J. Am. Chem. Soc*. **2011**, *133*, 1526−1533.
21) Zhao, D.; Moore, J. S. *Org. Biomol. Chem*. **2003** , *1*, 3471–3491.
22) Mahadevi, A. S.; Sastry, G. N. *Chem. Rev.* **2016***, 116,* 2775−2825.
23) Wackerly, J. W.; Moore, J. S. *Macromolecules* **2006**, *39*, 7269–7276.
24) Schmidt, R.; Stolte, M.; Grüne, M.; Würthner, F. *Macromolecules* **2011**, *44,* 3766–3776.
25) Gong, H. -Y.; Rambo, B. M.; Karnas, E.; Lynch, V. M.; Sessler, J. L. *Nat. Chem*. **2010**, *2*, 406–409.

26) Martin, R. B. *Chem*. *Rev*. **1996**, *96*, 3043–3064.
27) Xu, J.; Fogleman, E. A.; Craig, S. L. *Macromolecules* **2004**, *37,* 1863–1870.
28) Tang, F.; Cao, R.; Gong, H. -Y.; *Tetrahedron Lett*. **2015**, *56*, 820–823.
29) Zhang, H.; Lee, J.; Lammer, A. D. Chi, X.; Brewster, J. T.; Lynch, V. M.; Li, H.; Zhang, Z.; Sessler, J. L. *J. Am. Chem. Soc*. **2016**, *138*, 4573–4579.
30) Stoddart, J. F. *Chem. Soc. Rev.* **2009**, *38*, 1802–1820.
31) Balzani, V.; Gómez-López, M.; Stoddart, J. F. *Acc. Chem. Res.* **1998**, *31*, 405–414.

Chapter 3: Physical Removal of Anions from Aqueous Media by Means of a Macrocycle-Containing Polymeric Network

3.1 INTRODUCTION

Industrialization and agriculture have made potentially hazardous anions ubiquitous. These anions can have a serious impact on water quality and can affect human health.[1] For example, the nitrate (NO_3^-) anion and inorganic phosphates (*e.g.*, $H_2PO_4^-$) from agricultural runoff can lead to eutrophication of waterways.[2] The nitrate and nitrite (NO_2^-) anions can induce methemoglobinemia.[3] The sulfate (SO_4^{2-}) and hydrogen sulfate (HSO_4^-) anions are present in radioactive waste and present problems in terms of reprocessing; they decrease the durability of glass logs and promote corrosion of the glass smelter and constituent electrodes.[4a,b] Hydrogen sulfide (HS^-), the deprotonated form of H_2S, is an anion whose toxicity is comparable to those of CO and NO.[4c] Concentrated fluoride (F^-) anion solutions are corrosive.[5] Organic anions, including a number of anionic dyes, display potential toxic effects even at low concentrations.6 Innovative materials that can be used to remove hazardous anions from aqueous media are thus of interest. Here we report a supramolecular hydrogel-based approach to water purification that relies on the use of a tetracationic anion receptor and which involves a simple two step sequence of anion absorption followed by physical separation.

Supramolecular hydrogels are typically formed via the self-assembly of macromolecules or low-molecular-weight building blocks through non-covalent interactions in water.[7] They have solid-like 3D network structures and rheological properties comparable to solid materials. When brought into contact with water,

§ Ji, X.; **Wu**, **R**. **-T**.; Long, L.; Guo, C.; Khashab, N. M.; Huang, F.; Sessler, J. L. Physical Removal of Anions from Aqueous Media by Means of a Macrocycle-Containing Polymeric Network. *J. Am. Chem. Soc*. **2018**, *140*, 2777–2780.
The candidate is the second author on this publication and was responsible for syntheses of the nonfunctionalized and functionalized macrocyclic receptors, as well as the characterization of related products.

supramolecular hydrogels can absorb solutes present in the aqueous medium within their nano-/micro-structures. Given this, we considered that appropriately designed anion-responsive supramolecular hydrogels might be useful in removing toxic anions from aqueous environments. While a number of elegant anion-responsive supramolecular hydrogels have been reported in the contest of anion sensing, to our knowledge anion-binding hydrogels have yet to be extensively exploited in the context of water purification.[8]

To date, two basic approaches have been used to create hydrogels that respond to anions.[9] The first relies on anion-triggered gel−sol transitions, while the second involves anion-induced conversions from sol to gel.[9] While elegant examples of materials embodying these strategies are now known, neither strategy appears suitable for removing unwanted anions from aqueous environments. This is because anion-triggered hydrogel disruption leads to loss in structure and release of the anions into the aqueous medium, whereas in the case of anion induced hydrogel formation, water and anions are intimately involved in the self-assembled structure. What is needed is a hydrogel that (1) permits anion recognition in aqueous media and does so without (2) disrupting the hydrogel structure.

To address the above need, we have designed a polymeric network **P1** (dried hydrogel **G1**) whose covalent cross-linker contains a tetracationic anion receptor (Scheme 3.1a). Due to the putative macrocycle-anion interactions imparted by the tetracationic receptor (Scheme 3.1b), it was expected that **P1** would absorb anions during and after hydrogel formation in water (Scheme 3.1c). Physical removal of the hydrogel from the aqueous medium after anion absorption would then complete the water purification process (Scheme 3.1c). Treating the anion-trapped hydrogel with dilute acid

would then lead to the protonation-induced release of the bound anion (Scheme 3.1d), allowing reuse of the polymeric material.

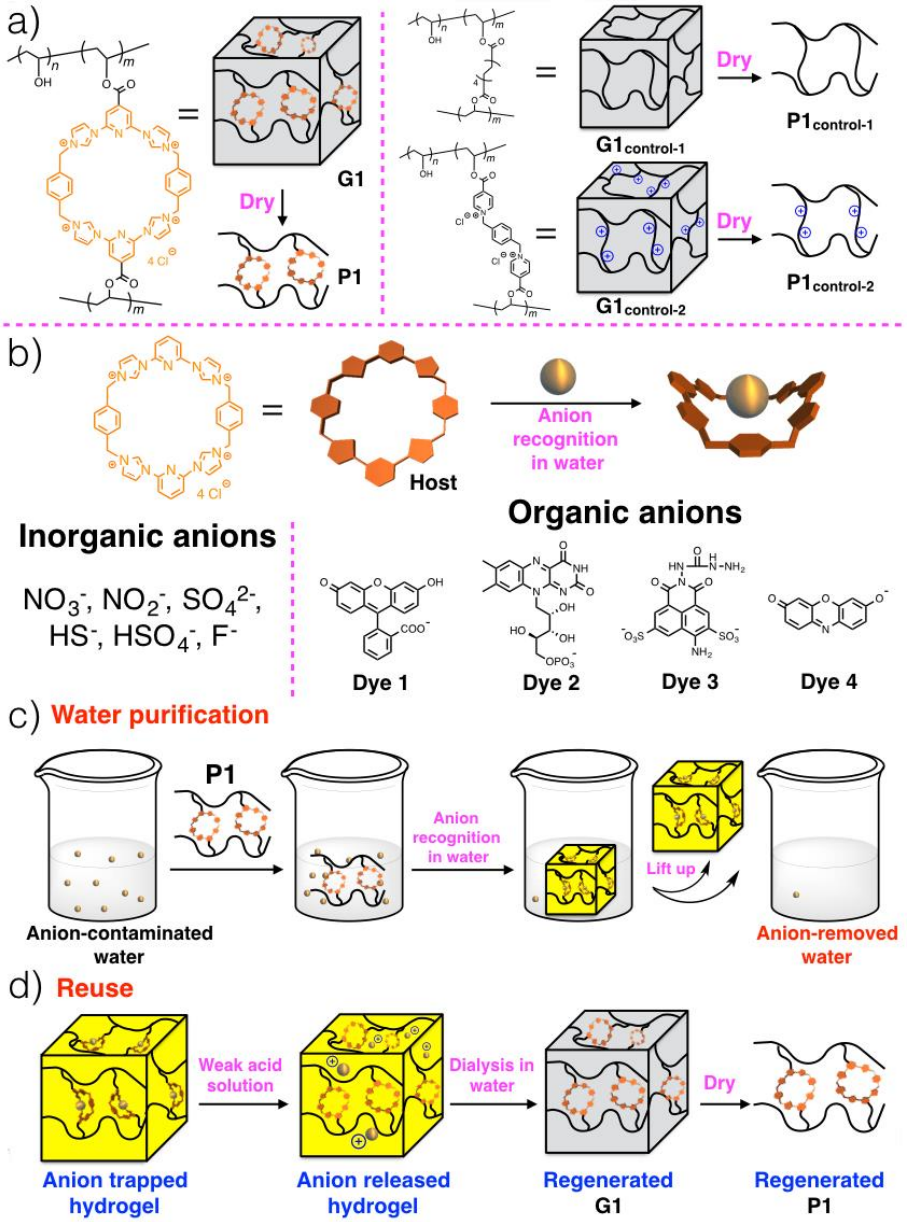

Scheme 3.1 (a) Chemical structures and cartoon representations of polymeric materials used in this study. (b) Proposed macrocycle-anion binding interactions operating in aqueous environments. (c) Anion removal from water using a polymeric network **P1** containing tetracationic macrocyclic anion receptor. (c) Regeneration process for **P1**. Reproduced with permission from *J. Am. Chem. Soc*. **2018**, *140*, 2777. Copyright 2018 American Chemical Society.[10]

3.2 RESULTS AND DISCUSSION

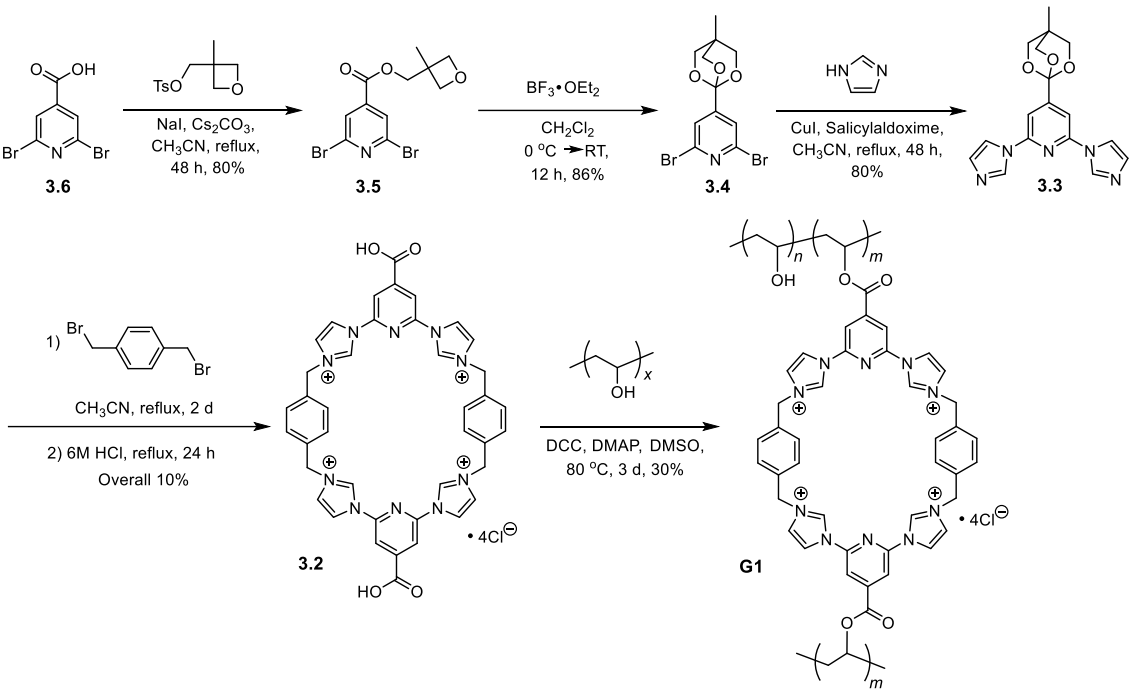

Scheme 3.2 Synthesis of the dicarboxylic acid-functionalized tetracationic macrocycle **3.2** and hydrogel **G1**.

The tetracationic receptor chosen for hydrogel construction is a dicarboxylic acid-functionalized analogue **3.2** of the so-called "Texas-sized" molecular box, cyclo[2](2,6-di(1H-imidazol-1-yl)pyridine)[2](1,4-dimethylenebenzene).[11] Its synthesis is outlined in Scheme 3.2. Briefly, the commercially available carboxylic acid **3.6** was used to produce the oxetane ester **3.5**. BF_3-catalyzed isomerization yielded orthoester **3.4**, which was transformed into **3.3** via an Ullmann-type coupling with imidazole. Next, macrocycle **3.2** was attached to poly(vinyl alcohol) (PVA),[12] a commercially available water-soluble polymer via an esterification reaction carried out in DMSO.[12] The resulting gel was then washed repeatedly with water to give hydrogel **G1**. Drying gave the hydrophilic polymer network **P1**. Furthermore, two control polymer networks, $\mathbf{P1}_{\textbf{control-1}}$ and $\mathbf{P1}_{\textbf{control-2}}$, lacking the macrocyclic moieties, were also prepared by drying hydrogels $\mathbf{G1}_{\textbf{control-1}}$ and $\mathbf{G1}_{\textbf{control-2}}$ (*cf.* Scheme 3.1a and Scheme 3.3).

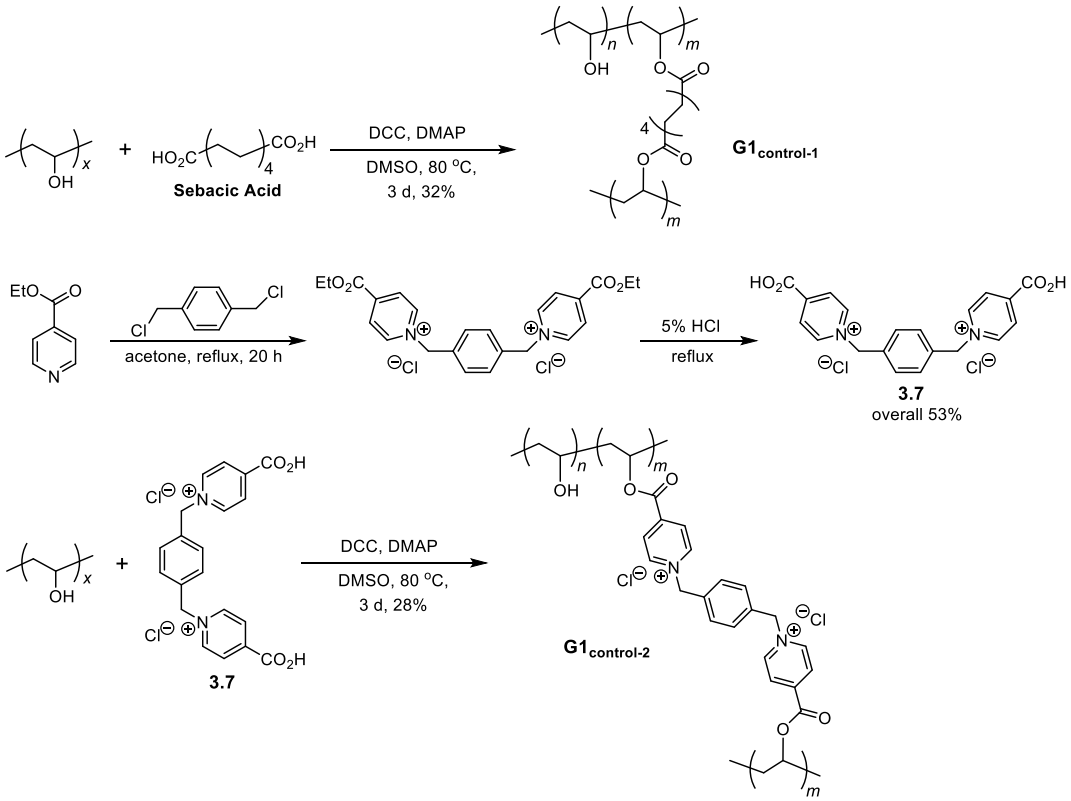

Scheme 3.3 Syntheses of hydrogels **G1**$_{\textbf{control-1}}$ and **G1**$_{\textbf{control-2}}$ lacking a macrocyclic motif.

The three hydrogels in question were characterized by standard methods, including Fourier transform infrared spectroscopy spectroscopy (FTIR) (Figures 3.1−3.3), rheological experiments (Figures 3.4a, 3.4c, and 3.4e), and scanning electron microscopy (SEM) (Figures 3.4b, 3.4d, and 3.4f).

FTIR was first used to study the chemical structure of PVA, precursor **3.2**, and polymer **G1**. As shown in Figure 3.1 of PVA, a wide-ranging peak is seen between 3000 and 3600 cm^{-1}. This feature is attributed to an O−H stretching mode. Features between 2900 and 2800 cm^{-1} are also seen that are assigned to (−CH_2−) asymmetric and symmetric stretching modes, respectively.[12] A peak at around 1600−1700 cm^{-1} is visible that is assignable to a carbonyl (C=O) stretching band.[13a] Peaks between 1550−1400 cm^{-1} are seen that are ascribed to in-ring C=C and C=N stretching modes within the

benzene,[13b] pyridine,[13c] and imidazole rings.[13d] These features are also present in the FTIR spectrum of **3.2**. However, clear differences are seen between the spectra for **3.2** and **G1** (as well as between **G1** and PVA).

Analogous FTIR spectroscopic analyses were also performed to investigate hydrogels $\mathbf{G1}_{\text{control-1}}$ and $\mathbf{G1}_{\text{control-2}}$ (*cf.* Figures 3.2 and 3.3). A comparison between Figure elements 3.2a, 3.2b, and 3.2c reveals the presence of features between 1700−1600 cm^{-1} that on the basis of the literature were considered consistent with the presence of a C=O stretching mode in the case of $\mathbf{G1}_{\text{control-1}}$.[10] A comparison between Figure elements 3.3a, 3.3b, and 3.3c reveals the presence of features between 1700−1600 cm^{-1} that on the basis of the literature were in agreement with the presence of a C=O stretching mode in the case of $\mathbf{G1}_{\text{control-2}}$.[10]

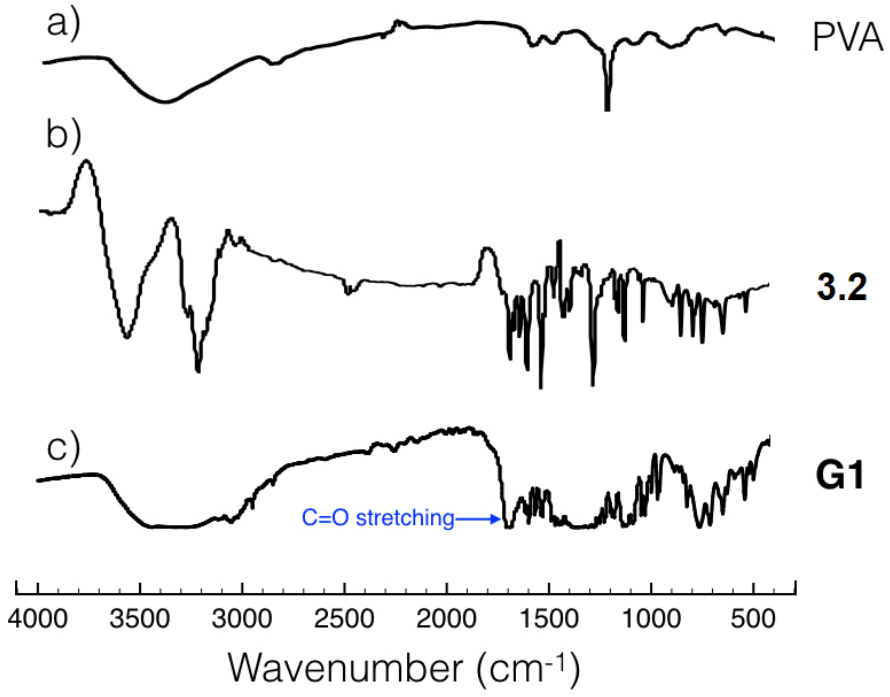

Figure 3.1 FTIR spectra of (a) PVA, (b) macrocycle **3.2**, and (c) **G1**. Reproduced with permission from *J. Am. Chem. Soc*. **2018**, *140*, 2777. Copyright 2018 American Chemical Society.[10]

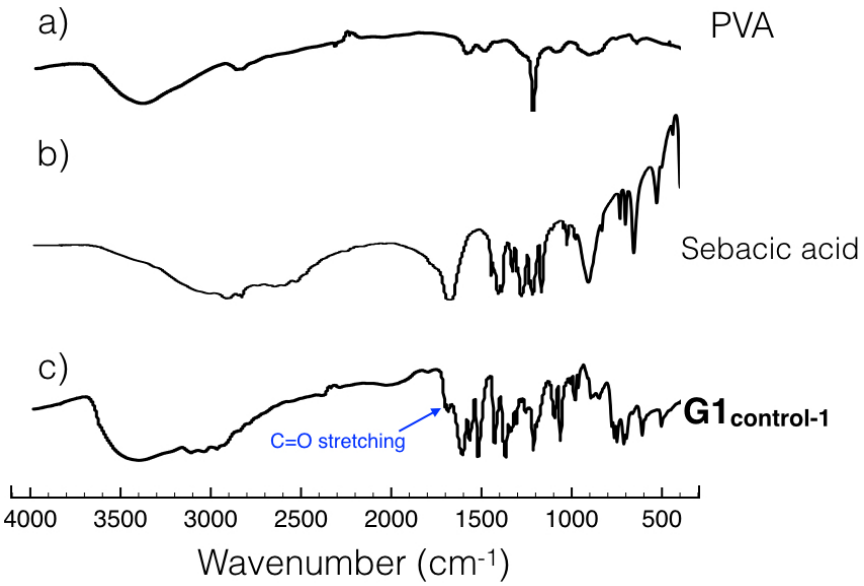

Figure 3.2 FTIR spectra of (a) PVA, (b) sebacic acid, and (c) **G1**$_{\textbf{control-1}}$. Reproduced with permission from *J. Am. Chem. Soc*. **2018**, *140*, 2777. Copyright 2018 American Chemical Society.[10]

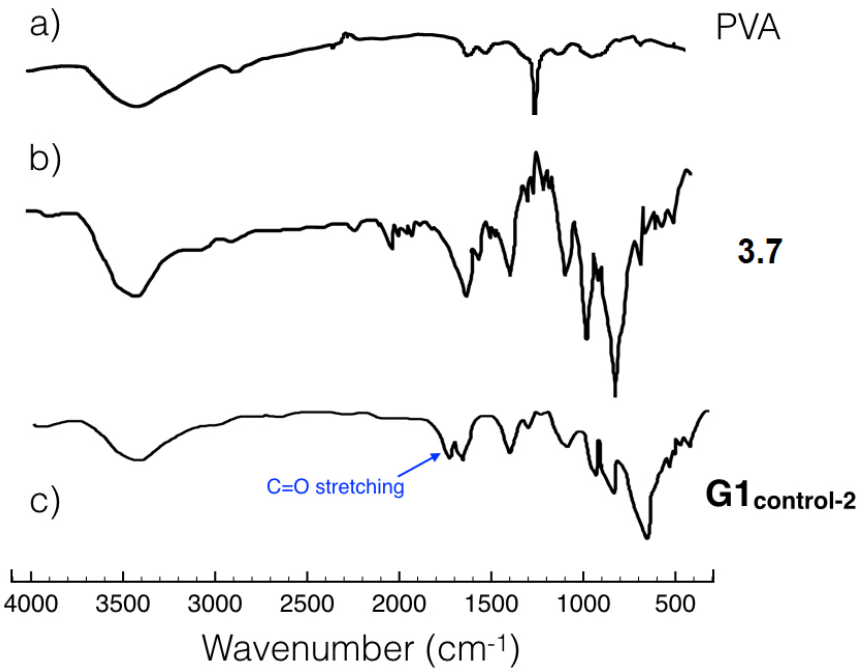

Figure 3.3 FTIR spectra of (a) PVA, (b) compound **3.7**, and (c) **G1**$_{\textbf{control-2}}$. Reproduced with permission from *J. Am. Chem. Soc*. **2018**, *140*, 2777. Copyright 2018 American Chemical Society.[10]

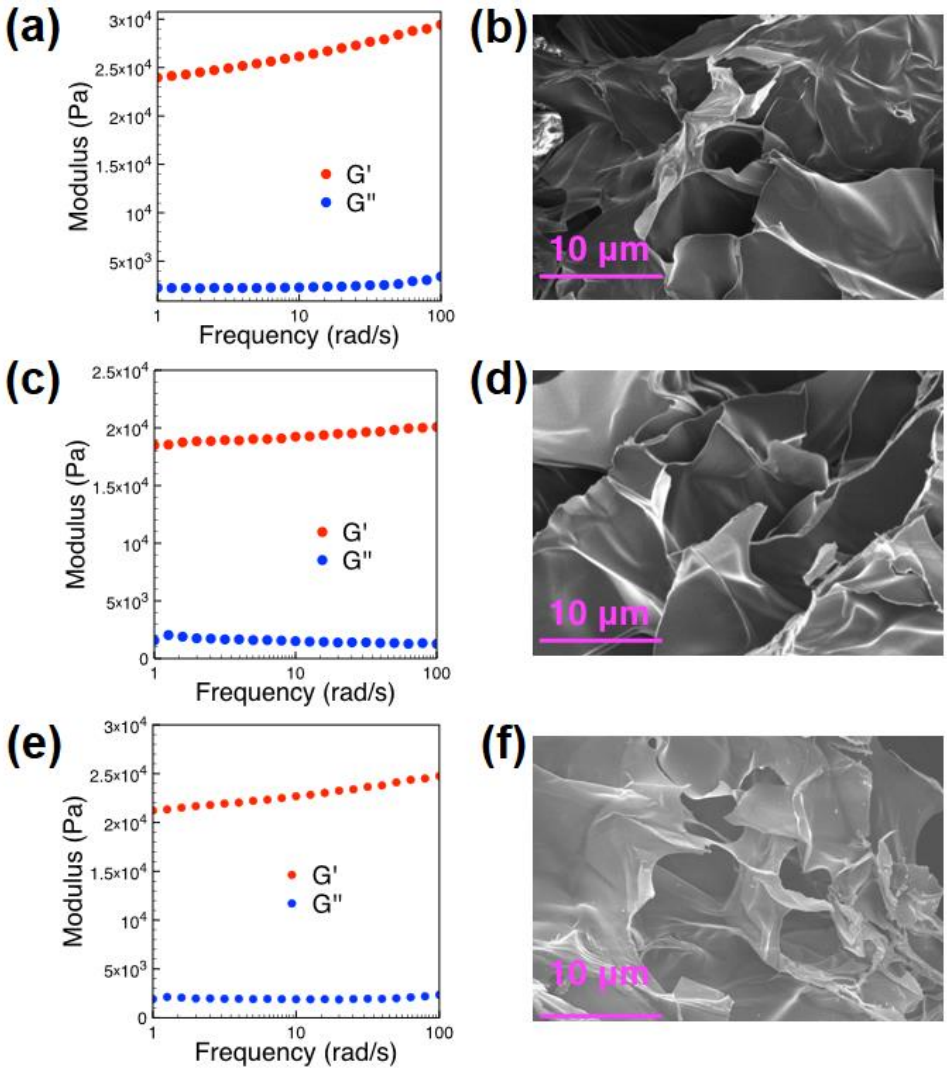

Figure 3.4 (a) Rheological data of storage modulus (G') and loss modulus (G''), and (b) SEM image of hydrogel **G1**. (c) Rheological data of storage modulus (G') and loss modulus (G''), and (d) SEM image of hydrogel $\mathbf{G1}_{\textbf{control-1}}$. (e) Rheological data of storage modulus (G') and loss modulus (G''), and (f) SEM image of hydrogel $\mathbf{G1}_{\textbf{control-2}}$. For these rheology experiments, the material was studied as prepared, where it was subject to freeze-drying prior to the SEM studies. Reproduced with permission from *J. Am. Chem. Soc*. **2018**, *140*, 2777. Copyright 2018 American Chemical Society.[10]

Rheological experiments were carried out to measure the storage modulus (G') and loss modulus (G'') and thus define the elasticity and viscosity of hydrogel **G1**. In dynamic frequency sweep experiments, the value of G' proved much higher than that of G'' (Figure 3.4a). This is consistent with what is predominantly elastic behavior and

provides supporting evidence for the formation of a hydrogel. The microstructure of hydrogel **G1** was also characterized by means of SEM after freeze-drying. The results of this study, shown in Figure 3.4b, revealed formation of an interconnected porous polymer network. Such a finding is in agreement with the cross-linked network structure proposed for **G1**. The rheological and SEM data provided further support for the gel structure proposed for **G1**$_{\textbf{control-1}}$. In fact, to a first approximation a strong analogy between **G1** and **G1**$_{\textbf{control-1}}$ was seen (*cf*. Figures 3.4c and 3.4d). The rheological and SEM data provided further support for the gel structure proposed for **G1**$_{\textbf{control-2}}$ (*cf*. Figures 3.4e and 3.4f).

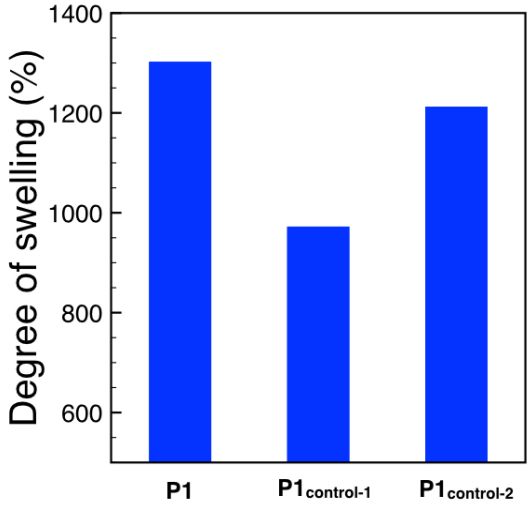

Figure 3.5 Degree of swelling seen for **P1**, **P1**$_{\textbf{control-1}}$, and **P1**$_{\textbf{control-2}}$ upon exposure to water. Reproduced with permission from *J. Am. Chem. Soc*. **2018**, *140*, 2777. Copyright 2018 American Chemical Society.[10]

Swelling experiments were performed in the case of the cross-linked polymers (13 mg of **P1**, 8 mg of **P1**$_{\textbf{control-1}}$, and 8.5 mg of **P1**$_{\textbf{control-2}}$, respectively) in water (10 mL) at room temperature. The degree of swelling was defined as the difference in the weight of the swollen gel ($W_{swollen}$) versus the dried gel (W_{dry}), according to the equation below:[14]

$$\text{Degree of swelling (\%)} = [(W_{swollen} - W_{dry})/W_{dry}]\times 100$$

Therefore, the degree of swelling for the three polymers could be calculated; the results are shown in Figure 3.5. Among them, **P1** shows the highest ratio.

Prior to testing whether **P1** could be used to remove anions from aqueous environments, qualitative tests were carried out to ascertain whether the core macrocyclic receptor (termed **Host** and shown in Scheme 3.1b) would interact with different anions in water. For this purpose, the **Host** (an unsubstituted version of **3.2**) was allowed to interact with salts of inorganic ($NaNO_3$, $NaNO_2$, Na_2SO_4, NaHS, $NaHSO_4$, and NaF) and organic anions (including fluorescein[15a] (**Dye 1**), flavin mononucleotide[15b] (**Dye 2**), Lucifer yellow[15c] (**Dye 3**), and resorufin[15d] (**Dye 4**)) in D_2O. The changes, if any, were monitored using ^{1}H NMR spectroscopy (Figures 3.6–3.15). Monotonic changes were seen for the benzene proton resonances H_1 on **Host** as the relative concentration of guest was increased up to 1 molar equivalent. Treatment with greater quantities of the anion salt led to less consistent changes (Figures 3.6–3.15). The chemical shift changes ($\Delta\delta$) induced by the organic dyes were generally larger than those produced by the inorganic salts (Table 3.1). Such findings are consistent with anion-receptor binding and are in line with prior studies involving this tetracationic receptor.[11] In the case of **Dye 3**, a yellow precipitate was observed at a 1:1 molar ratio.

In order to interpret the discrepancies observed from the above concentration-dependent ^{1}H NMR studies, theoretical calculations of the interactions between the macrocyclic receptor **Host** and organic anions **Dyes 1**–**4** were carried out using DFT methods (Figure 3.16 and Table 3.2).[16] As delineated below (pp. 81−82 of this dissertation), this computational analysis also provides support for a stronger binding affinity of **Host** towards **Dye 3**, which could result in the formation of a yellow precipitate upon adding **Dye 3** to a D_2O solution of **Host**.

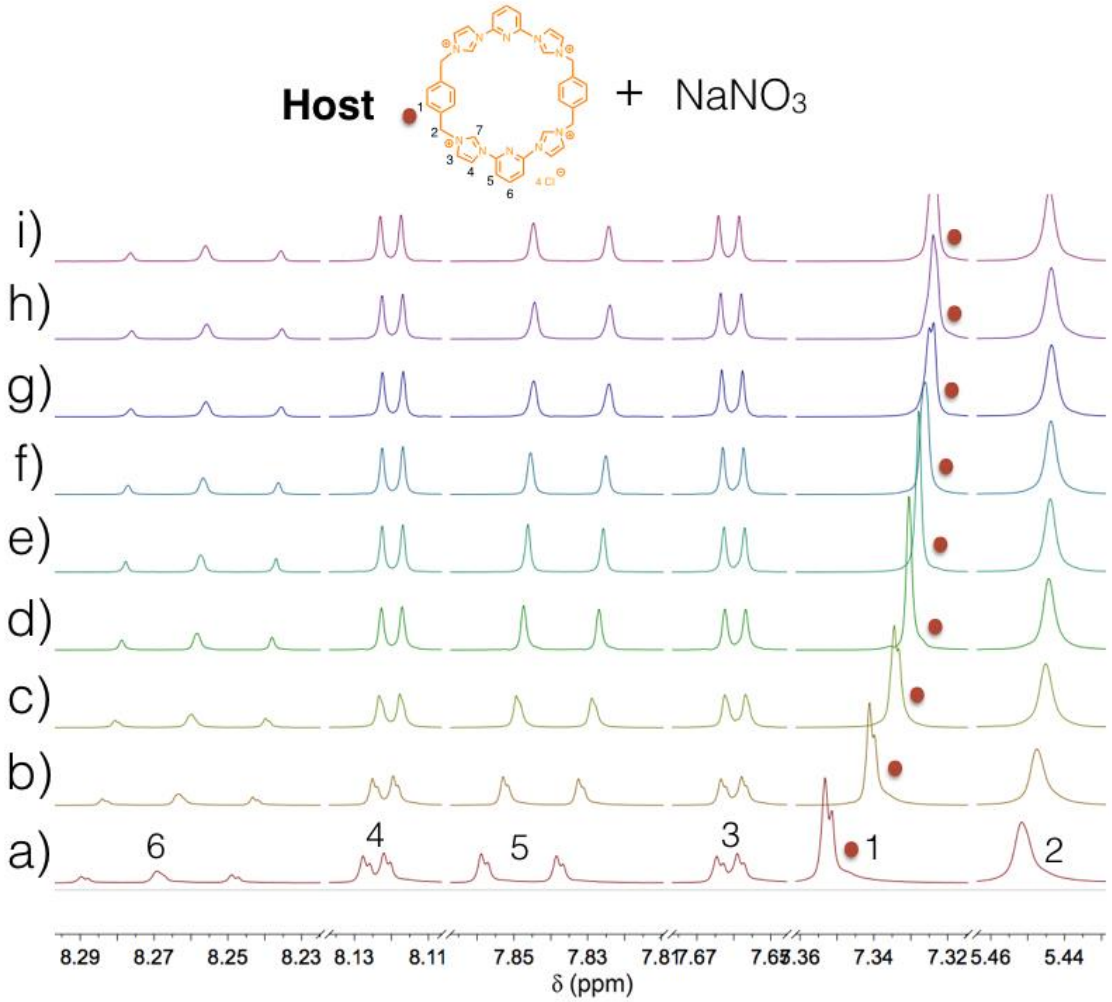

Figure 3.6 Truncated ^{1}H NMR spectra (400 MHz, D_2O, 298 K) of the tetracationic macrocycle (**Host**) recorded at a concentration of 0.5 mM in the presence of differing concentrations of $NaNO_3$: (a) 0 mM, (b) 0.5 mM, (c) 1.0 mM, (d) 1.5 mM, (e) 2.0 mM, (f) 2.5 mM, (g) 3.0 mM, (h) 3.5 mM, and (i) 4.0 mM. Reproduced with permission from *J. Am. Chem. Soc*. **2018**, *140*, 2777. Copyright 2018 American Chemical Society.[10]

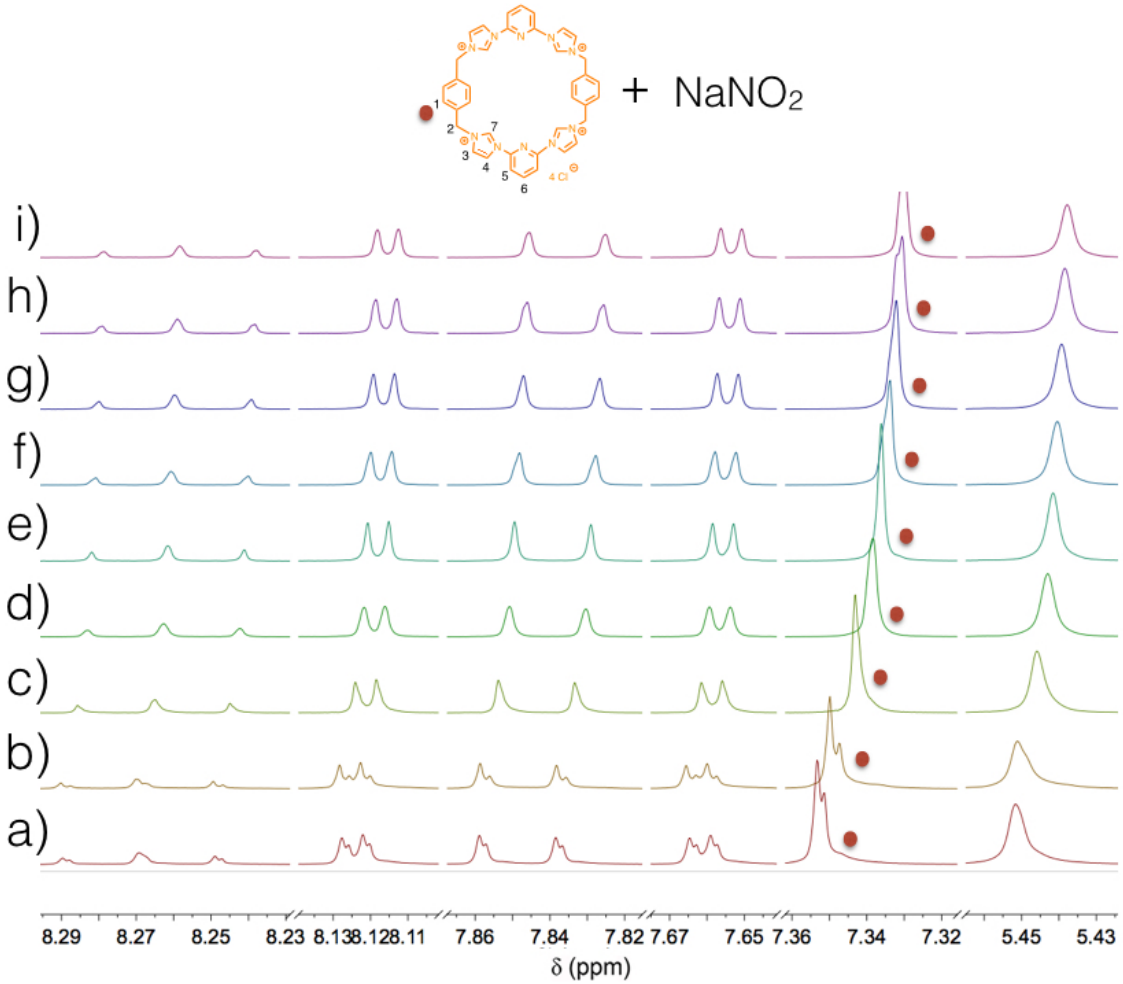

Figure 3.7 Truncated ^{1}H NMR spectra (400 MHz, D_2O, 298 K) of the tetracationic macrocycle (**Host**) recorded at a concentration of 0.5 mM in the presence of differing concentrations of $NaNO_2$: (a) 0 mM, (b) 0.5 mM, (c) 1.0 mM, (d) 1.5 mM, (e) 2.0 mM, (f) 2.5 mM, (g) 3.0 mM, (h) 3.5 mM, and (i) 4.0 mM. Reproduced with permission from *J. Am. Chem. Soc*. **2018**, *140*, 2777. Copyright 2018 American Chemical Society.[10]

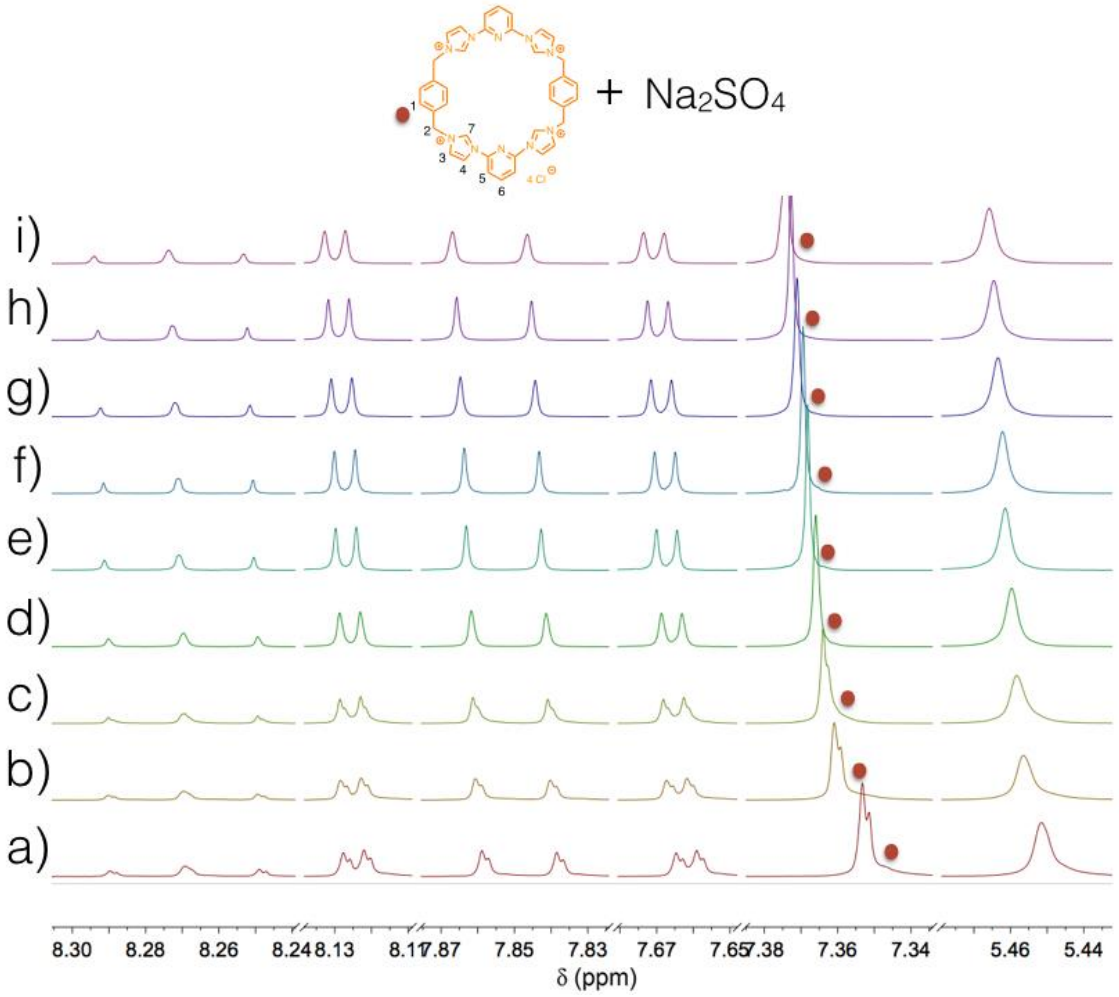

Figure 3.8 Truncated ^{1}H NMR spectra (400 MHz, D_2O, 298 K) of the tetracationic macrocycle (**Host**) recorded at a concentration of 0.5 mM in the presence of differing concentrations of Na_2SO_4: (a) 0 mM, (b) 0.5 mM, (c) 1.0 mM, (d) 1.5 mM, (e) 2.0 mM, (f) 2.5 mM, (g) 3.0 mM, (h) 3.5 mM, and (i) 4.0 mM. Reproduced with permission from *J. Am. Chem. Soc*. **2018**, *140*, 2777. Copyright 2018 American Chemical Society.[10]

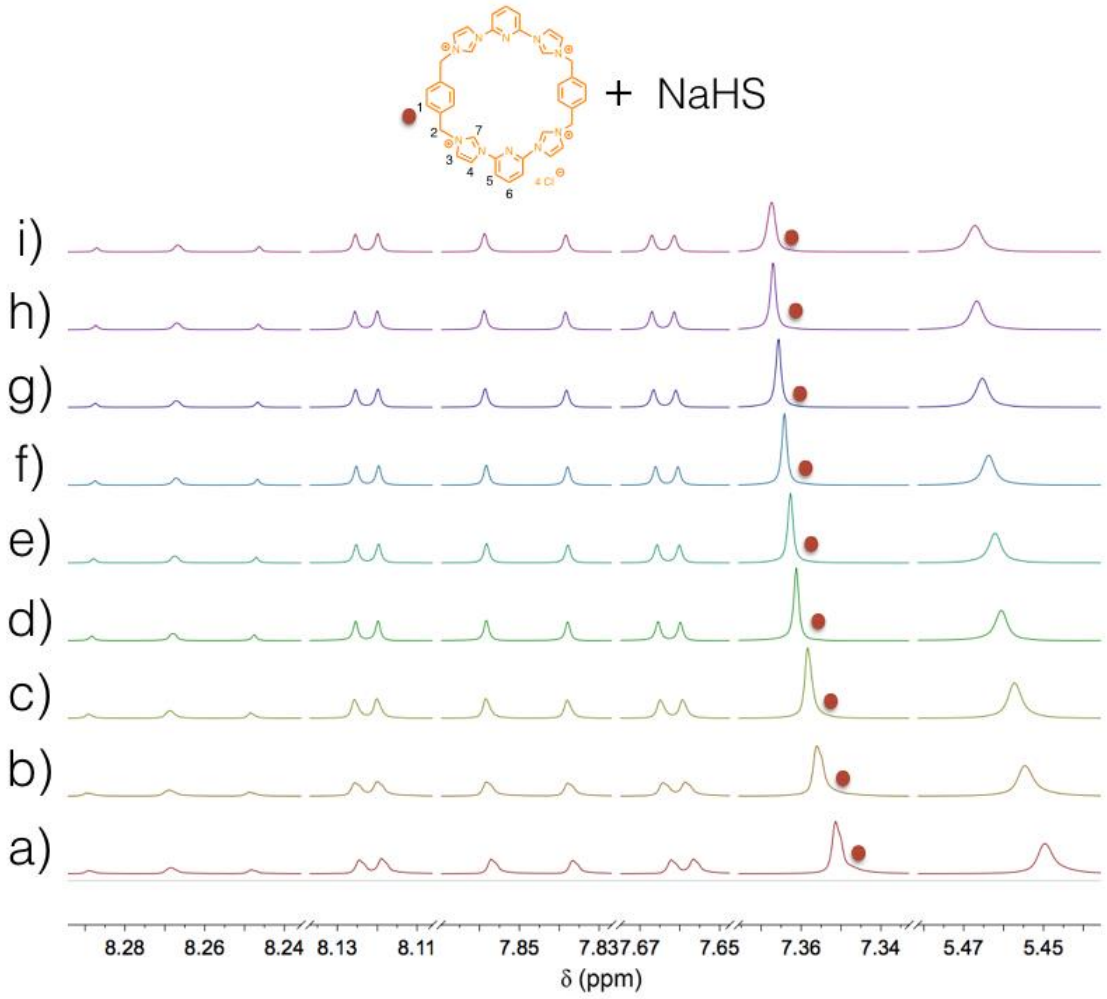

Figure 3.9 Truncated ^{1}H NMR spectra (400 MHz, D_2O, 298 K) of the tetracationic macrocycle (**Host**) recorded at a concentration of 0.5 mM in the presence of differing concentrations of NaHS: (a) 0 mM, (b) 0.5 mM, (c) 1.0 mM, (d) 1.5 mM, (e) 2.0 mM, (f) 2.5 mM, (g) 3.0 mM, (h) 3.5 mM, and (i) 4.0 mM. Reproduced with permission from *J. Am. Chem. Soc*. **2018**, *140*, 2777. Copyright 2018 American Chemical Society.[10]

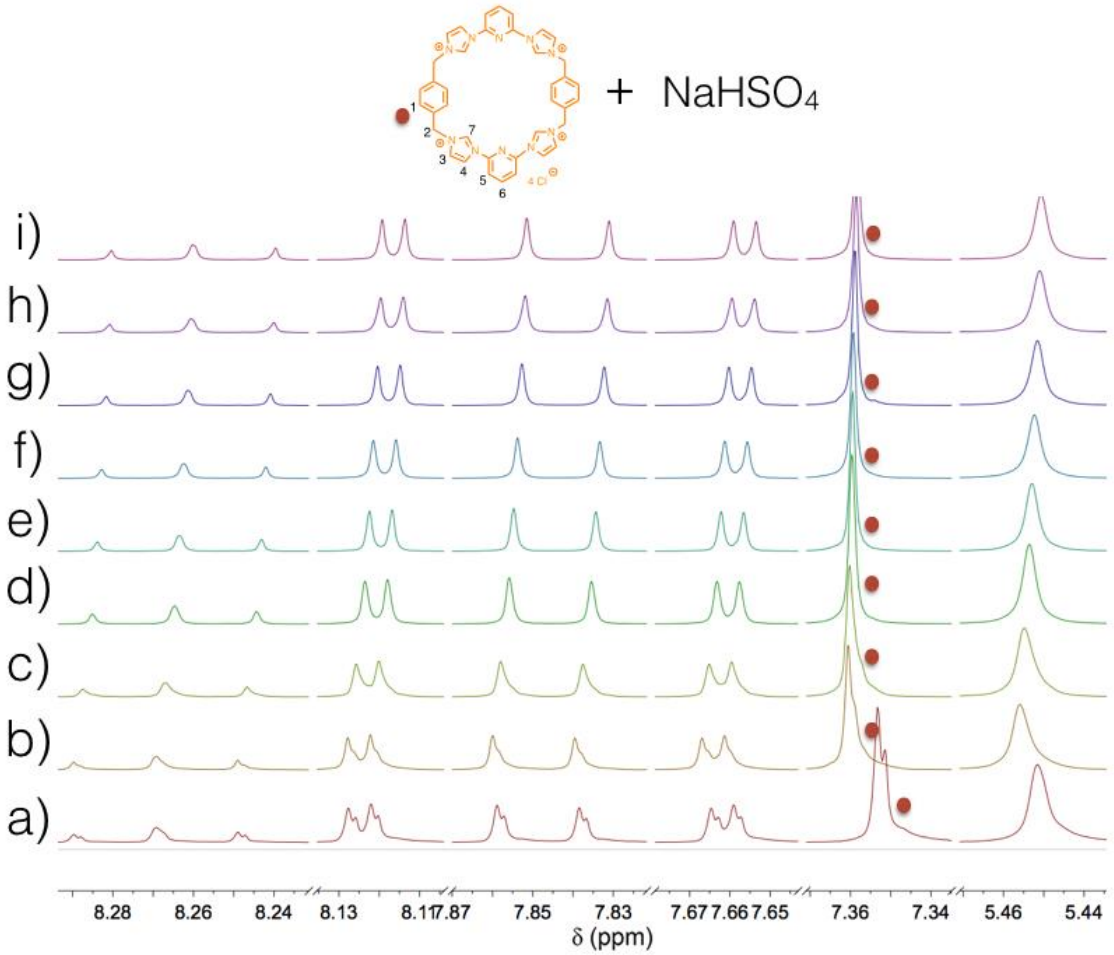

Figure 3.10 Truncated ^{1}H NMR spectra (400 MHz, D_2O, 298 K) of the tetracationic macrocycle (**Host**) recorded at a concentration of 0.5 mM in the presence of differing concentrations of $NaHSO_4$: (a) 0 mM, (b) 0.5 mM, (c) 1.0 mM, (d) 1.5 mM, (e) 2.0 mM, (f) 2.5 mM, (g) 3.0 mM, (h) 3.5 mM, and (i) 4.0 mM. Reproduced with permission from *J. Am. Chem. Soc*. **2018**, *140*, 2777. Copyright 2018 American Chemical Society.[10]

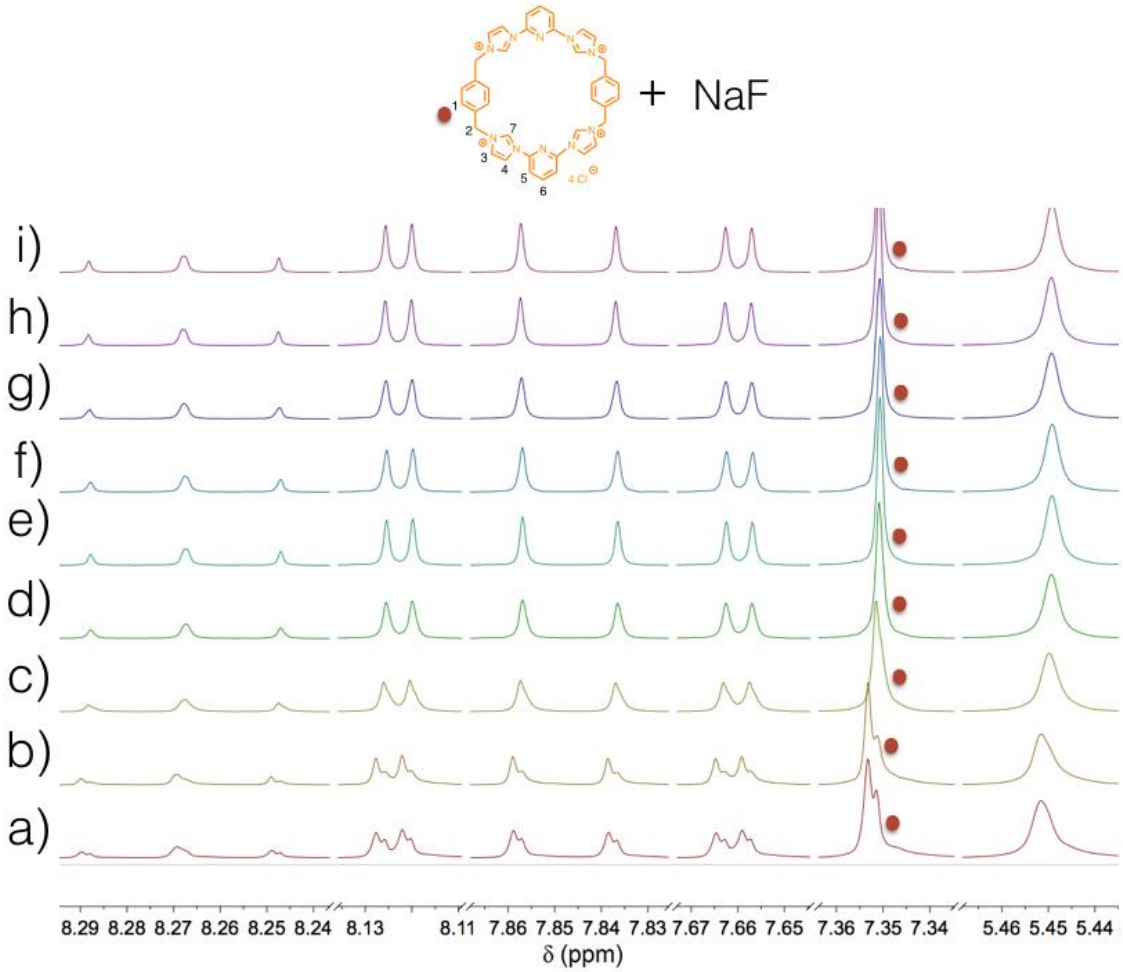

Figure 3.11 Truncated ^{1}H NMR spectra (400 MHz, D_2O, 298 K) of the tetracationic macrocycle (**Host**) recorded at a concentration of 0.5 mM in the presence of differing concentrations of NaF: (a) 0 mM, (b) 0.5 mM, (c) 1.0 mM, (d) 1.5 mM, (e) 2.0 mM, (f) 2.5 mM, (g) 3.0 mM, (h) 3.5 mM, and (i) 4.0 mM. Reproduced with permission from *J. Am. Chem. Soc*. **2018**, *140*, 2777. Copyright 2018 American Chemical Society.[10]

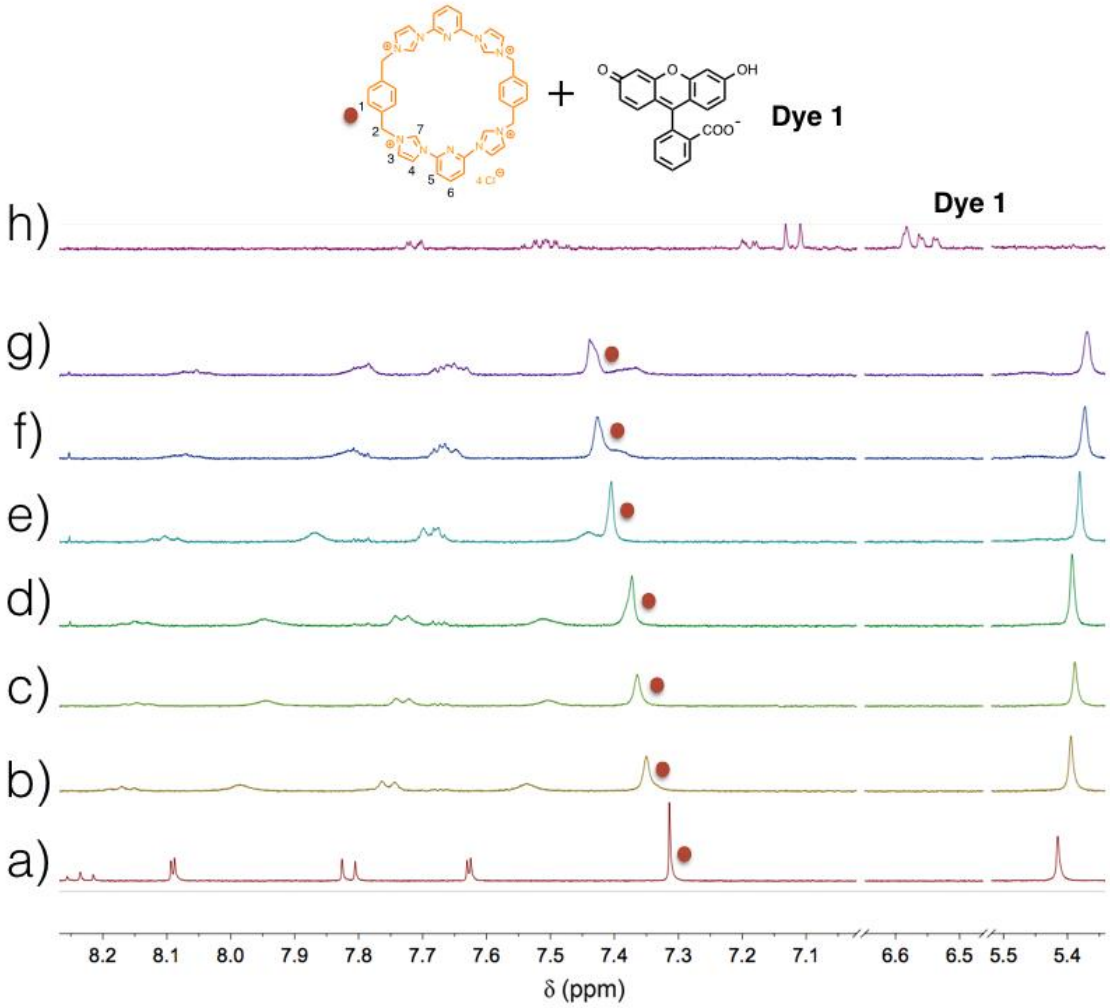

Figure 3.12 Truncated ^{1}H NMR spectra (400 MHz, D_2O, 298 K) of the tetracationic macrocycle (**Host**) recorded at a concentration of 0.5 mM in the presence of differing concentrations of **Dye 1**: (a) 0 mM, (b) 0.25 mM, (c) 0.5 mM, (d) 1.0 mM, (e) 2.0 mM, (f) 3.0 mM, (g) 4.0 mM, and (h) 0.5 mM of **Dye 1** alone. Reproduced with permission from *J. Am. Chem. Soc*. **2018**, *140*, 2777. Copyright 2018 American Chemical Society.[10]

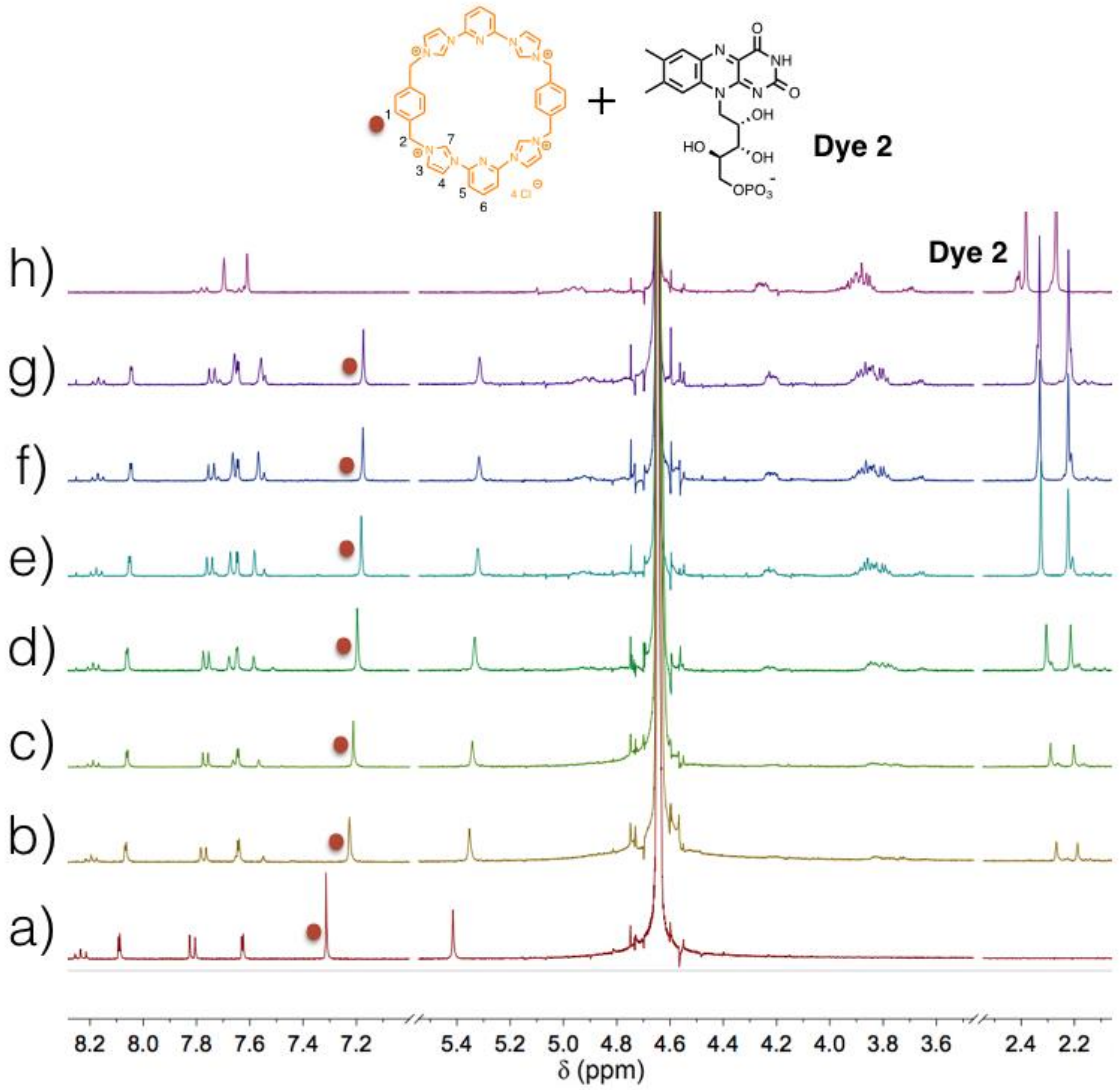

Figure 3.13 Truncated ^{1}H NMR spectra (400 MHz, D_2O, 298 K) of the tetracationic macrocycle (**Host**) recorded at a concentration of 0.5 mM in the presence of differing concentrations of **Dye 2**: (a) 0 mM, (b) 0.25 mM, (c) 0.5 mM, (d) 1.0 mM, (e) 2.0 mM, (f) 3.0 mM, (g) 4.0 mM, and (h) 0.5 mM of **Dye 2** alone. Reproduced with permission from *J. Am. Chem. Soc*. **2018**, *140*, 2777. Copyright 2018 American Chemical Society.[10]

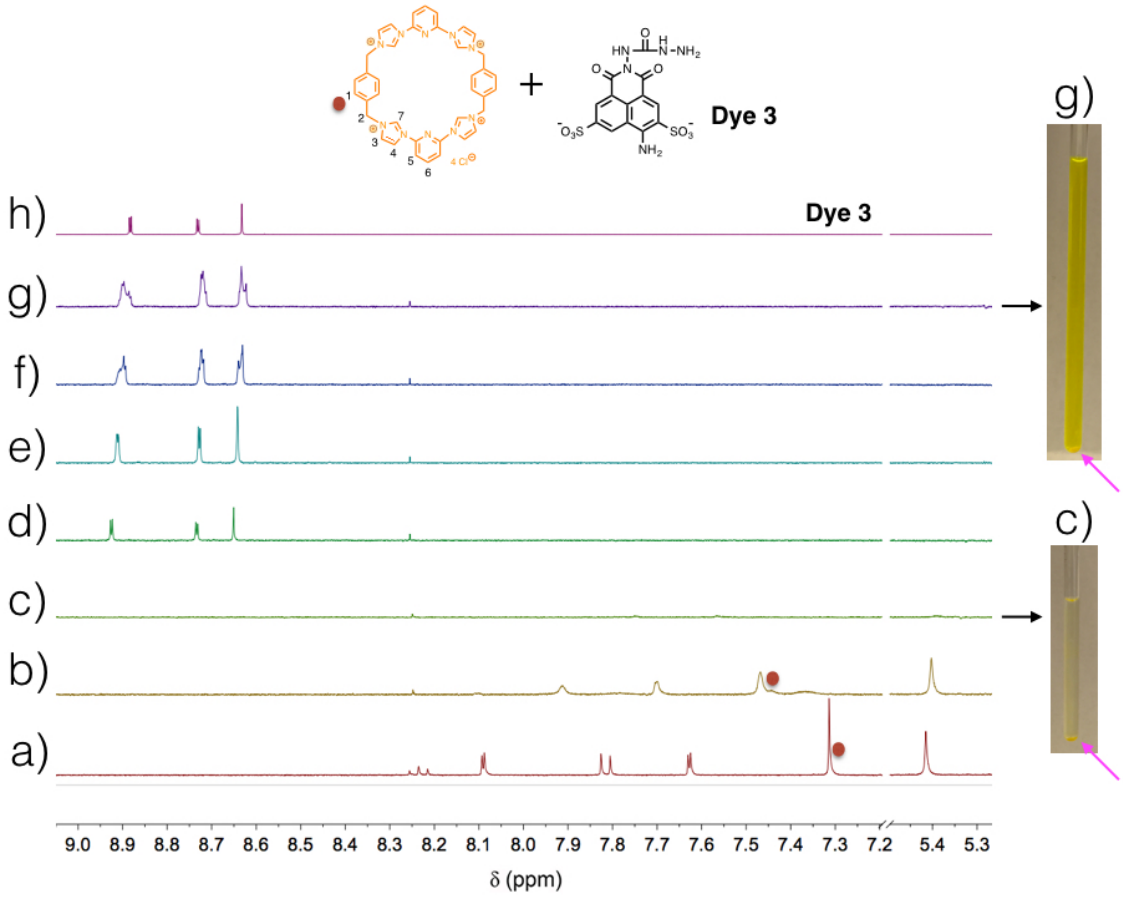

Figure 3.14 Truncated ^{1}H NMR spectra (400 MHz, D_2O, 298 K) of the tetracationic macrocycle (**Host**) recorded at a concentration of 0.5 mM in the presence of differing concentrations of **Dye 3**: (a) 0 mM, (b) 0.25 mM, (c) 0.5 mM, (d) 1.0 mM, (e) 2.0 mM, (f) 3.0 mM, (g) 4.0 mM, and (h) 0.5 mM of **Dye 3** alone. The arrows on the panels to the right indicate the formation of a precipitate in the sample used for the ^{1}H NMR spectroscopic studies. Reproduced with permission from *J. Am. Chem. Soc*. **2018**, *140*, 2777. Copyright 2018 American Chemical Society.[10]

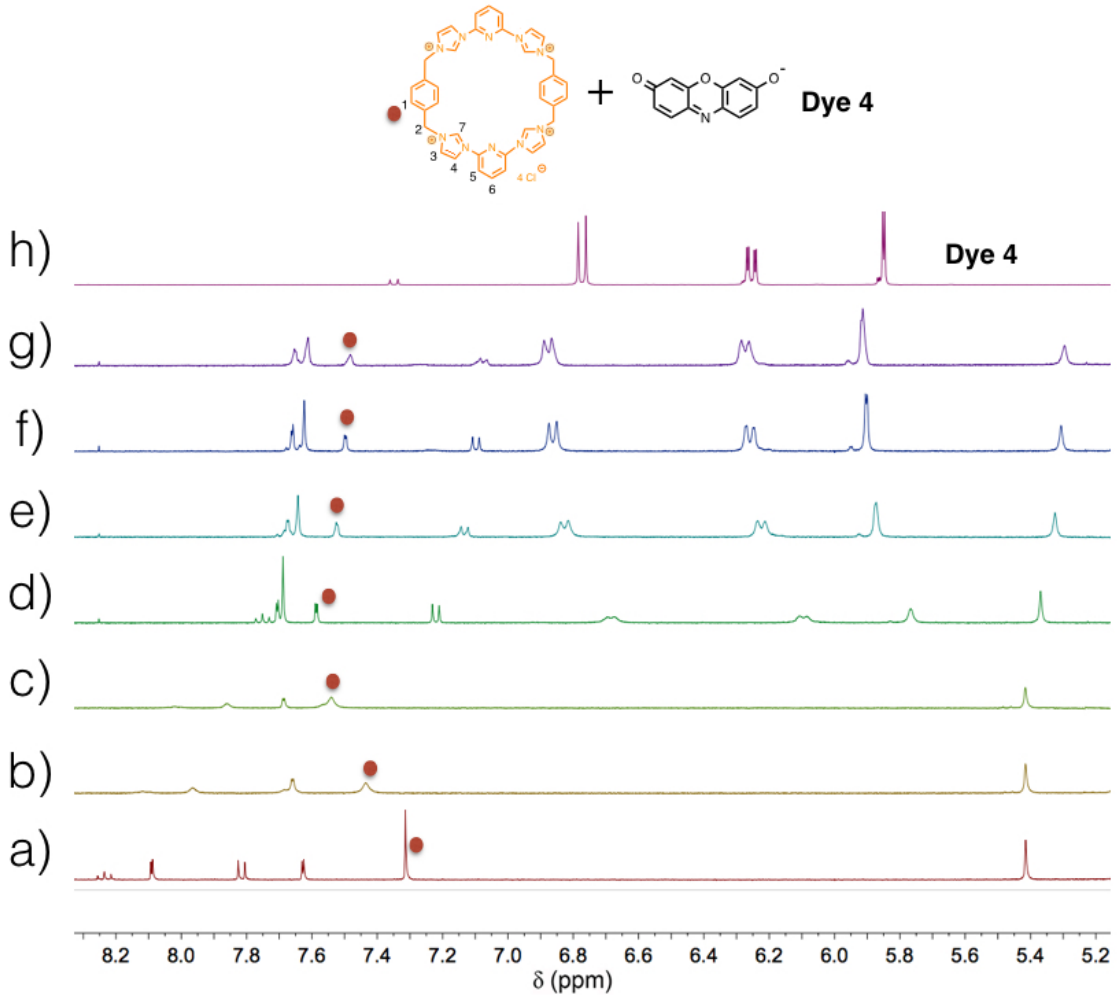

Figure 3.15 Truncated ^{1}H NMR spectra (400 MHz, D_2O, 298 K) of the tetracationic macrocycle (**Host**) recorded at a concentration of 0.5 mM in the presence of differing concentrations of **Dye 4**: (a) 0 mM, (b) 0.25 mM, (c) 0.5 mM, (d) 1.0 mM, (e) 2.0 mM, (f) 3.0 mM, (g) 4.0 mM, and (h) 0.5 mM of **Dye 4** alone. Reproduced with permission from *J. Am. Chem. Soc*. **2018**, *140*, 2777. Copyright 2018 American Chemical Society.[10]

	$NaNO_3$	$NaNO_2$	Na_2SO_4	NaHS	$NaHSO_4$	NaF	Dye 1	Dye 2	Dye 3	Dye 4
$\Delta\delta$ (ppm)	0.030	0.023	0.021	0.020	0.006	0.003	0.130	0.140	↓	0.180

Table 3.1 Chemical shift changes ($\Delta\delta$) of protons H_1 on the macrocycle **Host** (0.5 mM) after adding substoichiometric quantities of the indicated anionic salts (4.0 mM, 8.0 molar equiv. of **Host**) in accord with the parameters used for the studies shown in Figures 3.6–3.15. Reproduced with permission from *J. Am. Chem. Soc*. **2018**, *140*, 2777. Copyright 2018 American Chemical Society.[10]

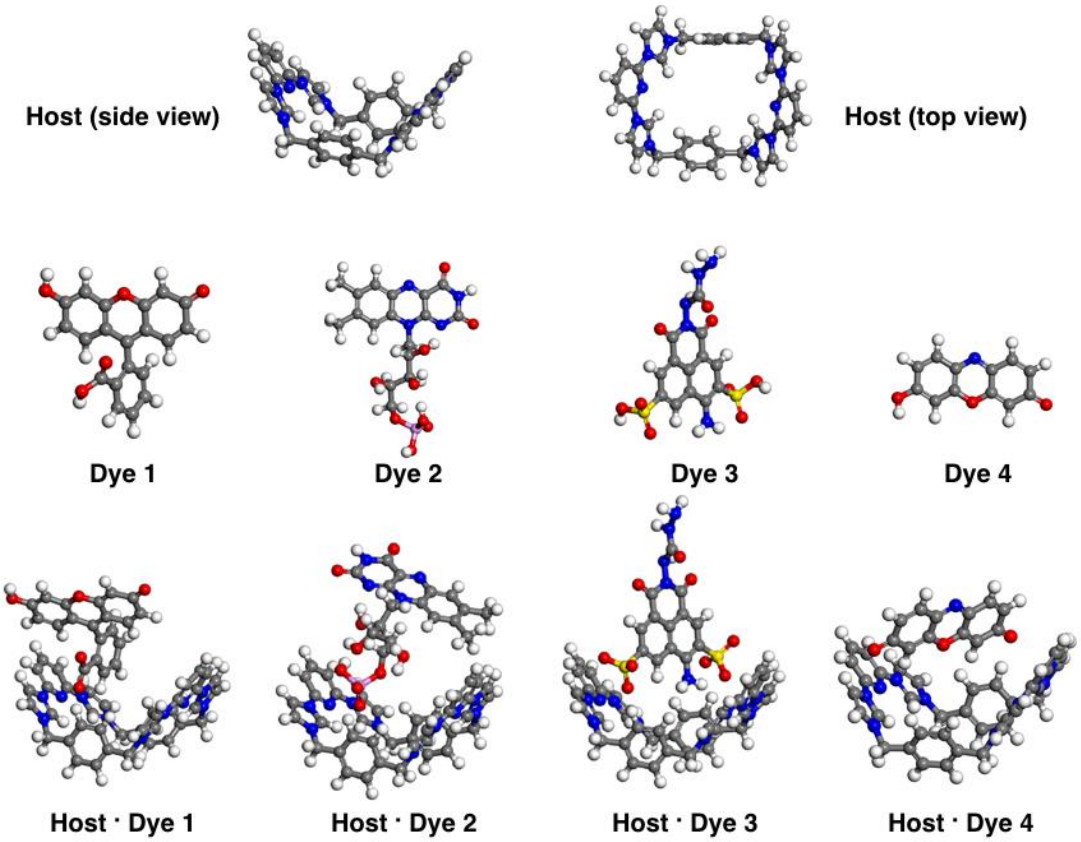

Figure 3.16 Low-energy configurations of **Host**, organic anions, and their complexes. Reproduced with permission from *J. Am. Chem. Soc*. **2018**, *140*, 2777. Copyright 2018 American Chemical Society.[10]

Items	Host · Dye 1	Host · Dye 2	Host · Dye 3	Host · Dye 4
Ads. energy (eV)	-0.87	-1.44	-2.68	-1.17

Table 3.2 Binding energies for the complexes formed between **Host** and organic anions. Reproduced with permission from *J. Am. Chem. Soc*. **2018**, *140*, 2777. Copyright 2018 American Chemical Society.[10]

The DFT calculations supporting the present study were carried out using the package VASP5.4,[16] and the GGA+PBE exchange correlation functional. The cutoff energy was set to 400 eV, converging to 0.03 eV $Å^{-1}$. A single Γ point was sampled in

the first Brillouin zone and a super large box was used to contain each of the molecules or complexes. The binding energy was calculated as: $\Delta E_{ads} = E_{tot} + 1/2\ E_{H2} - (E_{\mathbf{Dye}} + E_{\mathbf{Host}})$

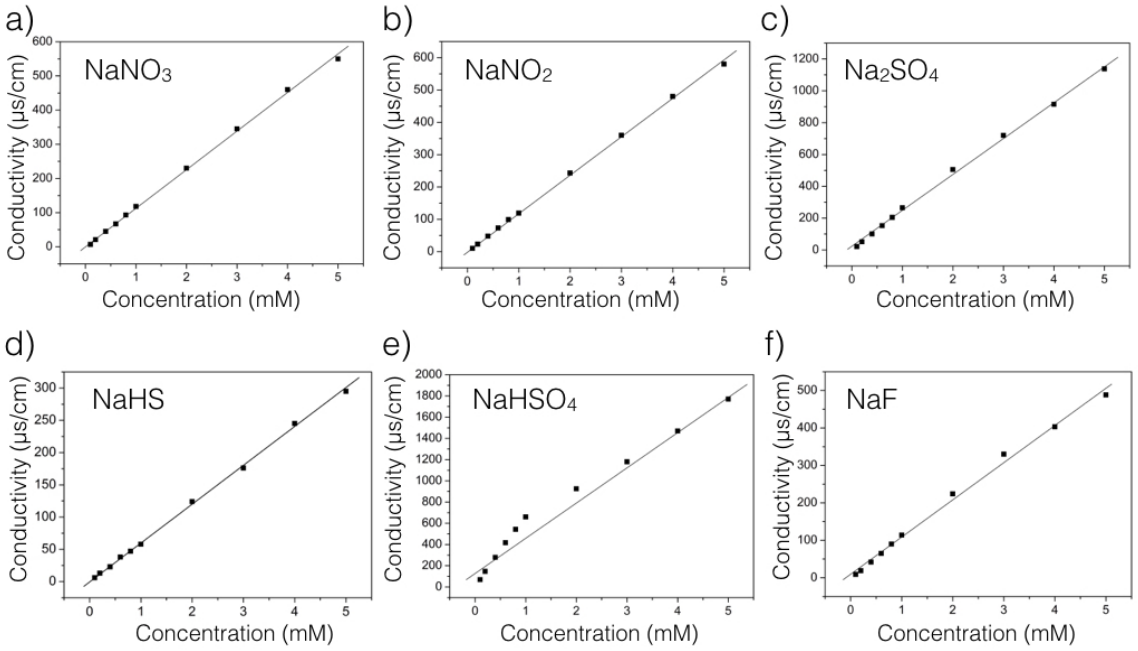

Figure 3.17 Plots of conductivity of aqueous solutions containing selected inorganic anions versus varying anion concentrations: (a) $NaNO_3$, (b) $NaNO_2$, (c) Na_2SO_4, (d) NaHS, (e) $NaHSO_4$, and (f) NaF. These are calibration curves. No polymeric material is present in these samples. Reproduced with permission from *J. Am. Chem. Soc*. **2018**, *140*, 2777. Copyright 2018 American Chemical Society.[10]

As a first test of whether **P1** could be used to capture various anions in aqueous media, 13 mg of this polymer was contacted with 100 µM solutions of, respectively, $NaNO_3$, $NaNO_2$, Na_2SO_4, NaHS, $NaHSO_4$, and NaF (10 mL each). It was expected that changes in concentration would be reflected in differences in the solution conductivity (Figure 3.17). As shown in Figure 3.18, the conductivity of all six solutions decreased as a function of time. For example, the conductivity of the $NaHSO_4$ solution decreased from 68 to 30 µs/cm after 30 h of exposure to **P1**, with a leveling off then being observed. Correlating the conductivity with concentration (Figure 3.17), allowed corresponding plots of the change in concentration as a function of time (Figure 3.18b) and net

percentage of anion salt removed (Figure 3.18c) to be constructed. On this basis, it was concluded that **P1** was most efficient at removing $NaNO_3$ (68%) and least effective for NaF capture (47%) under the test conditions described above.[1d] This conclusion is in accord with what would be predicted based on the basis of the Hofmeister series and the relevant anion hydration energies.[17] It is also in agreement with the qualitative binding studies carried out with the free **Host** (vide supra and Table 3.1).

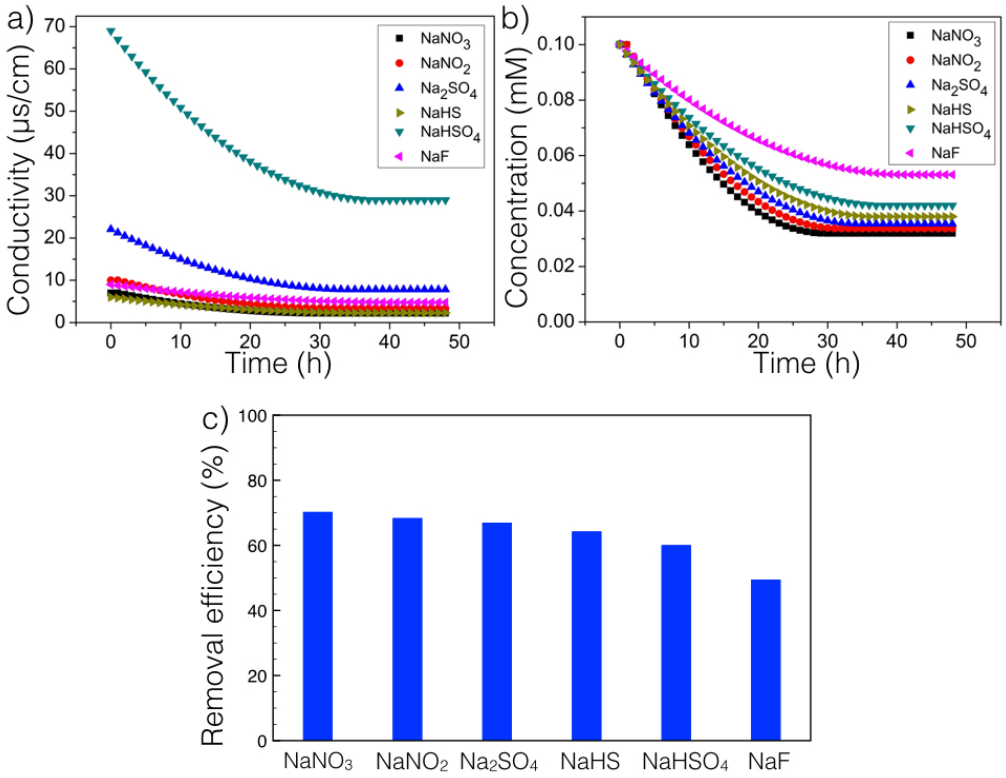

Figure 3.18 (a) Conductivity of aqueous inorganic salt solutions (10 mL each at an initial concentration of 100 μM) after contacting with **P1** (13 mg) for different times. (b) Concentration of the indicated salt in the aqueous medium of (a) after contacting with **P1** as a function of time. (c) Extraction efficiency as the percentage of the indicated salt removed by **P1** after 48 h under the conditions of (a). Reproduced with permission from *J. Am. Chem. Soc*. **2018**, *140*, 2777. Copyright 2018 American Chemical Society.[10]

Comparable tests were carried out using the control polymer networks, $\mathbf{P1}_{\textbf{control-1}}$ and $\mathbf{P1}_{\textbf{control-2}}$. As noted above, these systems resemble **P1** but lack the tetracationic receptor **3.2**. When $\mathbf{P1}_{\textbf{control-1}}$ and $\mathbf{P1}_{\textbf{control-2}}$ are added, respectively, to the various salt

solutions under the same conditions, the conductivity and concentration as those tested with **P1**, hydrogelation occurs. However, little appreciably change in conductivity is observed (Figures 3.19 and 3.20). This lack of difference is ascribed to the absence of a macrocyclic anion receptor capable of effective anion recognition and hence appreciable salt binding.

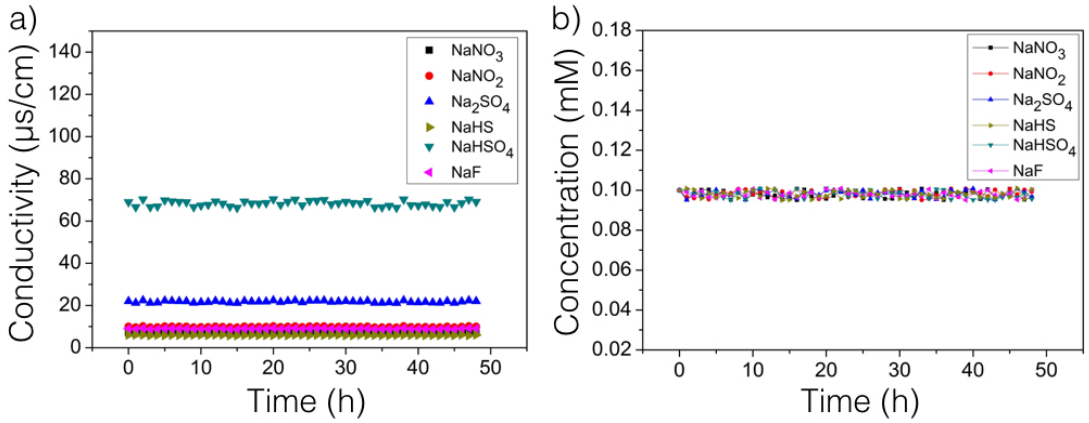

Figure 3.19 (a) Conductivity as a function of time for various inorganic anionic aqueous solutions (each at an initial concentration of 100 µM and a volume of 10 mL) after exposure to **P1**$_{\textbf{control-1}}$ (8 mg). (b) Corresponding concentration plots. Reproduced with permission from *J. Am. Chem. Soc*. **2018**, *140*, 2777. Copyright 2018 American Chemical Society.[10]

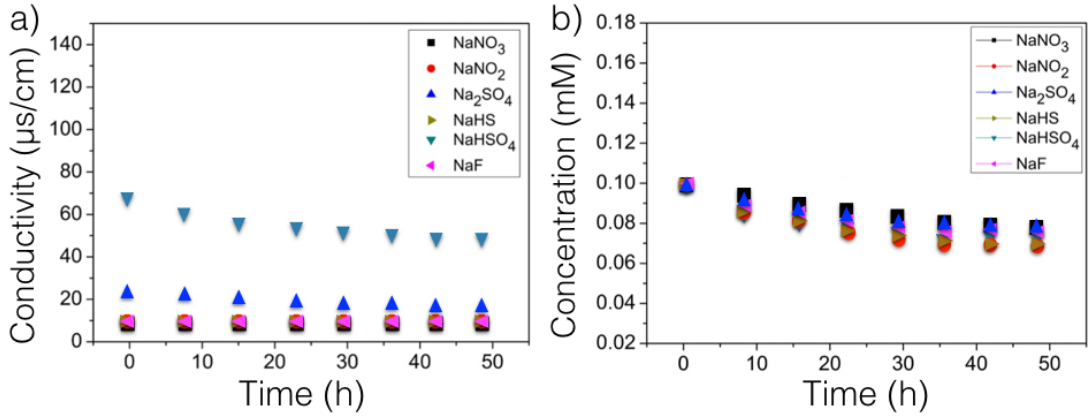

Figure 3.20 (a) Conductivity as a function of time for various inorganic anionic aqueous solutions (each at an initial concentration of 100 µM and a volume of 10 mL) after exposure to **P1**$_{\textbf{control-2}}$ (8.5 mg). (b) Corresponding concentration plots. Reproduced with permission from *J. Am. Chem. Soc*. **2018**, *140*, 2777. Copyright 2018 American Chemical Society.[10]

The ability of **P1** to capture organic anions in water was also studied. **Dyes 1**−**4** were chosen for this purpose because (1) all four give aqueous solutions that are colored and (2) they embody a range of anionic groups (CO_2^-, PO_3^-, SO_3^-, and O^-). When **P1** was immersed separately in aqueous solutions containing these test organic anions, changes in the UV-Vis spectra were seen (Figure 3.21): the absorbance intensity of all four solutions decreased as a function of immersion time. Assuming a Beer-Lambert relationship between absorbance intensity and concentration (Figure 3.22), the corresponding change in aqueous dye concentration as a function of time could be calculated (Figure 3.23). For example, in one study it was found that the concentration of **Dye 1** (10 mL solution) decreased from 50 μM gradually to 4 μM upon exposure to 13 mg of **P1**. In a similar way (*cf*. Figure 3.23b), the removal efficiencies could be calculated at times past where significant kinetic effects were observed (*ca*. 48 h). The corresponding color changes could be monitored by the naked eye (Figure 3.24). In this way, it was found that **Dye 3** was removed most efficiently (98%). As in the case of the inorganic salts, $\mathbf{P1_{control\text{-}1}}$ and $\mathbf{P1_{control\text{-}2}}$ were used for comparison. No obvious changes were found in the absorbance intensity and inferred concentrations in the case of all four test dyes (Figures 3.25 and 3.26); again, this is ascribed to the lack of an effective anion receptor within these two polymer networks.

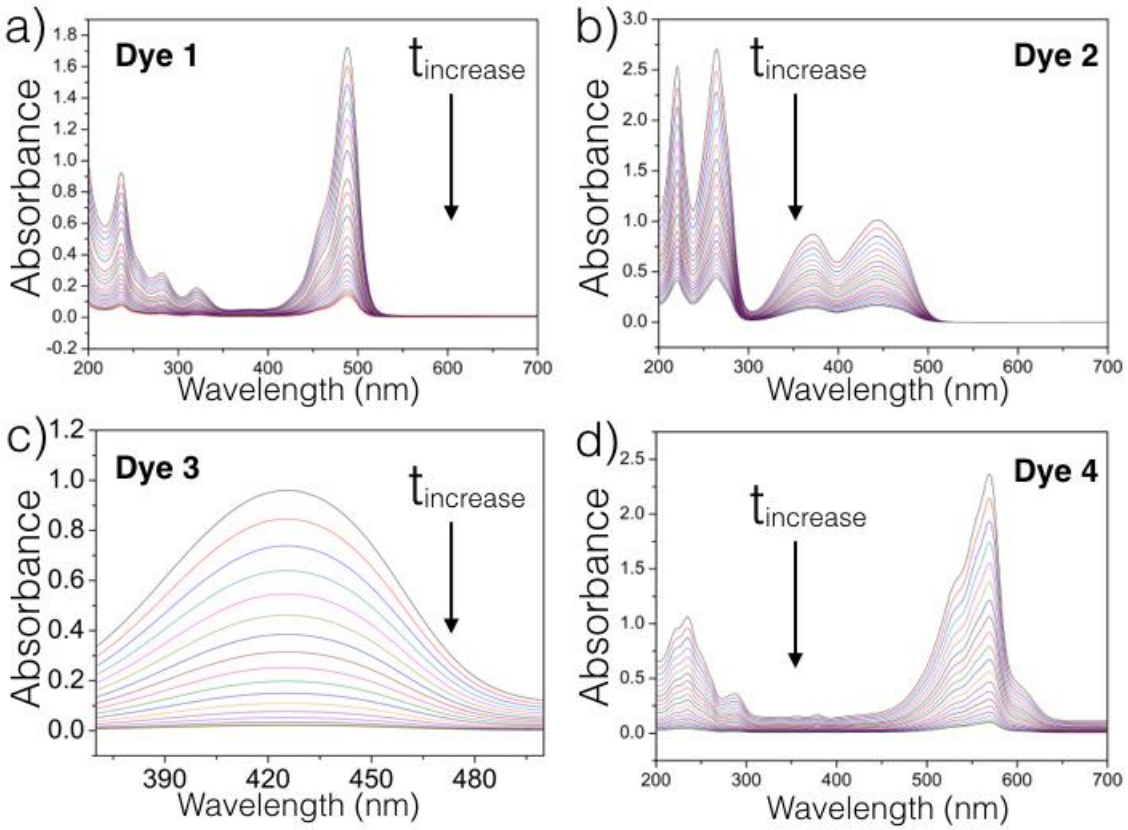

Figure 3.21 Time-dependent changes in the UV-Vis spectra of aqueous solutions containing organic anionic salts (each with an initial concentrations of 50 μM and a volume of 10 mL) exposed to **P1** (13 mg): (a) **Dye 1**, (b) **Dye 2**, (c) **Dye 3**, and (d) **Dye 4**. Reproduced with permission from *J. Am. Chem. Soc*. **2018**, *140*, 2777. Copyright 2018 American Chemical Society.[10]

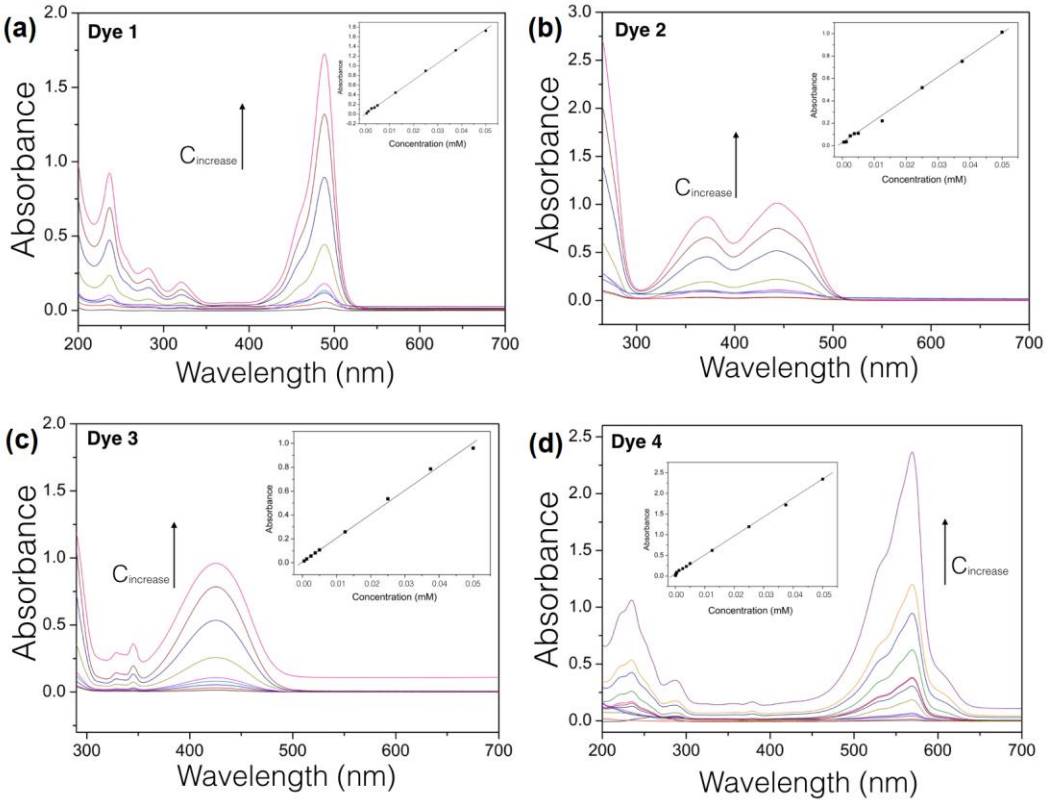

Figure 3.22 UV-Vis spectra of aqueous solutions containing differing concentrations of (a) **Dye 1**, (b) **Dye 2**, (c) **Dye 3**, and (d) **Dye 4**. Four separate plots of concentration versus absorbance intensity at (a) 490 nm, (b) 445 nm, (c) 425 nm, and (d) 575 nm are shown in the corresponding inserts. Reproduced with permission from *J. Am. Chem. Soc*. **2018**, *140*, 2777. Copyright 2018 American Chemical Society.[10]

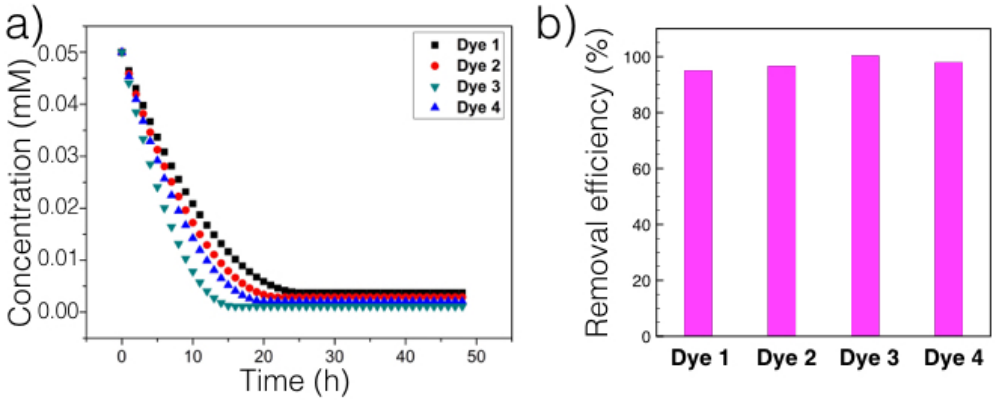

Figure 3.23 (a) Organic anionic dye concentration in the aqueous phase after exposure to **P1** (13 mg) to aqueous solutions (at an initial dye concentration of 50 μM and a volume of 10 mL) as a function of time. (b) Amount (%) of dye removed by **P1** after 48 h. Reproduced with permission from *J. Am. Chem. Soc*. **2018**, *140*, 2777. Copyright 2018 American Chemical Society.[10]

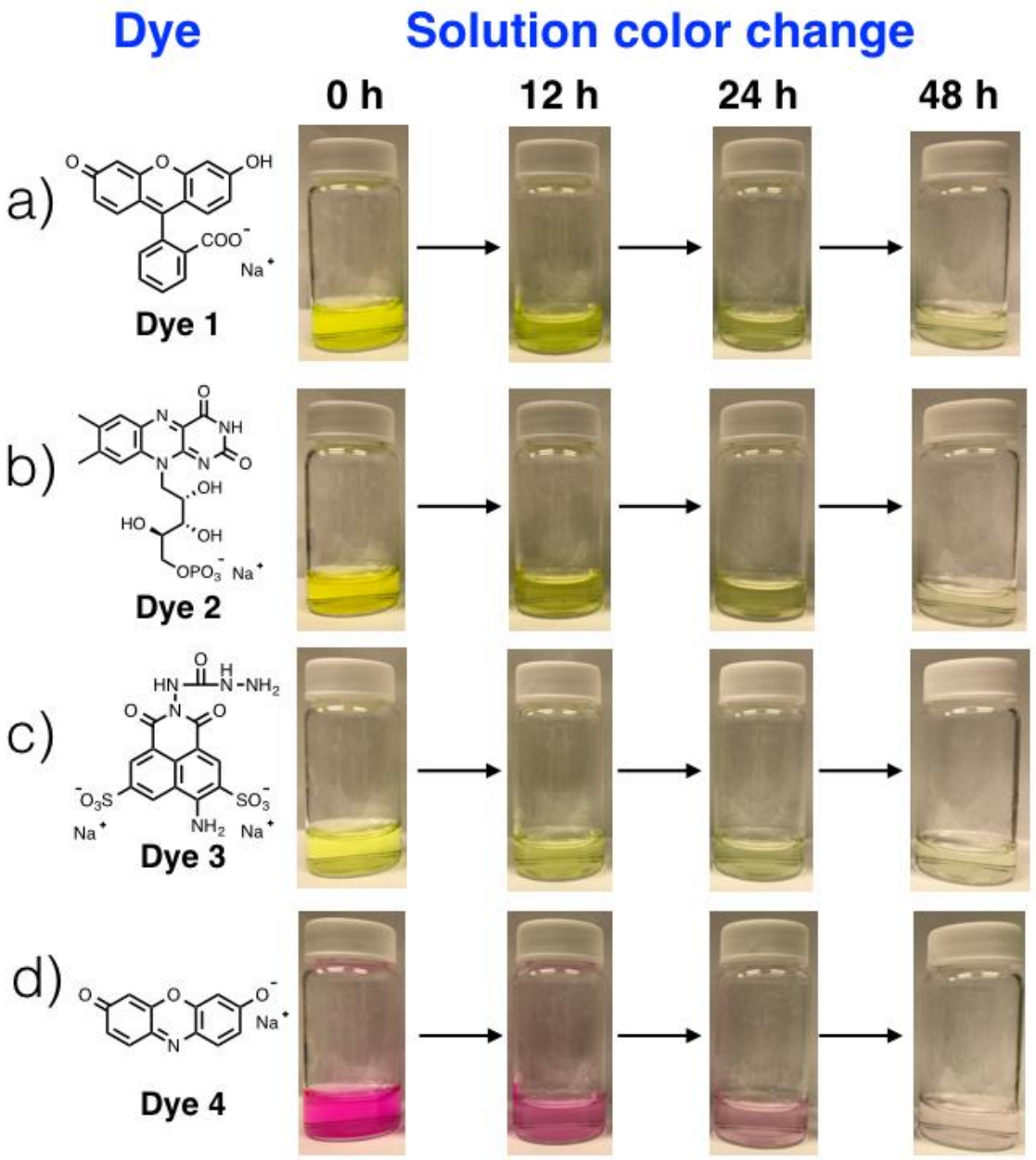

Figure 3.24 (a) Color changes seen over time for aqueous solutions containing various organic anionic dyes (initial dye concentration = 50 μM; solution volume = 10 mL) after exposure to **P1** (13 mg): (a) **Dye 1**, (b) **Dye 2**, (c) **Dye 3**, and (d) **Dye 4**. Reproduced with permission from *J. Am. Chem. Soc*. **2018**, *140*, 2777. Copyright 2018 American Chemical Society.[10]

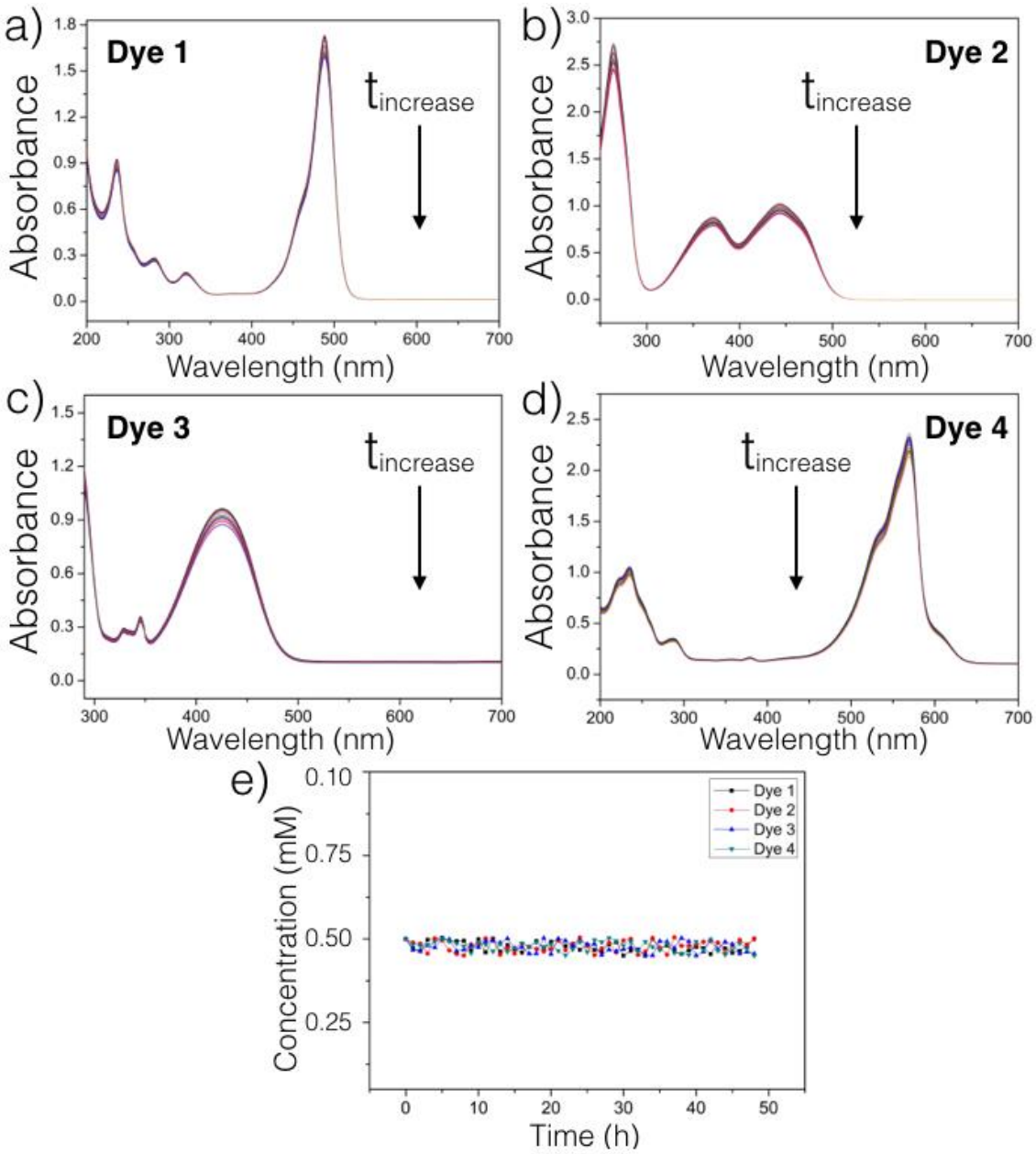

Figure 3.25 Time-dependent changes in the UV-Vis spectra of aqueous solutions containing organic anionic salts (each with an initial concentration of 50 μM and a volume of 10 mL) exposed to $\mathbf{P1}_{\textbf{control-1}}$ (8 mg): (a) **Dye 1**, (b) **Dye 2**, (c) **Dye 3**, and (d) **Dye 4**. (e) Plot of the change in concentration of the organic anionic dyes in the aqueous solutions as a function of time after exposure to $\mathbf{P}_{\textbf{1control-1}}$. Reproduced with permission from *J. Am. Chem. Soc*. **2018**, *140*, 2777. Copyright 2018 American Chemical Society.[10]

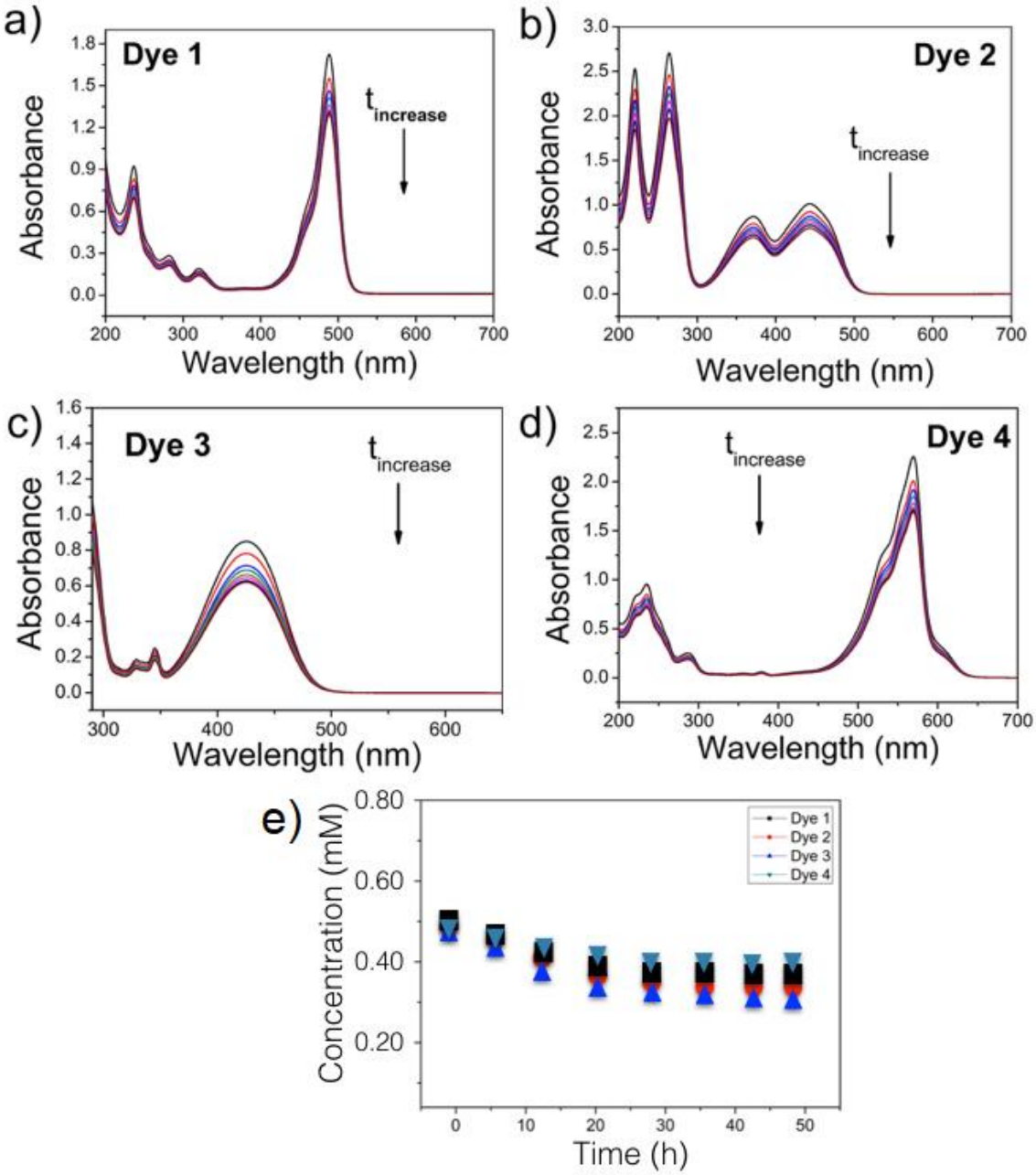

Figure 3.26 Time-dependent changes in the UV-Vis spectra of aqueous solutions containing organic anionic salts (each with an initial concentration of 50 μM and a volume of 10 mL) exposed to $\mathbf{P1}_{\mathbf{control\text{-}2}}$ (8.5 mg): (a) **Dye 1**, (b) **Dye 2**, (c) **Dye 3**, and (d) **Dye 4**. (e) Plot of the change in concentration of the organic anionic dyes in the aqueous solutions as a function of time after exposure to $\mathbf{P1}_{\mathbf{control\text{-}2}}$. Reproduced with permission from *J. Am. Chem. Soc*. **2018**, *140*, 2777. Copyright 2018 American Chemical Society.[10]

As a complement to determining the changes in concentration produced by **P1**, the mechanical properties of the resulting anion salt-containing hydrogels were checked. Figure 3.27 provides the code names (**G2**−**G11**) assigned to the putative hydrogel products formed from each anionic salt along with associated photographs. These latter serve to confirm that **G2**−**G7** produced using inorganic anion salts are colorless, whereas **G8**−**G11** produced from the test organic dyes are colored. Although the macrocyclic "box" used to generate **P1** is conformationally flexible,[11] it was expected to become more rigid after accommodating an anionic guest. Support for this notion came from the finding that compared to **G1** (the salt-free hydrated form of **P1**), gels **G2**−**G11** all displayed larger tensile moduli and fracture stress points, while being characterized by smaller fracture strain values (*cf*. Figures 3.28 and 3.29).[18]

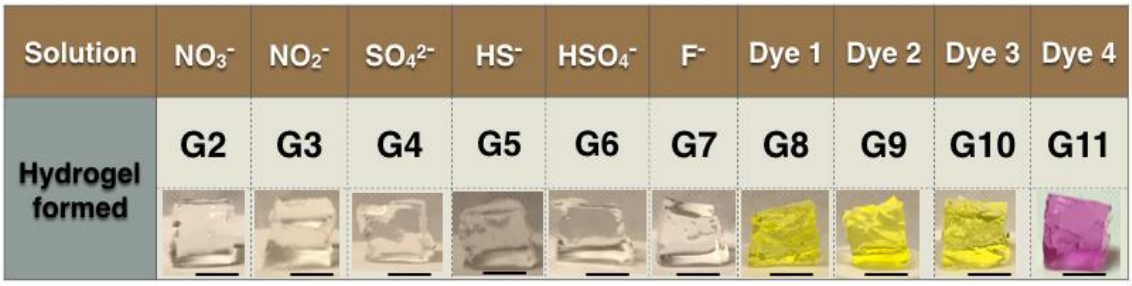

Figure 3.27 Hydrogels **G2**−**G11** formed by contacting **P1** with aqueous salt solutions of various anions for 48 h (scale bar = 0.5 cm). Reproduced with permission from *J. Am. Chem. Soc*. **2018**, *140*, 2777. Copyright 2018 American Chemical Society.[10]

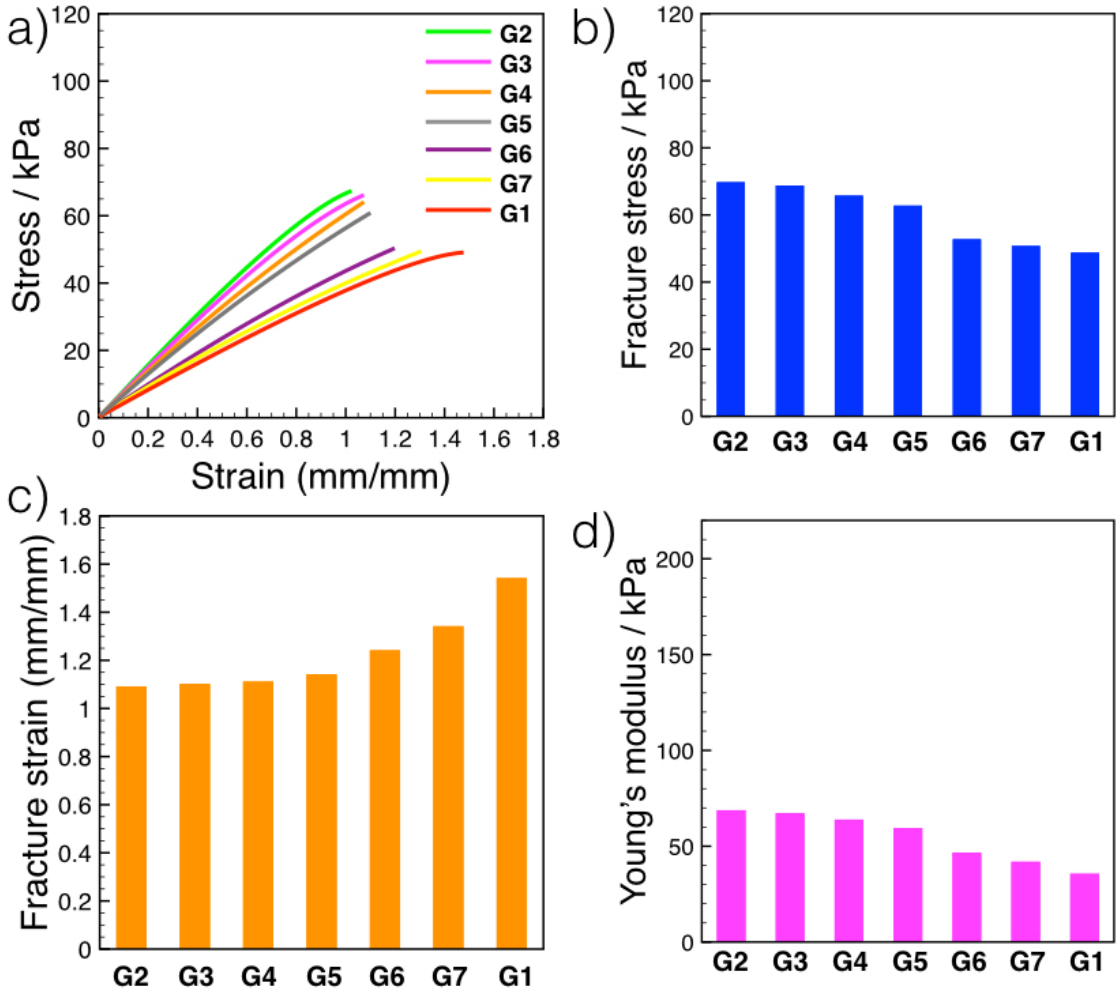

Figure 3.28 (a) Tensile stress-strain curves, (b) fracture stress, (c) fracture strain, and (d) Young's modulus values of the hydrogels formed by contacting **P1** with various aqueous inorganic anionic salt solutions for 48 h. **G1** is the hydrogel obtained by exposure to pure water. **G2**, **G3**, **G4**, **G5**, **G6**, and **G7** correspond to hydrogels obtained upon exposure of 13 mg of **P1** to 100 μM solutions of $NaNO_3$, $NaNO_2$, Na_2SO_4, NaHS, $NaHSO_4$, and NaF, respectively. In all cases the initial salt concentration was 100 μM and the solution volume was 10 mL. Reproduced with permission from *J. Am. Chem. Soc*. **2018**, *140*, 2777. Copyright 2018 American Chemical Society.[10]

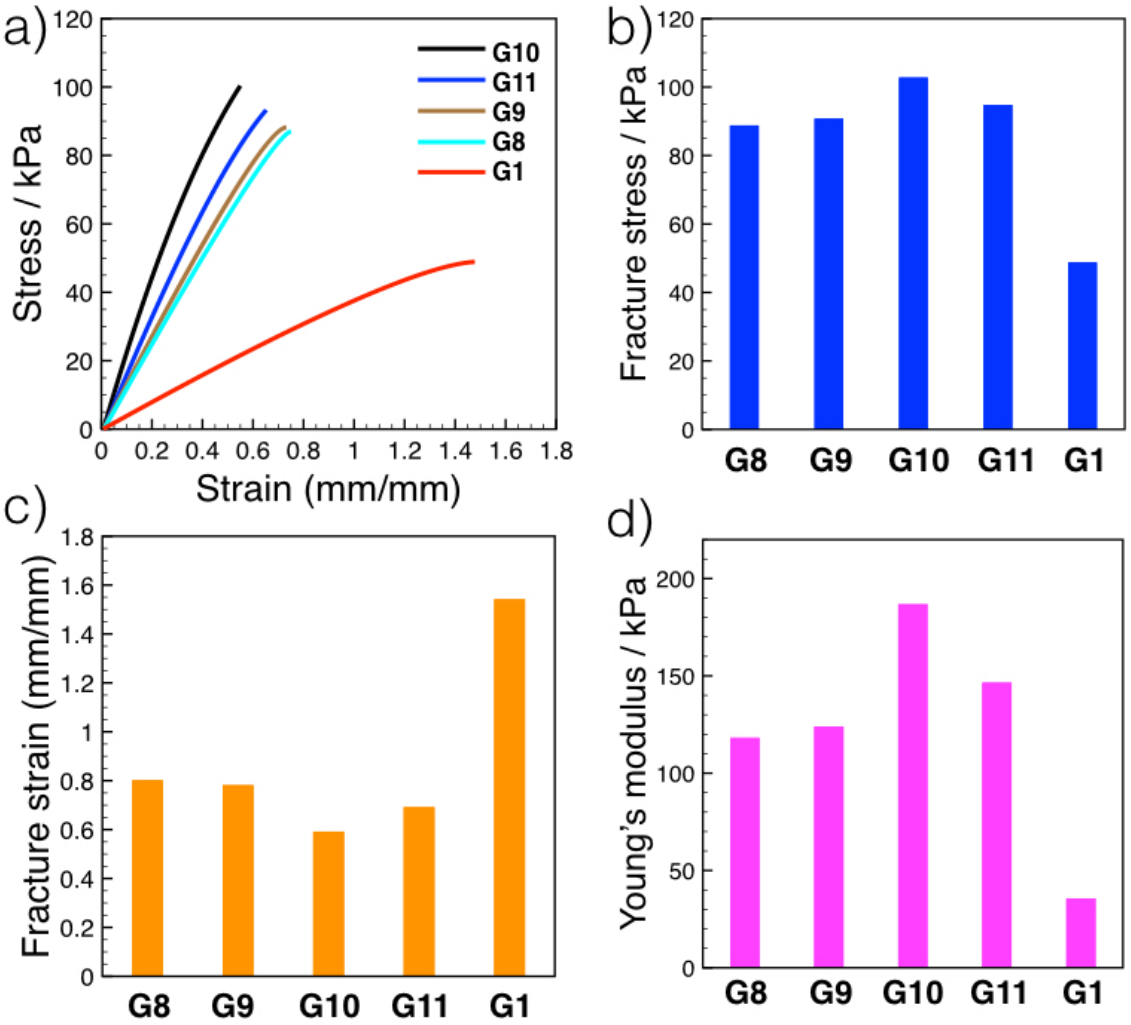

Figure 3.29 (a) Tensile stress-strain curves, (b) fracture stress, (c) fracture strain, and (d) Young's modulus values of the hydrogels formed by contacting **P1** with various aqueous anionic organic dyes solutions for 48 h. **G1** is the hydrogel obtained by exposure to pure water. **G8**, **G9**, **G10**, and **G11** correspond to hydrogels obtained upon exposure of 13 mg of **P1** to 50 μM solutions of **Dye 1**, **Dye 2**, **Dye 3**, and **Dye 4**, respectively. In all cases the initial salt concentration was 100 μM and the solution volume was 10 mL. Reproduced with permission from *J. Am. Chem. Soc*. **2018**, *140*, 2777. Copyright 2018 American Chemical Society.[10]

Once the organic anion salts were absorbed into **P1**, physical removal of the resulting hydrogels from the aqueous medium was used to complete the water purification process. Subsequent treatment with dilute HCl served to release the bound anions. Subjecting the resulting gel to dialysis in water allowed removal of the free anionic salts and any excess acid (Figures 3.30 and 3.31). The mechanical parameters of the recovered material proved almost identical to those of **G1** (Figure 3.31b). The original network **P1** could be obtained by drying this recovered hydrogel, allowing the free hydrogel **G1** to be regenerated and reused if so desired (Figures 3.30−3.32). This regeneration and reuse capability was explicitly demonstrated through two repeat cycles in the case of **Dye 1**, which allowed the initial release process to be followed by the naked eye (Figure 3.31a).

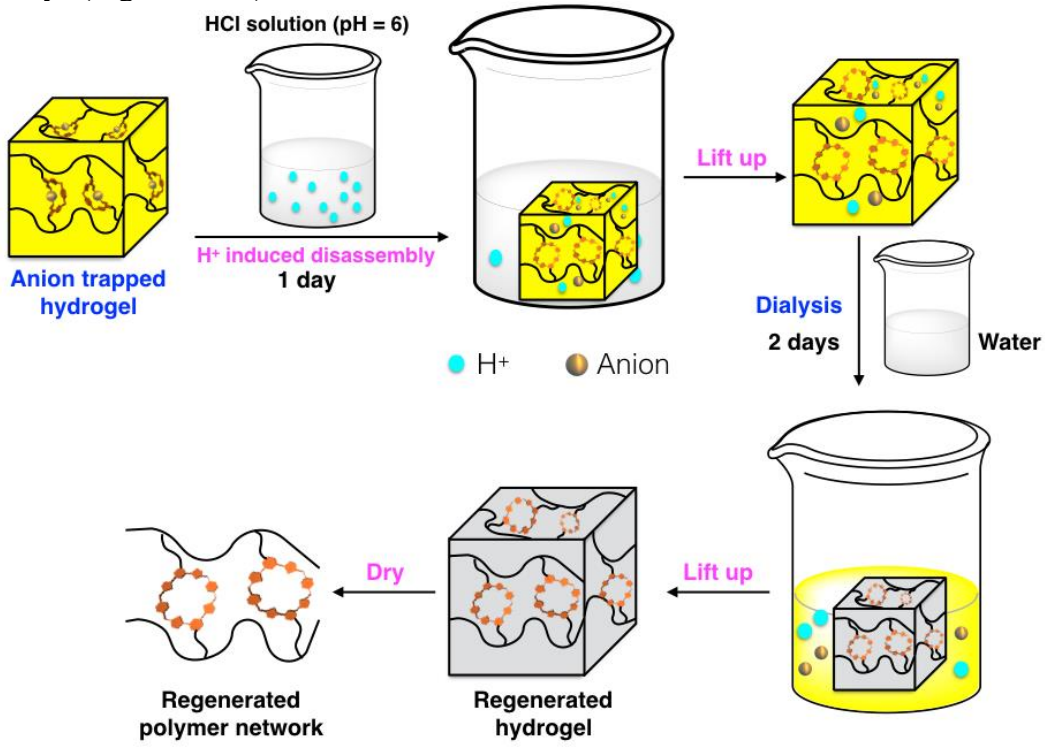

Figure 3.30 Cartoon representation of the stepwise process used to regenerate **P1** after the formation of the hydrogels obtained upon exposure to different anionic salts. Reproduced with permission from *J. Am. Chem. Soc*. **2018**, *140*, 2777. Copyright 2018 American Chemical Society.[10]

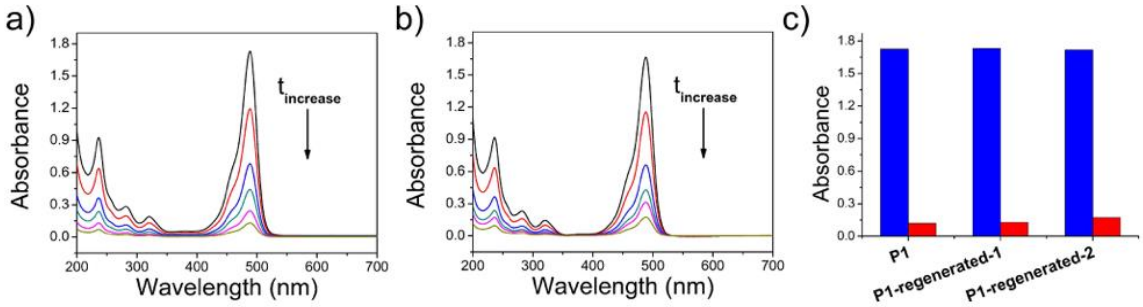

Figure 3.31 Time-dependent changes in the UV-vis spectra of aqueous solutions of **Dye 1** (with an initial concentration of 50 μM and a volume of 10 mL) exposed to (a) **P1**-**regenerated-1** and (b) **P1**-**regenerated-2** for 48 h. Here, the terms **P1**-**regenerated-1** and **P1**-**regenerated-2** refer to systems that have been subject to one and two cycles of washing and regeneration, respectively. (c) Absorbance intensity of aqueous solutions of **Dye 1** before (blue bar) and after (red bar) being treated with **P1**, **P1**-**regenerated-1**, and **P1**-**regenerated-2**, respectively. To a first approximation all three polymer systems are equally effective. Reproduced with permission from *J. Am. Chem. Soc*. **2018**, *140*, 2777. Copyright 2018 American Chemical Society.[10]

3.3 CONCLUSIONS

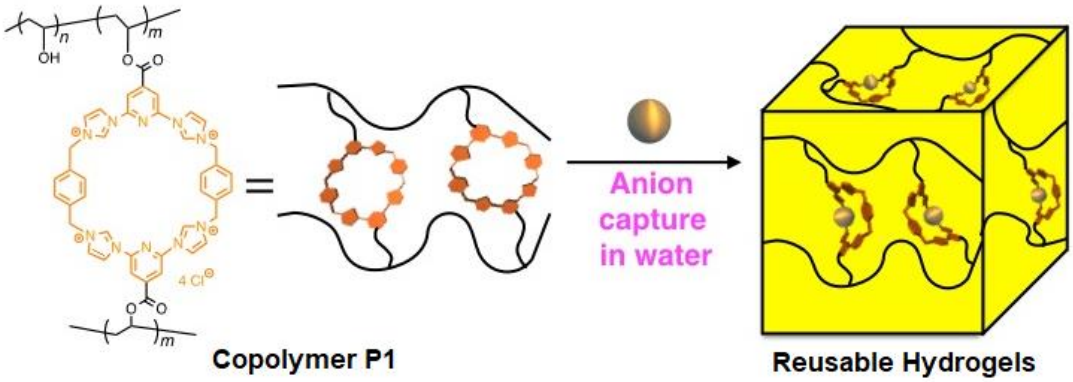

Figure 3.32 Schematic representation of the anion-capture process using hydrogel using macrocycle-anion binding interactions. Reproduced with permission from *J. Am. Chem. Soc*. **2018**, *140*, 2777. Copyright 2018 American Chemical Society.[10]

In summary, a hydrogel-forming polymer network that contains a water-soluble tetracationic macrocycle was synthesized and characterized in this work. Upon immersion of this polymer network in aqueous solutions containing various inorganic and organic salts, changes in the physical properties are observed that are consistent with absorption of the constituent anions into the polymer network. This absorption is ascribed to host-guest interactions involving the tetracationic macrocyclic receptor. Removal of the anions may then be achieved by lifting the resulting hydrogels out of the aqueous phase. Treating the anion-containing hydrogels with dilute HCl leads to the protonation-induced release of the bound anions. This allows the hydrogels to be recycled for reuse. The present polymer network thus provides a potentially attractive approach to removing undesired anions from aqueous environments.

3.4 REFRENCES

1) (a) Albelda, M. T.; Frias, J. C.; Garcia-Espana, E.; Schneider, H. J. *Chem*. *Soc*. *Rev*. **2012**, *41*, 3859−3877. (b) Busschaert, N.; Caltagirone, C.; Van Rossom, W.; Gale, P. A. *Chem*. *Rev*. **2015**, *115*, 8038−8155. (c) Okesola, B. O.; Smith, D. K. *Chem*. *Soc*. *Rev*. **2016**, *45*, 4226−4251. (d) Aydogan, A.; Coady, D. J.; Kim, S. K.; Akar, A.; Bielawski, C. W.; Marquez, M.; Sessler, J. L. *Angew*. *Chem*. *Int*. *Ed.* **2008**, *120*, 9794−9798.
2) (a) Liu, G.; You, S.; Ma, M.; Huang, H.; Ren, N. *Environ*. *Sci*. *Technol*. **2016**, *50*, 11218−11225. (b) Wang, X.; Lü, S.; Gao, C.; Feng, C.; Xu, X.; Bai, X.; Gao, N.; Yang, J.; Liu, M.; Wu, L. *ACS Sustainable Chem*. *Eng*. **2016**, *4*, 2068−2079.
3) (a) Jiao, S.; Jin, J.; Wang, L. *Sens*. *Actuators*, *B* **2015**, *208*, 36−42. (b) Zhang, Y.; Su, Z.; Li, B.; Zhang, L.; Fan, D.; Ma, H. *ACS Appl*. *Mater*. *Interfaces* **2016**, *8*, 12344−12351.
4) (a) Fowler, C. J.; Haverlock, T. J.; Moyer, B. A.; Shriver, J. A.; Gross, D. E.; Marquez, M.; Sessler, J. L.; Hossain, M. A.; Bowman-James, K. *J*. *Am*. *Chem*. *Soc*. **2008**, *130*, 14386−14387. (b) Kim, S. K.; Lee, J.; Williams, N. J.; Lynch, V. M.; Hay, B. P.; Moyer, B. A.; Sessler, J. L. *J*. *Am*. *Chem*. *Soc*. **2014**, *136*, 15079−15085. (c) Hartle, M. D.; Hansen, R. J.; Tresca, B. W.; Prakel, S. S.; Zakharov, L. N.; Haley, M. M.; Pluth, M. D.; Johnson, D. W. *Angew*. *Chem*. *Int*. *Ed*. **2016**, *55*, 11480−11484.
5) (a) Guha, S.; Saha, S. *J*. *Am*. *Chem*. *Soc*. **2010**, *132*, 17674−17677. (b) Pan, B.; Xu, J.; Wu, B.; Li, Z.; Liu, X. *Environ*. *Sci*. *Technol*. **2013**, *47*, 9347−9354.
6) (a) Hai, F. I.; Yamamoto, K.; Fukushi, K. *Crit*. *Rev*. *Environ*. *Sci*. *Technol*. **2007**, *37*, 315−377. (b) Kim, H.; Watthanaphanit, A.; Saito, N. *ACS Sustainable Chem*. *Eng*. **2017**, *5*, 5842−5851.
7) (a) Appel, E. A.; Biedermann, F.; Hoogland, D.; Del Barrio, J.; Driscoll, M. D.; Hay, S.; Wales, D. J.; Scherman, O. A. *J*. *Am*. *Chem*. *Soc*. **2017**, *139*, 12985−12993. (b) Appel, E. A.; Loh, X. J.; Jones, S. T.; Biedermann, F.; Dreiss, C. A.; Scherman, O. A. *J*. *Am*. *Chem*. *Soc*. **2012**, *134*, 11767−11773. (c) Chen, H.; Ma, X.; Wu, S.; Tian, H. *Angew*. *Chem*. *Int*. *Ed*. **2014**, *53*, 14149−14152. (d) Liu, J.; Tan, C. S.; Yu, Z.; Lan, Y.; Abell, C.; Scherman, O. A. *Adv*. *Mater*. **2017**, *29*, 1604951. (e) Zheng, W.; Chen, L. J.; Yang, G.; Sun, B.; Wang, X.; Jiang, B.; Yin, G. Q.; Zhang, L.; Li, X.; Liu, M.; Chen, G.; Yang, H. B. *J*. *Am*. *Chem*. *Soc*. **2016**, *138*, 4927−4937. (f) He, X.; Fan, J.; Wooley, K. L. *Chem*. -*Asian J*. **2016**, *11*, 437−447. (g) Zheng, W.; Yang, G.; Shao, N.; Chen, L. J.; Ou, B.; Jiang, S. T.; Chen, G.; Yang, H. B. *J*. *Am*. *Chem*. *Soc*. **2017**, *139*, 13811−13820. (h) Fan, J.; Li, R.; Wang, H.; He, X.; Nguyen, T. P.; Letteri, R. A.; Zou, J.; Wooley, K. L. *Org*. *Biomol*. *Chem*. **2017**, *15*, 5145−5154.
8) Plank, T.N.; Skala, L. P.; Davis, J. T. *Chem*. *Commun*. **2017**, *53*, 6253−6238.
9) (a) Kim, H. J.; Lee, J. H.; Lee, M. *Angew*. *Chem*. *Int*. *Ed*. **2005**, *44*, 5810−5814. (b) Shen, J. -S.; Li, D.-H.; Cai, Q. -G.; Jiang, Y. -B. *J*. *Mater*. *Chem*. **2009**, *19*, 6219. (c) Becker, T.; Yong Goh, C.; Jones, F.; McIldowie, M. J.; Mocerino, M.; Ogden, M. I. *Chem*. *Commun*. **2008**, 3900−3902. (d) Shen, J. S.; Cai, Q. G.; Jiang, Y. B.; Zhang, H. W. *Chem*. *Commun*. **2010**, *46*, 6786−6788.

10) Ji, X.; Wu, R. -T.; Long, L.; Guo, C.; Khashab, N. M.; Huang, F.; Sessler, J. L. *J. Am. Chem. Soc*. **2018**, *140*, 2777–2780.
11) (a) Gong, H. Y.; Rambo, B. M.; Karnas, E.; Lynch, V. M.; Sessler, J. L. *Nat*. *Chem*. **2010**, *2*, 406−409. (b) Rambo, B. M.; Gong, H. Y.; Oh, M.; Sessler, J. L. *Acc*. *Chem*. *Res*. **2012**, *45*, 1390−1401. (c) Ji, X.; Wang, H.; Li, Y.; Xia, D.; Li, H.; Tang, G.; Sessler, J. L.; Huang, F. *Chem*. *Sci*. **2016**, *7*, 6006−6014.
12) (a) Cheng, H. K.; Sahoo, N. G.; Tan, Y. P.; Pan, Y.; Bao, H.; Li,L.; Chan, S. H.; Zhao, J. *ACS Appl*. *Mater*. *Interfaces* **2012**, *4*, 2387−2394. (b) Salavagione, H. J.; Gómez, M. A.; Martínez, G. *Macromolecules* **2009**, *42*, 6331−6334.
13) (a) Takashima, Y.; Hatanaka, S.; Otsubo, M.; Nakahata, M.; Kakuta, T.; Hashidzume, A.; Yamaguchi, H.; Harada, A. *Nat*. *Commun*. **2012**, *3*, 1270. (b) Wu, Z. -S.; Tan, Y. -Z.; Zheng, S.; Wang, S.; Parvez, K.; Qin, J.; Shi, X.; Sun, C.; Bao, X.; Feng, X.; Müllen, K. *J. Am*. *Chem*. *Soc*. **2017**, *139*, 4506–4512. (c) Shi, Y.; Wang, M.; Ma, C.; Wang, Y.; Li, X.; Yu, G. *Nano Lett*. **2015**, *15*, 6276−6281. (d) Zhang, J.; Xu, D.; Guo, J.; Sun, Z.; Qian, W.; Zhang, Y.; Yan, F. *Macromol*. *Rapid Commun*. **2016**, *37*, 1194−119.
14) Sawada, J.; Aoki, D.; Uchida, S.; Otsuka, H.; Takata, T. *ACS Macro Lett*. **2015**, *4*, 598−601.
15) (a) Ali, M.; Dutta, P.; Pandey, S. *J. Phys*. *Chem*. *B* **2010**, *114*, 15042−15051. (b) Sikorska, E.; Khmelinskii, I. V.; Koput, J.; Sikorski, M. *J. Mol*. *Struct*.: *THEOCHEM* **2004**, *676*, 155−160. (c) Diaz, S. A.; Giordano, L.; Azcarate, J. C.; Jovin, T. M.; Jares-Erijman, E. A. *J. Am*. *Chem*. *Soc*. **2013**, *135*, 3208−3217. (d) Choi, M. G.; Hwang, J.; Eor, S.; Chang, S. K. *Org*. *Lett*. **2010**, *12*, 5624−5627.
16) (a) Kresse, G.; Hafner, J. *Phys. Rev. B* **1993**, *47*, 558. (b) Kresse, G.; Furthmüller, J. *Comput. Mat. Sci.* **1996**, *6*, 15. (c) Kresse, G.; Furthmüller, J. *Phys. Rev. B* **1996**, *54*, 11169.
17) Marcus, Y.; Hefter, G. *Chem*. *Rev*. **2006**, *106*, 4585−4621.
18) Xing, H.; Li, Z.; Wu, Z.; Huang, F. *Macromol*. *Rapid Commun*. **2018**, *39*, 1700361.

Chapter 4: Encoding, Reading, and Transforming Information Using Multifluorescent Supramolecular Polymeric Hydrogels

4.1 Introduction

Figure 4.1 Evolution of information codes. Reproduced with permission from *Int. J. Comput. Appl.* **2017***, 37, 17*. Copyright 2017 Taylor & Francis Group.[3]

Manufacturers and suppliers depend on information to help them deal with the complexity caused by global operations, value chains, and markets. An ability to transform or adjust encoded information, rather than just storing it in a static form, would allow increased benefits to producers and consumers alike.[1,2] In this context, barcodes continue to receive enormous attention.[3–6] They are usually divided into three types: 1D, 2D, and 3D codes. Classic 1D barcodes allow the facile labeling and recognition of products by use of lines and spaces with different widths.[3] 2D barcodes use intricate arrays and matrices to encode information with higher density and better readout fidelity.[3–5] So-called 3D codes, whose third dimension is color (blue, green, and red), are currently being developed as a means to increase the information density per unit area (Figure 4.1).[3] While promising, these traditional approaches (1D, 2D, and 3D codes) do not allow information to be transformed once it is encoded. Here, we report an approach to fluorescent 3D color code generation that permits the encoding of information and its subsequent masking, demasking, erasure, and dedicated conversion to different encoded

§ Ji, X.; **Wu**, **R**. **-T**.; Long, L.; Ke, X. -S.; Guo, C.; Ghang, Y. -J.; Lynch, V. M.; Huang, F.; Sessler, J. L. Encoding, Reading, and Transforming Information Using Multifluorescent Supramolecular Polymeric Hydrogels. *Adv. Mater*. **2018**, *30*, 1705480.
The candidate is the second author of the publication and was responsible for the syntheses of nonfunctionalized and functionalized macrocyclic receptors and the characterization of related products.

forms. It relies on the use of anion recognition-based self-healing multifluorescent hydrogels that can be reprogramed by both chemical and physical means. Due to the nature of the soft materials involved, the codes can be used as wearable materials allowing modulation-amenable information to be read out in a way that is not possible by the use of nondynamic physical attributes, such as fingerprints.

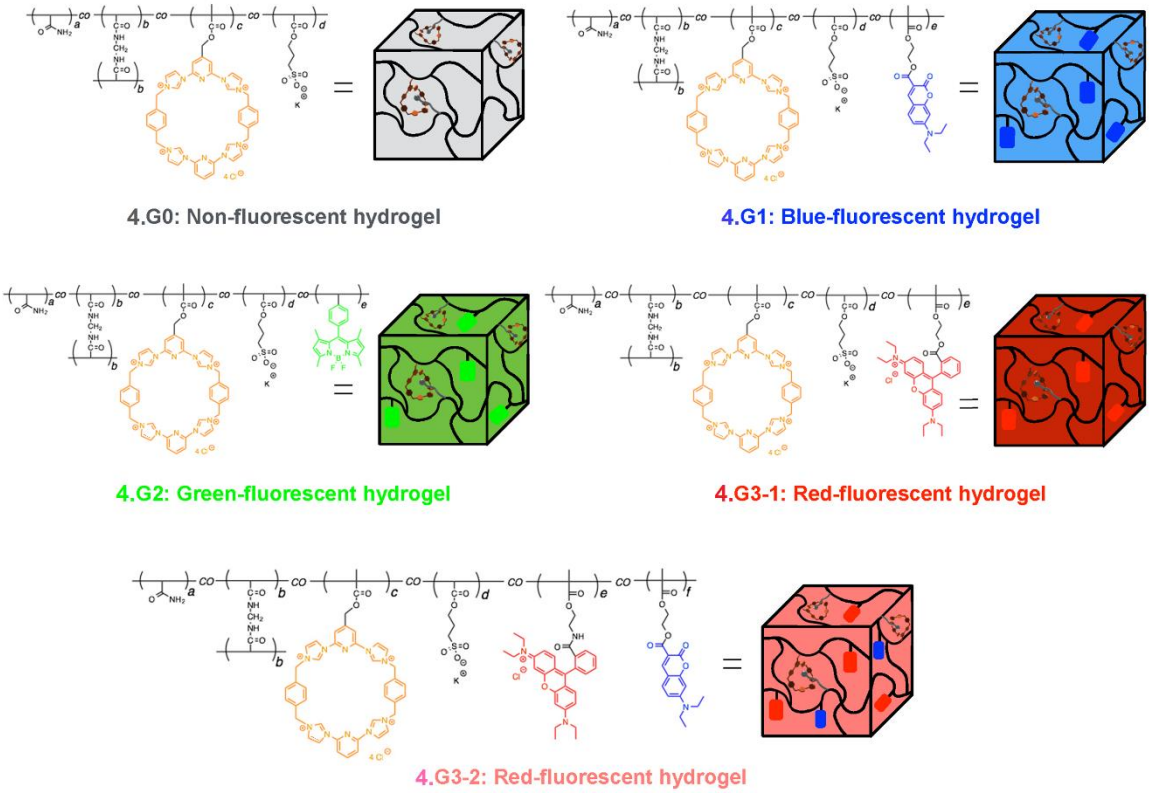

Figure 4.2 Chemical structures and cartoon representations of the non-fluorescent hydrogel **4.G0**, blue-fluorescent hydrogel **4.G1**, green-fluorescent hydrogel **4.G2**, non-responsive red-fluorescent hydrogel **4.G3-1**, and ammonia-responsive red-fluorescent hydrogel **4.G3-2**. Reproduced with permission from *Adv. Mater*. **2018**, *30*, 1705480. Copyright 2018 John Wiley and Sons.[7]

The hydrogels[8–11] used in this study are shown in Figure 4.2. They consist of a poly(acrylamide) (pAAm) network cross-linked by *N*,*N*'-methylenebis(acrylamide) (MBAAm), as well as tethered tetracationic macrocyclic anion receptors and pendant

alkyl sulfonate subunit (hydrogel **4.G0**; non-fluorescent). The blue (**4.G1**), green (**4.G2**), and red (**4.G3-1** and **4.G3-2**) hydrogels further contained coumarin,[12] boron-dipyrromethene (BODIPY),[13] and rhodamine B[14] domains, respectively. When excited at 365 nm using a UV lamp, hydrogels **4.G1**, **4.G2**, and **4.G3-1** give rise to blue, green, and red fluorescence, respectively. A doubly functionalized hydrogel containing both coumarin units and base-responsive rhodamine B chromophores (*i.e.*, ring-opening rhodamine B spirolactam derivatives,[15] **RORS**) was also synthesized. This system, designated as **4.G3-2** to distinguish it from the nonresponsive rhodamine B ester (**RE**)[14] hydrogel (**4.G3-1**), was found to produce a red fluorescence in its native state but emitted blue after exposure to ammonia vapor. All these hydrogels encode for tertracationic imidazolium macrocycle-alkyl sulfonate anion interactions,[16–19] both within the interior of the hydrogel and at the surface.[20,21] Thus, they can be used to produce different multicolor fluorescent patterns when pushed together manually on a black nitrile substrate.

As detailed below, this has made it possible to create three representative patterns, namely **Code A**, **Code B**, and **Code C**, each of which contains different encoded information (Figure 2a). For **Code A** (Figure 4.3b): its encoded information can only be read out under UV light (Figure 2b, left); simple cutting and reassembly ("homohealing") allowed information removed from **Code A** to be reinstated (Figure 4.3b, middle); exposure of certain hydrogel blocks to solid $CuCl_2$ allowed the information within these codes to be erased[22] (Figure 4.3b, right). Moreover, cutting and reinsertion of a different hydrogel block (so-called "heterohealing") allowed **Code B** to be physically transformed into **Code A** (Figure 4.3c, left). Hydrogels producing **Code C** could be converted to **Code A** by treating with ammonia vapor (Figure 4.3c, right). Thus, the information initially encoded within the hydrogel arrays may be deliberately transformed by either

physical or chemical means. The systems are flexible and the encoded information can be read when the codes are used as wearable materials[23,24] on, *e.g.*, latex gloves.

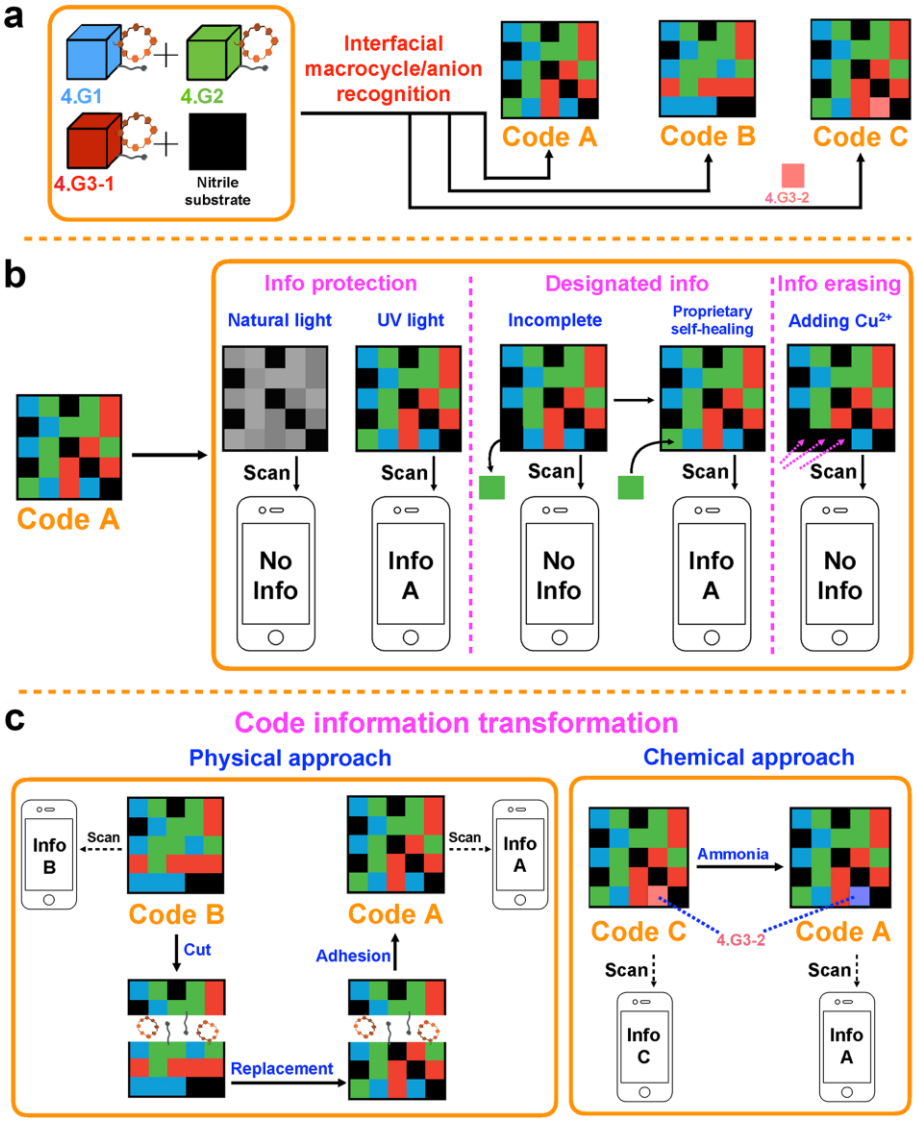

Figure 4.3 Cartoon representations: (a) Formation of 3D color codes via the interfacial adhesion of individual domains made up of hydrogels **4.G1**, **4.G2**, and **4.G3** (**4.G3-1** and **4.G3-2**). (b) Information protection, designated information, and information erasing of **Code A**. (c) Transformation of encoded information by physical and chemical approaches. Reproduced with permission from *Adv. Mater*. **2018**, *30*, 1705480. Copyright 2018 John Wiley and Sons.[7]

4.2 Results and Discussion

Prior work with the tetracationic imidazolium derived "molecular box" **Host** used in this study,[18,19] as well as a range of predicative studies involving it and acrylate propyl sulfonate ester[19] carried out in the context of the present work (*cf*. Figures 4.4–4.10), provided support for the notion that this receptor-anion combination would interact strongly in aqueous media. This cationic receptor-anion binding was expected to support formation of hydrogels when the components were incorporated into a suitable polymeric matrix.

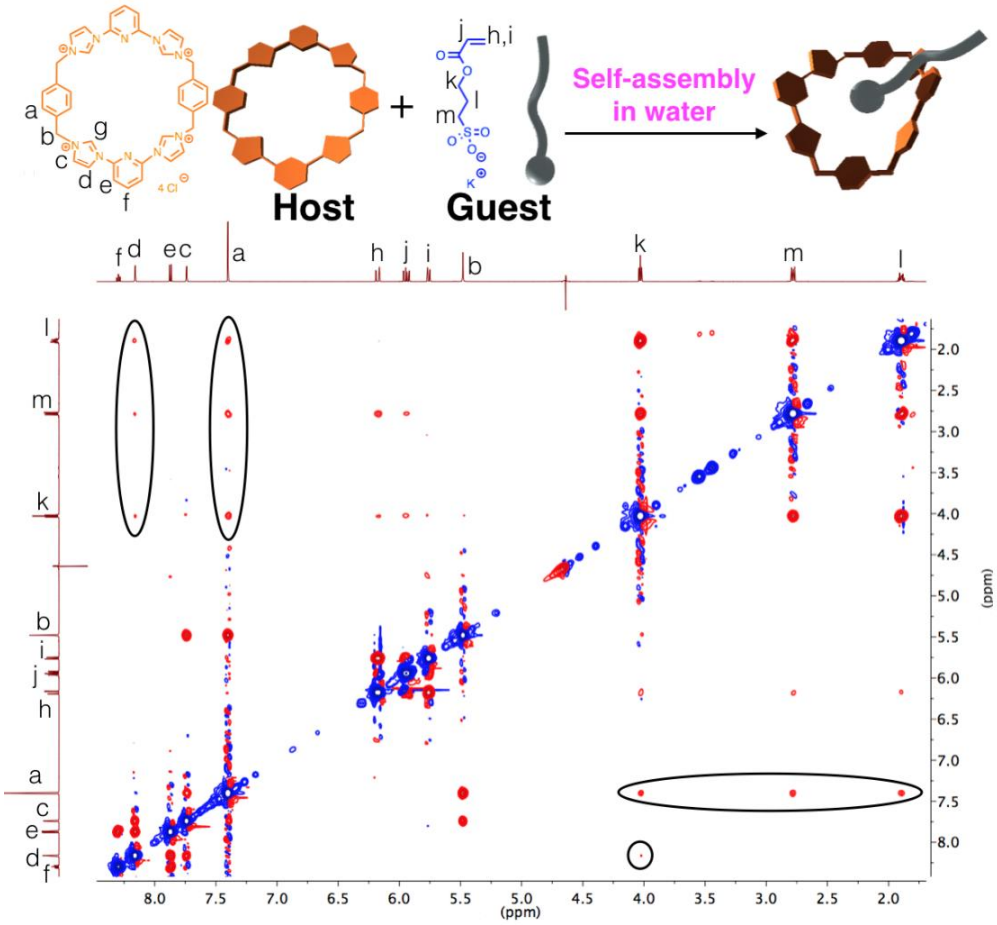

Figure 4.4 Chemical structures and cartoon representation of self-assembly of **Host** and **Guest** in water, and full view of the NOSEY NMR spectrum (600 MHz, D_2O, 298 K) of **Host** and **Guest** (5.00 mM for each). Reproduced with permission from *Adv. Mater.* **2018**, *30*, 1705480. Copyright 2018 John Wiley and Sons.[7]

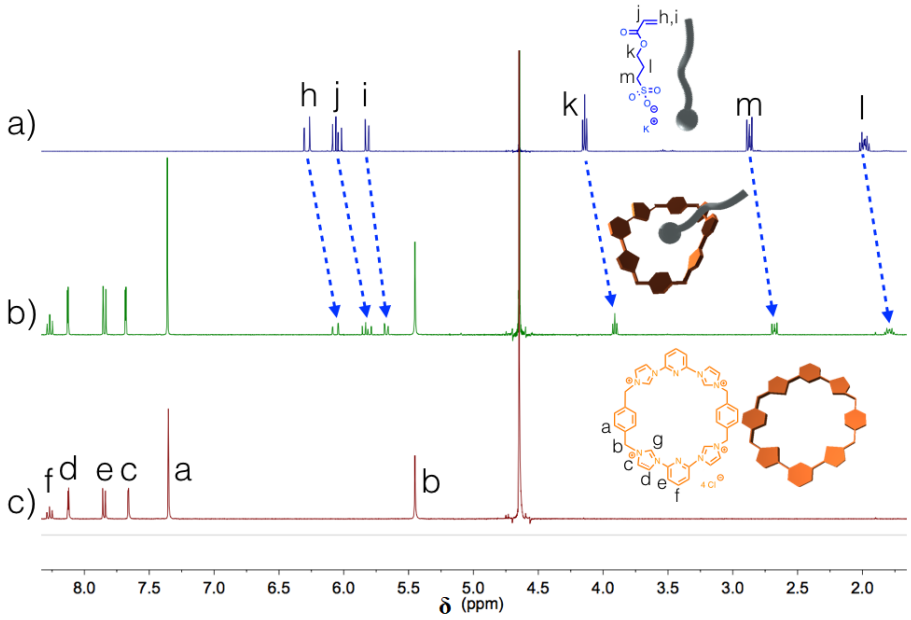

Figure 4.5 ^{1}H NMR spectroscopic analyses (400 MHz, D_2O, 298 K): (a) 5.00 mM **Guest**; (b) 1:1 mixture of **Host** and **Guest** (5.00 mM for each); (c) 5.00 mM **Host**. Reproduced with permission from *Adv. Mater*. **2018**, *30*, 1705480. Copyright 2018 John Wiley and Sons.[7]

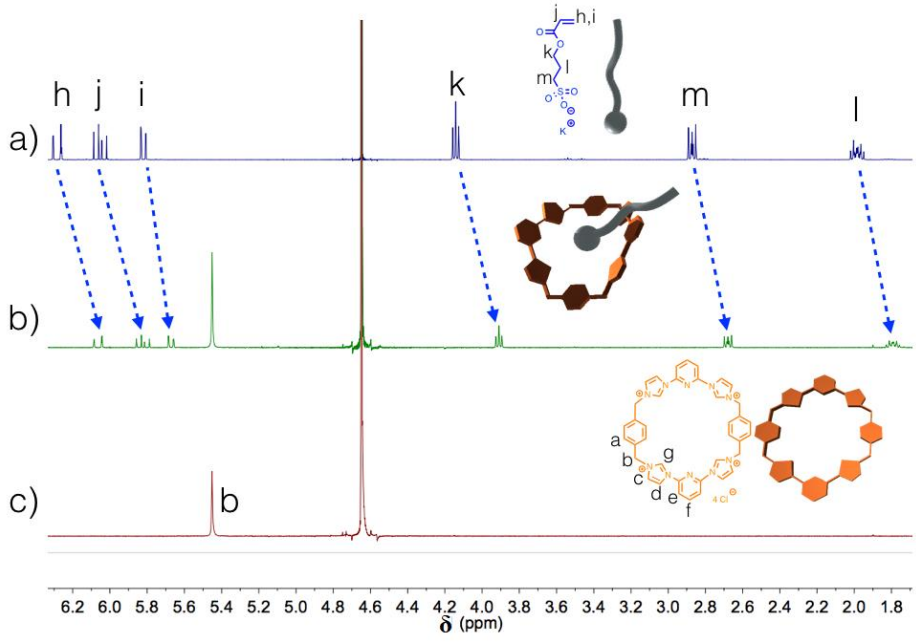

Figure 4.6 Truncated ^{1}H NMR spectra (400 MHz, D_2O, 298 K) of (a) 5.00 mM **Guest**, (b) 1:1 mixture of **Host** and **Guest** (5.00 mM for each), and (c) 5.00 mM **Host**. Reproduced with permission from *Adv. Mater*. **2018**, *30*, 1705480. Copyright 2018 John Wiley and Sons.[7]

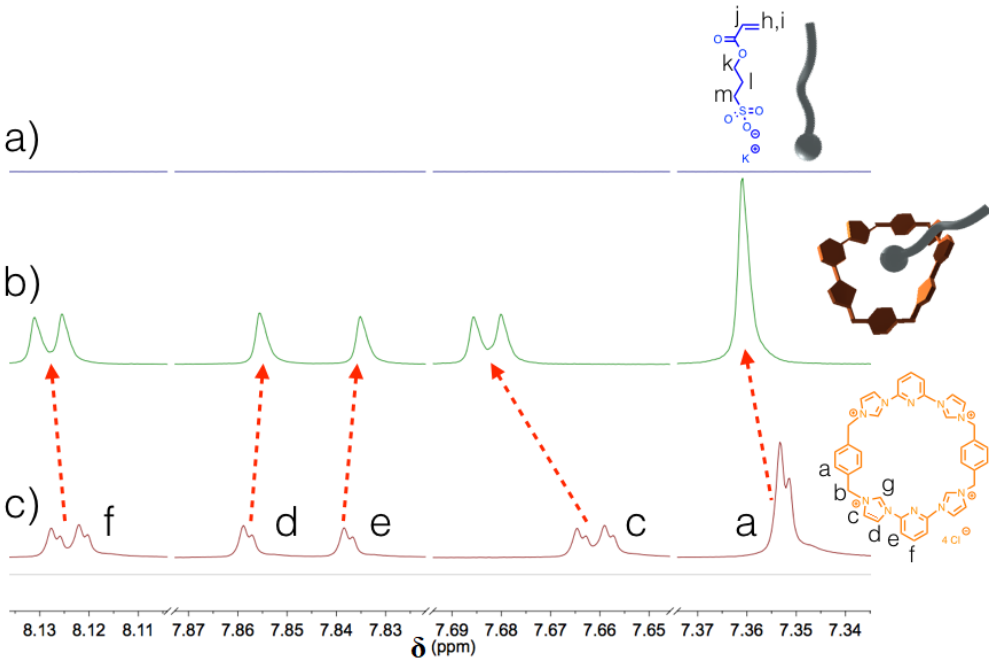

Figure 4.7 Truncated ^{1}H NMR spectra (400 MHz, D_2O, 298 K) of (a) 5.00 mM Guest, (b) 1:1 mixture of **Host** and **Guest** (5.00 mM for each); (c) 5.00 mM **Host**. Reproduced with permission from *Adv. Mater*. **2018**, *30*, 1705480. Copyright 2018 John Wiley and Sons.[7]

To determine the stoichiometry and association constant corresponding to the interaction between macrocycle **Host** and ammonium sulfonate **Guest**, ^{1}H NMR spectroscopic titrations were carried out using solutions that had a constant concentration of **Host** (5.00 mM) and varying concentrations of **Guest**. Using a non-linear curve-fitting method, the association constant between **Guest** and receptor **Host** was calculated. From a mole ratio plot, evidence for a 1:1 stoichiometry was obtained. The non-linear curve-fitting was based on the following equation:[25]

$$\Delta\delta=(\Delta\delta_\infty/[G]_0)\times(0.5[H]_0+0.5([G]_0+1/K_a)-(0.5\times([H]_0^2+(2[H]_0(1/K_a-[G]_0))+(1/K_a+[G]_0)^2)^{0.5})) \quad \text{(Equation 5)}$$

Where $\Delta\delta$ is the chemical shift change of H_c on **Host** at $[G]_0$, $\Delta\delta_\infty$ is the chemical shift change of H_c when the host is completely complexed, $[H]_0$ is the fixed initial concentration of the host **Host**, and $[G]_0$ is the varying concentration of the guest **Guest**.

Fitting the ^{1}H NMR spectroscopic titration curve to Equation 5 allowed an effective association constant, K_a, of (5.50 ± 0.200) × 10^3 M^{-1} to be calculated. (Figure 4.10).

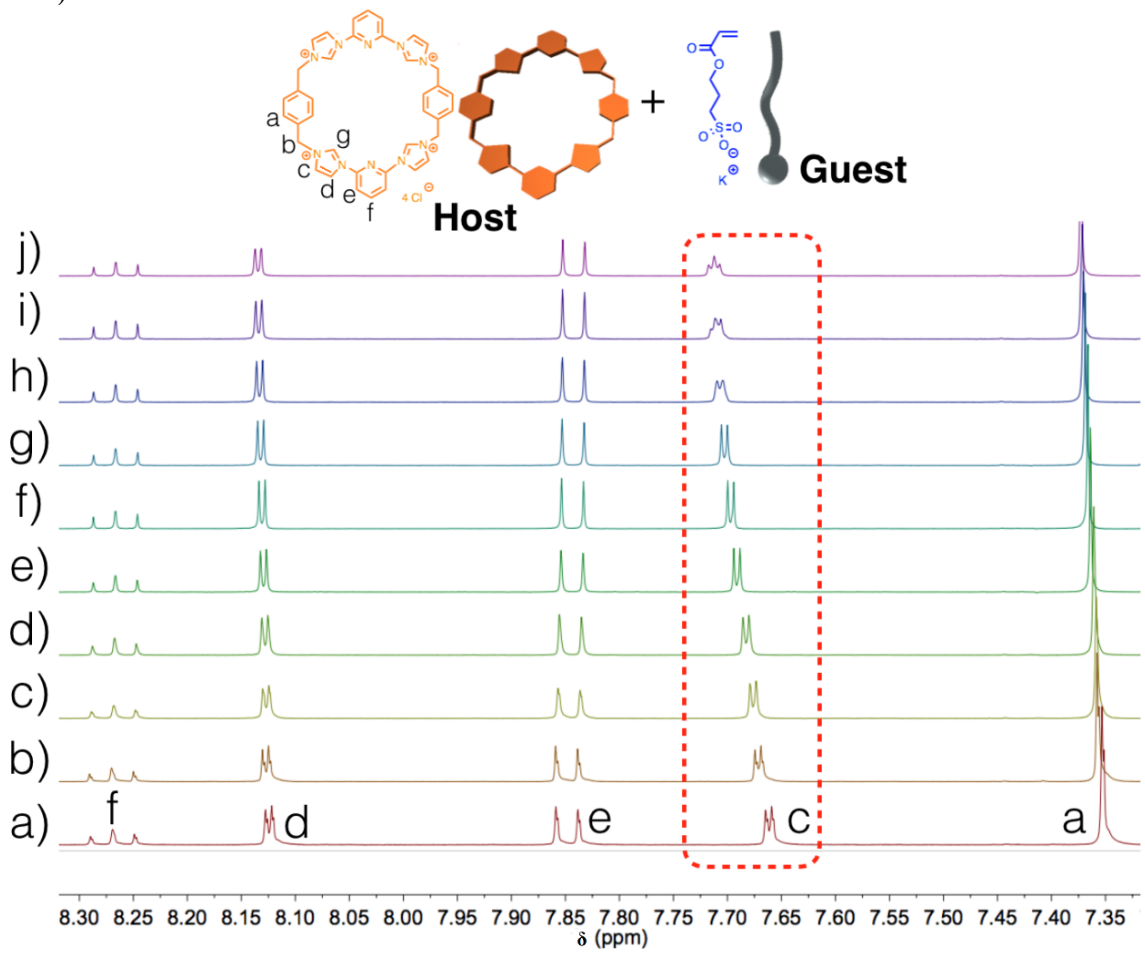

Figure 4.8 ^{1}H NMR spectra (D_2O, 298 K, 400 MHz) of **Host** recorded at a concentration of 5.00 mM in the presence of different concentrations of **Guest**: (a) 0.00 mM; (b) 1.53 mM; (c) 2.96 mM; (d) 4.90 mM; (e) 7.70 mM; (f) 10.0 mM; (g) 12.6 mM; (h) 15.0 mM; (i) 17.8 mM; (j) 20.0 mM. Reproduced with permission from *Adv. Mater*. **2018**, *30*, 1705480. Copyright 2018 John Wiley and Sons.[7]

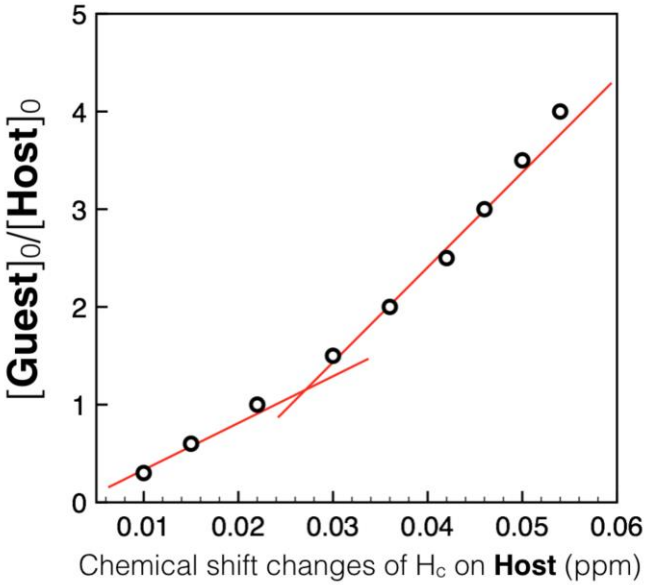

Figure 4.9 Mole ratio plot for the interactions between **Host** and **Guest**; the break seen at a 1:1 molar ratio of these two species was taken as an indication of a 1:1 binding stoichiometry. Reproduced with permission from *Adv. Mater*. **2018**, *30*, 1705480. Copyright 2018 John Wiley and Sons.[7]

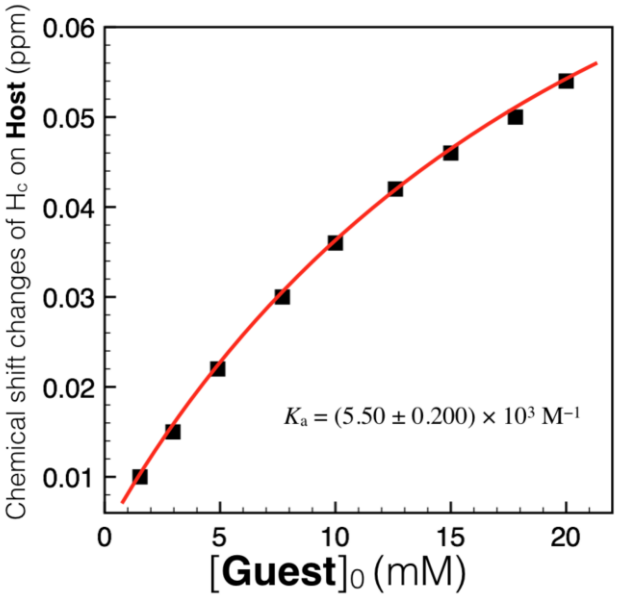

Figure 4.10 Changes in the chemical shift corresponding to H_c on **Host** as a function of added **Guest**. The red solid line was obtained from the non-linear curve-fitting using Equation 5. Reproduced with permission from *Adv. Mater*. **2018**, *30*, 1705480. Copyright 2018 John Wiley and Sons.[7]

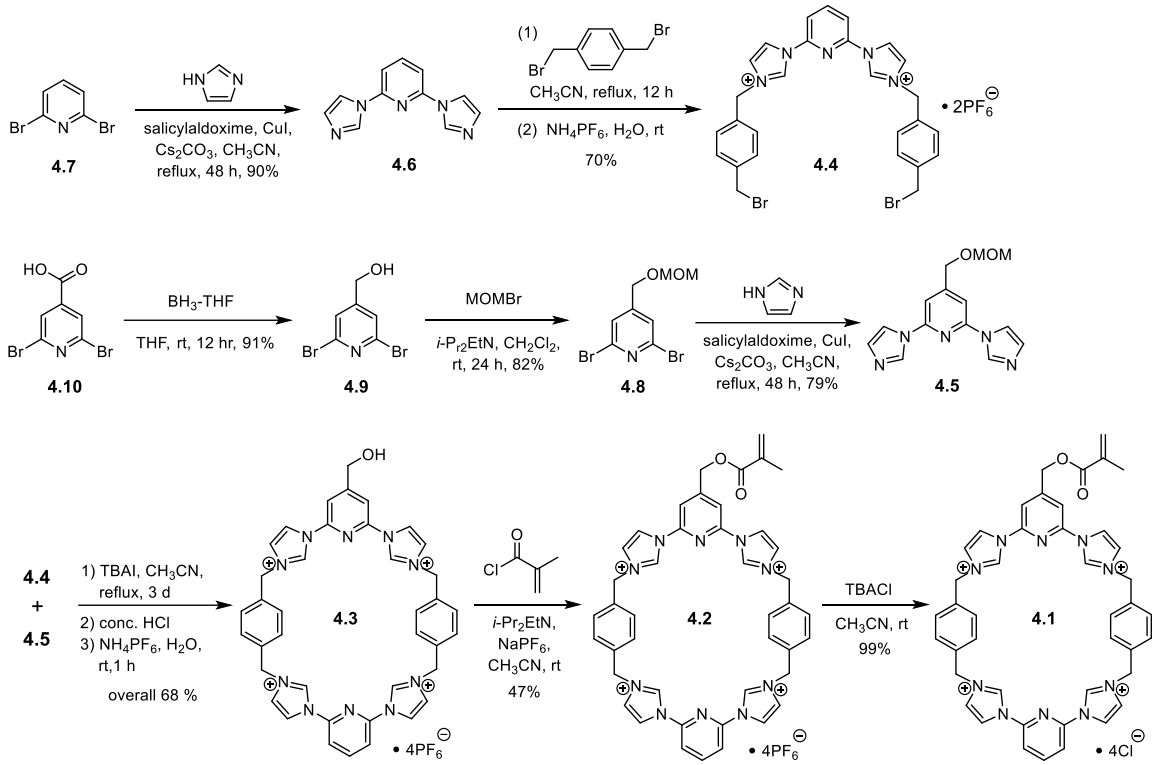

Scheme 4.1 Synthesis of the methacrylate-derived tetracationic macrocycle **4.1**.

Details of hydrogel syntheses containing both imidazolium box and sulfonate anionic domains are detailed in Schemes 4.1 and 4.2. Briefly, a methacrylate-functionalized tetracationic macrocycle monomer (**4.1**) was synthesized in eight steps from commercially available starting materials (Scheme 4.1). Methacrylate or styrene monomers containing coumarin, BODIPY, and rhodamine B functionalities are known compounds and they were prepared according to the reported procedures.[26–30] **4.G0** was then prepared by free radical copolymerization of acrylamide, MBAAm (a covalent cross-linker), **4.1**, and acrylate propyl sulfonate ester,[19] using azobisisobutyronitrile (AIBN) in aqueous media (Scheme 4.2). For **4.G1**, **4.G2**, and **4.G3** (**4.G3-1** and **4.G3-2**), the corresponding fluorescent monomers were used, respectively, in addition to the components used to prepare **4.G0**.

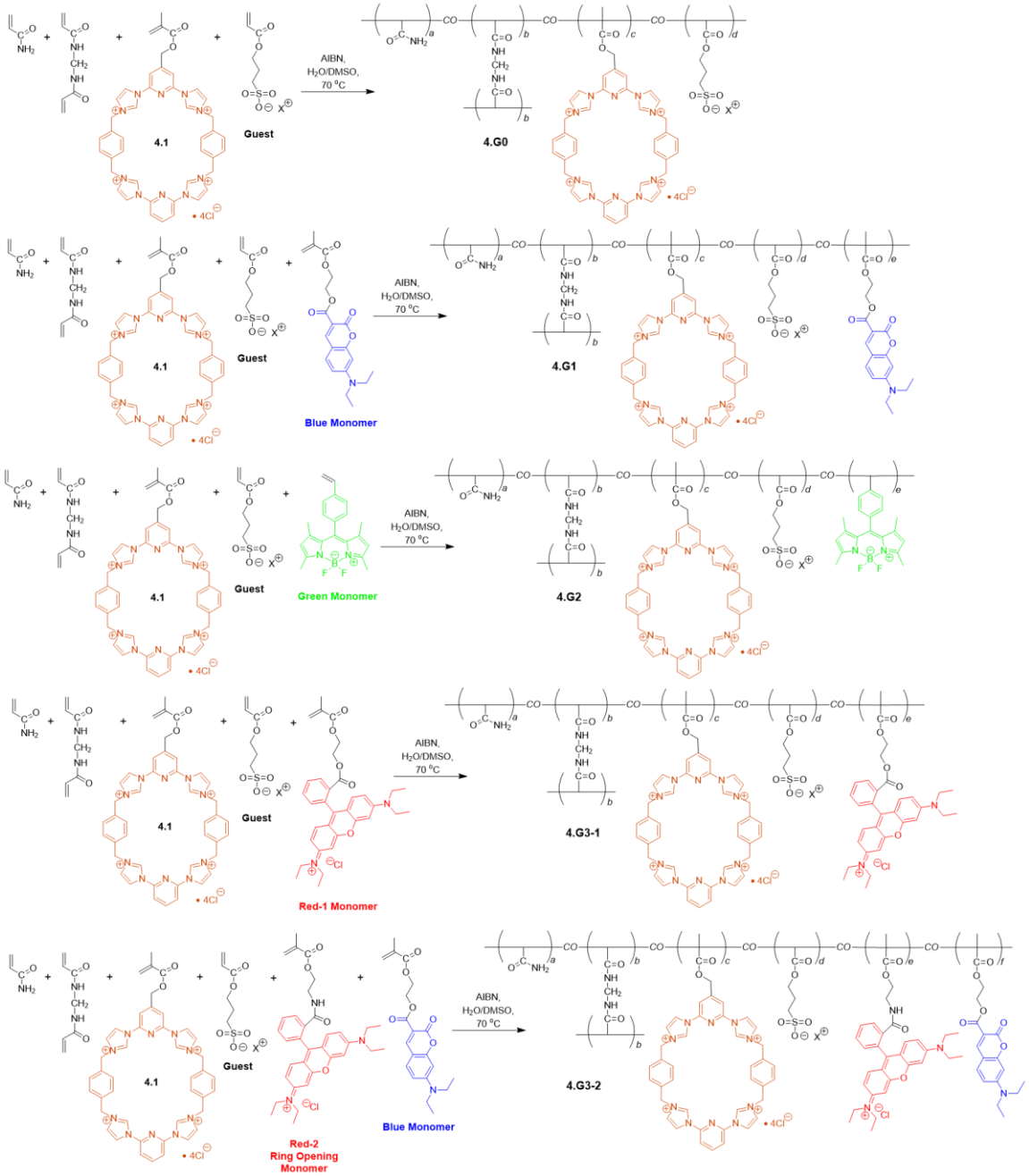

Scheme 4.2 Synthetic routes towards polymeric hydrogels **4.G0**, **4.G1**, **4.G2**, **4.G3-1**, and **4.G3-2**.

Once prepared, the hydrogels were characterized by Fourier transform infrared (FTIR) spectroscopy (Figure 4.11), as well as by fluorescence measurements (Figure

4.12). When illuminated by a handheld UV lamp, no fluorescence was observed for **4.G0** as was expected given the absence of a fluorophore (Figure 4.12a). However, blue, green, and red fluorescence were seen for **4.G1**, **4.G2**, and **4.G3** (**4.G3-1** and **4.G3-2**), respectively (Figures 4.12b–e). When excited at 365 nm, no discernible emission feature was seen in the case of **4.G0** (Figure 4.12); however, emission maxima at 475 (coumarin),[12] 530 (BODIPY),[13] and 615 (**RE**)[14] nm were observed for **4.G1**, **4.G2**, and **4.G3-1**, respectively (Figures 4.12g–i). When **4.G3-2** (Figure 4.12j) was excited at 365 nm, a strong emission feature centered at 595 nm ascribed to the **RORS** fluorophore,[15] along with a relatively weak peak at 455 nm arising from the coumarin moiety, was seen. Rheological experiments were then used to investigate the viscoelasticity of the hydrogels.[31–33] The data (Figures 4.12k–o) provided evidence for dominant elastic behavior, as would be expected for a gel state.[32,33] Strain-dependent oscillatory rheological experiments and step-strain rheological measurements[32,33] provided evidence that the hydrogels could both self-heal (*i.e.*, after cutting and reannealing with the same gel) or "heteroheal" within seconds after cutting and adhering to a different gel (*cf.* Figures 4.13–4.15). Notably, both the homo and heterohealed gels could support their own weight when allowed to reanneal by physical contact on a black nitrile substrate in the absence of a solvent or when contacted in water (*cf.* Figures 4.14–4.18). Illumination with a handheld UV lamp revealed that the individual fluorescent domains were retained after healing.

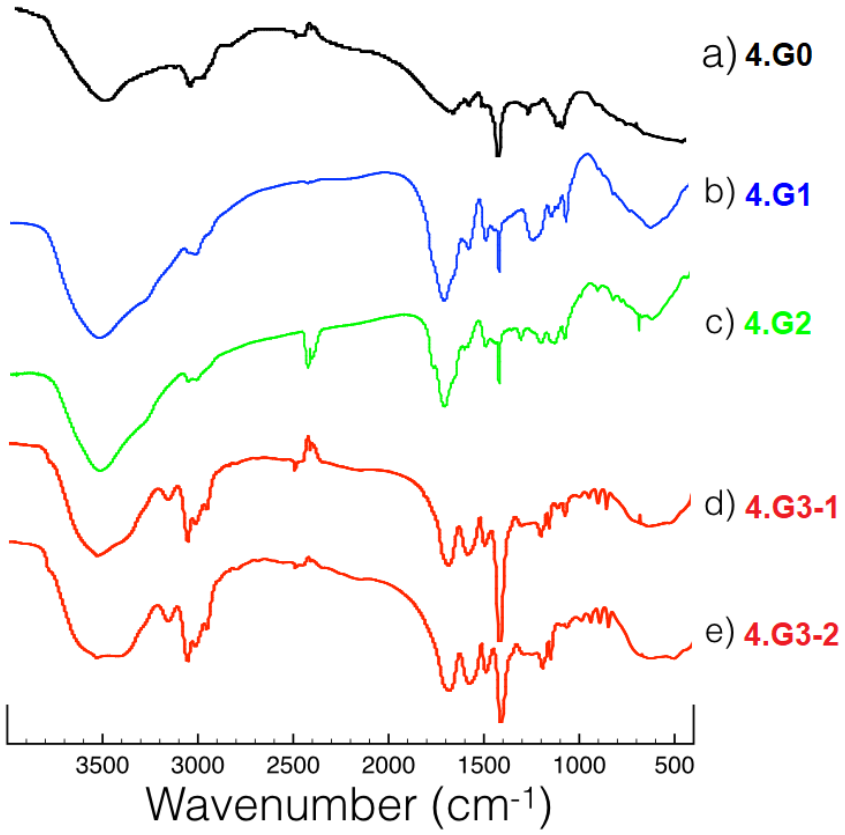

Figure 4.11 FTIR spectra of (a) **4.G0**, (b) **4.G1**, (c) **4.G2**, (d) **4.G3-1**, and (e) **4.G3-2**. Reproduced with permission from *Adv. Mater*. **2018**, *30*, 1705480. Copyright 2018 John Wiley and Sons.[7]

Fourier transform infrared spectroscopy (FTIR) was first used to obtain insights into the chemical structures of hydrogels. As shown in Figure 4.11, characteristic peaks associated with the monomers were found in the hydrogels. This was taken as initial evidence for the formation of each hydrogel. In detail, a broad peak at around 3000–3500 cm^{-1} was seen that is ascribed to an N–H stretching vibration,[34] while a peak at around 2900 cm^{-1} corresponding to the methylene C–H stretching vibration band was also seen.[34] Features at around 1600–1700 cm^{-1} were seen that are attributed to the C=O stretching vibration band and the N–H bending vibration, respectively.[34] The absorption peaks at around 1550–1400 cm^{-1} is assigned to in-ring stretching modes for the C=C bonds and C=N bonds present in the benzene,[35] pyridine,[36] and imidazole rings,[37] respectively.

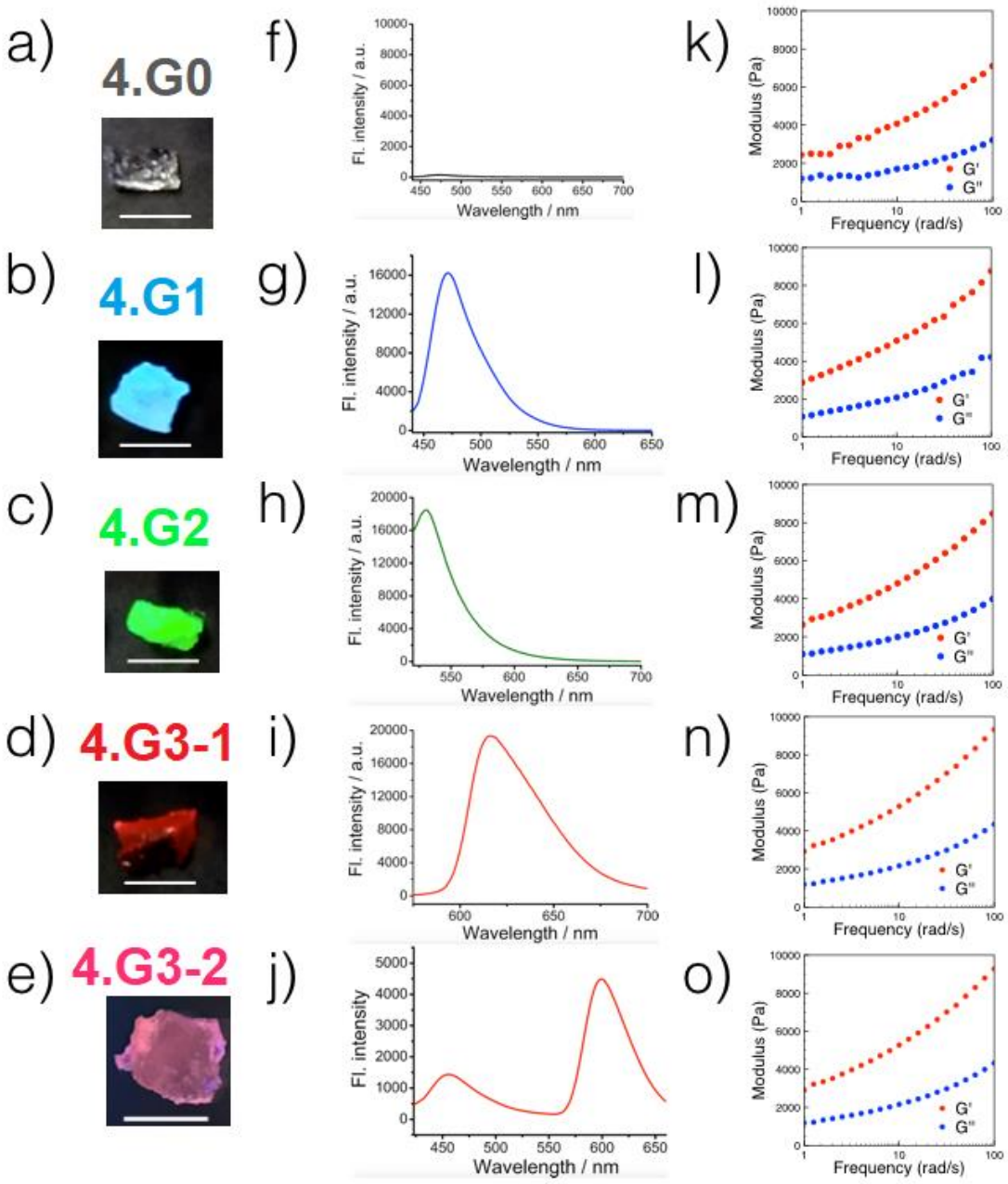

Figure 4.12 Photographs of (a) **4.G0**, (b) **4.G1**, (c) **4.G2**, (d) **4.G3-1**, and (e) **4.G3-2** taken under a UV lamp (λ_{ex} = 365 nm, scale bar = 1 cm). Fluorescence emission spectra (λ_{ex} = 365 nm) of (f) **4.G0**, (g) **4.G1**, (h) **4.G2**, (i) **4.G3-1**, and (j) **4.G3-2**. Plots of P_a *versus* scanning frequency from 1 to 100 rad/s (2% strain, 25 °C) and corresponding *G′* and *G″* curves for (k) **4.G0**, (l) **4.G1**, (m) **4.G2**, (n) **4.G3-1**, and (o) **4.G3-2**. Reproduced with permission from *Adv. Mater*. **2018**, *30*, 1705480. Copyright 2018 John Wiley and Sons.[7]

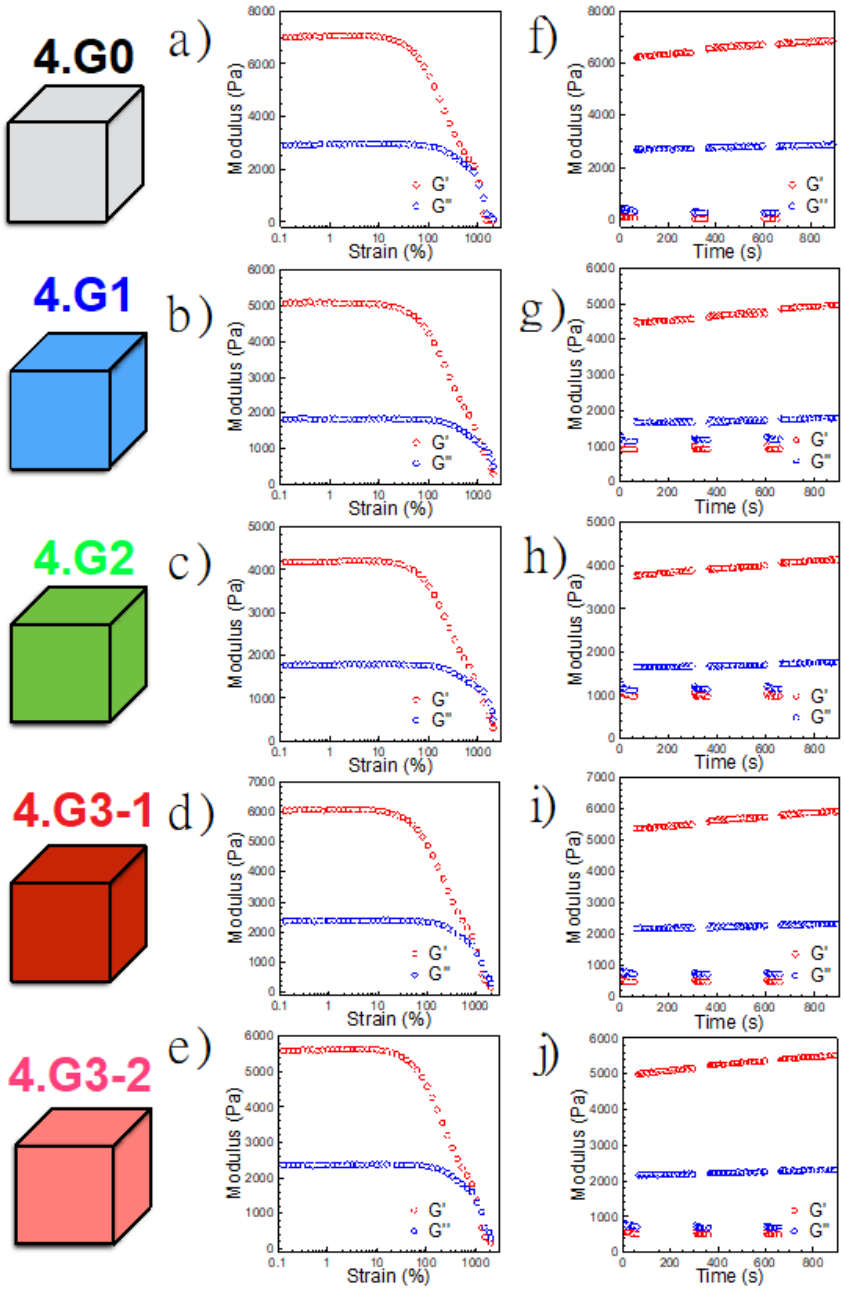

Figure 4.13 Strain-dependent oscillatory shear measurements of (a) **4.G0**, (b) **4.G1**, (c) **4.G2**, (d) **4.G3-1**, and (e) **4.G3-2** at 10 rad/s. Step-rate time-sweep measurements of (f) **4.G0**, (g) **4.G1**, (h) **4.G2**, (i) **4.G3-1**, and (j) **4.G3-2**: The hydrogels were first subjected to 1500% strain for 60 s, then 1% strain for 240 s. Three cycles of strain and relaxation were performed. The scanning frequency was 10 rad/s at 25 °C. Reproduced with permission from *Adv. Mater*. **2018**, *30*, 1705480. Copyright 2018 John Wiley and Sons.[7]

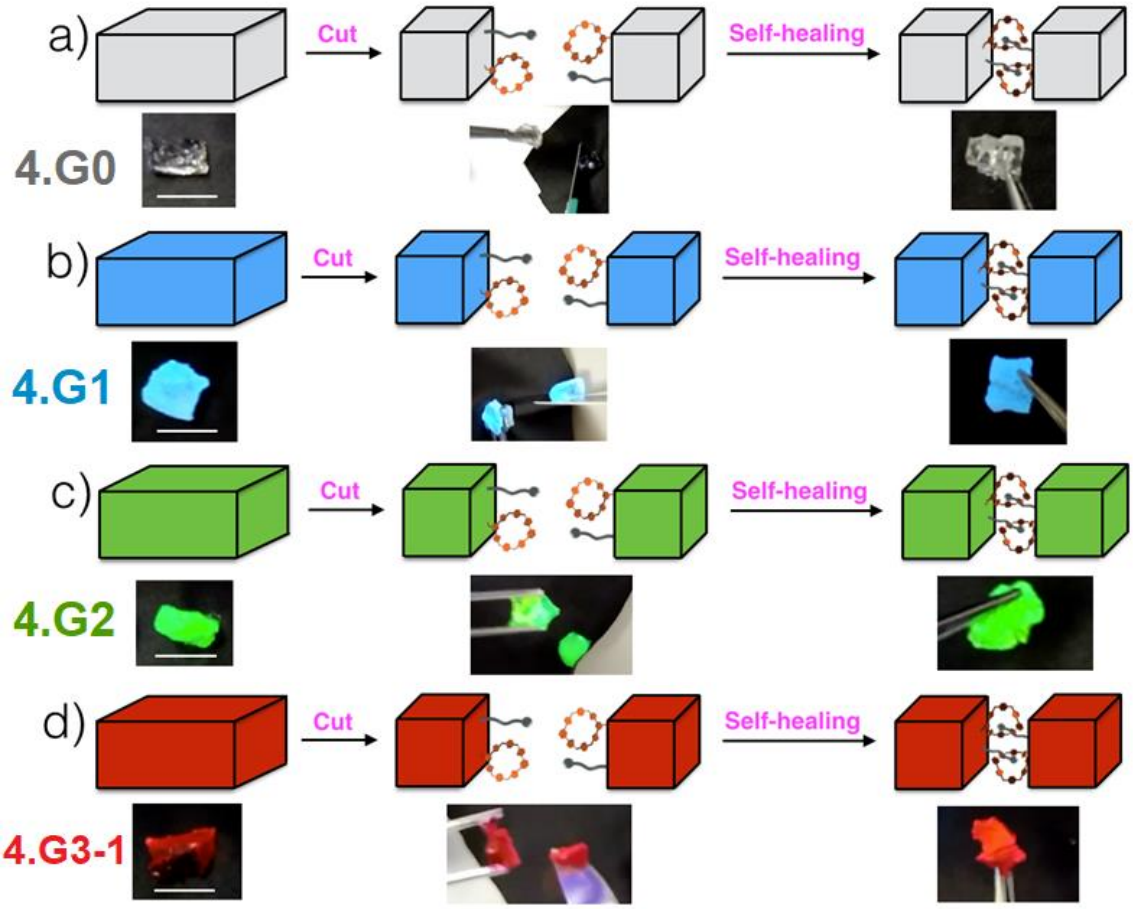

Figure 4.14 Cut/heal tests of (a) **4.G0**, (b) **4.G1**, (c) **4.G2**, and (d) **4.G3-1** taken under a UV lamp (λ_{ex} = 365 nm, scale bar = 1 cm). Reproduced with permission from *Adv. Mater.* **2018**, *30*, 1705480. Copyright 2018 John Wiley and Sons.[7]

The presence of supramolecular cross-linking interactions was expected to endow hydrogels **4.G0**–**4.G3-1** with the ability to self-heal. To test this, strain-dependent oscillatory rheology experiments were carried out at a scan frequency of 10 rad/s (Figures 4.13a–4.13e). Initially gel **4.G0** was examined (Figure 4.13a). It was found that both G' and G'' were relatively stable over a strain range of 0.1% to 30%. Moreover, over this regime, G' always proved much larger than G''. However, starting from 30% strain G' decreased dramatically, while G'' began to decrease when the strain was >100%. G' decreased faster than G'', and a G'/G'' crossover point was observed around 1000% strain.

When the strain was increased further, G'' became larger than G', reflecting damage to the hydrogel. Step-strain rheological measurements (Figures 4.13f–4.13j) of G' and G'' were then carried out in an effort to probe whether self-healing of the hydrogel structure occurs. This was done by alternating between high (1500% for 60 s) and low (1% for 240 s) strain (Figure 4.13f). Under high strain conditions (1500%, 10 rad/s), G'' proved larger than G'. However, under low strain conditions (1%, 10 rad/s), G' was found to be larger than G'', indicating recovery of the hydrogel state. In fact, the supramolecular polymeric hydrogel was found to revert to its original G'/G'' state within seconds, with the recovery behavior proving reproducible over three cycles involving different strains. On this basis, it was concluded that **4.G0** is able to self-heal quickly on the laboratory time scale. Support for this conclusion came from direct cut/heal tests.

As shown in Figure 4.14, **4.G0** could be easily cut into two pieces. The resulting fragments were then brought into physical contact at room temperature. The two pieces rejoined into one piece within seconds. The healed hydrogel could be lifted up off the black nitrile substrate used for these experiments and held against its own weight without breaking apart. The combined rheological, cut/heal, and weight bearing integrity tests were thus all consistent with the fact that **4.G0** could recover its initial gel-like state after being subject to strain or physical rupture. Similar strain-dependent oscillatory rheological experiments, step-strain rheological measurements, and cut/heal tests were carried out for **4.G1**, **4.G2** and **4.G3** (Figures 4.13 and 4.14). In analogy to what was found for **4.G0**, these studies provided support for the conclusion that the fluorescent hydrogels also self-heal. Importantly, the optical properties of the healed hydrogels proved essentially identical to those of the as-prepared materials.

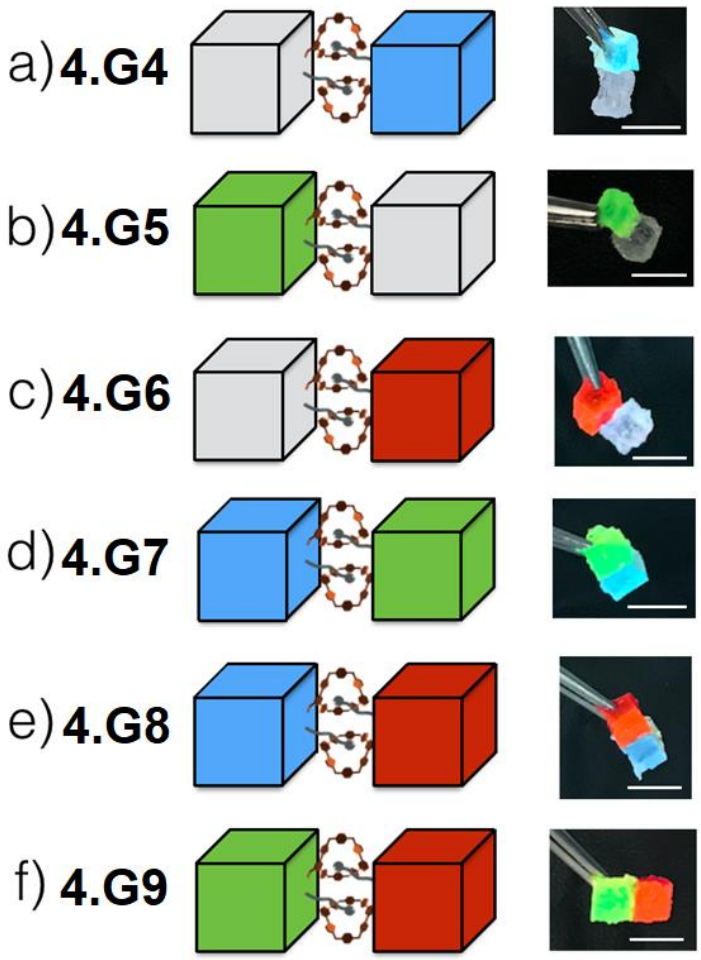

Figure 4.15 Cartoon representations and photographs of (a) **4.G4** (made from adhering **4.G0** with **4.G1**), (b) **4.G5** (**4.G2** + **4.G0**), (c) **4.G6** (**4.G0** + **4.G3-1**), (d) **4.G7** (**4.G1** + **4.G2**), (e) **4.G8** (**4.G1** + **4.G3-1**), and (f) **4.G9** (**4.G2** + **4.G3-1**) taken under a UV lamp (λ_{ex} = 365 nm, scale bar = 1 cm). Reproduced with permission from *Adv. Mater*. **2018**, *30*, 1705480. Copyright 2018 John Wiley and Sons.[7]

Based on the self-healing observed for hydrogels **4.G0**, **4.G1**, **4.G2**, and **4.G3-1** and the presence of similar cationic macrocycle and anion recognition motifs in all these systems, we anticipated that it would be possible to prepare adhesive hydrogels by contacting individual hydrogels with one another. Hydrogels **4.G0**, **4.G1**, **4.G2**, and **4.G3-1** were specifically designed to test this proposition since each displays distinct fluorescence (or non-fluorescence) emission features (Figures 4.12a–4.12e). First, **4.G0** and **4.G1** were selected as building blocks and pushed together manually on the black

nitrile substrate in the absence of any additional solvent. They joined into one integrated hydrogel in seconds. After setting aside for a while, the newly formed hydrogel, **4.G4**, made from **4.G0** + **4.G1**, could be lifted up off the substrate support without disintegration (Figure 4.15). When excited at 365 nm using a UV lamp, **4.G4** displayed blue fluorescent emission, but only in the portion of the bulk material originating from **4.G1**; no appreciable emission was seen for the **4.G0**-derived side of **4.G4**. Such behavior is taken as evidence that **4.G4** is a macroscopic Janus-type hydrogel with blue and non-fluorescent domains. Similarly, adhesion between the remaining hydrogels results in hydrogels **4.G5**–**4.G9** with individual distinct color and fluorescent domains (Figures 4.15b–4.15f).

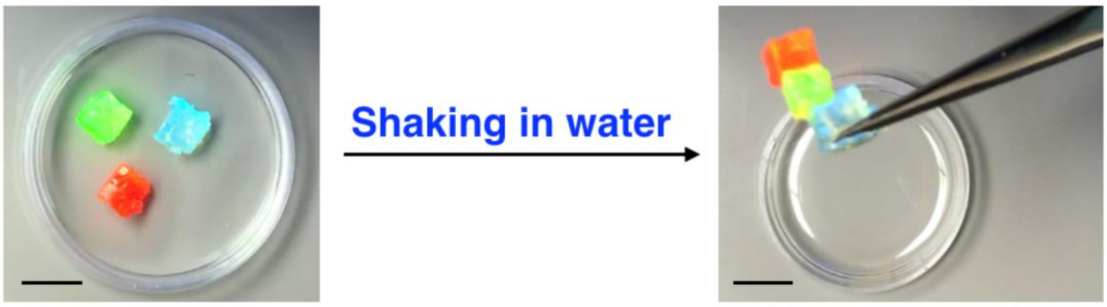

Figure 4.16 Photographs of the fluorescent hydrogels before and after shaking in water taken under a UV lamp (λ_{ex} = 365 nm, scale bar = 1 cm). Here **4.G3-1** was used to represent red **4.G3**. Reproduced with permission from *Adv. Mater*. **2018**, *30*, 1705480. Copyright 2018 John Wiley and Sons.[7]

The above adhesion phenomena or "heterohealing" between the individual hydrogels also occurs in water. When **4.G1**, **4.G2**, and **4.G3-1** were mixed and shaken in water, they stuck to each other to form a combined multi-fluorescent hydrogel that could also be lifted up without disintegration (Figure 4.16). The requisite inter-hydrogel adhesion, which does not affect the fluorescence of each individual building block, is

ascribed to macrocycle-anion recognition interactions involving the tetracationic receptor and alkyl sulfonate domains present in each of the individual hydrogels.

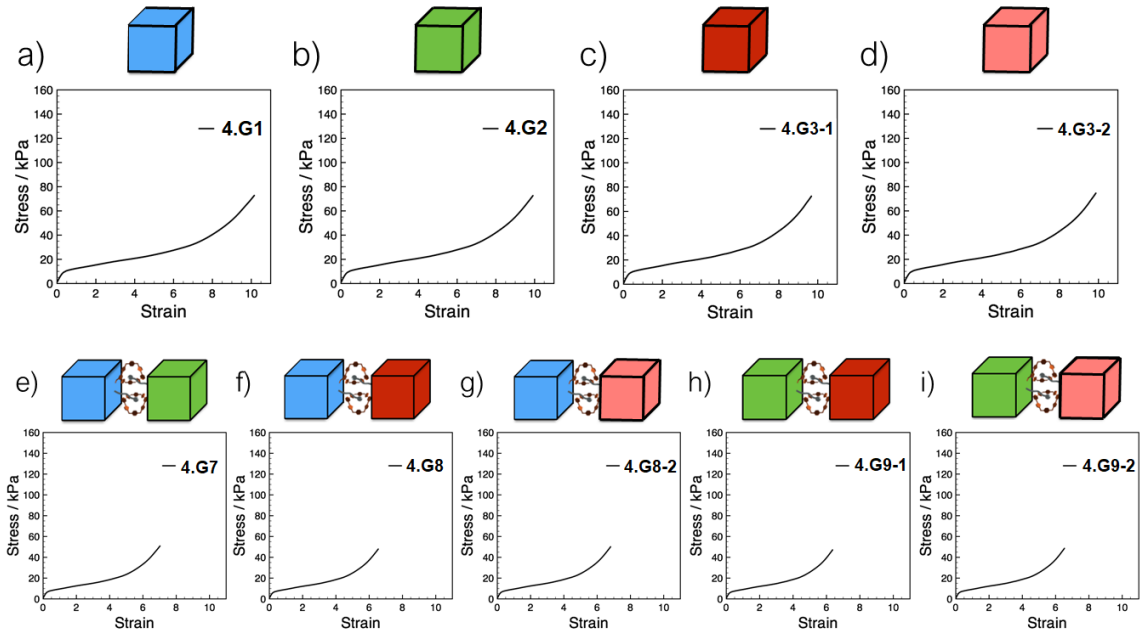

Figure 4.17 The tensile stress–strain curves of (a) **4.G1**, (b) **4.G2**, (c) **4.G3-1**, (d) **4.G3-2**, (e) **4.G7**, (f) **4.G8-1**, (g) **4.G8-2**, (h) **4.G9-1**, and (i) **4.G9-2** (strain rate: 100 mm/min, 25 °C). **4.G1** and **4.G3-1** forms **4.G8-1**, **4.G1** and **4.G3-2** forms **4.G8-2**, **4.G2** and **4.G3-1** forms **4.G9-1**, and **4.G2** and **4.G3-2** forms **4.G9-2**. Reproduced with permission from *Adv. Mater*. **2018**, *30*, 1705480. Copyright 2018 John Wiley and Sons.[7]

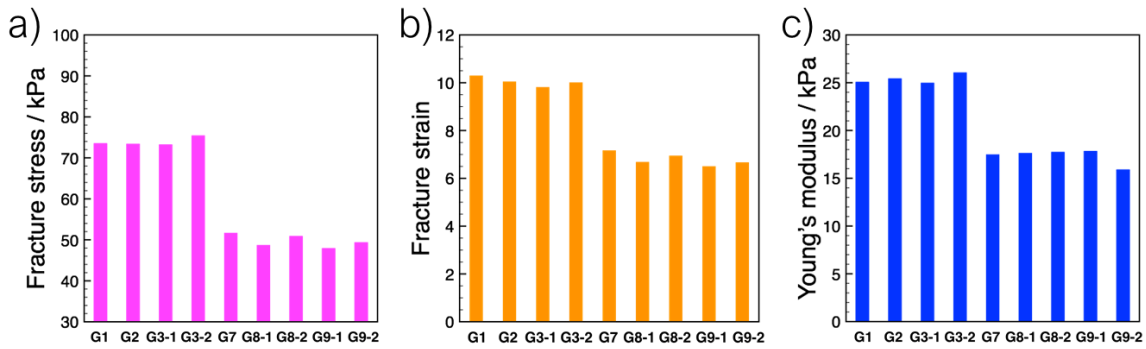

Figure 4.18 The mechanical parameters: (a) fracture stress, (b) fracture strain, and (c) Young's modulus of the hydrogels. Reproduced with permission from *Adv. Mater*. **2018**, *30*, 1705480. Copyright 2018 John Wiley and Sons.[7]

To prepare fluorescent color 3D codes, fluorescent hydrogels **4.G1**–**4.G3** were used as the building blocks to produce gels **4.G7** (**4.G1** + **4.G2**), **4.G8** (**4.G1** + **4.G3**), and **4.G9** (**4.G2** + **4.G3**). To characterize quantitatively the adhesion strength of hydrogels **4.G7**–**4.G9**, stretching studies were carried out. The tensile stress-strain curves and corresponding mechanical parameters were obtained (Figures 4.17 and 4.18). The fracture stress, fracture strain, and Young's modulus of **4.G1**–**4.G3** were 70–80, 9–11, and 24–27 kPa, respectively, while for **4.G7**–**4.G9**, the corresponding parameters were 45–55, 6.5–7.5, and 15–18 kPa, respectively. The decrease in mechanical strength for the hetero gel systems is ascribed to a lack of covalent cross-linking in the interfacial adhesion domain: Both covalent and non-covalent cross-linking exist in **4.G1**–**4.G3**, while only macrocycle-anion recognition interactions stabilize the gel-to-gel contacts.

The fluorescent hydrogels **4.G1**, **4.G2**, and **4.G3-1** were then used to construct a fluorescent color code. As shown in Figure 4.19, various individual blocks of **4.G1**, **4.G2**, and **4.G3-1** were placed on a black nitrile substrate and contacted with each other. The result was a multiblock, adhesion-based array that provides a pattern corresponding to **Code A**. As with the simpler adhesion (healing) studies described above, this pattern is stabilized in a bulk sense through molecular scale interfacial macrocycle-anion recognition interactions. When this code is observed under natural light, the colors making up the pattern are dim. As a consequence, the code is not recognized by the freely available application software ("app") COLORCODE downloaded onto a smartphone. However, when **Code A** was placed under a UV lamp (λ_{ex} = 365 nm), the basic fluorescent blue, green, and red colors of **4.G1**, **4.G2**, and **4.G3-1** become easily recognized by the COLORCODE app, allowing readout of specific information (**Info A**). This information may be programed by the user and, for the sake of illustration, was used to load a specific website (Figure 4.19a). This ability to read the pattern of **Code A** under

conditions of UV illumination, but not natural light, provides support for the notion that physical assembly of hydrogels of **4.G1**, **4.G2**, and **4.G3-1** into specific patterns can be used to mask and display information as desired.

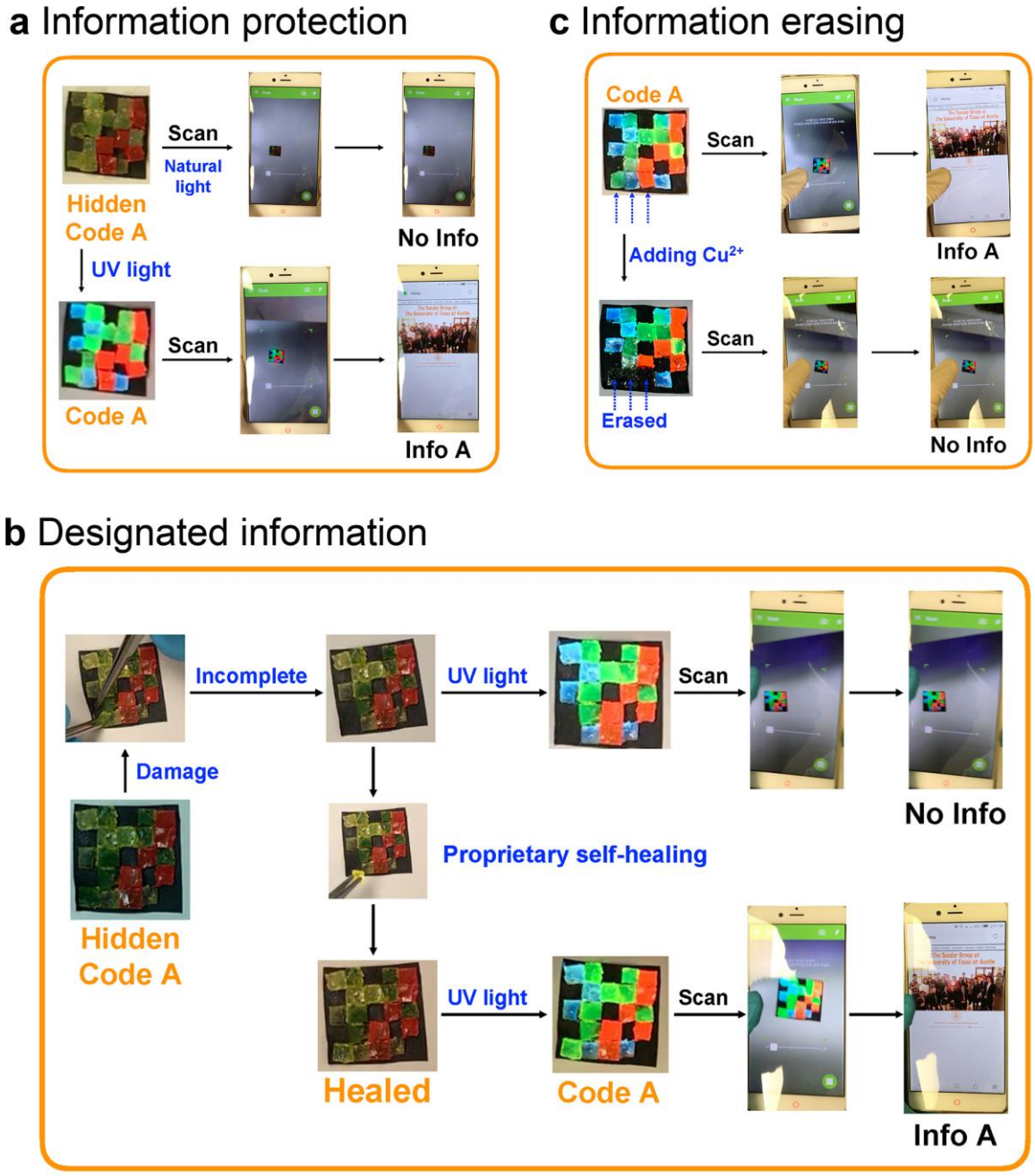

Figure 4.19 (a) Photographs of the masking and reading out of information inherent in **Code A**, a pattern made up from the assembly of individual domains of hydrogels **4.G1**, **4.G2**, and **4.G3-1** on a black nitrile supporting substrate. (b) Photographs of designated information of fluorescent color **Code A**. (c) Photographs showing Cu(II)-induced information erasing within **Code A**. The individual hydrogel blocks subject to Cu(II) treatment (in the form of $CuCl_2$ powder). The size of the substrate is 2.5 cm × 2.5 cm. Reproduced with permission from *Adv. Mater.* **2018**, *30*, 1705480. Copyright 2018 John Wiley and Sons.[7]

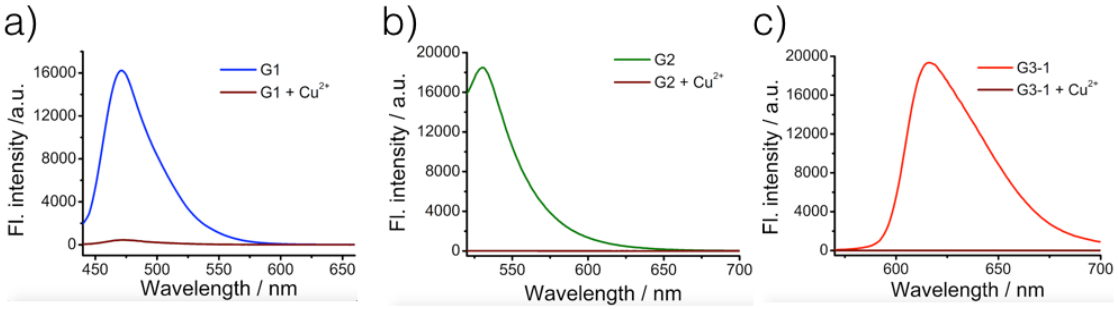

Figure 4.20 Fluorescence emission spectra (λ_{ex} = 365 nm) of (a) **4.G1**, (b) **4.G2**, and (c) **4.G3-1** before and after adding excess $CuCl_2$ (5 mg) for 4 min. Reproduced with permission from *Adv. Mater*. **2018**, *30*, 1705480. Copyright 2018 John Wiley and Sons.[7]

Information could also be masked by removing an individual hydrogel block from the combined hydrogel array making up **Code A**. The resulting incomplete hydrogel pattern cannot be recognized by the smartphone app. The missing gel block could then be replaced in its original location, where it re-adhered to the remaining part of the code rapidly on the laboratory time scale. The repaired **Code A** could be lifted up without disintegration. Upon UV illumination, the original **Info A** of repaired **Code A** could again be read out (*cf*. Figure 4.19b). Information within a hydrogel-based code may also be erased by treating with $CuCl_2$ powder, a paramagnetic salt that quenches the fluorescence emission of the dyes present in the hydrogels.[22] Thus, when the surfaces of selected **4.G1**, **4.G2**, and **4.G3-1** blocks in the domain making up **Code A** were covered with excess $CuCl_2$ powder, an incomplete fluorescence pattern was produced within 4 min that could not be recognized by the smartphone app (Figures 4.19c and 4.20).

The encoded information within a given hydrogel-based 3D code-producing array may be transformed by changing the pattern of the array. For instance, the hydrogels, **4.G1**, **4.G2**, and **4.G3-1**, making up **Code A** were reorganized by changing the amount and position of each; this gave a new array (**Code B**). Under UV illumination, the newly encoded information (**Info B**) could be read out easily using the smartphone app (*cf*.

Figure 4.21a). Selected hydrogel blocks making up **Code B** could also be removed physically (*i.e.*, cut off) and replaced with new hydrogel components. By way of illustration, this was done in such a way as to reconstitute the pattern making up **Code A**. Under UV light, **Info A** was again produced. A variety of other patterns were assembled using this same cut and reassembly approach (Figure 4.22). Indeed, in principle, a nearly limitless number of information-rich codes (fluorescent hydrogel arrays) can be produced from combinations of **4.G1**, **4.G2**, and **4.G3**. The codes made up from the present self- and heterohealing fluorescent gels may also be modified by chemical means. The fluorescence of **RORS** is typically quenched by base[15] (Figure 4.23a). Thus, it was expected that hydrogel **4.G3-2**, containing both **RORS** and coumarin fluorophores would prove responsive to ammonia. As-prepared **4.G3-2** gives rise to a red fluorescence because the fluorescence intensity of the **RORS** fluorophore dominates over that of the coumarin (Figure 4.12j). However, upon exposure to ammonia vapor (from a concentrated aqueous NH_4OH solution), the **RORS** subunits in **4.G3-2** become nonfluorescent, presumably as the result of base-induced formationof ring closed rhodamine B spirolactam derivatives (**RCRS**)[15] (Figure 4.23a). Under these conditions, **4.G3-2** produces a blue fluorescence (Figures 4.23b–4.25). However, no changes in the fluorescence features of **4.G1**, **4.G2**, or **4.G3-1** were seen upon exposure to ammonia vapor (Figures 4.23c, d, and 4.24). The response time of the color changes produced by the responsive hydrogel **4.G3-2** upon exposure to ammonia vapor for different times is shown in Figure 4.25. From the time course photographs shown in this figure (Figure S40a), it is seen that the initial red color changes to blue within 10 min. From the time course of the corresponding time-dependent fluorescence emission spectra (Figure 4.25b), it is found that the fluorescence intensity of **RORS** is quenched by about 50% after 2 min of exposure to ammonia, and is totally quenched after 10 min.

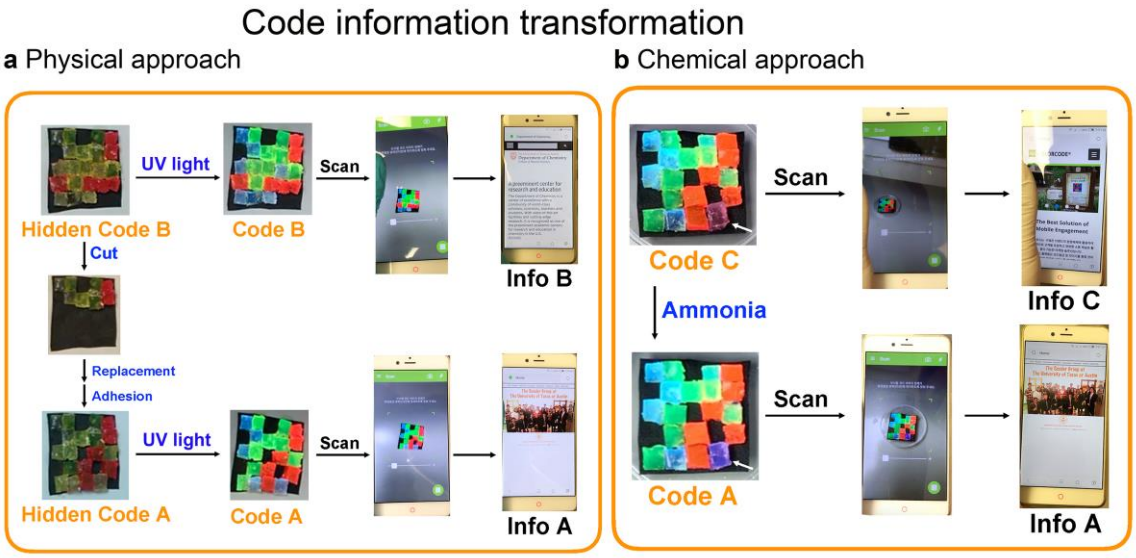

Figure 4.21 (a) Photographs showing the transformation of information in **Code B** (**Info B**) into **Code A** (**Info A**) by means of a cut and re-adhesion strategy. (b) Photographs of code information transformation from **Info C** to **Info A** by exposure to ammonia vapor. The size of the substrate is 2.5 cm × 2.5 cm. Reproduced with permission from *Adv. Mater*. **2018**, *30*, 1705480. Copyright 2018 John Wiley and Sons.[7]

4.G1, **4.G2**, **4.G3-1**, and **4.G3-2** were then used to construct **Code C**. This latter array differs from **Code A** in that one blue **4.G1** hydrogel block is replaced with one red **4.G3-2** hydrogel block (Figure 4.3). As true for **Code A** and **Code B**, the information inherent in **Code C** (**Info C**) can only be read out under conditions of UV illumination (Figure 4.21b). In this case, when **Code C** was exposed to ammonia vapor for 10 min, the fluorescence color of the **4.G3-2** block changed from red to blue. Therefore, the pattern of **Code C** after exposure to ammonia is recognized as **Code A** by the smartphone app. In other words, **Info C** is transformed into **Info A** by chemical means (Figure 4.21b).

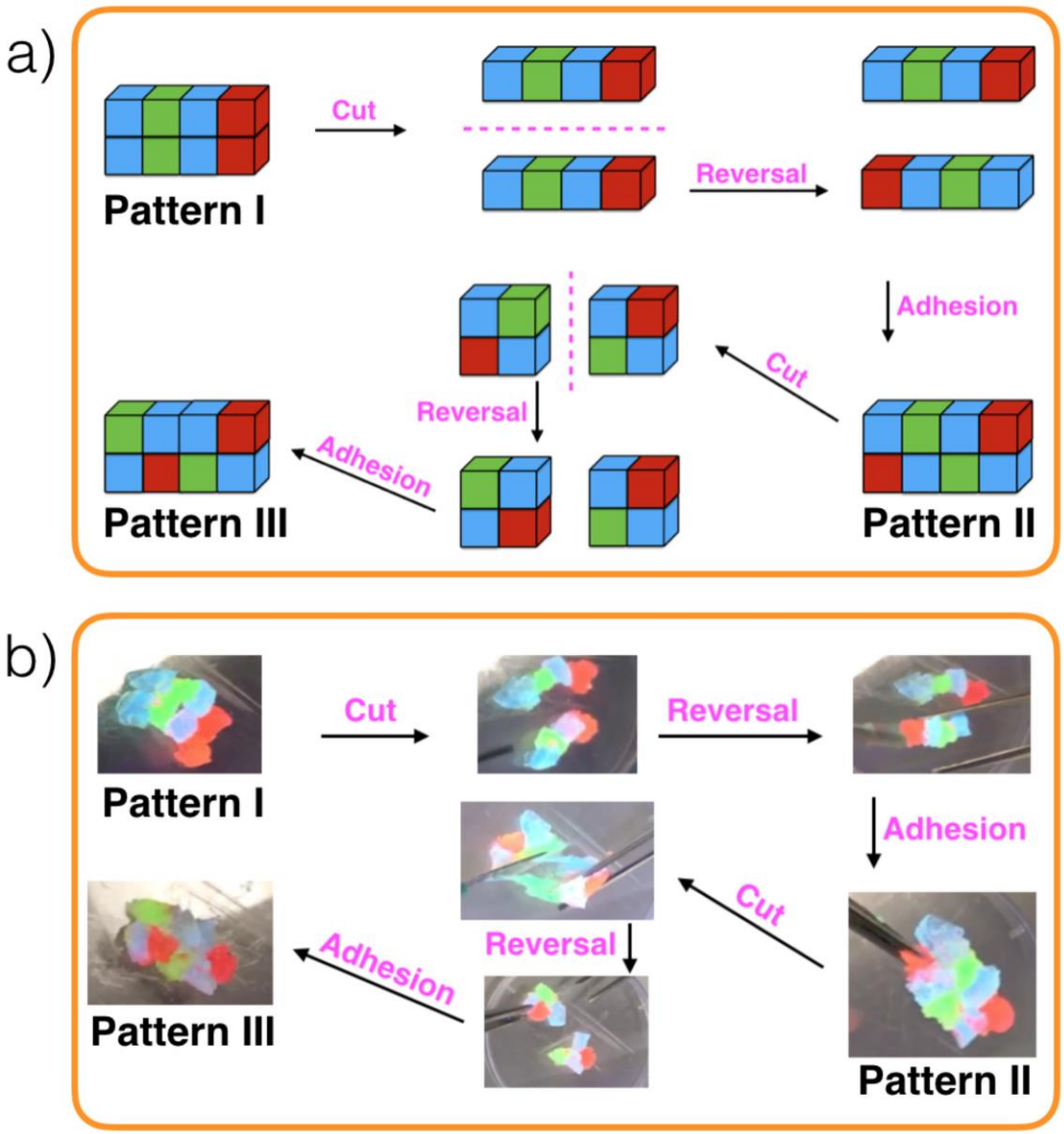

Figure 4.22 (a) Cartoon representations and (b) photographs of the cut/adhesion reorganization tests taken under a UV lamp (λ_{ex} = 365 nm, scale bar = 1 cm). Reproduced with permission from *Adv. Mater*. **2018**, *30*, 1705480. Copyright 2018 John Wiley and Sons.[7]

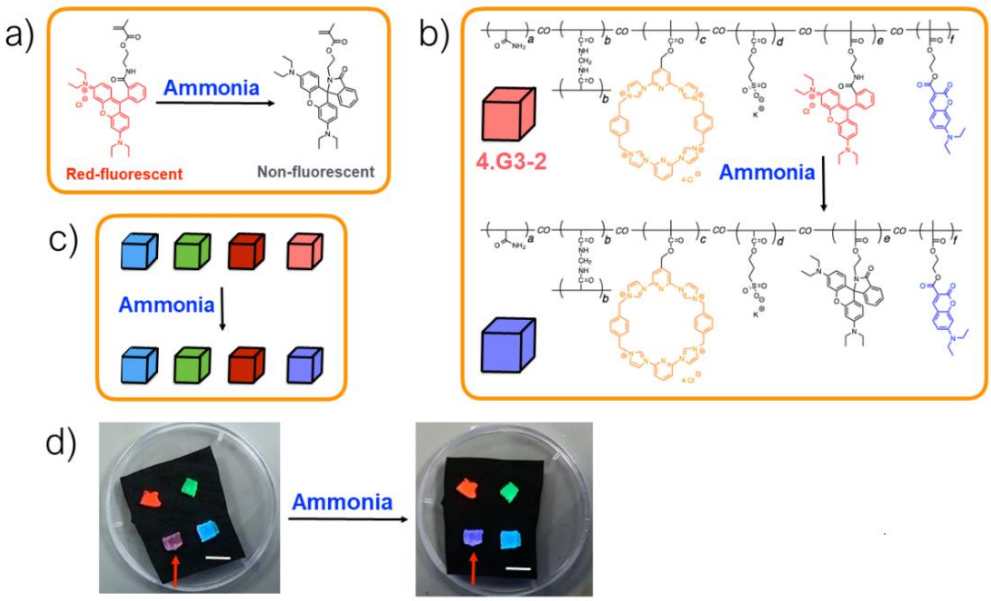

Figure 4.23 Ammonia-induced chemical structure changes of (a) **Red-2-ring opening monomer**, and (b) **4.G3-2**. (c) Cartoon representation and d) photographs of ammonia-induced fluorescent color change of **G3-2** taken under a UV lamp (λ_{ex} = 365 nm, scale bar = 1 cm). Reproduced with permission from *Adv. Mater*. **2018**, *30*, 1705480. Copyright 2018 John Wiley and Sons.[7]

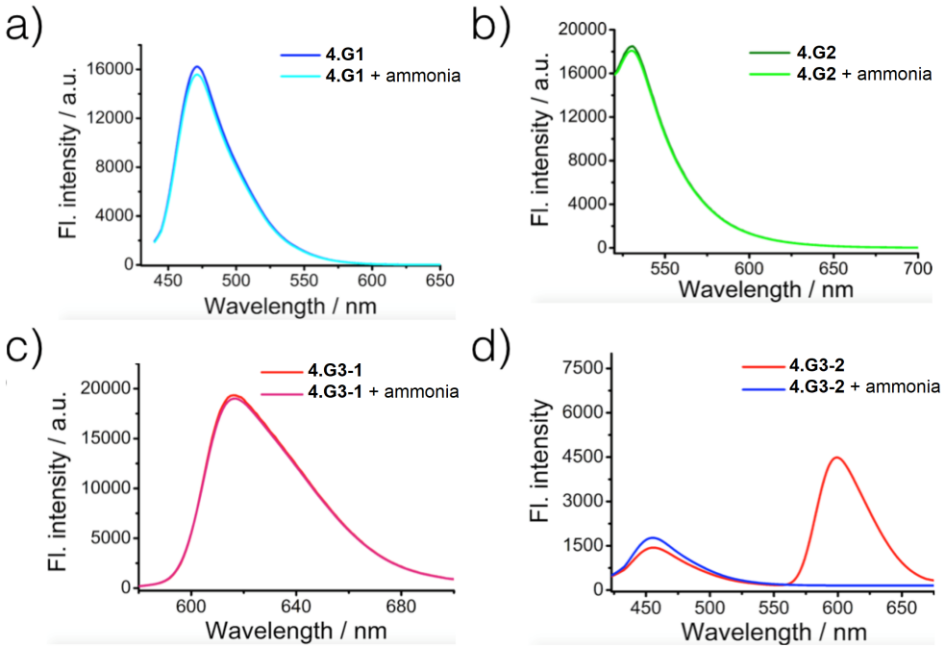

Figure 4.24 Fluorescence emission spectra (λ_{ex} = 365 nm) of (a) **4.G1**, (b) **4.G2**, c) **4.G3-1**, and (d) **4.G3-2** before and after exposure to ammonia for 10 min. Reproduced with permission from *Adv. Mater*. **2018**, *30*, 1705480. Copyright 2018 John Wiley and Sons.[7]

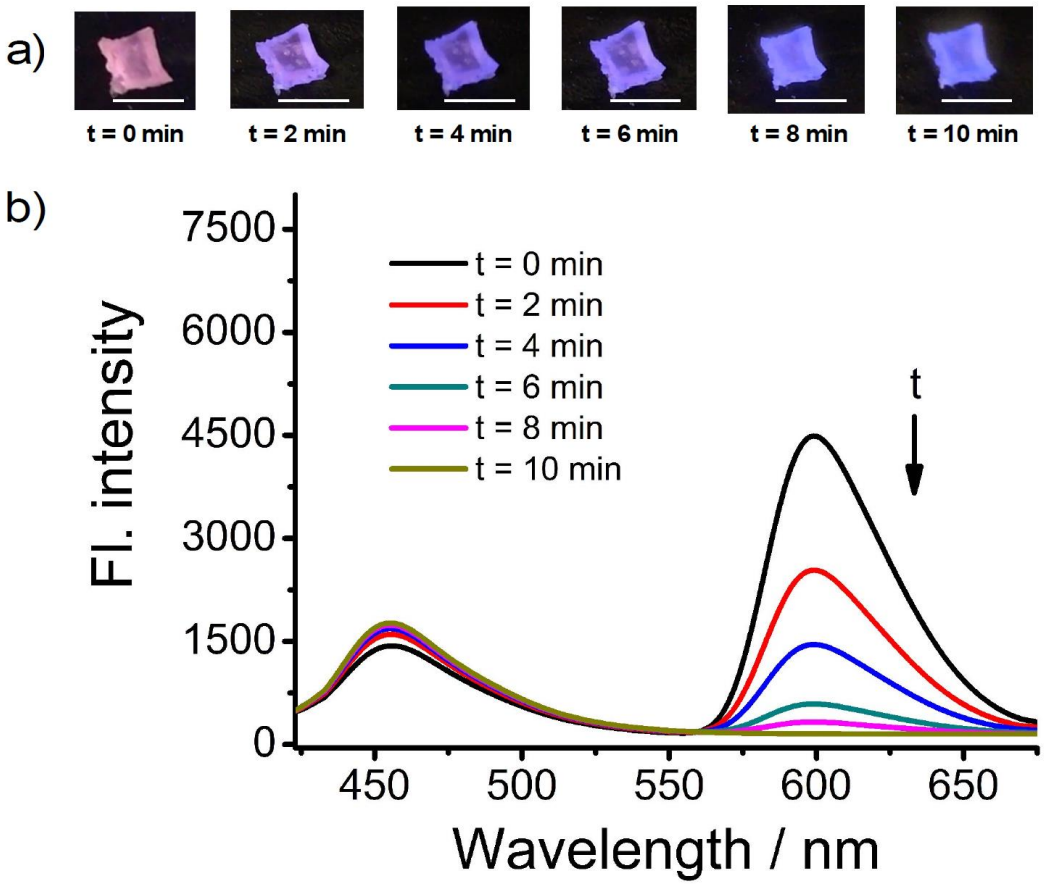

Figure 4.25 (a) Photographs of the ammonia-induced fluorescent color changes for **4.G3-2** as seen at different times with visualization provided by a UV lamp (λ_{ex} = 365 nm, scale bar = 1 cm). (b) Fluorescence emission spectra (λ_{ex} = 365 nm) of **4.G3-2** after exposure to ammonia vapor for different times. The vapor was produced from concentrated aqueous ammonium hydroxide and a petri dish cover was used to minimize vapor loss into the laboratory atmosphere. Reproduced with permission from *Adv. Mater*. **2018**, *30*, 1705480. Copyright 2018 John Wiley and Sons.[7]

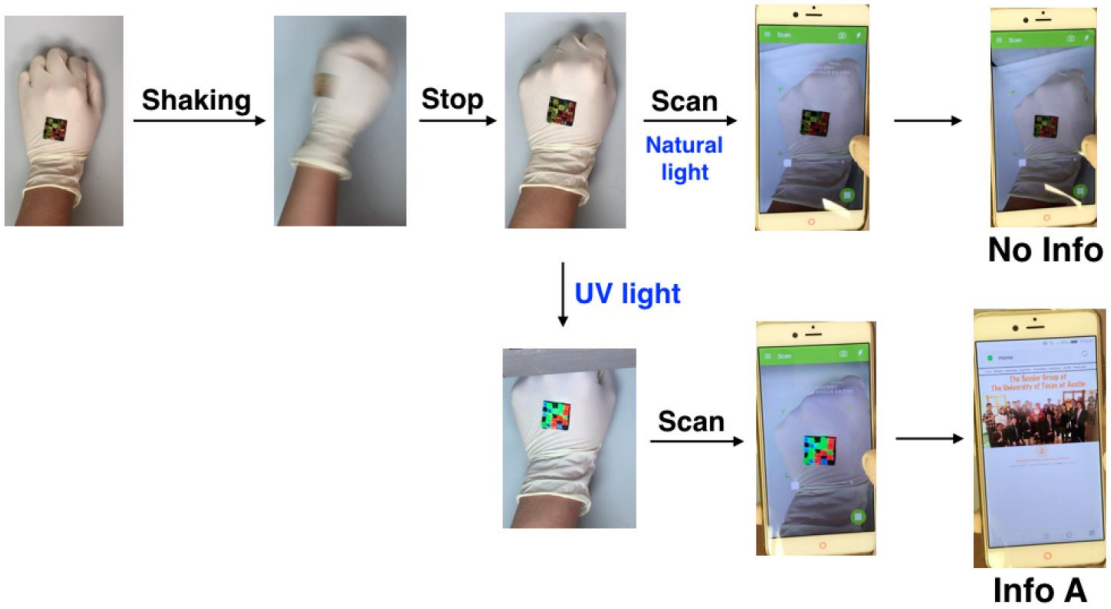

Figure 4.26 Photographs of **Code A** on a latex-gloved hand, view enhanced motions, and reading out of information inherent in **Code A** using a UV lamp (λ_{ex} = 365 nm, and the size of the substrate is 2.5 cm × 2.5 cm). Reproduced with permission from *Adv. Mater.* **2018**, *30*, 1705480. Copyright 2018 John Wiley and Sons.[7]

The present codes are made up of soft materials. They have the potential to be used as wearable materials.[23,24] To test this possibility, **Code A** was attached to the back of a latex-gloved hand (Figure 4.26). The code was not dislodged by shaking or by normal hand movements. This combination of robustness and flexibility derives directly from the reversible (albeit strong) nature of the interfacial macrocycle-anion interactions that are inherent to the present gel arrays. When worn in this way, the masking and reading out of information functions inherent in **Code A** were fully retained. The present work thus serves to illustrate a new chemical-based approach to information storage, modification, and readout. It also highlights what might be an attractive means of creating smart, wearable materials that can be reprogramed as the need arises.

4.3 CONCLUSIONS

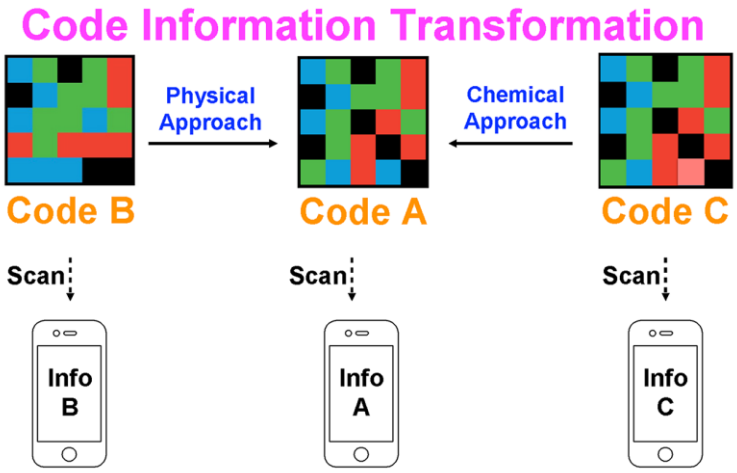

Figure 4.27 Cartoon representation of the chemical and physical approaches to transform encoded information. Reproduced with permission from *Adv. Mater*. **2018**, *30*, 1705480. Copyright 2018 John Wiley and Sons.[7]

In summary, a set of hydrogels consisting of a pAAm network cross-linked by MBAAm and a complex of tethered tetracationic macrocyclic anion receptor and pendant alkyl sulfonate subunits have been prepared. Fluorescent coumarin, BODIPY, and rhodamine subunits were incorporated, respectively, into the polymer backbones of three hydrogels based on this platform, giving rise to materials producing blue, green, and red fluorescence upon UV irradiation. An additional red fluorescent hydrogel was prepared that contains both coumarin and rhodamine fluorophores; its fluorescence was found to change from red to blue upon exposure to aqueous ammonia. The various hydrogels could be physically assembled into different integrated multicolor fluorescent hydrogel arrays when pushed together manually on a black nitrile substrate with the adhesion being stabilized through presumed interfacial macrocycle-anion interactions. Three illustrative 3D color code arrays, **Code A**, **Code B**, and **Code C**, were prepared in this way. Depending on the specific manipulations in question, the information they encode, as read out by a commercially available smartphone app, could be erased, transformed, or re-healed. Both physical and chemical means could be used to effect changes. The

systems are flexible and the encoded information can be read when the codes are used as wearable materials. The present work thus serves to illustrate what might be a new chemical-based approach to information storage, modification, and readout. It also points the way for a new potential application for self-healing soft materials.

4.4 REFERENCES

1) Erevelles, S.; Fukawa, N.; Swayne, L. *J. Bus. Res.* **2016**, *69*, 897–904.
2) Li, M.; Zheng, X.; Zhuang, G. *J. Bus. Res.* **2017**, *78*, 268–276.
3) Meruga, J. M.; Fountain, C.; Kellar, J.; Crawford, G.; Baride, A.; May, P. S.; Cross, W.; Hoover, R.; *Int. J. Comput. Appl.* **2015**, *37*, 17–27.
4) R. Won, *Nat. Photonics* **2012**, *6*, 801.
5) Graydon, O. *Nat. Photonics* **2013**, *7*, 343.
6) Park, D. H.; Han, C. J.; Shul, Y. G.; Choy, J. H.; *Sci. Rep.* **2014**, *4*, 4879.
7) Ji, X.; Wu, R. -T.; Long, L.; Ke, X. -S.; Guo, C.; Ghang, Y. -J.; Lynch, V. M.; Huang, F.; Sessler, J. L. *Adv. Mater*. **2018**, *30*, 1705480.
8) Appel, E. A.; del Barrio, J.; Loh, X. J.; Scherman, O. A.; *Chem. Soc. Rev.* **2012**, *41*, 6195–6214.
9) Qi, Z.; Schalley, C. A.; *Acc. Chem. Res.* **2014**, *47*, 2222–2233.
10) Ni, M.; Zhang, N.; Xia, W.; Wu, X.; Yao, C.; Liu, X.; Hu, X. -Y.; Lin, C.; Wang, L. *J. Am. Chem. Soc.* **2016**, *138*, 6643–6649.
11) Zheng, W.; Chen, L. -J.; Yang, G.; Sun, B.; Wang, X.; Jiang, B.; Yin, G. -Q.; Zhang, L.; Li, X.; Liu, M.; Chen, G.; Yang, H. -B.; *J. Am. Chem. Soc.* **2016**, *138*, 4927–4937.
12) Liu, J.; Sun, Y. -Q.; Huo, Y.; Zhang, H.; Wang, L.; Zhang, P.; Song, D.; Shi, Y.; Guo, W. *J. Am. Chem. Soc.* **2014**, *136*, 574–577.
13) Mendive-Tapia, L.; Subiros-Funosas, R.; Zhao, C.; Albericio, F.; Read, N. D.; Lavilla, R.; Vendrell, M. *Nat. Protoc.* **2017**, *12*, 1588–1619.
14) Beija, M.; Afonso, C. A.; Martinho, J. M. *Chem. Soc. Rev.* **2009**, *38*, 2410–2433.
15) Chen, X.; Pradhan, T.; Wang, F.; Kim, J. S.; Yoon, J. *Chem. Rev.* **2012**, *112*, 1910–1956.
16) Busschaert, N.; Caltagirone, C.; Van Rossom, W.; Gale, P. A. *Chem. Rev.* **2015**, *115*, 8038–8155.
17) Gale, P. A.; Davis, J. T.; Quesada, R. *Chem. Soc. Rev.* **2017**, *46*, 2497–2519.
18) Gong, H. Y.; Rambo, B. M.; Karnas, E.; Lynch, V. M.; Sessler, J. L.; *Nat. Chem.* **2010**, *2*, 406–409.
19) Ji, X.; Wang, H.; Li, Y.; Xia, D.; Li, H.; Tang, G.; Sessler, J. L.; Huang, F. *Chem. Sci.* **2016**, *7*, 6006–6014.
20) Harada, A.; Kobayashi, R.; Takashima, Y.; Hashidzume, A.; Yamaguchi, H. *Nat. Chem.* **2011**, *3*, 34–37.
21) Nakahata, M.; Takashima, Y.; Yamaguchi, H.; Harada, A. *Nat. Commun.* **2011**, *2*, 511.
22) Jung, H. S.; Kwon, P. S.; Lee, J. W.; Kim, J. I.; Hong, C. S.;. Kim, J. W; Yan, S.; Lee, J. Y.; Lee, J. H.; Joo, T.; Kim, J. S.; *J. Am. Chem. Soc.* **2009**, *131*, 2008–2012.
23) Suzuki, D.; Oda, S.; Kawano, Y. *Nat. Photonics* **2016**, *10*, 809–813.
24) Gao, W.; Emaminejad, S.; Nyein, H. Y. Y.; Challa, S.; Chen, K.; Peck, A.; Fahad, H. M.; Ota, H.; Shiraki, H.; Kiriya, D.; Lien, D. -H.; Brooks, G. A.; Davis, R. W.; Javey, A. *Nature* **2016**, *529*, 509–514.
25) (a) Connors, K. A. Binding Constants, Wiley: New York, 1987. (b) Corbin, P. S. Ph.D. Dissertation, University of Illinois at Urbana-Champaign, Urbana, IL, 1999. (c) Ashton, P. R.; Ballardini, R.; Balzani, V.; Belohradsky, M.; Gandolfi, M. T.; Philp, D.;

Prodi, L.; Raymo, F. M.; Reddington, M. V.; Spencer, N.; Stoddart, J. F.; Venturi, M.; Williams, D. J. *J. Am. Chem. Soc.* **1996**, *118*, 4931–4951.
26) Hoshino, T.; Shirota, N.; Asakawa, A. Compound Having Fluorescent Functional Group and Method for Producing Polymer of The Same. Patent WO2009011427A1, 2009.
27) S, Z.; Q, Z.; B, Y. Near Infrared BODIPY (Boron Dipyrromethene Compounds) Hydroxyl Radical Probes and Synthesis Method and Usage Thereof. Patent CN103342720A, 2013.
28) L. Wang, M. Sibrian-Vazquez, J. O. Escobedo, J. Wang, R. G. Moore, R. M. Strongin, *Chem. Commun.* **2015**, *51*, 1697–1700.
29) Hu, B.; D. M. Henn, D. M.; Wright, R. A. E.; Zhao, B. *Langmuir* **2014**, *30*, 11212−11224.
30) Yu, K. -K.; Li, K.; Hou, J. -T.; Yang, J.; Xie, Y. -M.; Yu, X. -Q. *Polym. Chem.* **2014**, *5*, 5804–5812.
31) Wojtecki, R. J.; Meador, M. A.; Rowan, S. J.; *Nat. Mater.* **2010**, *10*, 14–17.
32) Liu, J.; Tan, C. S. Y.; Yu, Z.; Lan, Y.; Abell, C.; Scherman, O. A. *Adv. Mater.* **2017**, *29*, 1604951.
33) Liu, J.; Tan, C. S. Y.; Yu, Z.; Li, N.; Abell, C.; Scherman, O. A. *Adv. Mater.* **2017**, *29*, 1605325.
34) Takashima, Y.; Hatanaka, S.; Otsubo, M.; Nakahata, M.; Kakuta, T.; Hashidzume, A.; Yamaguchi, H.; Harada, A.; *Nat. Commun.* **2012**, *3*, 1270.
35) Wu, Z. -S.; Tan, Y. -Z.; Zheng, S.; Wang, S.; Parvez, K.; Qin, J.; Shi, X.; Sun, C.; Bao, X.; Feng, X.; Müllen, K. *J. Am. Chem. Soc.* **2017**, *139*, 4506–4512.
36) Shi, Y.; Wang, M.; Ma, C.; Wang, Y.; Li, X.; Yu, G. *Nano Lett.* **2015**, *15*, 6276−6281.
37) Zhang, J.; Xu, D.; Guo, J.; Sun, Z.; Qian, W.; Zhang, Y.; Yan, F. *Macromol. Rapid Commun.* **2016**, *37*, 1194−119.

Chapter 5: Experimental Procedures

5.1 General Procedures

All reagents and starting materials were obtained from commercial suppliers and used without further purification unless otherwise noted. Dichloromethane (DCM; CH_2Cl_2) was distilled over calcium hydride under a nitrogen atmosphere. Acetonitrile (CH_3CN) was purified using a Vac ISO 9001 Vacuum Atmospheres Solvent Purifier. Flash column chromatography was performed on silica gel (40–63 μm, Sorbent Technologies Inc.). One- and two-dimensional nuclear magnetic resonance (NMR) spectra were recorded on Agilent MR 400, VARIAN DirectDrive 600, and Varian Inova 500 instruments. Chemical shifts are reported on the delta (δ) scale in ppm relative to residual chloroform (δ = 7.26 for $CHCl_3$ (^{1}H) and 77.16 for $CDCl_3$ (^{13}C), respectively), acetonitrile (δ = 1.94 for CHD_2CN (^{1}H) and 118.26 for CD_3CN (^{13}C), respectively), deuterium oxide (δ = 4.80 for DOH (^{1}H)), and dimethyl sulfoxide (δ = 2.50 for DMSO-d_5 (^{1}H) and 39.52 for DMSO-d_6 (^{13}C), respectively). DMSO-d_6 containing 1% TFA-d_1 (deuterated trifluoroacetic acid) was used as solvents for selected one- and two-dimensional ^{1}H NMR measurements of **TxSB-CO$_2$H**·4PF$_6$. High resolution mass spectra (HRMS) were obtained on an Agilent Technologies 6530 Accurate-Mass Q-TOF LC/MS and Thermo Scientific TSQ Quantum GC/MS. Melting points were determined using a MEL-TEMP capillary melting point apparatus.

X-ray crystallographic analyses were carried out on a Rigaku AFC12 diffractometer with a Saturn 724+ CCD using a graphite monochromator with MoKα radiation (λ = 0.71073 Å). Each sample for SEM analysis was prepared by placing a droplet of a selected sample solution onto a silicon wafer, followed by vacuum drying. SEM measurements were carried out using a HITACHI HI-7700 system. Dynamic light

scattering (DLS) measurements were carried out using 200-mW polarized laser source Nd: YAG (λ = 532 nm). The polarized scattered light data were collected at 90° in a self-beating mode with a Hamamatsu R942/02 photomultiplier, and the signals were sent to a Malvern 4700 submicrometer particle analyzer system. The Fourier transform infrared (FTIR) spectrum of the hydrogels were recorded by using an FTIR spectrometer (Thermo Mattson, Infinity Gold FTIR) equipped with a liquid nitrogen cooled narrow band MCT detector. An attenuated total reflection cell equipped with a Ge crystal was employed. Rheological experiments were performed using a rheometer (AR 2000EX, TA instrument) with a Peltier plate in the frequency sweep mode (25 °C). Tensile tests were performed using a tensile Hounsfield machine equipped with a 5-N load cell. The experiments were performed at room temperature using a deformation rate of 100 mm min^{-1}. The conductivity of aqueous anion salt solutions were determined on a DDS-307 instrument. UV-Vis spectroscopic analyses were carried out using a Varian Cary 5000 spectrophotometer. Fluorescence measurements were performed on a Perkin-Elmer Luminescence Spectrophotometer LS 50B or a Gilden Photonics Ltd. fluorimeter. The black nitrile substrate used in the present experiments was cut from a standard laboratory glove. Standard latex gloves were used as the substrate for the wearable materials tests. The commercially available smartphone App used in the present studies was COLORCODE^{TM} and at the time the work was performed could be downloaded for free from the Apple app store.

5.2 Synthetic Procedures and Characterization Data

Synthesis of 2,6-bis(imdazol-1-yl)pyridine, 2.6 and 4.6

In a 50 mL Schlenk flask charged with a stir bar, 2,6-dibromopyridine (**2.5** or **4.7**) (2.37 g, 10.0 mmol), imidazole (1.70 g, 25.0 mmol), copper(I) iodide (0.10 g, 0.53 mmol), salicylaldoxime (0.274 g, 2.0 mmol), and cesium carbonate (9.78 g, 30.0 mmol) were dissolved in dry CH_3CN (15 mL). The reaction mixture was degassed through three cycles of freeze-pump-thaw procedure and was later heated at 85°C under a nitrogen atmosphere for 48 hours. The resulting suspension was filtered off and the residue on the funnel was rinsed with CH_2Cl_2 (2 × 150 mL). The filtrate was first washed with 1 M aqueous solution of Na_4EDTA (60 mL) and then with water (3 × 100 mL), and the resulting organic phase was dried over Na_2SO_4 and evaporated to dryness. The crude compound was purified by flash column chromatography on silica gel (20:1 CH_2Cl_2/CH_3OH) to yield 2,6-bis(imdazol-1-yl)pyridine (**2.6** or **4.6**) (1.90 g, 90%) as a white solid: mp 142–144 °C (lit.[1] 142–143 °C); ^{1}H-NMR ($CDCl_3$, 400 MHz): δ 8.38 (bs, 2H), 7.97 (t, 1H, J = 8 Hz), 7.67 (pseudot, 2H, J = 1.6 Hz), 7.29 (d, 2H, J = 8 Hz), 7.23–7.22 (m, 2H).

Synthesis of *N*,*N*'-bis(*α*-bromo-*p*-xylene)-2,6-bis(imadzol-1-yl)pyridine bis(hexafluorophosphate), 2.7 and 4.4

A solution of 2,6-bis(imdazol-1-yl)pyridine (**2.6** or **4.6**) (1.06 g, 4.79 mmol) in dry CH_3CN (130 mL) was added over a period of 20 hours to a refluxing solution of 1,4-bis(bromomethyl)benzene (13.2 g, 50.0 mmol) in dry CH_3CN (70 mL) under a nitrogen atmosphere. The resulting mixture was continuously heated under reflux for another 12 hours, and the crude product was formed as a white suspension. After allowing to cool to ambient temperature, the suspension was filtered off, washed with $CHCl_3$ (2 × 100 mL), and then dissolved in water (200 mL). A saturated aqueous solution of NH_4PF_6 was

added to the aqueous solution until no further precipitation was observed. The precipitate was filtered off, washed with water (3 × 100 mL), and dried to give a white solid **7**·2PF_6 (3.04 g, 70%): mp 190–192 ºC; ^{1}H NMR (CD_3CN, 400 MHz): δ 9.56 (s, 2H), 8.42 (t, 1H, *J* = 8 Hz), 8.22 (s, 2H), 7.90 (d, 2H, *J* = 8 Hz), 7.64 (s, 2H), 7.54 (d, 4H, *J* = 8 Hz), 7.46 (d, 4H, *J* = 8 Hz), 5.48 (s, 4H), 4.61 (s, 4H). ^{13}C NMR (CD_3CN, 100 MHz): δ 146.8, 146.2, 141.0, 136.4, 134.6, 131.2, 130.5, 125.0, 121.4, 118.7, 116.3, 54.5, 34.0; HRMS (ESI) calcd for $[M + Na]^+$: 889.9653; found: 889.9654.

Synthesis of (3-methyloxetan-3-yl)methyl 2,6-dibromoisonicotinate, 2.9 and 3.5

To a solution of 2,6-dibromoisonicotinic acid (**2.8** or **3.6**) (5.62 g, 20.0 mmol), Cs_2CO_3 (3.91 g, 12.0 mmol), and NaI (0.60 g, 4.0 mmol) in dry CH_3CN (160 mL) was added oxetane tosylate (5.38 g, 21.0 mmol). The reaction mixture was brought to reflux under a nitrogen atmosphere and held there for 48 hours before being allowed to cooled to room temperature. The suspension was filtered off and the filtrate was evaporated to dryness. The crude product was purified with flash column chromatography on silica gel (20:1 CH_2Cl_2/Et_2O) to afford a white solid (**2.9** or **3.5**) (6.20 g, 85%): mp 74–76 ºC; ^{1}H NMR ($CDCl_3$, 400 MHz): δ 7.97 (s, 2H), 4.57 (d, 2H, *J* = 6 Hz), 4.48 (d, 2H, *J* = 6 Hz), 4.46 (s, 2H), 1.42 (s, 3H); ^{13}C NMR ($CDCl_3$, 100 MHz): δ 162.7, 141.8, 141.4, 126.8, 79.5, 70.8, 39.4, 21.3; HRMS (CI) calcd for $[M+H]^+$: 363.9178; found: 363.9179.

Synthesis of 2,6-dibromo-4-(4-methyl-2,6,7-trioxabicyclo[2.2.2]octan-1-yl)pyridine, 2.10 and 3.4

3-Methyloxetan-3-yl)methyl 2,6-dibromoisonicotinate (**2.9** or **3.5**) (4.60 g, 12.6 mmol) was dissolved in dry CH_2Cl_2 (55 mL) and cooled to *ca.* 0 ºC in an ice bath. A solution of BF_3·Et_2O (0.22 mL, 1.8 mmol) in dry CH_2Cl_2 (5 mL) was then dropwise added over a period of 5 minutes. The mixture was stirred for 12 hours under a nitrogen atmosphere and allowed to reach room temperature. After the reaction was deemed

complete, triethylamine (~1 mL) was added to the solution, which was then evaporated to dryness. The residue was subject to chromatography over silica gel using CH_2Cl_2/hexanes (20:1 v/v) as the eluent to give a white solid (3.96 g, 86%): mp 268–270 ºC; ^{1}H NMR ($CDCl_3$, 400 MHz): δ 7.66 (s, 2H), 4.06 (s, 6H), 0.90 (s, 3H); ^{13}C NMR ($CDCl_3$, 100 MHz): δ 150.1, 140.8, 124.8, 105.6, 73.6, 31.0, 14.5; HRMS (ESI) calcd for $[M+H]^+$: 363.9178; found: 363.9176.

Synthesis of 2,6-di(1H-imidazol-1-yl)-4-(4-methyl-2,6,7-trioxabicyclo[2.2.2]octan-1-yl)pyridine, 2.11 and 3.3

In a 50 mL Schlenk flask charged with a stir bar, (**2.10** or **3.4**) (3.65 g, 10.0 mmol), imidazole (1.70 g, 25.0 mmol), copper(I) iodide (0.10 g, 0.53 mmol), salicylaldoxime (0.27 g, 2.0 mmol), and cesium carbonate (9.78 g, 30.0 mmol) were dissolved in dry CH_3CN (15 mL). The reaction mixture was degassed through three cycles of a freeze-pump-thaw procedure and was later heated at 85 °C under a nitrogen atmosphere with the latter temperature maintained for 48 hours. The resulting suspension was filtered off and the residue on the funnel was rinsed with CH_2Cl_2 (2 × 100 mL). The filtrate was first washed with 1 M aqueous solution of Na_4EDTA (60 mL) and then with water (3 × 50 mL), and the organic phase was dried over Na_2SO_4. The crude product was subject to column chromatography over silica gel (20:1 CH_2Cl_2/CH_3OH, eluent) to yield 2,6-di(1H-imidazol-1-yl)-4-(4-methyl-2,6,7-trioxabicyclo[2.2.2]octan-1-yl)pyridine (**2.11** or **3.3**) (2.7 g , 80%) as a white solid: mp 268–270 ºC; ^{1}H NMR (CD_3CN, 400 MHz): δ 8.46 (s, 2H), 7.85 (s, 2H), 7.59 (s, 2H), 7.13 (s, 2H), 4.12 (s, 6H), 0.89 (s, 3H); ^{13}C NMR ($CDCl_3$, 100 MHz): δ 152.4, 148.6, 135.3, 131.2, 116.5, 107.4, 106.2, 73.7, 31.0, 14.5; HRMS (ESI) calcd for $[M+H]^+$: 340.1404; found: 340.1405.

Synthesis of monocarboxylic acid-functionalized Texas-sized molecular box (TxSB-$CO_2H \cdot 4PF_6$)

A solution of diimidazolyl orthoester (**2.11** or **3.3**) (0.679 g, 2.00 mmol) in dry CH_3CN (300 mL) was added to a solution of dibromide (**2.7** or **4.4**) (1.74 g, 2.00 mmol) and tetrabutylammonium iodide (0.148 g, 0.400 mmol) at reflux in dry CH_3CN (700 mL) over a period of 6 hours. Heating under reflux was maintained for another 3 days. After allowing to cool to ambient temperature, the mixture was placed in an ice bath, and concentrated HCl (~30 mL) was then added to stop the reaction and precipitate an orange, the presumed intermediate from the CH_3CN solution. This orange solid was filtered off and washed with acetone and CH_2Cl_2 to remove the residual tetrabutylammonium salt. The solid collected in this way was dissolved in a 6 N HCl solution (25 mL) and then heated at 60 ºC for 24 hours. After the completion of what was presumed to be an acid hydrolysis reaction, NH_4PF_6 (16.3 g, 100 mmol) was added to precipitate the crude product from the aqueous solution as a light orange solid. This solid was filtered off and purified via flash column chromatography over silica gel (loaded with CH_3CN; packed and eluted with 7:2:1 CH_3OH/2M-NH_4Cl/CH_3NO_2). The fractions containing the product were concentrated by evaporating CH_3OH and CH_3NO_2 to give an aqueous solution of **TxSB-CO_2H**·4Cl, and saturated aqueous NH_4PF_6 solution was added until no further precipitation was observed. The precipitate was filtered off, washed with water (3 × 50 mL), and dried to yield **TxSB-CO_2H**·$4PF_6$ as a light orange solid (1.26 g, 50%): mp > 250 ºC (decomp); ^{1}H NMR (DMSO-d_6) δ 10.55 (s, 2H), 10.44 (s, 2H), 8.82 (s, 2H), 8.67 (s, 2H), 8.56 (t, ^{1}H, J = 8 Hz), 8.54 (s, 2H), 8.19 (s, 2H), 8.14 (d, 2H, J = 8 Hz), 7.55 (s, 8 H), 5.57 (s, 8H); ^{13}C NMR (DMSO-d_6) δ164.1, 158.8, 158.5, 146.8, 146.1, 145.3, 145.0, 136.2, 135.7, 135.6, 129.0, 129.0, 124.1, 120.4, 120.2, 114.8, 114.3, 52.5, 52.4; HRMS (ESI) calcd for $[M\text{-}4PF_6\text{-}2H]^{2+}$: 336.1349; found: 336.1360.

Synthesis of dicarboxylic acid-functionalized Texas-sized molecular box, 3.2

A solution of diimidazolyl orthoester (**2.11** or **3.3**) (1.70 g, 5.0 mmol) in dry CH_3CN (500 mL) was added to a solution of 1,4-bis(bromomethyl)benzene (1.32 g, 5.0 mmol) in dry CH_3CN (750 mL) at reflux under a nitrogen atmosphere over a period of 6 hours. Heating under reflux was maintained for another 3 days. After allowing to cool to ambient temperature, the mixture was placed in an ice bath, and concentrated HCl (~30 mL) was then added to stop the reaction and to precipitate the white intermediate from the CH_3CN solution. The white solid obtained in this way was filtered off and washed with acetone and CH_2Cl_2. After washing in this way, the solid was dissolved in water and subject to anion-exchange using excess NH_4PF_6. This give the PF_6 salt of **TxSB-diorthoester** in crude form as a white precipitate. This crude intermediate was purified via column chromatography over silica gel (loaded with CH_3CN; packed and eluted with 7:2:1 CH_3OH/2M-NH_4Cl/CH_3NO_2). The collected fractions containing the pure intermediate were concentrated by removing most of the volatiles (presumed to be CH_3OH and CH_3NO_2) to give an aqueous solution of **TxSB-diorthoester·4Cl**. This residue was dissolved in 6 N aqueous HCl aqueous (30 mL) and then heated to and held at 60 ºC for 24 hours. Over the course of the hydrolysis reaction, the product began to precipitate. After cooling to room temperature, the precipitate was filtered off, washed with acetone and diethyl ether, and dried in vacuo to yield **TxSB-(CO2H)2·4Cl** (**3.2**) as a white solid (0.40 g, 10%): mp > 260 ºC (decomp); 1H NMR (D_2O, 400 MHz, 298 K) δ 9.81 (s, 4H), 8.30 (s, 4H, J = 1.7 Hz), 8.25 (s, 4H), 7.81 (s, 4H), 7.50 (s, 8H), 5.59 (s, 8H); 13C NMR (D_2O, 100 MHz, 363 K) δ 168.4, 153.4, 146.8, 135.2, 129.9, 125.0, 121.0, 115.3, 54.0; HRMS (ESI) calcd for $[M\text{-}4Cl\text{-}3H]^+$: 715.2524; found: 715.2511.

Synthesis of 2,6-dibromopyridin-4-yl)methanol, 4.9

To a solution of **4.10** (5.62 g, 20.0 mmol) in dry THF (110 mL) cooled in an ice bath, borane (1 M in THF, 55 mL) was slowly added. The ice bath was then removed, and the reaction mixture was stirred for 12 hours under a nitrogen atmosphere. After consumption of the limiting starting material, water was slowly added to the reaction mixture in an ice bath until gas evolution ceased. The solution was concentrated to ~50% of its original volume under reduced pressure. NaOH (3M, 75 mL) was added and the resulting mixture was heated under reflux for 1 hour. After removing the remaining THF, the solution was extracted with CH_2Cl_2 (3 × 30 mL). The combined organic layers were dried over $MgSO_4$ and evaporated to dryness. The crude product was purified via flash column chromatography over silica gel (3:1 CH_2Cl_2/hexanes, eluent) to afford a white solid (2.86 g, 91%): mp 106–108 ºC (lit.[2] 110–111 ºC); ^{1}H NMR (CD_3CN) δ 7.52 (s, 2H), 4.57 (d, 2H, J = 6 Hz), 3.55 (t, 2H, J = 6 Hz).

Synthesis of 2,6-dibromo-4-((methoxymethoxy)methyl)pyridine, 4.8

Bromomethyl methyl ether (1.87 g, 1.2 mL, 15.0 mmol) was slowly added to a solution of (2,6-dibromopyridin-4-yl)methanol **4.9** (2.67 g, 10.0 mmol) and *N*,*N*-diisopropylethylamine (1.94 g, 2.6 mL, 15.0 mmol) in dry CH_2Cl_2 (75 mL). The mixture was stirred for 24 hours at room temperature under a nitrogen atmosphere. Upon the completion of reaction, water (50 mL) was added. The layers were separated and the aqueous phase was extracted with CH_2Cl_2 (3 × 30 mL). After the combined organic layers were dried over $MgSO_4$ and the volatiles removed under reduced pressure, the residue was chromatographed over silica gel using a 1:1 mixture of CH_2Cl_2/hexanes as the eluent to give a colorless oil (2.57 g, 82%): ^{1}H NMR (CD_2Cl_2) δ 7.47 (s, 2H), 4.70 (s, 2H), 4.55 (s, 2H), 3.37 (s, 3H); ^{13}C NMR (CD_2Cl_2) δ 153.7, 140.9, 125.3, 96.7, 66.4. HRMS (ESI) calcd for $[M+H]^+$: 309.9073; found: 309.9075.

Synthesis of 2,6-di(1H-imidazol-1-yl)-4-((methoxymethoxy)methyl)pyridine, 4.5

In a 50 mL Schlenk flask charged with a stir bar, 2,6-dibromo-4-((methoxymethoxy)methyl)pyridine **4.8** (3.11 g, 10.0 mmol), imidazole (1.70 g, 25.0 mmol), copper(I) iodide (0.10 g, 0.53 mmol), salicylaldoxime (0.274 g, 2.0 mmol), and cesium carbonate (9.78 g, 30.0 mmol) were dissolved in dry CH_3CN (15 mL). The reaction mixture was degassed through three freeze-pump-thaw cycles and then later heated at 85 °C under a nitrogen atmosphere for 48 hours. The resulting suspension was filtered off and the residue on the funnel was rinsed with CH_2Cl_2 (2 × 100 mL). The filtrate was first washed with 1 M aqueous solution of Na_4EDTA (60 mL) and then with water (3 × 50 mL), and the organic phase was dried over Na_2SO_4. The crude product was chromatographed over silica gel (20:1 CH_2Cl_2/CH_3OH, eluent) to yield 2,6-di(1H-imidazol-1-yl)-4-((methoxymethoxy)methyl)pyridine **4.5** (2.26 g, 79%) as a yellowish-white solid: mp 108-110 ºC; ^{1}H NMR (CD_2Cl_2) δ 8.38 (d, 2H, J = 0.8 Hz), 7.71 (t, 2H, J = 1.2 Hz), 7.30 (t, 2H, J = 0.8 Hz), 7.18 ((t, 2H, J = 1.2 Hz), 4.79 (s, 2H), 4.74 (s, 2H), 3.42 (s, 3H); ^{13}C NMR (CD_2Cl_2) δ 155.4, 148.82, 135.4, 131.1, 116.6, 107.8, 96.8, 67.4,; HRMS (ESI) calcd for $[M+H]^+$: 286.1299. Found: 286.1299.

Synthesis of hydroxymethyl-functionalized Texas-sized molecular box, 4.3

A solution of **4.5** (0.571 g, 2.0 mmol) in dry CH_3CN (300 mL) was added to a solution of **4.4** (1.74 g, 2.0 mmol) and tetrabutylammonium iodide (0.148 g, 0.4 mmol) in dry CH_3CN (700 mL) at reflux under a nitrogen atmosphere over a period of 6 hours. Heating under reflux was maintained for another 3 days. After allowing to cool to ambient temperature, the mixture was placed in an ice bath, and concentrated HCl (~30 mL) was added to stop the reaction to induce precipitation. The orange solid obtained in this wasy was filtered off and washed with acetone and CH_2Cl_2 to remove the residual tetrabutylammonium salt. The residue was dissolved in water (60 mL) and NH_4PF_6 (16.3

g, 100 mmol) was added to precipitate the crude product from the aqueous solution as a white solid. The crude product was filtered off and purified via flash column chromatography over silica gel (loaded with CH_3CN; packed and eluted with 7:2:1 CH_3OH/2M-NH_4Cl/CH_3NO_2). The fractions containing the product were concentrated by removing CH_3OH and CH_3NO_2 under reduced pressure to give an aqueous solution. Saturated aqueous NH_4PF_6 solution was then added until no further precipitation was observed. The precipitate was filtered off, washed with water (3 × 50 mL), and dried in vacuum to yield **4.3** as a light orange solid (1.69 g, 68%): mp > 250 °C (decomp); ^{1}H NMR (CD_3CN) δ 9.63 (s, 4H), 8.42 (t, 1H, J = 8 Hz), 8.14 (dd, 4H, $J_1 = J_2$ = 2 Hz), 7.93-7.90 (m, 4H), 7.72 (dd, 4H, $J_1 = J_2$ = 2 Hz), 7.48 (s, 8H), 5.52 (d, 8H, J = 2.4 Hz), 4.87 (d, 2H, J = 5.6 Hz), 3.92 (t, 1H, J = 5.6 Hz); ^{13}C NMR (CD_3CN) δ163.2, 146.3, 145.9, 135.7, 129.9, 125.3, 125.2, 121.1, 121.0, 116.1, 112.9, 62.5, 54.0; HRMS (ESI) calcd for $[M+Na]^+$: 1263.1533; found: 1263.1519.

Synthesis of methacrylate-appended Texas-sized molecular box, 4.2

The hydroxymethyl functionalized macrocycle **3** (1.24 g, 1.0 mmol), $NaPF_6$ (3.36 g, 20.0 mmol), and *N*,*N*-diisopropylethylamine (0.646 g, 0.87 mL, 5.0 mmol) were dissolved in dry CH_3CN (40 mL) under a nitrogen atmosphere. After cooling this mixture in an ice bath, a solution of methacryloyl chloride (5.22 g, 4.9 mL, 5.0 mmol) in CH_3CN (10 mL) was slowly added to over a period of 5 minutes. A precipitate formed during this time. The resulting suspension was allowed to stir at room temperature for 24 hours. CH_3OH (30 mL) was added to quench the reaction and to dissolve the precipitate that had formed during the course of the reaction. The solution was then concentrated under reduced pressure and purified via flash column chromatography over silica gel (loaded with CH_3CN; packed and eluted with 7:2:1 CH_3OH/2M-NH_4Cl/CH_3NO_2). The fractions containing the product were concentrated by evaporating off most of the volatiles (*e.g.*,

CH_3OH and CH_3NO_2) to give an aqueous solution, to which a saturated aqueous NH_4PF_6 solution was added until no further precipitation was observed. The precipitate obtained in this way was filtered off, washed with water (2 × 50 mL), and dried to yield **2** as an orange solid (0.62 g, 47%): mp 158-160 ºC (decomp); ^{1}H NMR (CD_3CN, 400 MHz): δ 9.50 (s, 4H), 8.43 (t, 1H, J = 8 Hz), 8.14-8.13 (m, 4H),7.93-7.89 (m, 4H), 7.72 (m, 4H, J_1 = J_2 = 2 Hz), 7.47 (s, 8H), 6.27 (s, 1H), 5.79 (t, 1H, J = 0.8 Hz), 5.52 (s, 8H), 5.42 (s, 2H); ^{13}C NMR (CD_3CN, 100 MHz): δ 167.3, 156.9, 146.5, 146.3, 145.9, 136.6, 135.8, 135.7, 129.9, 127.6, 125.3, 125.2, 121.1, 121.0, 116.0, 113.9, 64.4, 54.0; HRMS (ESI) calcd for $[M\text{-}PF_6]^+$:1163.2256; found: 1163.2257.

Synthesis of water-soluble methacrylate-appended Texas-sized molecular box, 4.1

Excess tetrabutylammonium chloride (TBACl) was added to a solution of **4.2** (0.262 g, 0.200 mM) in CH_3CN. This led to formation of a precipitate, which was collected by filtration and washed by CH_3CN to afford **1** (0.172 g, 0.198 mM, 99%) as a white solid: mp 163-165 ºC; ^{1}H NMR (D_2O) δ 9.85 (s, 4H), 8.42 (t, 1H, J = 8 Hz), 8.30-8.25 (m, 4H), 8.05-7.95 (m, 4H), 7.92-7.80 (m, 4H, J_1 = J_2 = 2 Hz), 7.51 (s, 8H), 6.28 (s, 1H), 5.82 (s, 1H), 5.61 (s, 8H), 5.48 (s, 2H), 2.04 (s, 3H), 1.97 (t, 2H, J = 8 Hz); ^{13}C NMR (D_2O) δ 168.72, 155.12, 145.75, 145.43, 144.78, 135.15, 134.59, 134.34, 134.28, 129.21, 129.11, 129.03, 129.02, 127.87, 124.03, 123.98, 119.81, 119.69, 114.90, 112.98, 64.17, 53.06, 17.24.

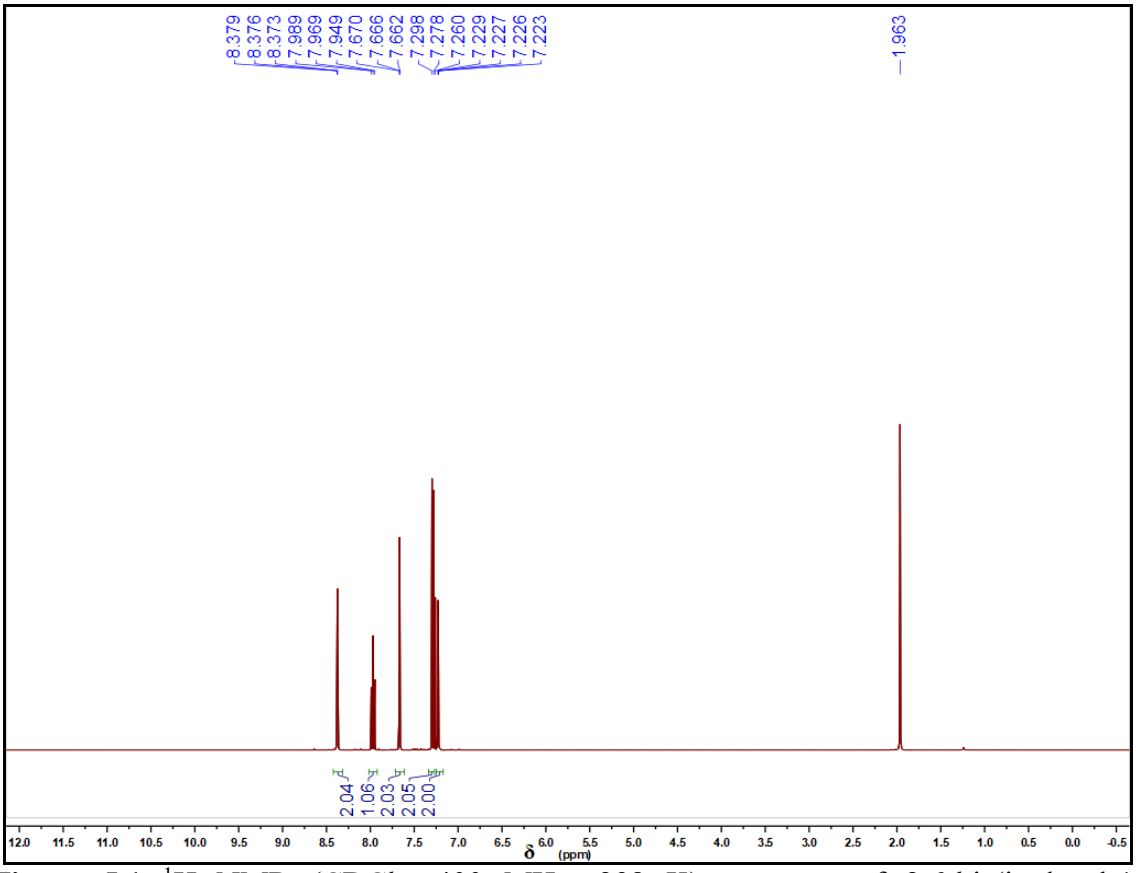

Figure 5.1 ^{1}H NMR ($CDCl_3$, 400 MHz, 298 K) spectrum of 2,6-bis(imdazol-1-yl)pyridine (**2.6** and **4.6**).

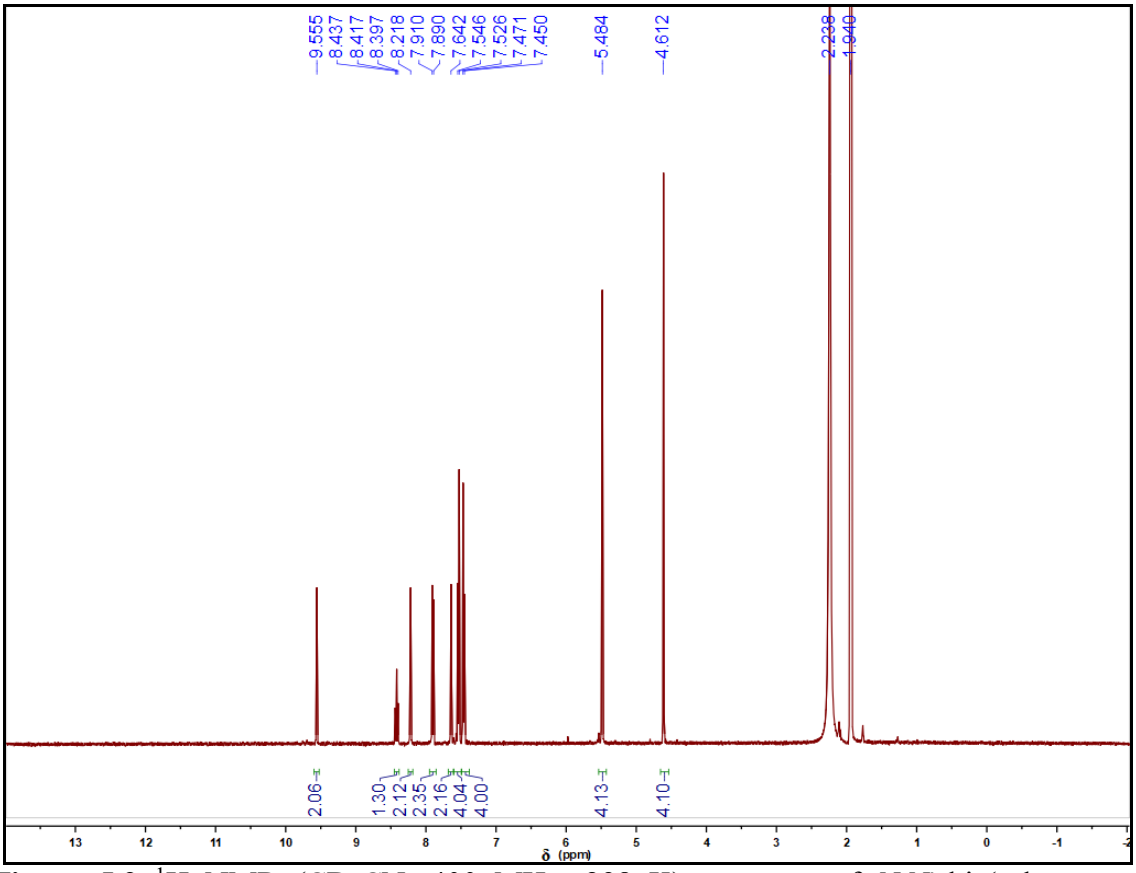

Figure 5.2 ^{1}H NMR (CD_3CN, 400 MHz, 298 K) spectrum of *N*,*N*'-bis(*α*-bromo-*p*-xylene)-2,6-bis(imadzol-1-yl)pyridine bis(hexafluorophosphate) (**2.7** and **4.4**).

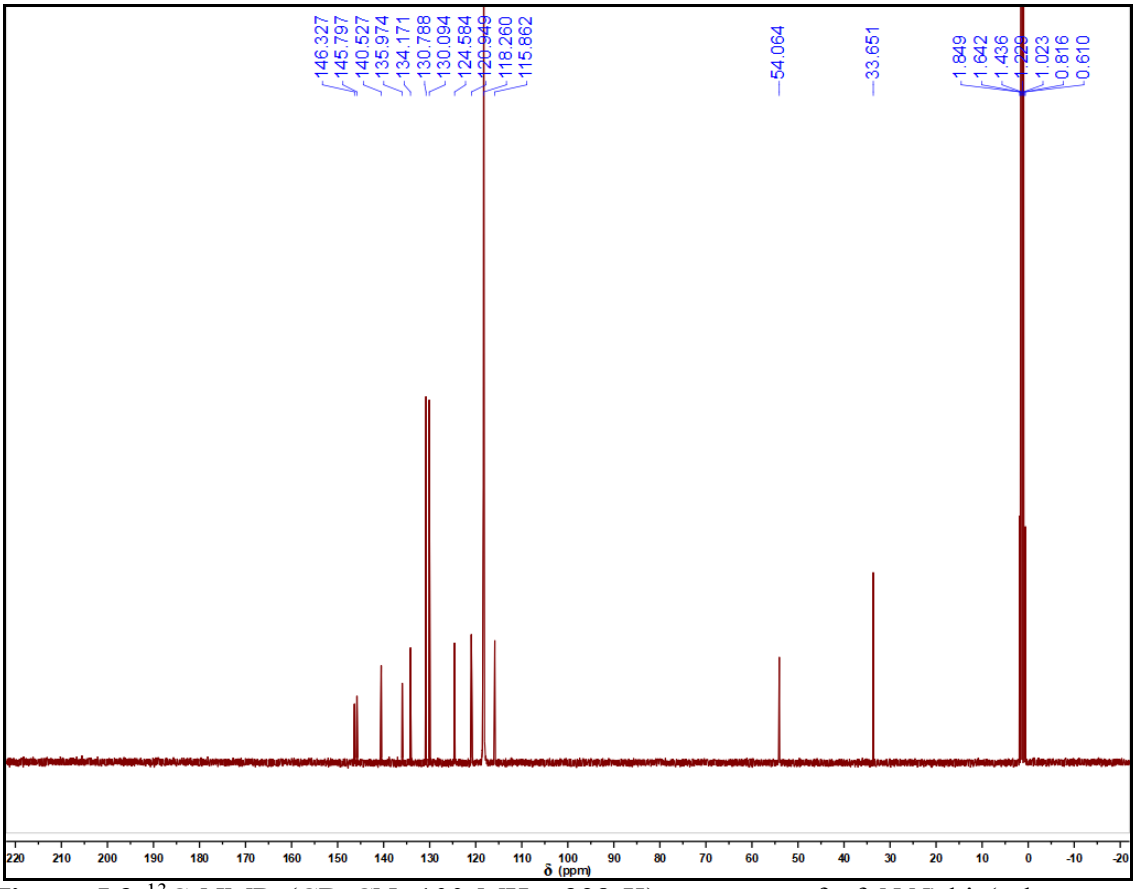

Figure 5.3 ^{13}C NMR (CD_3CN, 100 MHz, 298 K) spectrum of of *N*,*N*'-bis(*α*-bromo-*p*-xylene)-2,6-bis(imadzol-1-yl)pyridine bis(hexafluorophosphate) (**2.7** and **4.4**).

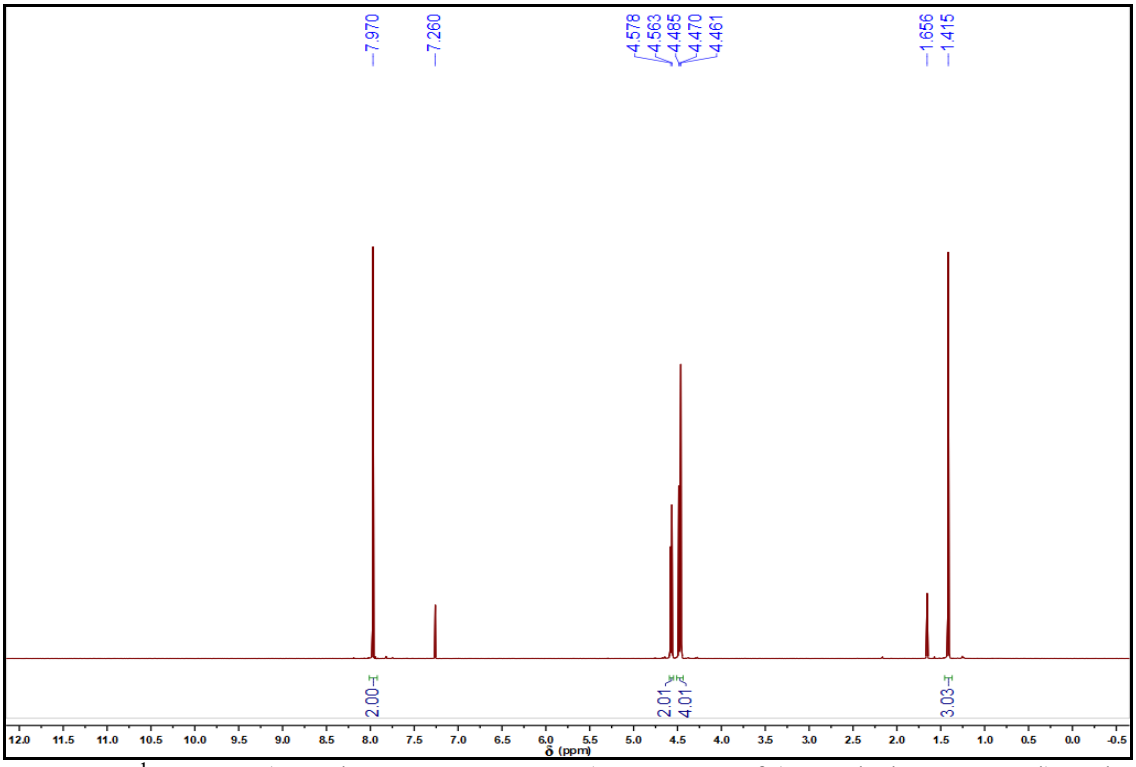

Figure 5.4 ^{1}H NMR ($CDCl_3$, 400 MHz, 298 K) spectrum of (3-methyloxetan-3-yl)methyl 2,6-dibromoisonicotinate (**2.9** and **3.5**).

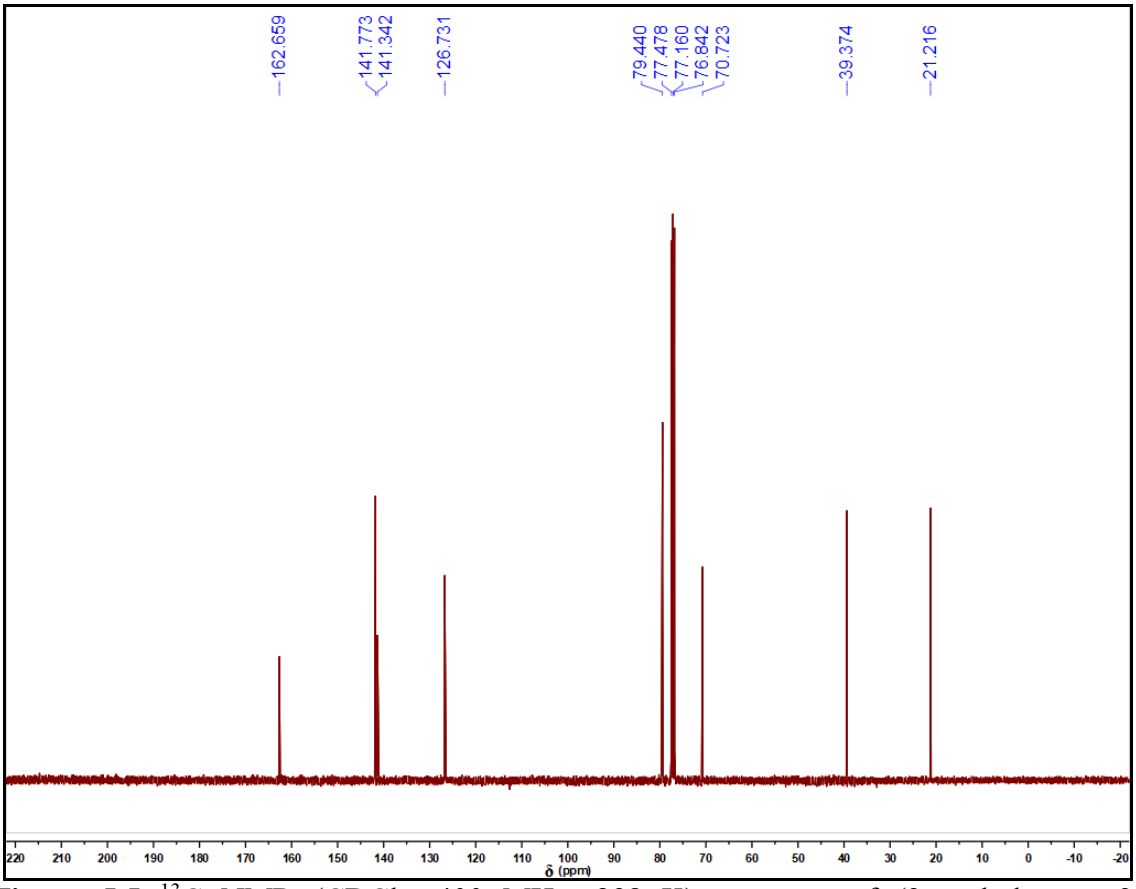

Figure 5.5 ^{13}C NMR ($CDCl_3$, 400 MHz, 298 K) spectrum of (3-methyloxetan-3-yl)methyl 2,6-dibromoisonicotinate (**2.9** and **3.5**).

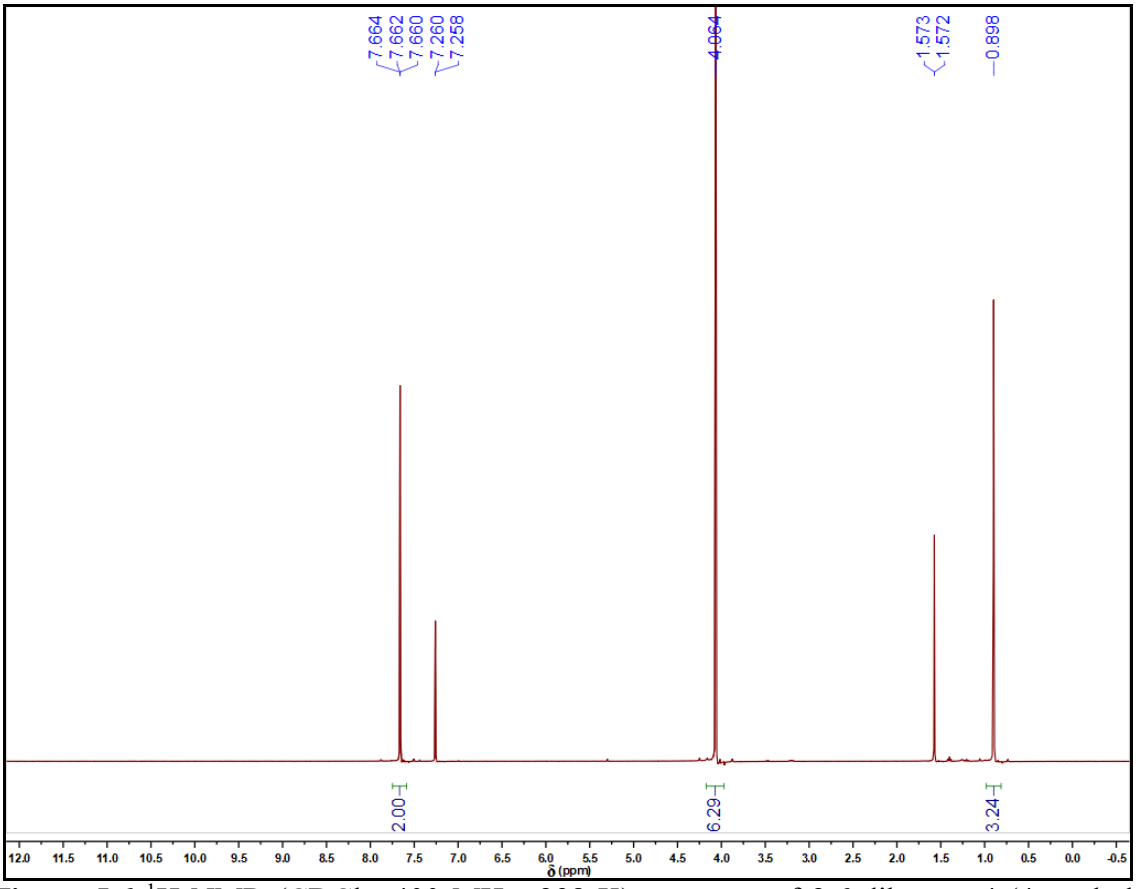

Figure 5.6 ^{1}H NMR ($CDCl_3$, 400 MHz, 298 K) spectrum of 2,6-dibromo-4-(4-methyl-2,6,7-trioxabicyclo[2.2.2]octan-1-yl)pyridine (**2.10** and **3.4**).

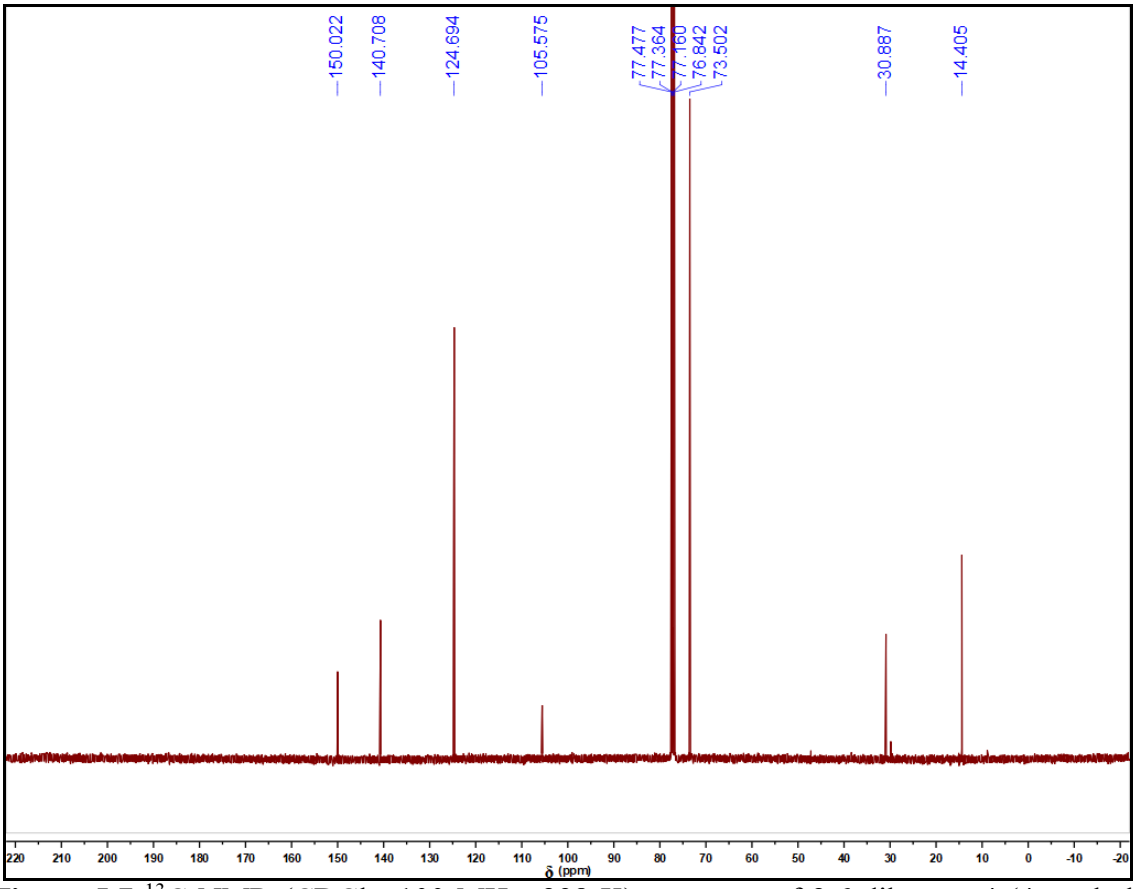

Figure 5.7 ^{13}C NMR ($CDCl_3$, 100 MHz, 298 K) spectrum of 2,6-dibromo-4-(4-methyl-2,6,7-trioxabicyclo[2.2.2]octan-1-yl)pyridine (**2.10** and **3.4**).

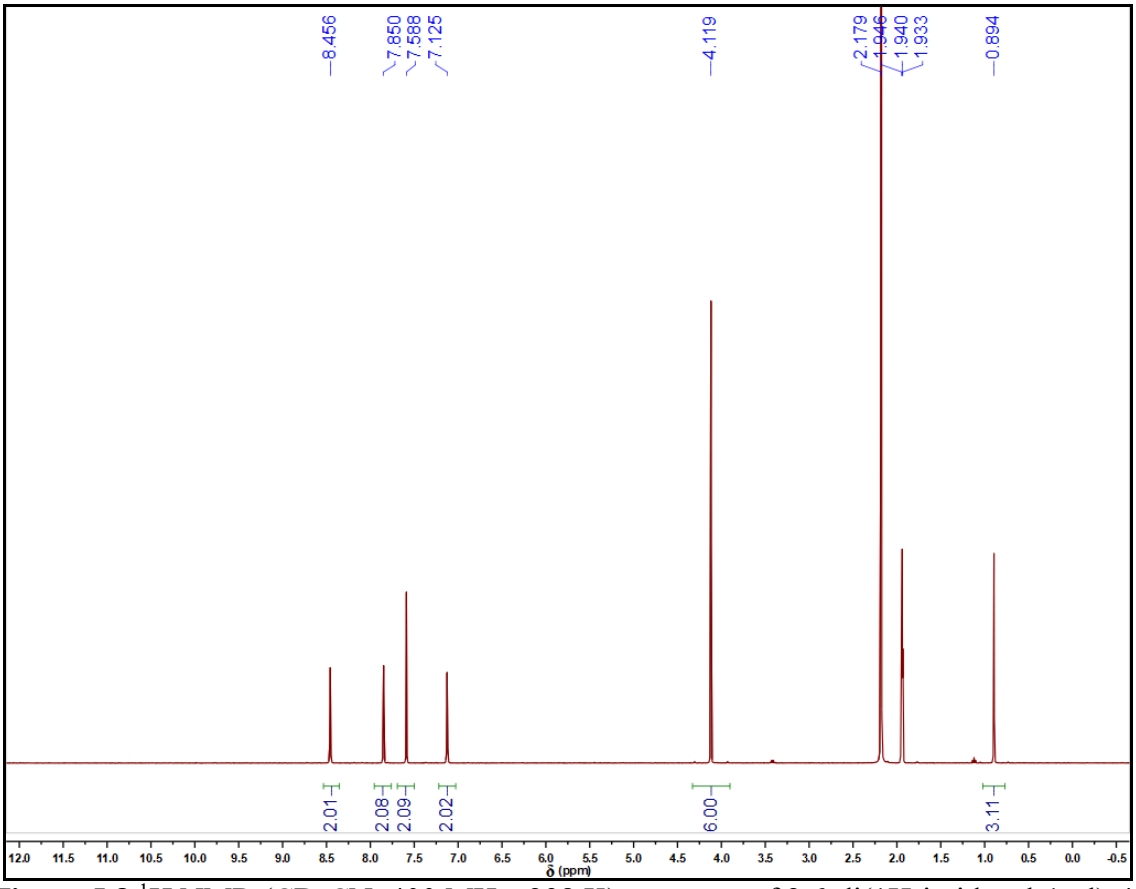

Figure 5.8 ^{1}H NMR (CD_3CN, 400 MHz, 298 K) spectrum of 2,6-di(1H-imidazol-1-yl)-4-(4-methyl-2,6,7-trioxabicyclo[2.2.2]octan-1-yl)pyridine (**2.11** and **3.3**).

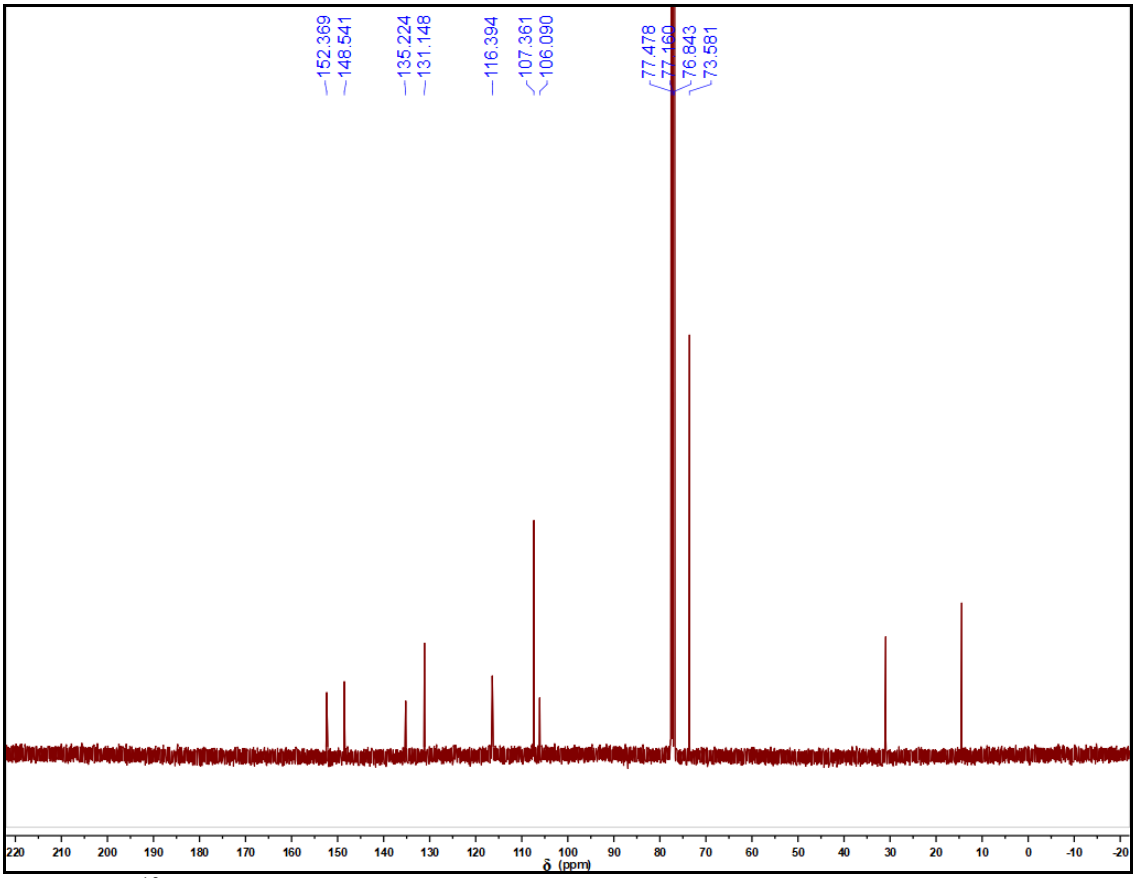

Figure 5.9 ^{13}C NMR ($CDCl_3$, 100 MHz, 298 K) spectrum of 2,6-di(1H-imidazol-1-yl)-4-(4-methyl-2,6,7-trioxabicyclo[2.2.2]octan-1-yl)pyridine (**2.11** and **3.3**).

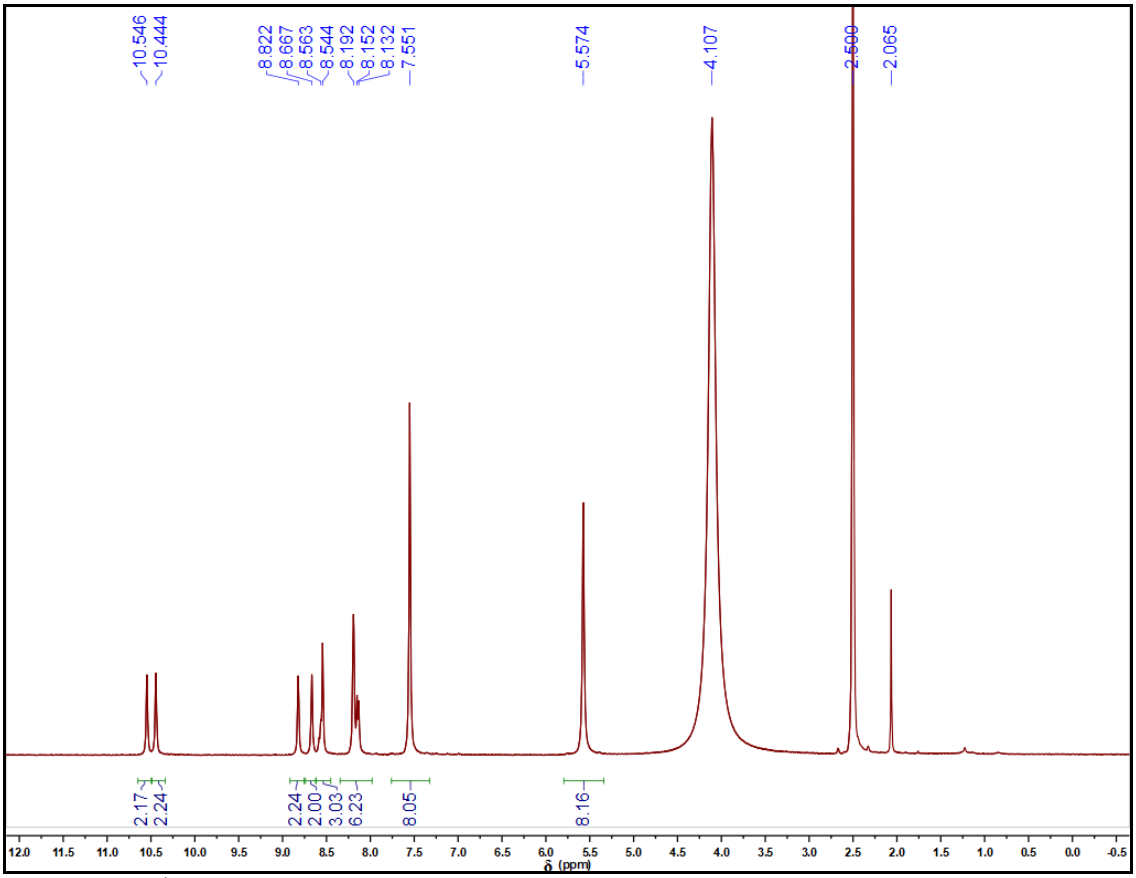

Figure 5.10 ^{1}H NMR (DMSO-d_6, 400 MHz, 298 K) spectrum of monocarboxylic acid-functionalized Texas-sized molecular box (**TxSB-CO$_2$H**·4PF$_6$).

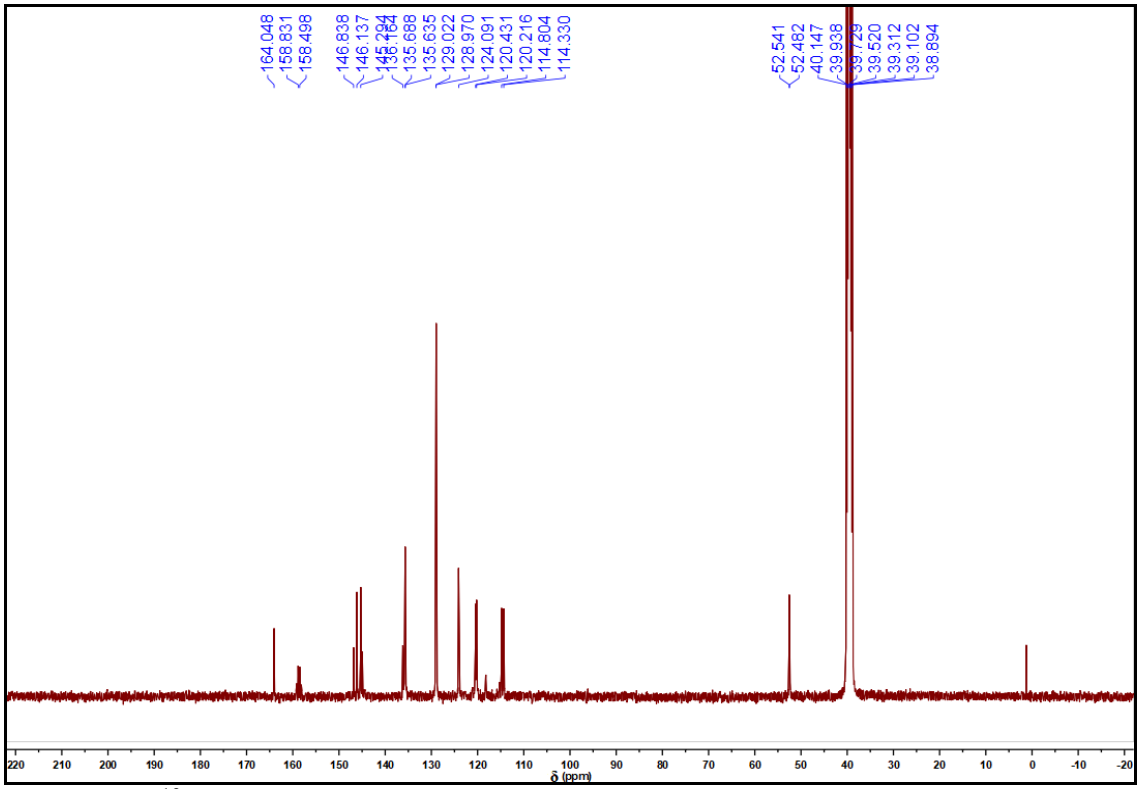

Figure 5.11 ^{13}C NMR (DMSO-d_6, 100 MHz, 298 K) spectrum of monocarboxylic acid-functionalized Texas-sized molecular box (**TxSB-CO$_2$H**·4PF$_6$).

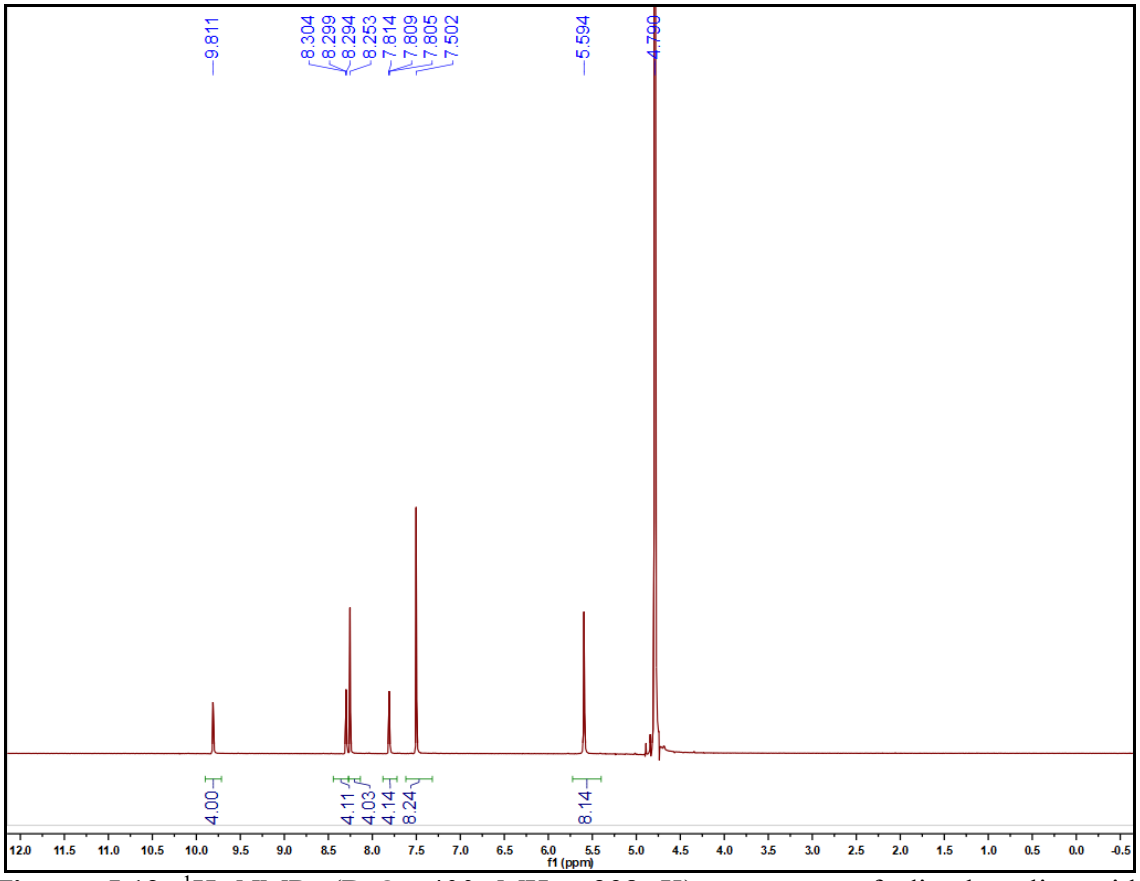

Figure 5.12 ^{1}H NMR (D_2O, 400 MHz, 298 K) spectrum of dicarboxylic acid-functionalized Texas-sized molecular box (**3.2**).

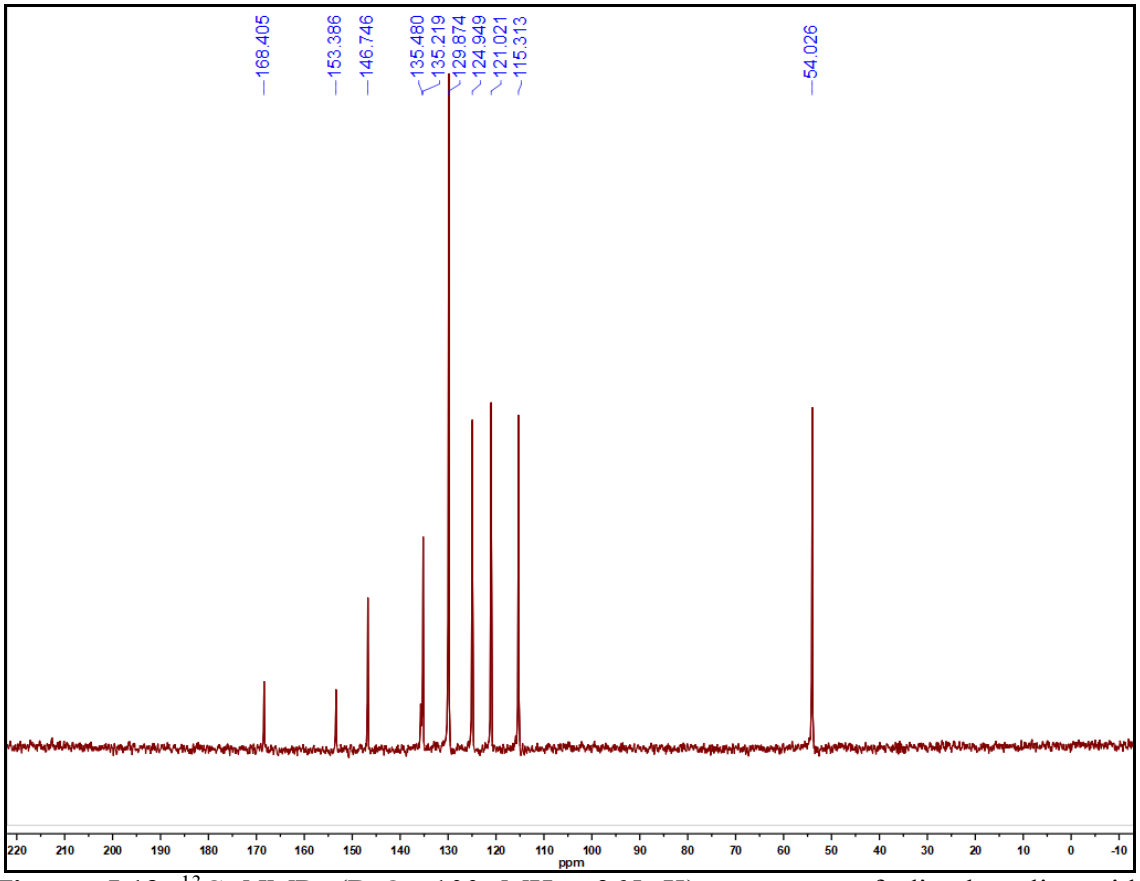

Figure 5.13 ^{13}C NMR (D_2O, 100 MHz, 365 K) spectrum of dicarboxylic acid-functionalized Texas-sized molecular box (**3.2**).

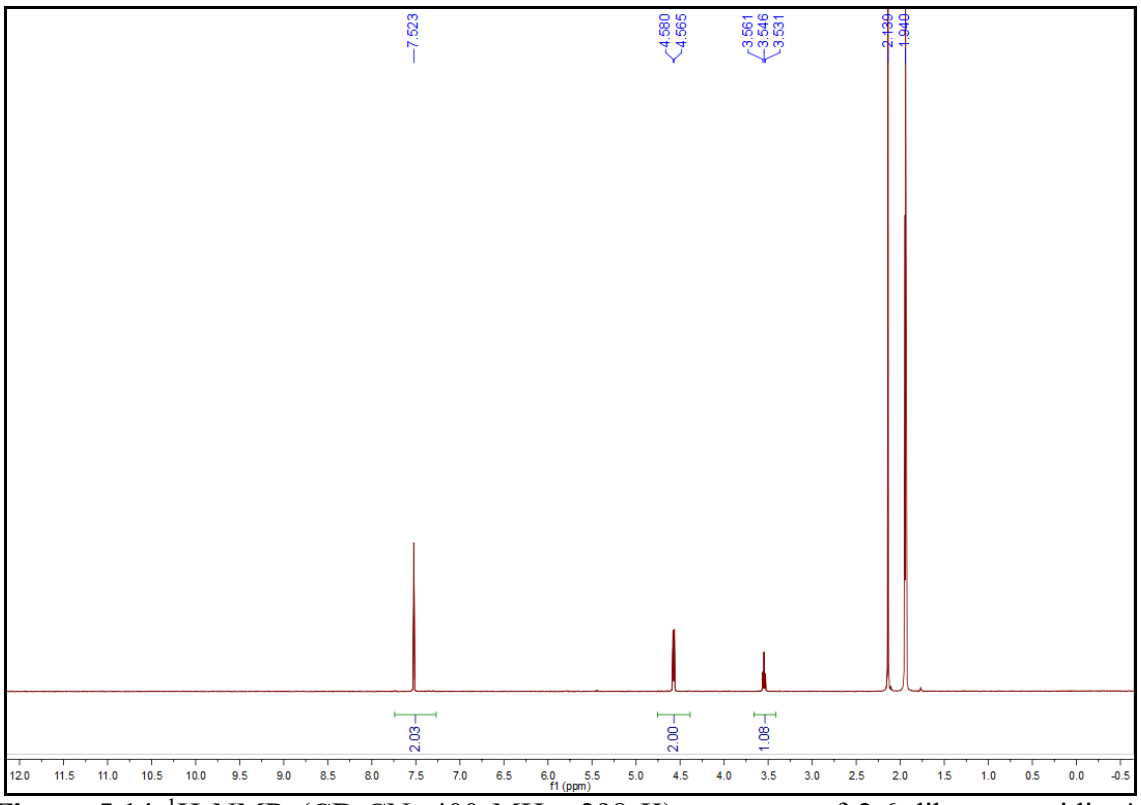

Figure 5.14 ^{1}H NMR (CD_3CN, 400 MHz, 298 K) spectrum of 2,6-dibromopyridin-4-yl)methanol **(4.9)**.

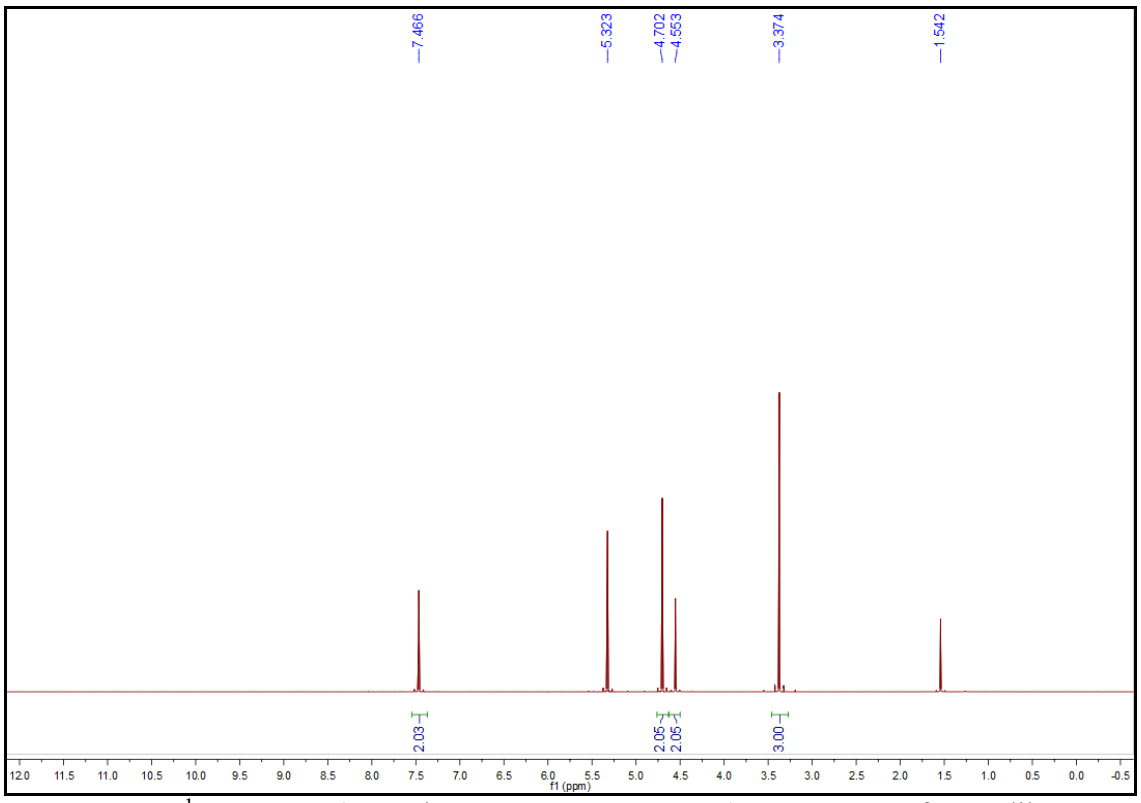

Figure 5.15 ^{1}H NMR (CD_2Cl_2, 400 MHz, 298 K) spectrum of 2,6-dibromo-4-((methoxymethoxy)methyl)pyridine (**4.8**).

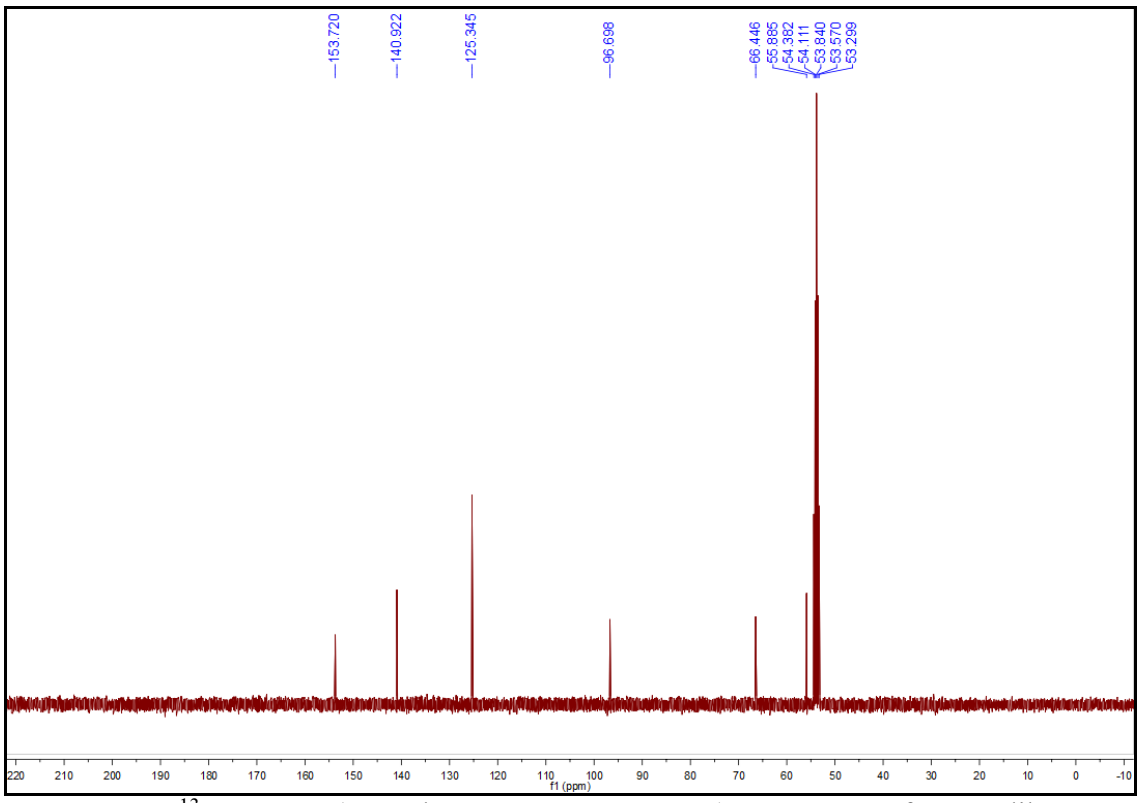

Figure 5.16 ^{13}C NMR (CD_2Cl_2, 100 MHz, 298 K) spectrum of 2,6-dibromo-4-((methoxymethoxy)methyl)pyridine (**4.8**).

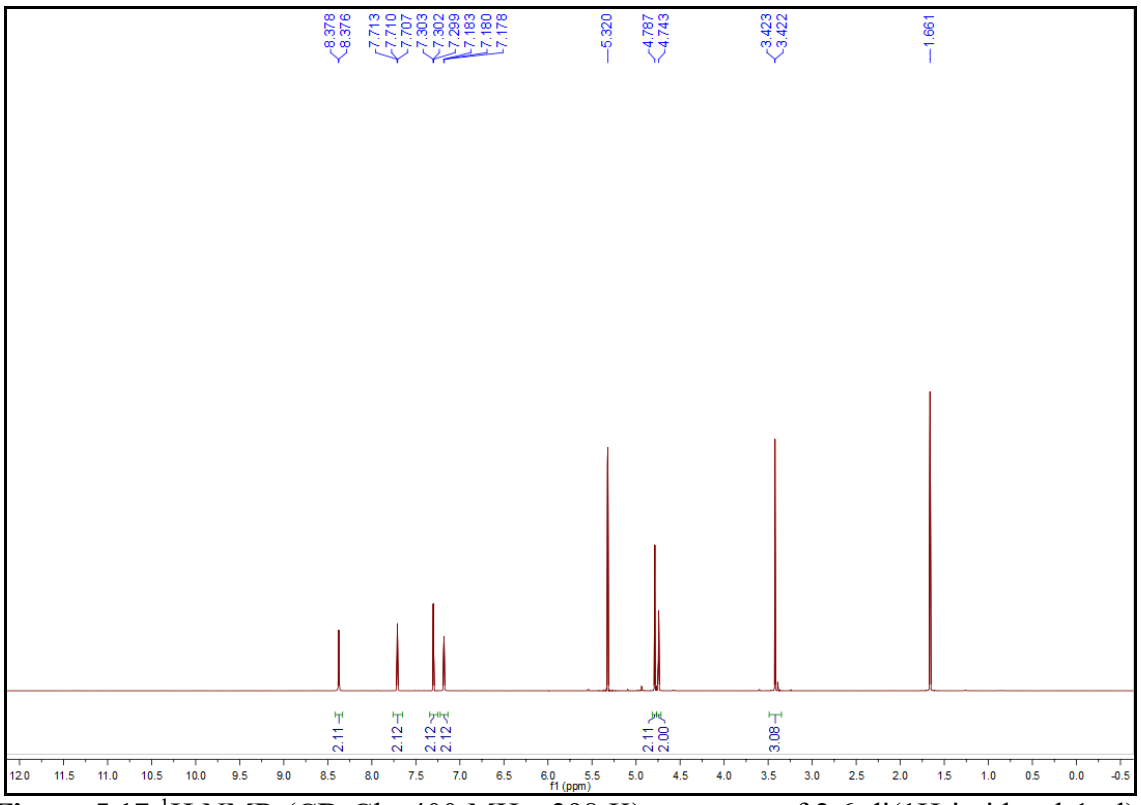

Figure 5.17 ^{1}H NMR (CD_2Cl_2, 400 MHz, 298 K) spectrum of 2,6-di(1H-imidazol-1-yl)-4-((methoxymethoxy)methyl)pyridin**e** (**4.5**).

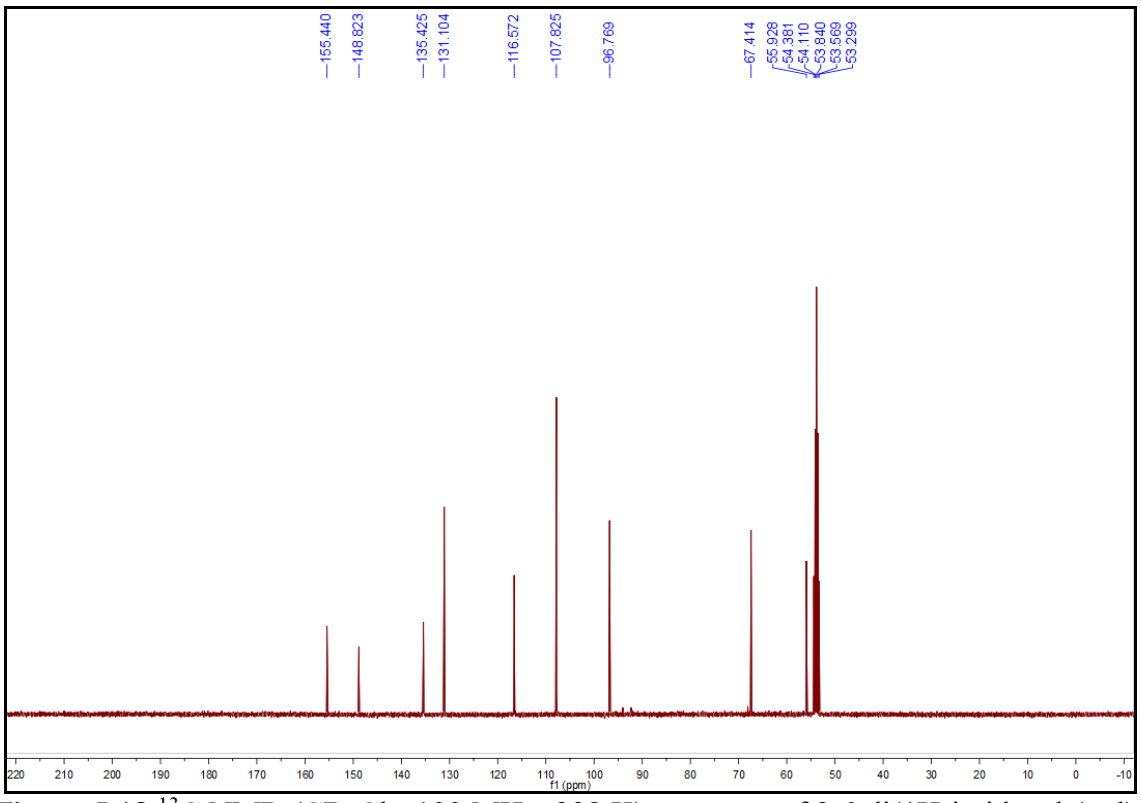

Figure 5.18 ^{13}C NMR (CD_2Cl_2, 100 MHz, 298 K) spectrum of 2,6-di(1H-imidazol-1-yl)-4-((methoxymethoxy)methyl)pyridine (**4.5**).

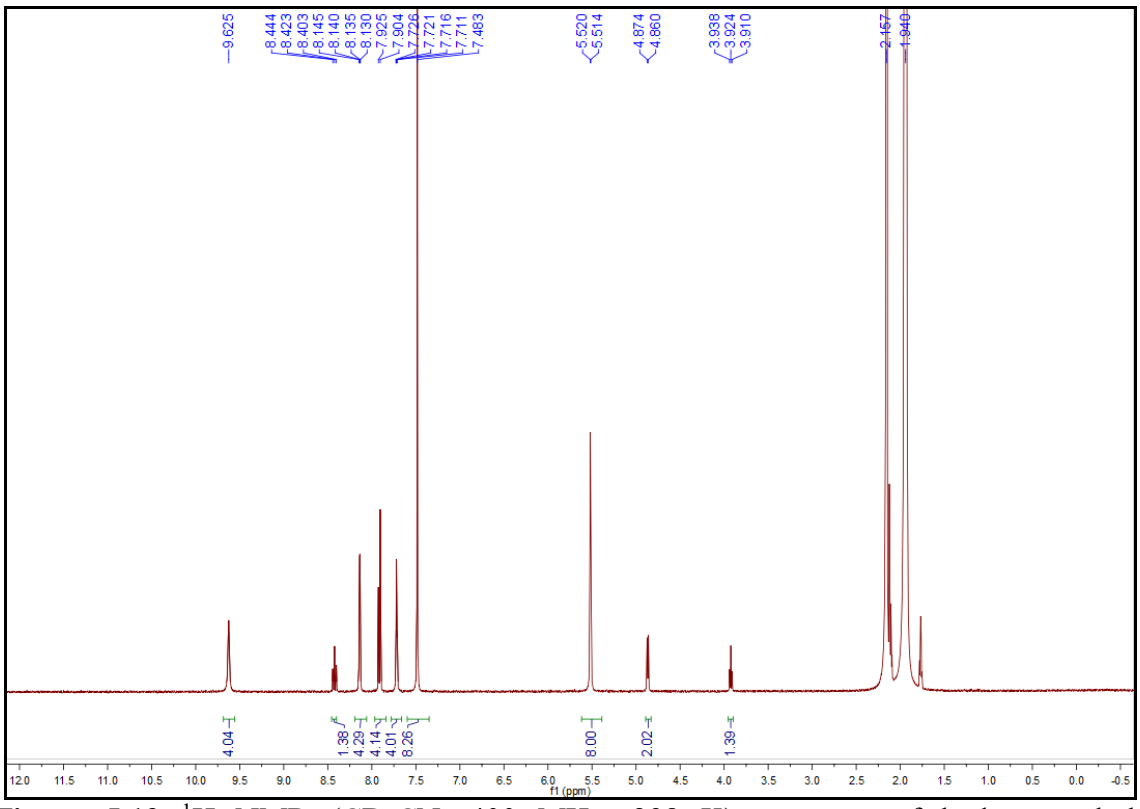

Figure 5.19 ^{1}H NMR (CD_3CN, 400 MHz, 298 K) spectrum of hydroxymethyl-functionalized Texas-sized molecular box (**4.3**).

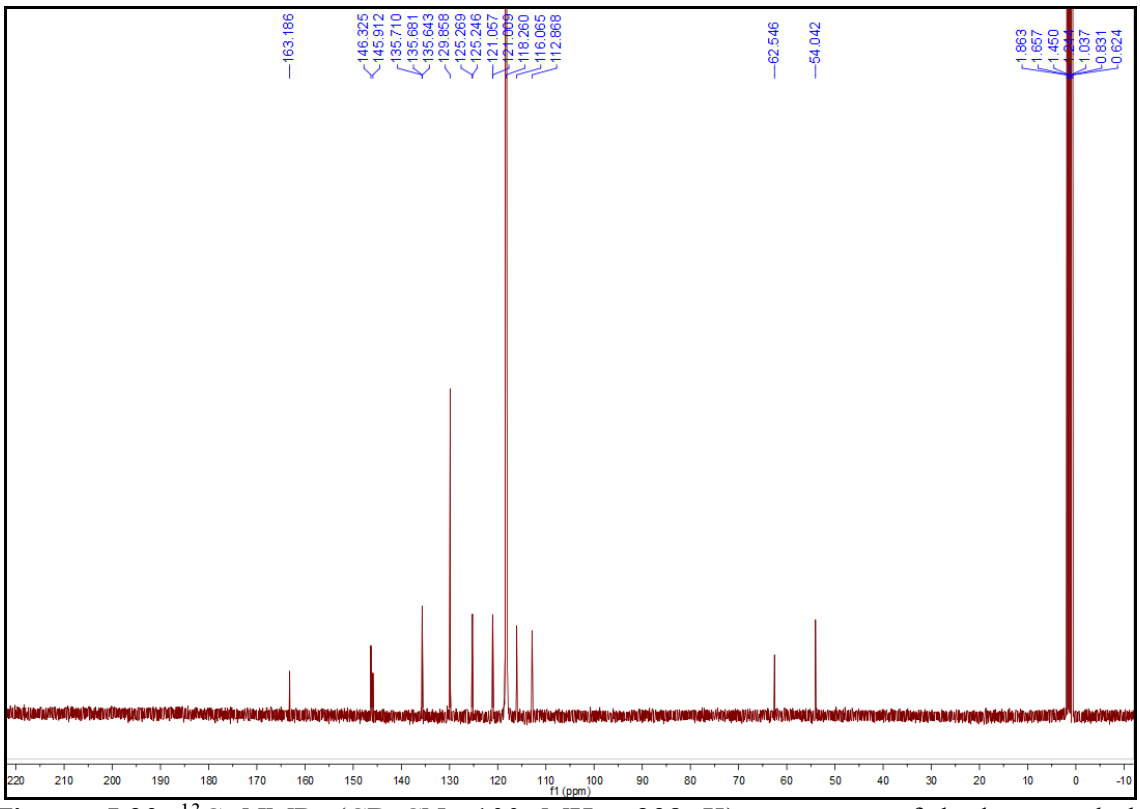

Figure 5.20 ^{13}C NMR (CD_3CN, 100 MHz, 298 K) spectrum of hydroxymethyl-functionalized Texas-sized molecular box (**4.3**).

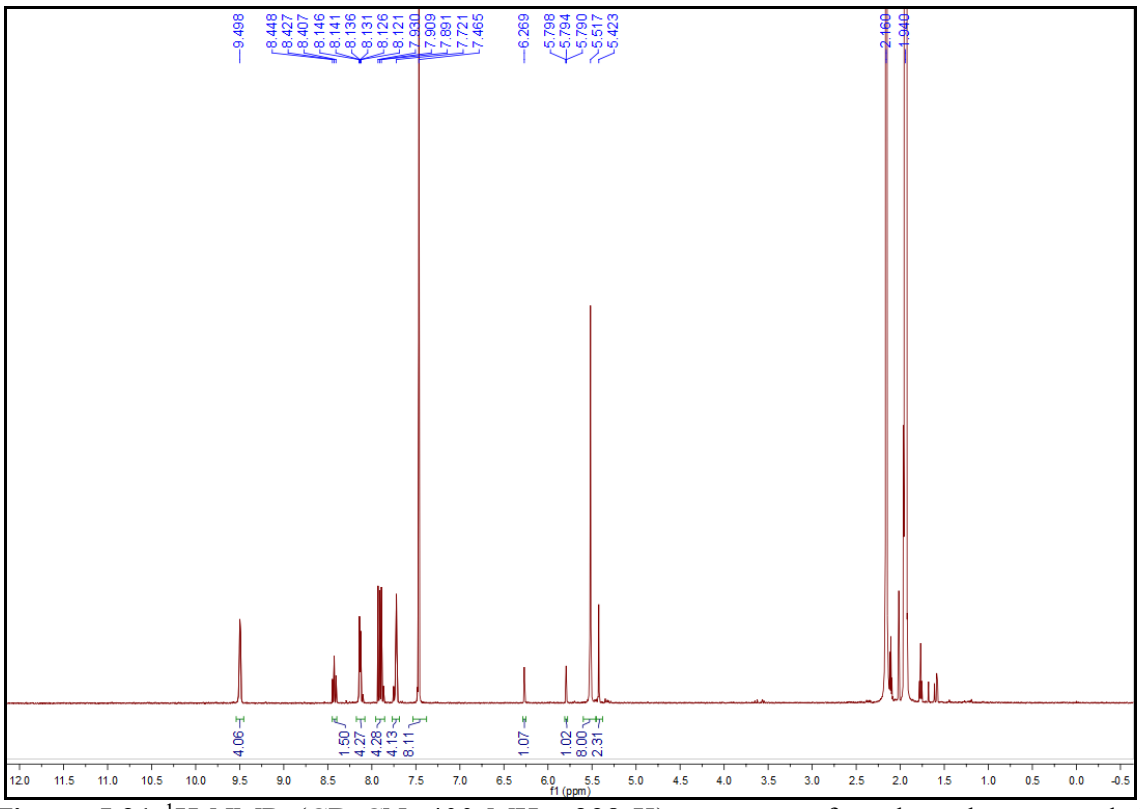

Figure 5.21 ^{1}H NMR (CD_3CN, 400 MHz, 298 K) spectrum of methacrylate-appended Texas-sized molecular box (**4.2**).

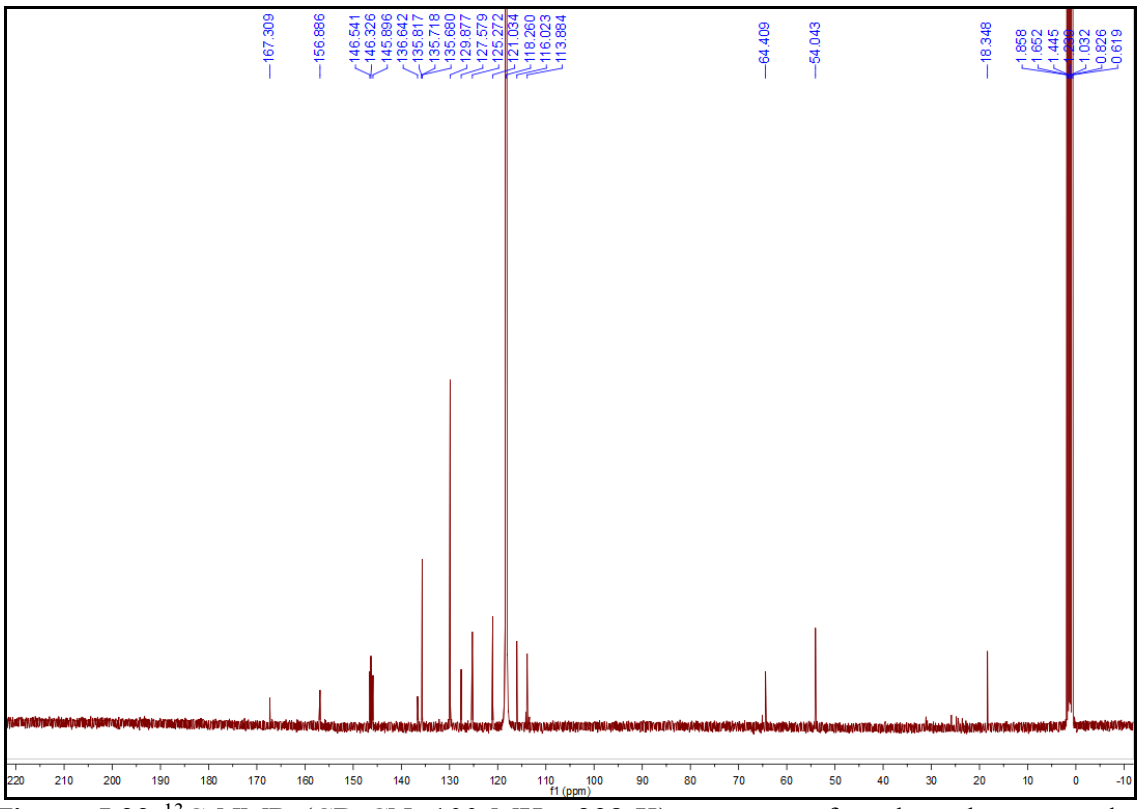

Figure 5.22 ^{13}C NMR (CD_3CN, 100 MHz, 298 K) spectrum of methacrylate-appended Texas-sized molecular box (**4.2**).

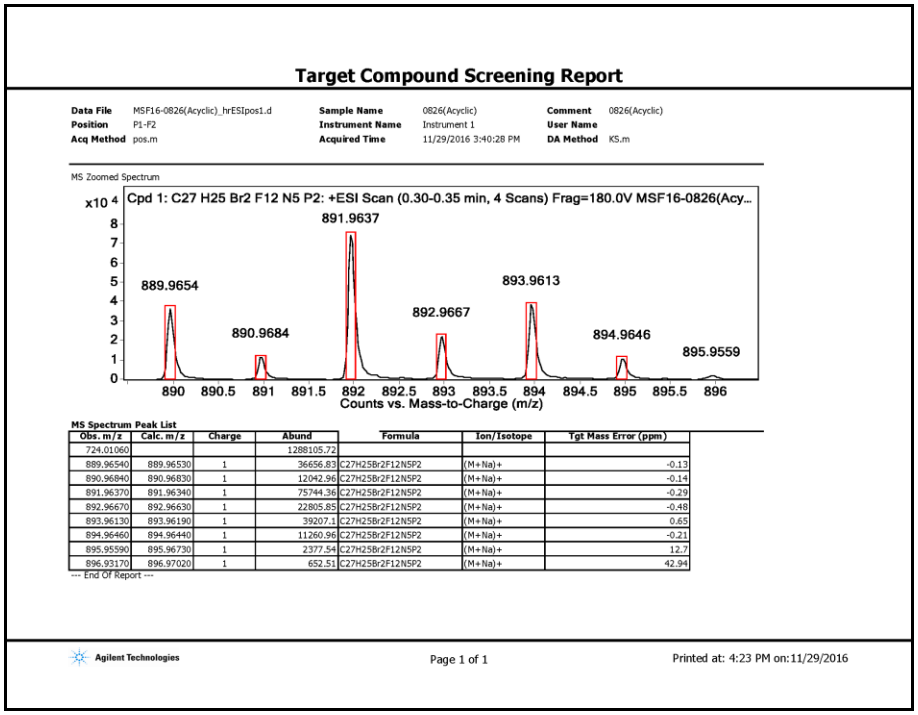

Target Compound Screening Report

Data File	MSF16-0826(Acyclic)_hrESIpos1.d	**Sample Name**	0826(Acyclic)	**Comment**	0826(Acyclic)
Position	P1-F2	**Instrument Name**	Instrument 1	**User Name**	
Acq Method	pos.m	**Acquired Time**	11/29/2016 3:40:28 PM	**DA Method**	KS.m

MS Zoomed Spectrum

MS Spectrum Peak List

Obs. m/z	Calc. m/z	Charge	Abund	Formula	Ion/Isotope	Tgt Mass Error (ppm)
724.01060			1288105.72			
889.96540	889.96530	1	36656.83	C27H25Br2F12N5P2	(M+Na)+	-0.13
890.96840	890.96830	1	12042.96	C27H25Br2F12N5P2	(M+Na)+	-0.14
891.96370	891.96340	1	75744.36	C27H25Br2F12N5P2	(M+Na)+	-0.29
892.96670	892.96630	1	22805.85	C27H25Br2F12N5P2	(M+Na)+	-0.48
893.96130	893.96190	1	39207.1	C27H25Br2F12N5P2	(M+Na)+	0.65
894.96460	894.96440	1	11260.96	C27H25Br2F12N5P2	(M+Na)+	-0.21
895.95590	895.96730	1	2377.54	C27H25Br2F12N5P2	(M+Na)+	12.7
896.93170	896.97020	1	652.51	C27H25Br2F12N5P2	(M+Na)+	42.94

--- End Of Report ---

Agilent Technologies Page 1 of 1 Printed at: 4:23 PM on:11/29/2016

Figure 5.23 High-resolution mass spectrum of *N*,*N*'-bis(*α*-bromo-*p*-xylene)-2,6-bis(imadzol-1-yl)pyridine bis(hexafluorophosphate) (**2.7** and **4.4**).

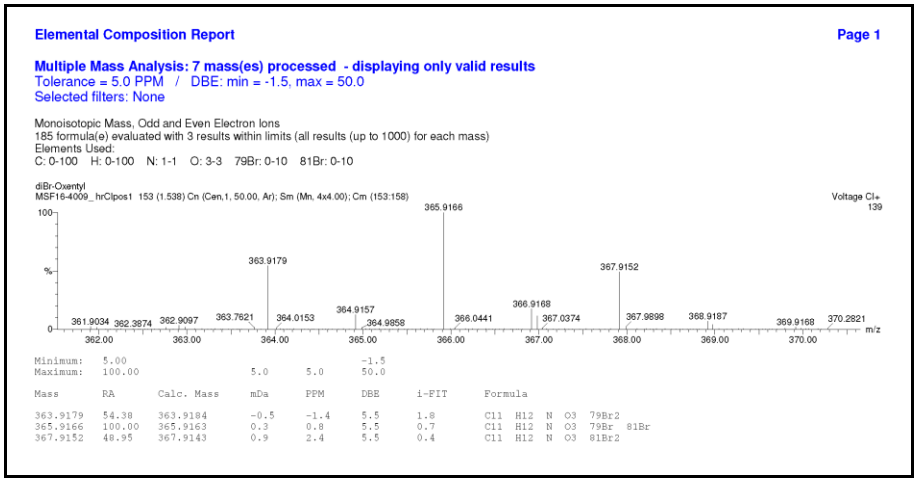

Elemental Composition Report Page 1

Multiple Mass Analysis: 7 mass(es) processed - displaying only valid results
Tolerance = 5.0 PPM / DBE: min = -1.5, max = 50.0
Selected filters: None

Monoisotopic Mass, Odd and Even Electron Ions
185 formula(e) evaluated with 3 results within limits (all results (up to 1000) for each mass)
Elements Used:
C: 0-100 H: 0-100 N: 1-1 O: 3-3 79Br: 0-10 81Br: 0-10

diBr-Oxentyl
MSF16-4009_ hrClpos1 153 (1.538) Cn (Cen,1, 50.00, Ar); Sm (Mn, 4x4.00); Cm (153:158) Voltage Cl+ 139

Minimum:	5.00				-1.5		
Maximum:	100.00		5.0	5.0	50.0		
Mass	RA	Calc. Mass	mDa	PPM	DBE	i-FIT	Formula
363.9179	54.38	363.9184	-0.5	-1.4	5.5	1.8	C11 H12 N O3 79Br2
365.9166	100.00	365.9163	0.3	0.8	5.5	0.7	C11 H12 N O3 79Br 81Br
367.9152	48.95	367.9143	0.9	2.4	5.5	0.4	C11 H12 N O3 81Br2

Figure 5.24 High-resolution mass spectrum of (3-methyloxetan-3-yl)methyl 2,6-dibromoisonicotinate (**2.9** and **3.5**).

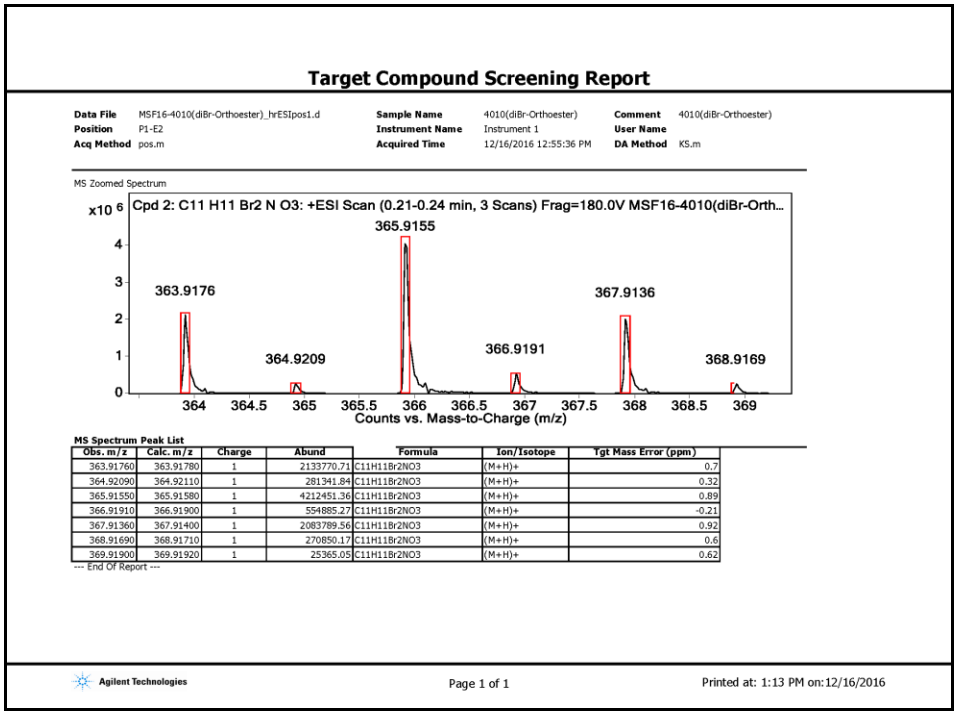

Figure 5.25 High-resolution mass spectrum of 2,6-dibromo-4-(4-methyl-2,6,7-trioxabicyclo[2.2.2]octan-1-yl)pyridine (**2.10** and **3.4**).

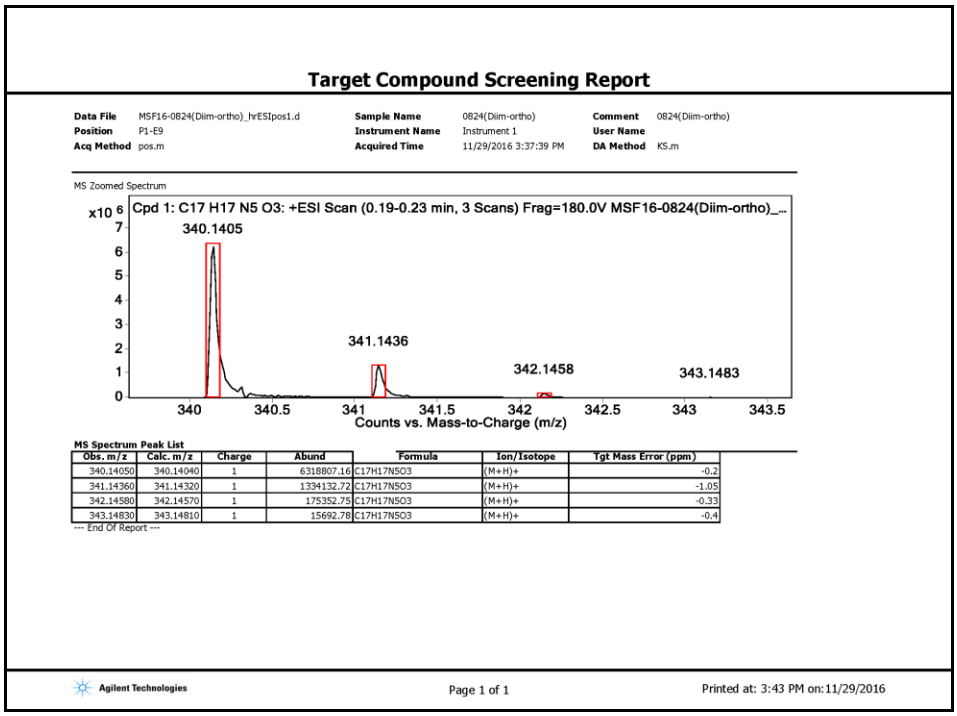

Figure 5.26 High-resolution mass spectrum of 2,6-di(1H-imidazol-1-yl)-4-(4-methyl-2,6,7-trioxabicyclo[2.2.2]octan-1-yl)pyridine (**2.11** and **3.3**).

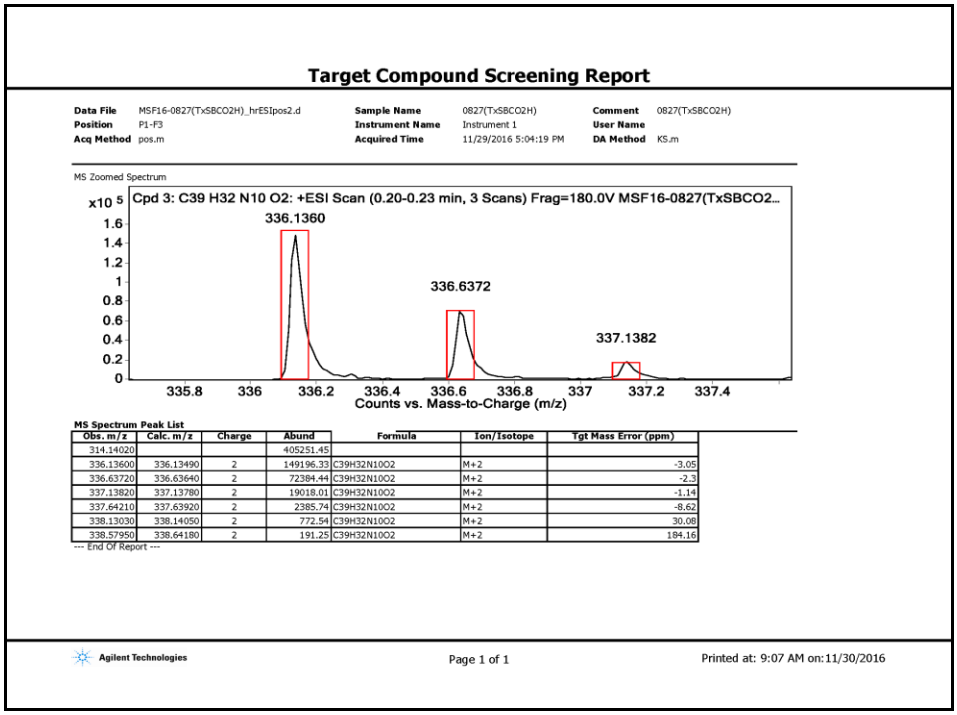

Target Compound Screening Report

Data File MSF16-0827(TxSBCO2H)_hrESIpos2.d
Sample Name 0827(TxSBCO2H)
Comment 0827(TxSBCO2H)
Position P1-F3
Instrument Name Instrument 1
User Name
Acq Method pos.m
Acquired Time 11/29/2016 5:04:19 PM
DA Method KS.m

MS Zoomed Spectrum

MS Spectrum Peak List

Obs. m/z	Calc. m/z	Charge	Abund	Formula	Ion/Isotope	Tgt Mass Error (ppm)
314.14020			405251.45			
336.13600	336.13490	2	149196.33	C39H32N10O2	M+2	-3.05
336.63720	336.63640	2	72384.44	C39H32N10O2	M+2	-2.3
337.13820	337.13780	2	19018.01	C39H32N10O2	M+2	-1.14
337.64210	337.63920	2	2385.74	C39H32N10O2	M+2	-8.62
338.13030	338.14050	2	772.54	C39H32N10O2	M+2	30.08
338.57950	338.64180	2	191.25	C39H32N10O2	M+2	184.16

--- End Of Report ---

Agilent Technologies Page 1 of 1 Printed at: 9:07 AM on:11/30/2016

Figure 5.27 High-resolution mass spectrum of monocarboxylic acid-functionalized Texas-sized molecular box (**TxSB-CO$_2$H**·4PF$_6$).

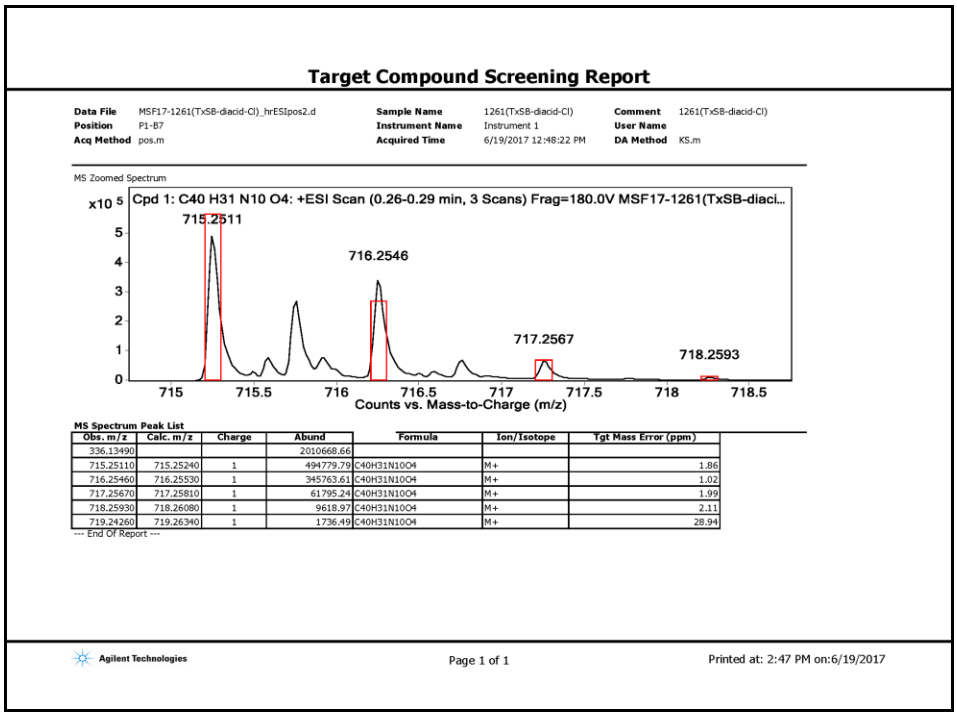

Target Compound Screening Report

Data File MSF17-1261(TxSB-diacid-Cl)_hrESIpos2.d
Sample Name 1261(TxSB-diacid-Cl)
Comment 1261(TxSB-diacid-Cl)
Position P1-B7
Instrument Name Instrument 1
User Name
Acq Method pos.m
Acquired Time 6/19/2017 12:48:22 PM
DA Method KS.m

MS Zoomed Spectrum

MS Spectrum Peak List

Obs. m/z	Calc. m/z	Charge	Abund	Formula	Ion/Isotope	Tgt Mass Error (ppm)
336.13490			2010668.66			
715.25110	715.25240	1	494779.79	C40H31N10O4	M+	1.86
716.25460	716.25530	1	345763.61	C40H31N10O4	M+	1.02
717.25670	717.25810	1	61795.24	C40H31N10O4	M+	1.99
718.25930	718.26080	1	9618.97	C40H31N10O4	M+	2.11
719.24260	719.26340	1	1736.49	C40H31N10O4	M+	28.94

--- End Of Report ---

Agilent Technologies Page 1 of 1 Printed at: 2:47 PM on:6/19/2017

Figure 5.28 High-resolution mass spectrum of dicarboxylic acid-functionalized Texas-sized molecular box (**3.2**).

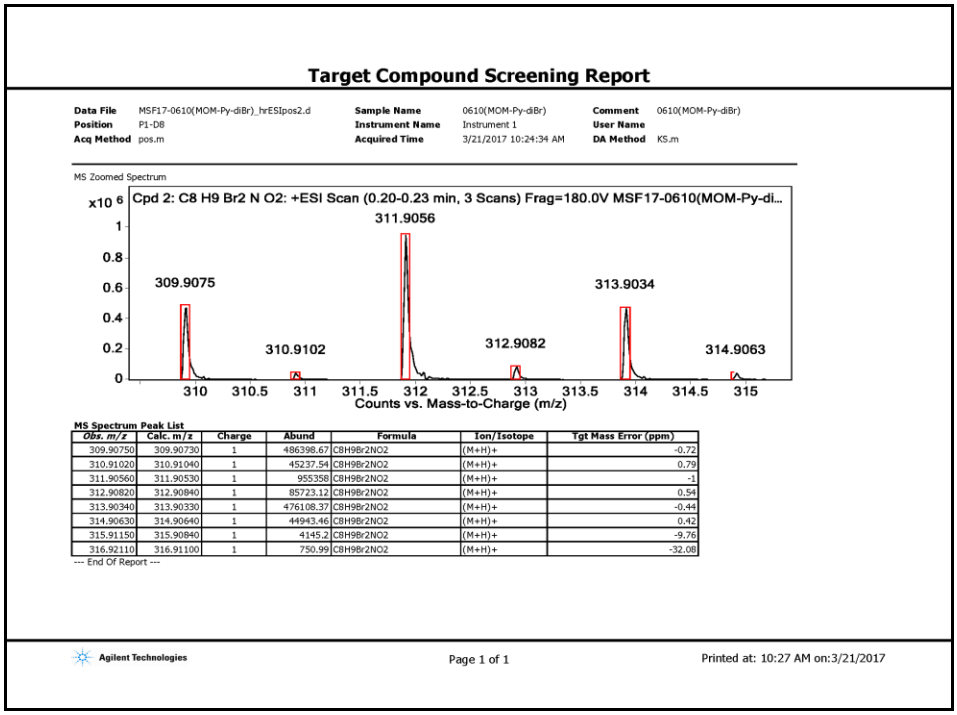

Target Compound Screening Report

Data File MSF17-0610(MOM-Py-diBr)_hrESIpos2.d
Position P1-D8
Acq Method pos.m
Sample Name 0610(MOM-Py-diBr)
Instrument Name Instrument 1
Acquired Time 3/21/2017 10:24:34 AM
Comment 0610(MOM-Py-diBr)
User Name
DA Method KS.m

MS Zoomed Spectrum

MS Spectrum Peak List

Obs. m/z	Calc. m/z	Charge	Abund	Formula	Ion/Isotope	Tgt Mass Error (ppm)
309.90750	309.90730	1	486398.67	C8H9Br2NO2	(M+H)+	-0.72
310.91020	310.91040	1	45237.54	C8H9Br2NO2	(M+H)+	0.79
311.90560	311.90530	1	955358	C8H9Br2NO2	(M+H)+	-1
312.90820	312.90840	1	85723.12	C8H9Br2NO2	(M+H)+	0.54
313.90340	313.90330	1	476108.37	C8H9Br2NO2	(M+H)+	-0.44
314.90630	314.90640	1	44943.46	C8H9Br2NO2	(M+H)+	0.42
315.91150	315.90840	1	4145.2	C8H9Br2NO2	(M+H)+	-9.76
316.92110	316.91100	1	750.99	C8H9Br2NO2	(M+H)+	-32.08

--- End Of Report ---

Agilent Technologies Page 1 of 1 Printed at: 10:27 AM on:3/21/2017

Figure 5.29 High-resolution mass spectrum of 2,6-dibromo-4-((methoxymethoxy)methyl)pyridine (**4.8**).

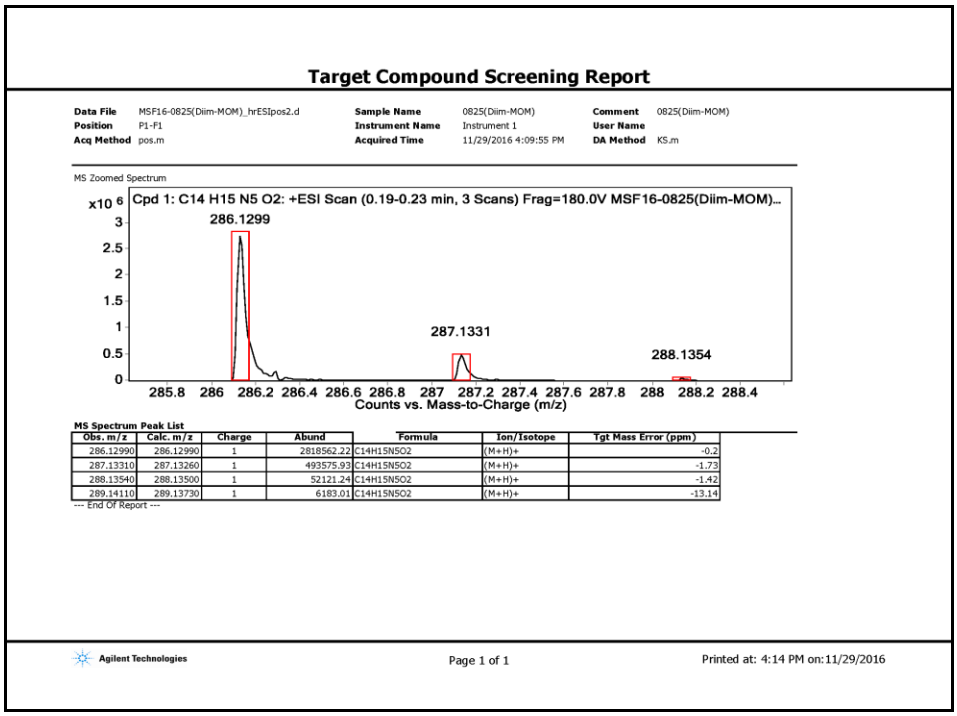

Target Compound Screening Report

Data File MSF16-0825(Diim-MOM)_hrESIpos2.d
Position P1-F1
Acq Method pos.m
Sample Name 0825(Diim-MOM)
Instrument Name Instrument 1
Acquired Time 11/29/2016 4:09:55 PM
Comment 0825(Diim-MOM)
User Name
DA Method KS.m

MS Zoomed Spectrum

MS Spectrum Peak List

Obs. m/z	Calc. m/z	Charge	Abund	Formula	Ion/Isotope	Tgt Mass Error (ppm)
286.12990	286.12990	1	2818562.22	C14H15N5O2	(M+H)+	-0.2
287.13310	287.13260	1	493575.93	C14H15N5O2	(M+H)+	-1.73
288.13540	288.13500	1	52121.24	C14H15N5O2	(M+H)+	-1.42
289.14110	289.13730	1	6183.01	C14H15N5O2	(M+H)+	-13.14

--- End Of Report ---

Agilent Technologies Page 1 of 1 Printed at: 4:14 PM on:11/29/2016

Figure 5.30 High-resolution mass spectrum of 2,6-di(1H-imidazol-1-yl)-4-((methoxymethoxy)methyl)pyridine (**4.5**).

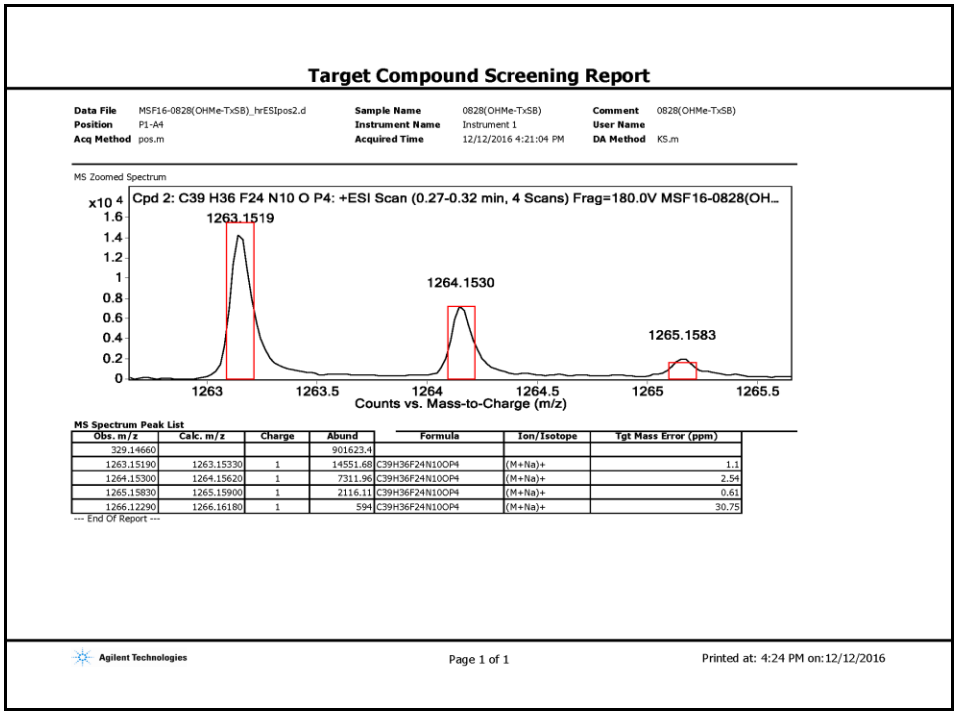

Target Compound Screening Report

Data File MSF16-0828(OHMe-TxSB)_hrESIpos2.d
Sample Name 0828(OHMe-TxSB)
Comment 0828(OHMe-TxSB)
Position P1-A4
Instrument Name Instrument 1
User Name
Acq Method pos.m
Acquired Time 12/12/2016 4:21:04 PM
DA Method KS.m

MS Zoomed Spectrum

MS Spectrum Peak List

Obs. m/z	Calc. m/z	Charge	Abund	Formula	Ion/Isotope	Tgt Mass Error (ppm)
329.14660			901623.4			
1263.15190	1263.15330	1	14551.68	C39H36F24N10OP4	(M+Na)+	1.1
1264.15300	1264.15620	1	7311.96	C39H36F24N10OP4	(M+Na)+	2.54
1265.15830	1265.15900	1	2116.11	C39H36F24N10OP4	(M+Na)+	0.61
1266.12290	1266.16180	1	594	C39H36F24N10OP4	(M+Na)+	30.75

--- End Of Report ---

Agilent Technologies Page 1 of 1 Printed at: 4:24 PM on:12/12/2016

Figure 5.31 High-resolution mass spectrum of hydroxymethyl-functionalized Texas-sized molecular box (**4.3**).

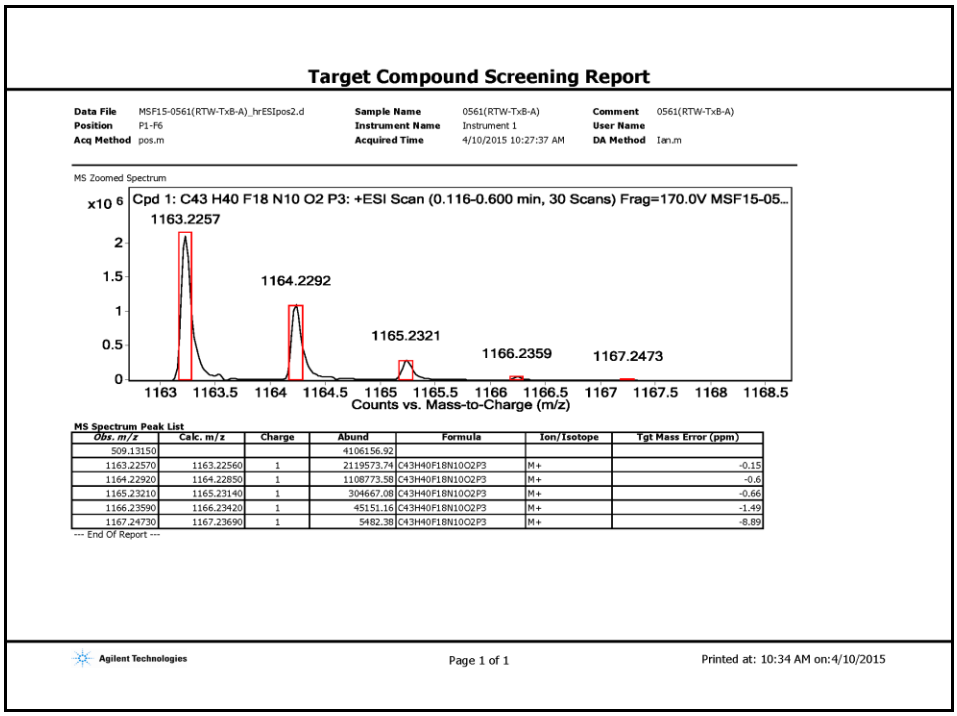

Target Compound Screening Report

Data File MSF15-0561(RTW-TxB-A)_hrESIpos2.d
Sample Name 0561(RTW-TxB-A)
Comment 0561(RTW-TxB-A)
Position P1-F6
Instrument Name Instrument 1
User Name
Acq Method pos.m
Acquired Time 4/10/2015 10:27:37 AM
DA Method Ian.m

MS Zoomed Spectrum

MS Spectrum Peak List

Obs. m/z	Calc. m/z	Charge	Abund	Formula	Ion/Isotope	Tgt Mass Error (ppm)
509.13150			4106156.92			
1163.22570	1163.22560	1	2119573.74	C43H40F18N10O2P3	M+	-0.15
1164.22920	1164.22850	1	1108773.58	C43H40F18N10O2P3	M+	-0.6
1165.23210	1165.23140	1	304667.08	C43H40F18N10O2P3	M+	-0.66
1166.23590	1166.23420	1	45151.16	C43H40F18N10O2P3	M+	-1.49
1167.24730	1167.23690	1	5482.38	C43H40F18N10O2P3	M+	-8.89

--- End Of Report ---

Agilent Technologies Page 1 of 1 Printed at: 10:34 AM on:4/10/2015

Figure 5.32 High-resolution mass spectrum of methacrylate-appended Texas-sized molecular box (**4.2**).

5.3 X-RAY EXPERIMENTAL AND CRYSTALLOGRAPHIC DATA

X-ray Experimental for [**TxSB-CO_2H**·4PF_6·5DMSO] ($C_{39}H_{34}N_{10}O_2^{4+}$ 4 PF_6^{1-} - 5 C_2H_6SO): Crystals grew as colorless prisms by slow diffusion of 2-propanol into a solution of **TxSB-CO_2H**·4PF_6 in DMSO containing a trace amount of trifluoroacetic acid. The data crystal had approximate dimensions; 0.20 × 0.10 × 0.05 mm. The data were collected on a Rigaku AFC12 diffractometer with a Saturn 724+ CCD using a graphite monochromator with MoKα radiation (λ = 0.71073 Å). A total of 1024 frames of data were collected using ω-scans with a scan range of 0.5° and a counting time of 75 seconds per frame. The data were collected at 100 K using an Rigaku XStream Cryostream low temperature device. Details of crystal data, data collection and structure refinement are listed in Table 5.1. Data collection were performed using the Rigaku Americas Corporation's Crystal Clear version 1.40.[3] Unit cell refinement and data reduction were performed using Agilent Technologies CrysAlisPro V 1.171.38.43f.[4] The structure was solved by direct methods using SHELXT[5] and refined by full-matrix least-squares on F^2 with anisotropic displacement parameters for the non-H atoms using SHELXL-2016/6.[6] Structure analysis was aided by use of the programs PLATON[7] and WinGX.[8] The hydrogen atoms on carbon were calculated in ideal positions with isotropic displacement parameters set to 1.2xUeq of the attached atom (1.5xUeq for methyl hydrogen atoms). The hydrogen atoms were calculated in idealized positions with Uiso set to 1.2xUeq of the attached atom (1.5xUeq for methyl hydrogen atoms. The hydrogen atom on the carboxylic acid was disordered over the two oxygen atoms, O1 and O2, and was not included in the final refinement model. Several of the DMSO molecules were disordered. The disorder was modeled in the same manner for each individually. For example, for one DMSO molecule, the variable x was assigned to the site occupancy factors for the non-H atoms of one component of the disordered molecule. The variable

(1-x) was assigned to the site occupancy factors for the atoms of the alternate component. A common isotropic displacement parameter was refined while refining the variable x. The geometry of the two components was restrained to be equivalent throughout the refinement process. When the value for x converged, the site occupancy factors were fixed and the displacement parameters were refined with restraints applied.

The function, $\Sigma w(|F_o|^2 - |F_c|^2)^2$, was minimized, where $w = 1/[(\sigma(F_o))^2 + (0.1132*P)^2 + (2.3555*P)]$ and $P = (|F_o|^2 + 2|F_c|^2)/3$. $R_W(F^2)$ refined to 0.317, with R(F) equal to 0.119 and a goodness of fit, S, = 1.08. Definitions used for calculating R(F), $R_W(F^2)$ and the goodness of fit, S, are given below.[9] The data were checked for secondary extinction effects but no correction was necessary. Neutral atom scattering factors and values used to calculate the linear absorption coefficient are from the International Tables for X-ray Crystallography (1992).[10] All figures were generated using SHELXTL/PC.[11] Tables of positional and thermal parameters, bond lengths and angles, torsion angles and figures are found in the cif files, which may be obtained from the Cambridge Crystallographic Data Centre by referencing CCDC number 1573263.

Table 5.1 Crystal data and structure refinement for [**TxSB-CO_2H**·4PF_6·5DMSO]

Empirical formula	C49 H63 F24 N10 O7 P4 S5	
Formula weight	1644.27	
Temperature	100(2) K	
Wavelength	0.71073 Å	
Crystal system	triclinic	
Space group	P -1	
Unit cell dimensions	a = 14.493(5) Å	α = 100.095(6)°.
	b = 14.921(5) Å	β = 107.797(8)°.
	c = 17.665(6) Å	γ = 98.626(7)°.
Volume	3495(2) $Å^3$	
Z	2	
Density (calculated)	1.562 Mg/m^3	
Absorption coefficient	0.375 mm^{-1}	
F(000)	1678	
Crystal size	0.2 x 0.1 x 0.05 mm^3	
Theta range for data collection	2.098 to 25.142°.	
Index ranges	-17<=h<=17, -15<=k<=17, -20<=l<=21	
Reflections collected	34788	
Independent reflections	12413 [R(int) = 0.1357]	
Completeness to theta = 25.142°	99.3 %	
Absorption correction	Semi-empirical from equivalents	
Refinement method	Full-matrix least-squares on F^2	
Data / restraints / parameters	12413 / 1824 / 1034	
Goodness-of-fit on F^2	1.110	
Final R indices [I>2sigma(I)]	R1 = 0.1189, wR2 = 0.2539	
R indices (all data)	R1 = 0.2665, wR2 = 0.3167	
Extinction coefficient	n/a	
Largest diff. peak and hole	0.971 and -0.506 e.$Å^{-3}$	
CCDC #	1573263	

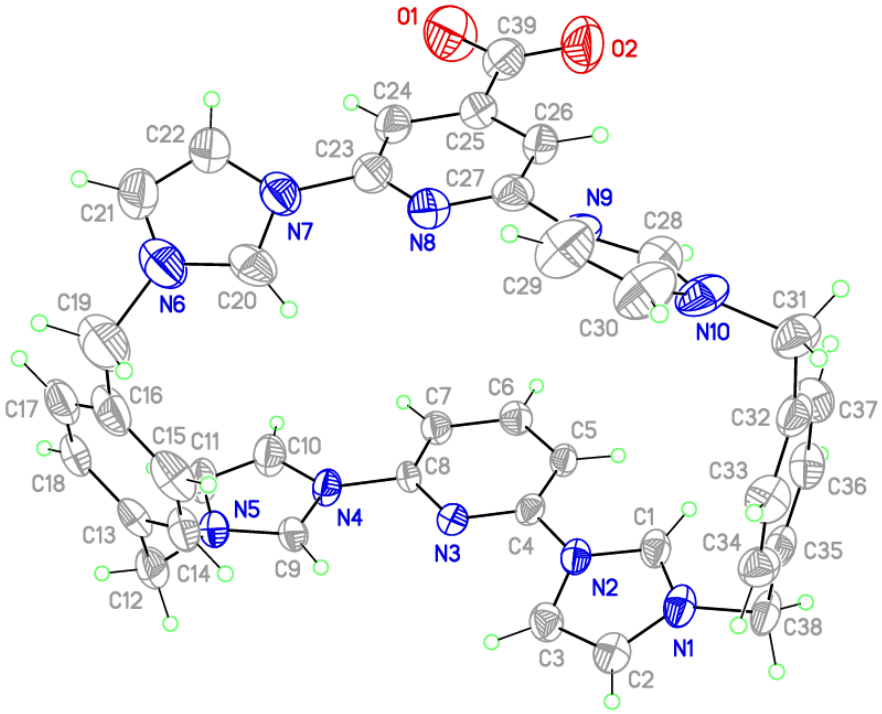

Figure 5.33 View of the macrocycle in [**TxSB-CO$_2$H**·4PF$_6$·5DMSO] showing the atom labeling scheme. Displacement ellipsoids are scaled to the 50% probability level. The hydrogen on the carboxylic acid was disordered over the two oxygen atom positions and was not included in the refinement model.

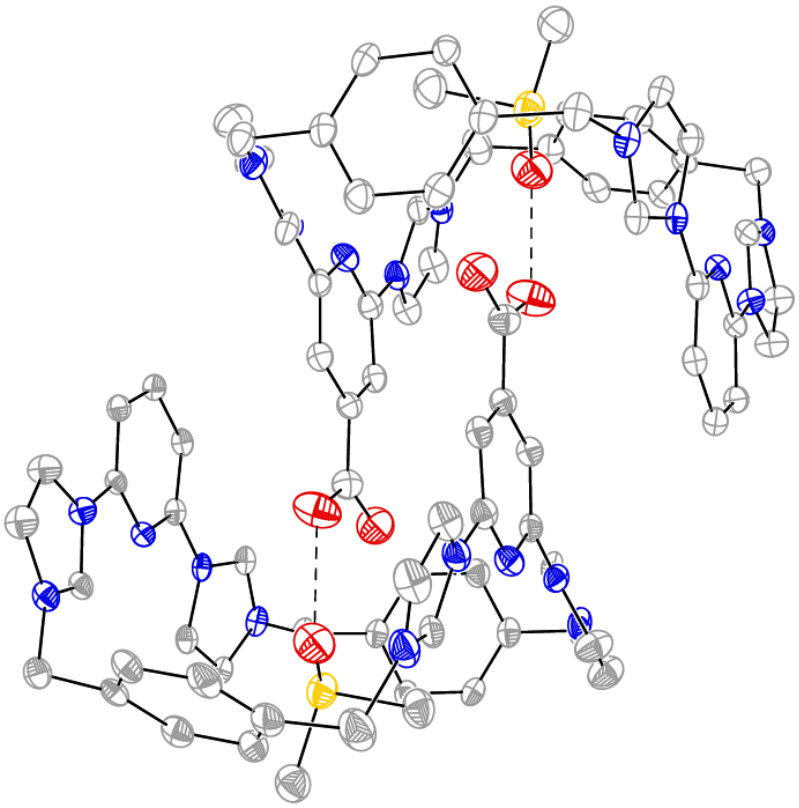

Figure 5.34 View of a noncovalent dimer formed in [**TxSB-CO$_2$H**·4PF$_6$·5DMSO]. Displacement ellipsoids are scaled to the 30% probability level. All hydrogen atoms, all counter anions, and some solvent molecules were omitted for clarity. The molecules are situated around a crystallographic inversion center at ½, ½, ½. Two sets of H-bonding formed between each in-cavity lower-rim-bound DMSO molecule and the carboxylic acid present in the complementary **TxSB-CO$_2$H** monomer are seen that presumably facilitate the mutual head-to-tail inclusion, thus supporting the formation of the resulting dimeric superstructure.

X-ray Experimental for [**TxSB-CO$_2$**·3PF_6·2DMSO] ($C_{39}H_{33}N_{10}O_2^{3-}$ 3PF_6^{1-} - 2C_2H_6SO): Crystals grew as colorless needles by slow diffusion of 2-propanol into a mixture of **TxSB-CO$_2$H**·4PF_6 and excess triethylamine in DMSO. The data were collected on a Rigaku ACF-12 with a Saturn 724+ CCD using a graphite monochromator with MoKα radiation (λ = 0.71073 Å). A total of 864 frames of data were collected using ω-scans with a scan range of 0.5° and a counting time of 45 seconds per frame. The data were collected at 100 K using a Rigaku XStream low temperature device. Details of crystal data, data collection and structure refinement are listed in Table 5.2. Data reduction were performed using the Rigaku Americas Corporation's Crystal Clear version 1.40.[3] The structure was solved by direct methods using Sir2004[12] and refined by full-matrix least-squares on F^2 with anisotropic displacement parameters for the non-H atoms using SHELXL-97.[6] One hexafluorophosphate anion was disordered around a crystallographic mirror plane of symmetry. It was modeled by assigning the variable x to the site occupancy factors for one component of the disordered anion and (1-x) to the site occupancy factors for the alternate component. The geometry of the two anions was restrained to be equivalent throughout the refinement process. A common isotropic displacement parameter was refined for all the fluorine atoms and a second isotropic displacement parameter was refined for the phosphorus atoms while refining x. A large region of the cell was composed of disordered molecules of DMSO. These molecules were disordered around a crystallographic mirror plane of symmetry. The contributions to the scattering factors due to this solvent molecule were removed by use of the utility SQUEEZE[13] in PLATON98.[8] Structure analysis was aided by use of the programs PLATON98 as incorporated into WinGX.[14] The hydrogen atoms on carbon were calculated in ideal positions with isotropic displacement parameters set to 1.2xUeq of the attached atom (1.5xUeq for methyl hydrogen atoms).

The function, $\Sigma w(|Fo|^2 - |Fc|^2)^2$, was minimized, where $w = 1/[(\sigma(Fo))^2 + (0.1107*P)^2 + (12.9006*P)]$ and $P = (|Fo|^2 + 2|Fc|^2)/3$. $Rw(F^2)$ refined to 0.236, with R(F) equal to 0.091 and a goodness of fit, S, = 1.04. Definitions used for calculating R(F), $Rw(F^2)$ and the goodness of fit, S, are given below.[9] The data were checked for secondary extinction effects but no correction was necessary. Neutral atom scattering factors and values used to calculate the linear absorption coefficient are from the International Tables for X-ray Crystallography (1992).[10] All figures were generated using SHELXTL/PC.[11] Tables of positional and thermal parameters, bond lengths and angles, torsion angles and figures are found in the cif files, which may be obtained from the Cambridge Crystallographic Data Centre by referencing CCDC number 1573264.

Table 5.2 Crystal data and structure refinement for [**TxSB-CO_2**·3PF_6·2DMSO].

Empirical formula	C43 H33 F18 N10 O4 P3 S2	
Formula weight	1252.82	
Temperature	100(2) K	
Wavelength	0.71073 Å	
Crystal system	orthorhombic	
Space group	P n m a	
Unit cell dimensions	a = 27.323(3) Å	α = 90°.
	b = 31.177(4) Å	β = 90°.
	c = 11.9178(15) Å	γ = 90°.
Volume	10152(2) $Å^3$	
Z	8	
Density (calculated)	1.639 Mg/m^3	
Absorption coefficient	0.320 mm^{-1}	
F(000)	5056	
Crystal size	0.23 x 0.05 x 0.05 mm^3	
Theta range for data collection	2.998 to 25.026°.	
Index ranges	-32<=h<=32, -29<=k<=36, -10<=l<=14	
Reflections collected	76417	
Independent reflections	9061 [R(int) = 0.1409]	
Completeness to theta = 25.026°	99.0 %	
Absorption correction	Semi-empirical from equivalents	
Max. and min. transmission	1.00 and 0.471	
Refinement method	Full-matrix least-squares on F^2	
Data / restraints / parameters	9061 / 960 / 745	
Goodness-of-fit on F^2	1.045	
Final R indices [I>2sigma(I)]	R1 = 0.0910, wR2 = 0.2027	
R indices (all data)	R1 = 0.1593, wR2 = 0.2361	
Extinction coefficient	n/a	
Largest diff. peak and hole	0.791 and -0.513 e.$Å^{-3}$	
CCDC #	1573264	

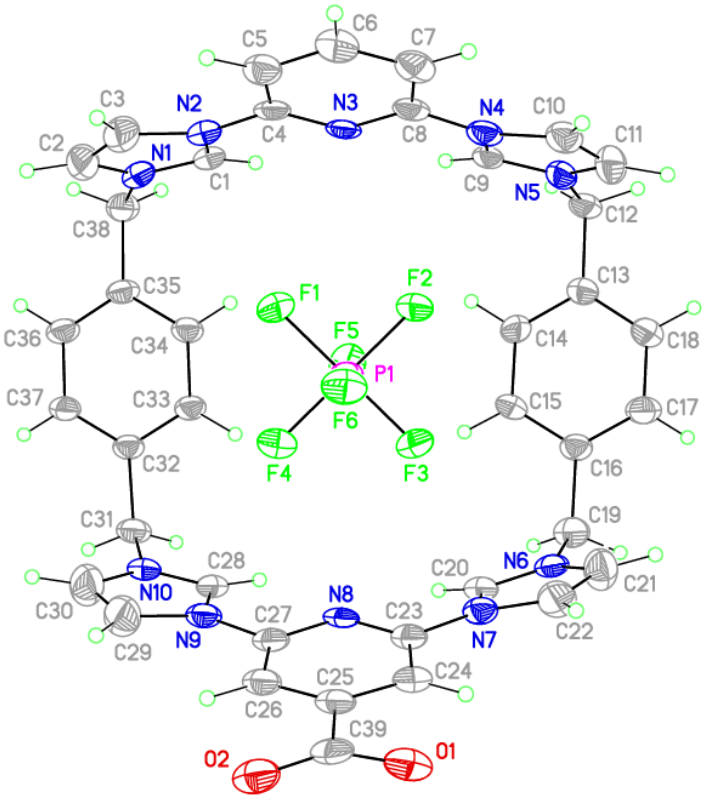

Figure 5.35 View of the macrocycle and an encapsulated hexafluorophosphate anion seen in the single crystal X-ray structure of [**TxSB-CO$_2$**·3PF$_6$·2DMSO]. This representation shows the atom labeling scheme. Displacement ellipsoids are scaled to the 50% probability level.

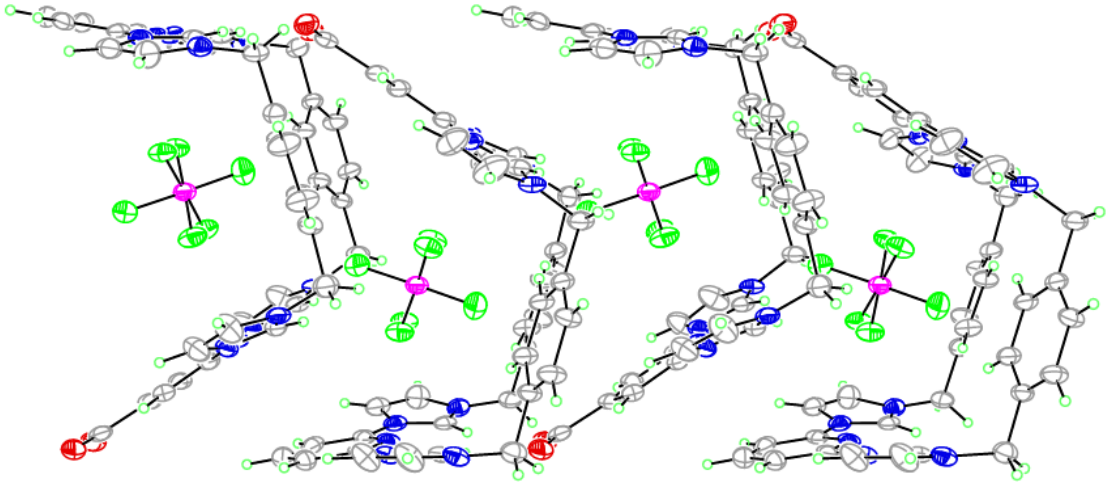

Figure 5.36 View of the macrocycle and an encapsulated hexafluorophosphate anion in [**TxSB-CO$_2$**·3PF$_6$·2DMSO] showing the stacking of the complex along the c-axis. Displacement ellipsoids are scaled to the 50% probability level.

X-ray Experimental for hydroxymethyl-functionalized Texas-sized molecular box **4.3** ($(C_{39}H_{36}N_{10}O)^{4+}$ - 4 PF_6^{1-} $2C_2H_3N$): Crystals grew as clusters of colorless prisms by slow evaporation diethyl ether into a concentrated acetonitrile solution containing **4.3**. The data crystal was cut from a larger crystal and had approximate dimensions; 0.28 x 0.18 x 0.16 mm. The data were collected on a Rigaku SCX-Mini with a Mercury 2+ CCD using a graphite monochromator with MoKα radiation (λ = 0.71073Å). A total of 1080 frames of data were collected using ω-scans with a scan range of 0.5° and a counting time of 24 seconds per frame. The data were collected at 100 K using Rigaku XStream low temperature device. Details of crystal data, data collection and structure refinement are listed in Table 5.3. Data reduction were performed using the Rigaku Americas Corporation's Crystal Clear version 1.40.[3] The structure was solved by direct methods using SIR2004[12] and refined by full-matrix least-squares on F^2 with anisotropic displacement parameters for the non-H atoms using SHELXL-97.[13] Structure analysis was aided by use of the programs PLATON98[14] and WinGX.[8] The hydrogen atoms on carbon were calculated in ideal positions with isotropic displacement parameters set to 1.2xUeq of the attached atom (1.5xUeq for methyl hydrogen atoms). The macrocycle sits around a crystallographic inversion center at ½, ½, ½. The inversion center of symmetry imposes a disorder on the unsymmetrically substituted macrocycle, which has a hydroxymethyl substituent at the para position on one of the pyridine groups and a hydrogen atom at that site on the pyridine group related by the inversion symmetry. One of the two hexafluorophosphate ions was also disordered. This disorder was modeled by assigning the variable x to the site occupancy factors of the atoms of one component. The variable (1-x) was assigned to the occupancy factors for the alternate component. The variable x was refined while requiring the isotropic displacement parameters of the phosphorus atoms of the two orientations to be equal. In addition, the fluorine atoms of

the two groups were refined with their isotropic displacement parameters constrained to be equal while refining x. The geometry of the two components was restrained to be equivalent throughout the refinement process. Ultimately, the atoms of the two groups were refined anisotropically with their displacement parameters restrained to be approximately isotropic. Although the intensity statistics indicated that the space group was centric, a model in the non-centrosymmetric space group, P1, was refined. In the P1 model, the disordered hexafluorophosphate ion was still disordered as was its mate related by the pseudo-inversion center. The hydroxymethyl group was also disordered. There was no improvement in the refined model in P1.

The function, $\Sigma w(|F_o|^2 - |F_c|^2)^2$, was minimized, where $w = 1/[(\sigma(F_o))^2 + (0.0651*P)^2 + (1.802*P)]$ and $P = (|F_o|^2 + 2|F_c|^2)/3$. $R_W(F^2)$ refined to 0.184, with R(F) equal to 0.0680 and a goodness of fit, S, = 1.19. Definitions used for calculating R(F), $R_W(F^2)$ and the goodness of fit, S, are given below.[9] The data were checked for secondary extinction effects but no correction was necessary. Neutral atom scattering factors and values used to calculate the linear absorption coefficient are from the International Tables for X-ray Crystallography (1992).[10] All figures were generated using SHELXTL/PC.[11] Tables of positional and thermal parameters, bond lengths and angles, torsion angles and figures are found elsewhere.

Table 5.3 Crystal data and structure refinement for **4.3**.

Empirical formula	C43 H42 F24 N12 O P4	
Formula weight	1322.76	
Temperature	100(2) K	
Wavelength	0.71073 Å	
Crystal system	triclinic	
Space group	P -1	
Unit cell dimensions	a = 9.371(3) Å	α= 83.259(7)°.
	b = 9.924(3) Å	β= 84.133(6)°.
	c = 14.547(4) Å	γ = 88.195(6)°.
Volume	1336.2(7) $Å^3$	
Z	1	
Density (calculated)	1.644 Mg/m^3	
Absorption coefficient	0.274 mm^{-1}	
F(000)	668	
Crystal size	0.280 x 0.180 x 0.160 mm	
Theta range for data collection	3.038 to 27.472°.	
Index ranges	-12<=h<=12, -12<=k<=12, -18<=l<=18	
Reflections collected	13873	
Independent reflections	6039 [R(int) = 0.0619]	
Completeness to theta = 25.242°	99.8 %	
Absorption correction	Semi-empirical from equivalents	
Max. and min. transmission	1.00 and 0.765	
Refinement method	Full-matrix least-squares on F^2	
Data / restraints / parameters	6039 / 876 / 453	
Goodness-of-fit on F^2	1.022	
Final R indices [I>2sigma(I)]	R1 = 0.0680, wR2 = 0.1660	
R indices (all data)	R1 = 0.0888, wR2 = 0.1835	
Extinction coefficient	n/a	
Largest diff. peak and hole	0.754 and -0.631 $e.Å^{-3}$	

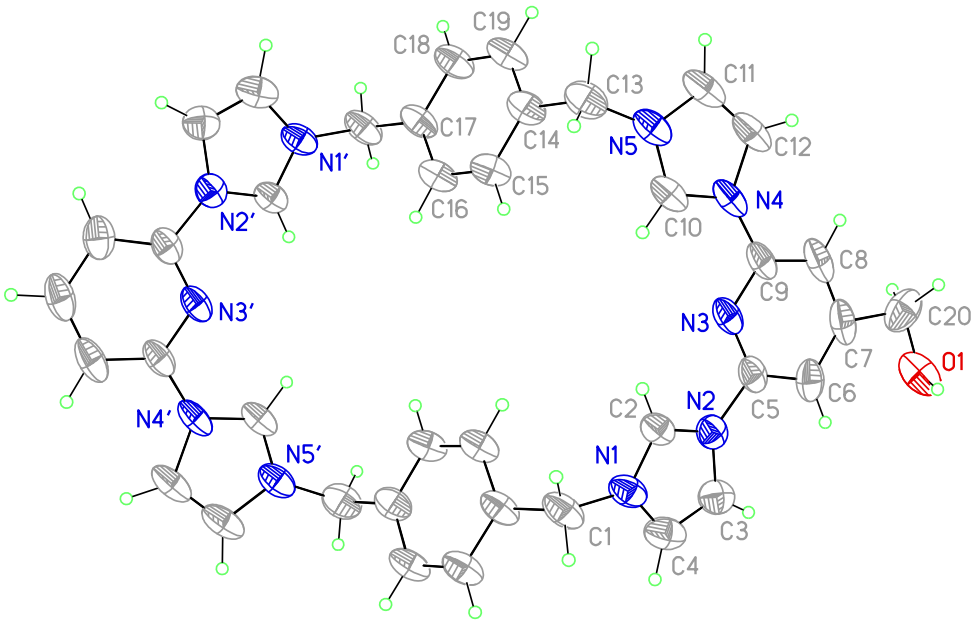

Figure 5.37 View of **4.3** showing the atom labeling scheme. Displacement ellipsoids are scaled to the 50% probability level. The macrocycle sits around a crystallographic inversion center at ½, ½, ½. Atoms with labels appended by a ’ are related by 1-x, 1-y, 1-z. The hydroxymethyl group is disordered by symmetry.

X-ray Experimental for methacrylate-appended Texas-sized molecular box **4.2** $(C_{43}H_{40}N_{10}O_2)^{4+}$ $4PF_6$ 1- 2 CH_2Cl_2 4 C_2H_3N: Crystals grew as colorless prisms by slow evaporation of dichloromethane into a concentrated acetonitrile solution containing **4.2**. The data crystal was cut from a larger crystal and had approximate dimensions; 0.43 x 0.22 x 0.15 mm. The data were collected on an Agilent Technologies SuperNova Dual Source diffractometer using a μ-focus Cu Kα radiation source (λ = 1.5418Å) with collimating mirror monochromators. A total of 2877 frames of data were collected using ω-scans with a scan range of 1° and a counting time of 1 seconds per frame with a detector offset of +/- 40.8° and 2.2 seconds per frame with a detector offset of +/- 112.0°. The data were collected at 100 K using an Oxford Cryostream low temperature device. Details of crystal data, data collection and structure refinement are listed in Table 5.4. Data collection, unit cell refinement and data reduction were performed using Agilent Technologies CrysAlisPro V 1.171.37.31.[3] The structure was solved by direct methods using SuperFlip[15] and refined by full-matrix least-squares on F^2 with anisotropic displacement parameters for the non-H atoms using SHELXL-2013.[13] Structure analysis was aided by use of the programs PLATON98[14] and WinGX.[8] The hydrogen atoms were calculated in ideal positions with isotropic displacement parameters set to 1.2xUeq of the attached atom (1.5xUeq for methyl hydrogen atoms). The macrocycle resides around a crystallographic inversion center at ½, ½, ½. This symmetry requires that the ester attached at C6 is disordered. The group at this site was required to have ½ occupancy by symmetry, which was consistent with the electron density at the atom positions compared to that of the ring atoms of the macrocycle. The half occupancy of the ester group left a void on the other side of the macrocycle, which was filled by two half-weighted molecules of acetonitrile. A non-centrosymmetric model in space group P1 was refined.

There was no real improvement in the structure and large correlations between parameters related by the inversion center.

The function, $\Sigma w(|F_o|^2 - |F_c|^2)$, was minimized, where $w = 1/[(\sigma(F_o))^2 + (0.16*P)^2]$ and $P = (|F_o|^2 + 2|F_c|^2)/3$. $R_w(F^2)$ refined to 0.325, with R(F) equal to 0.0903 and a goodness of fit, S, = 1.88. Definitions used for calculating R(F), $R_w(F^2)$ and the goodness of fit, S, are given below.[9] The data were checked for secondary extinction effects but no correction was necessary. Neutral atom scattering factors and values used to calculate the linear absorption coefficient are from the International Tables for X-ray Crystallography (1992).[10] All figures were generated using SHELXTL/PC.[11] Tables of positional and thermal parameters, bond lengths and angles, torsion angles and figures are found elsewhere. Tables of positional and thermal parameters, bond lengths and angles, torsion angles and figures are found in the cif files, which may be obtained from the Cambridge Crystallographic Data Centre by referencing CCDC number 1573264.

Table 5.4 Crystal data and structure refinement for **4.2**.

Empirical formula	C53 H55 Cl4 F24 N14 O2 P4	
Formula weight	1641.79	
Temperature	100(2) K	
Wavelength	1.54184 Å	
Crystal system	triclinic	
Space group	P -1	
Unit cell dimensions	a = 11.3273(4) Å	α= 81.260(3)°.
	b = 13.1504(5) Å	β= 68.318(3)°.
	c = 13.3664(4) Å	γ = 74.521(3)°.
Volume	1779.90(12) $Å^3$	
Z	1	
Density (calculated)	1.532 Mg/m^3	
Absorption coefficient	3.386 mm^{-1}	
F(000)	831	
Crystal size	0.43 x 0.22 x 0.15 mm	
Theta range for data collection	3.494 to 76.013°.	
Index ranges	-14<=h<=14, -16<=k<=16, -16<=l<=16	
Reflections collected	29840	
Independent reflections	7336 [R(int) = 0.0241]	
Completeness to theta = 67.684°	99.8 %	
Absorption correction	Semi-empirical from equivalents	
Max. and min. transmission	1.00 and 0.759	
Refinement method	Full-matrix least-squares on F^2	
Data / restraints / parameters	7336 / 84 / 524	
Goodness-of-fit on F^2	1.870	
Final R indices [I>2sigma(I)]	R1 = 0.0903, wR2 = 0.3156	
R indices (all data)	R1 = 0.0950, wR2 = 0.3253	
Extinction coefficient	n/a	
Largest diff. peak and hole	0.944 and -2.009 $e.Å^{-3}$	
CCDC #	1573264	

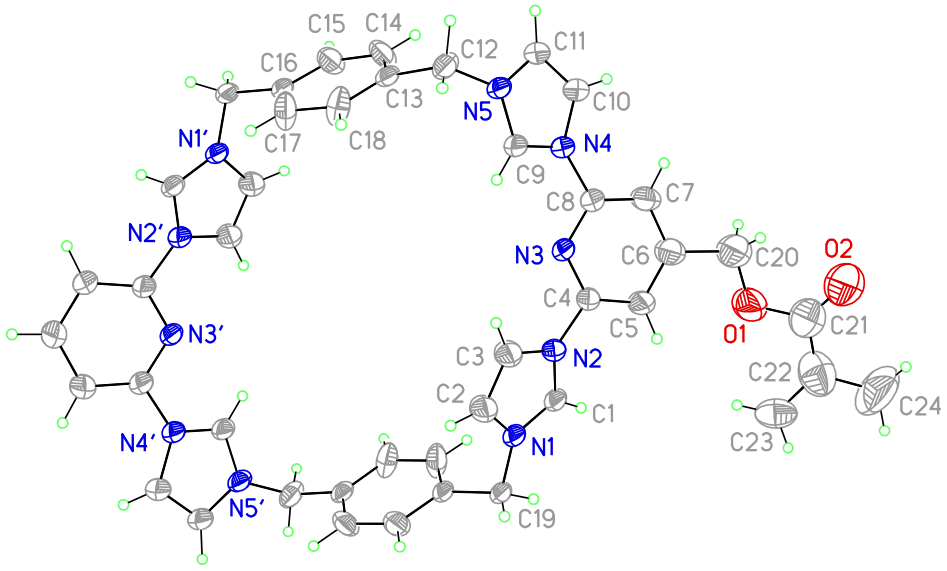

Figure 5.38 View of **4.2** showing the atom labeling scheme. Displacement ellipsoids are scaled to the 50% probability level. The macrocycle resides around a crystallographic inversion center at ½, ½, ½. The ester group is disordered about two equivalent positions. Atoms with labels appended by a ’ are related by 1-x, 1-y, 1-z.

5.4 REFERENCES

1) Caballero, A.; Díez-Barra, E.; Jalón, F. A.; Merino, S.; Tejeda, J. *J. Organomet. Chem.* **2001**, *617–618*, 395–398.
2) Lehmann, U.; Henze, O.; Schlüter, A. D. *Chem. Eur. J.* **1999**, *5*, 854–859.
3) CrystalClear, version 1.40; Rigaku Americas Corporation, The Woodlands, TX, 2008.
4) CrysAlicPro Software System, version 1.171.38.43f; Agilent Technologies UK Ltd.: Oxford, UK, 2013; SuperNova CCD System.
5) Sheldrick. G. M. *Acta Cryst.* **2015**, *A71*, 3–8.
6) Sheldrick, G. M. *Acta Cryst.* **2015**, *C71*, 9–18.
7) Spek, A. L. *Acta Cryst.* **2009**, *D65*, 148–155.
8) Farrugia, L. J. *J. Appl. Cryst.* **1999**, *32*. 837–838.
9) $R_W(F^2) = \{\Sigma w(|F_o|^2 - |F_c|^2)^2/\Sigma w(|F_o|)^4\}^{1/2}$ where w is the weight given each reflection. $R(F) = \Sigma(|F_o| - |F_c|)/\Sigma|F_o|\}$ for reflections with $F_o > 4(\sigma(F_o))$. $S = [\Sigma w(|F_o|^2 - |F_c|^2)^2/(n - p)]^{1/2}$, where n is the number of reflections and p is the number of refined parameters.
10) Tables 4.2.6.8 and 6.1.1.4, A. In *International Tables for X-ray Crystallography*, Vol. C, Wilson, J. C., Ed.; Kluwer Academic Press: Boston, 1992.
11) Sheldrick, G. M. SHELXTL/PC, version 5.03; Siemens Analytical X-ray Instruments, Inc.: Madison, Wisconsin, USA, 1994.
12) Altomare, A.; Burla, M. C.; Caliandro, M.; Camalli, M.; Carrozzini, B.; Cascarano, G. L.; De Caro, L.; Giacovazzo, C.; Polidori, G.; Spagna, R.; *J. Appl. Cryst.* **2005**, *38*, 381–388.
13) Sheldrick, G. M. *Acta Cryst.* **2008**, *A64*, 112–122.
14) Spek, A. L. PLATON, A Multipurpose Crystallographic Tool, Utrecht University, The Netherlands, 1998.
15) Palatinus, L.; Chaupuis, G.; *J. Appl. Cryst.* **2007**, *40*, 786–790.

References

Schmidtchen, F. P.; Berger, M. *Chem*. *Rev*. **1997**, *97*, 1609–1646.

Beer, P. D.; Gale, P. A. *Angew. Chem*. *Int*. *Ed*. **2001**, *40*, 486–516.

Steed, J. W.; Atwood, J. L. *Supramolecular Chemistry*, 2nd ed.; Wiley & Sons: Chichester, UK, 2009; pp. 308–382.

Kim, S. K.; Sessler, J. L. *Acc*. *Chem*. *Res*. **2014**, *47*, 2525–2536.

Liu, Z.; Nalluri, S. K. M.; Stoddart, J. F. *Chem. Soc. Rev.* **2017**, *46*, 2459–2478.

Odell, B.; Reddington, M. V.; Slawin, A. M. Z.; Spencer, N.; Stoddart, J. F.; Williams, D. J. *Angew*. *Chem. Int. Ed.* **1988**, *27*, 1547–1550.

Amabilino, D. B.; Stoddart, J. F. *Pure Appl. Chem*. **1996**, *68*, 2351–2359.

Langford, S. J.; Stoddart, J. F. *Pure Appl. Chem*. **1996**, *68*, 1255–1260.

Dale, E. J.; Vermeulen, N. A.; Juríček, M.; Barnes, J. C.; Young, R. M.; Wasielewski, M. R.; Stoddart, J. F. *Acc. Chem. Res.* **2016**, *49*, 262–273.

Raymo, F. M.; Stoddart, J. F. *Chem. Rev.* **1999,** *99,* 1643–1664.

Barin, G.; Coskun, A.; Fouda, M. M. G.; Stoddart, J. F. *ChemPlusChem* **2012**, *77*, 159–185.

Young, R. M.; Dyar, S. M.; Barnes, J. C.; Juríček, M.; Stoddart, J. F.; Co, D. T.; Wasielewski, M. R. *J. Phys. Chem. A* **2013**, *117*, 12438–12448.

Dyar, S. M.; Barnes, J. C.; Juríček, M.; Stoddart, J. F.; Co, D. T.; Young, R. M.; Wasielewski, M. R. *Angew. Chem. Int. Ed.* **2014**, *53*, 5371–5375.

Flood, A. H.; Stoddart, J. F.; Steuerman, D. W.; Heath, J. R. *Science* **2004**, *306*, 2055–2056.

Stoddart, J. F. *Chem. Soc. Rev.* **2009**, *38*, 1802–1820.

Balzani, V.; Gómez-López, M.; Stoddart, J. F. *Acc. Chem. Res.* **1998**, *31*, 405–414.

Erbas-Cakmak, S.; Leigh, D. A.; McTernan, C. T.; Nussbaumer, A. L. *Chem*. *Rev*. **2015**, *115*, 10081–10206.

Gong, H. -Y.; Rambo, B. M.; Karnas, E.; Lynch, V. M.; Sessler, J. L. *Nat. Chem.* **2010**, *2*, 406–409.

Gong, H. -Y.; Rambo, B. M.; Lynch, V. M.; Keller, K. M.; Sessler, J. L. *J. Am. Chem. Soc*. **2013**, *135*, 6330–6337.

Yang, Y. -D.; Sessler. J. L.; Gong, H. -Y. *Chem. Commun.* **2017**, *53*, 9684–9696.

Gong, H. -Y.; Rambo, B. M.; Lynch, V. M.; Keller, K. M.; Sessler, J. L. *Chem. –Eur. J.* **2012**, *18*, 7803–7809.

Gong, H. -Y.; Rambo, B. M.; Karnas, E.; Lynch, V. M.; Keller, K. M.; Sessler, J. L. *J. Am. Chem. Soc.* **2011**, *133*, 1526–1533.

Rambo, B. M.; Gong, H. -Y.; Oh, M.; Sessler, J. L. *Acc. Chem. Res.* **2012**, *45*, 1390–1401.

Tang, F.; Cao, R.; Gong, H. -Y.; *Tetrahedron Lett.* **2015**, *56*, 820–823.

Ding, C. -J.; Shen, M. -J.; Xu, L. -J.; Gong, H. -Y. *Tetrahedron* **2016**, *72*, 431–435.

Li, C.; Wu, T.; Hong, C.; Zhang, G.; Liu, S. *Angew. Chem. Int. Ed.* **2012**, *51*, 455–459.

Dong, R.; Zhu, B.; Zhou, Y.; Yan, D.; Zhu, X. *Angew. Chem. Int. Ed.* **2012**, *51*, 11633–11637.

Hu, X.; Hu, J.; Tian, J.; Ge, Z.; Zhang, G.; Luo, K.; Liu, S. *J. Am. Chem. Soc.* **2013**, *135*, 17617–17629.

Yan, Q.; Wang, J.; Yin, Y.; Yuan, J. *Angew. Chem. Int. Ed.* **2013**, *52*, 5070–5073.

Raghupathi, K. R.; Guo, J.; Munkhbat, O.; Rangadurai, P.; Thayumanavan, S. *Acc. Chem. Res.* **2014**, 47, 2200–2211.

Blanazs, A.; Madsen, J.; Battaglia, G.; Ryan, A. J.; Armes, S. P. *J. Am. Chem. Soc.* **2011**, *133*, 16581–16587.

Mai, Y.; Eisenberg, A. *Chem. Soc. Rev.* **2012**, *41*, 5969–5985.

Warren, N. J.; Armes, S. P. *J. Am. Chem. Soc.* **2014**, *136*, 10174–10185.

Ji, X.; Wang, H.; Li, Y.; Xia, D.; Li, H.; Tang, G.; Sessler, J. L.; Huang, F. *Chem. Sci.* **2016**, *7*, 6006–6014.

Qiao, Z. -Y.; Ji. R.; Huang, X. -N.; Du, F. -S.; Zhang, R.; Liang, D. -H.; Li, Z. -C.; *Biomacromolecules* **2013**, *14*, 1555–1563.

Silver, E. S.; Rambo, B. M.; Bielawski, C. W.; Sessler, J. L. *J. Am. Chem. Soc.* **2014**, *136*, 2252–2255.

Pressly, E. D.; Rossin, R.; Hagooly, A.; Fukukawa, K.; Messmore, B. W.; Welch, M. J.; Wooley, K. L.; Lamm, M. S.; Hule, R. A.; Pochan, D. J.; Hawker, C. J. *Biomacromolecules* **2007**, *8*, 3126–3134.

Fukukawa, K.; Rossin, R.; Hagooly, A.; Pressly, E. D.; Hunt, J. N.; Messmore, B. W.; Wooley, K. L.; Welch, M. J.; Hawker, C. J. *Biomacromolecules* **2008**, *9*, 1329–1339.

Ji, X.; Wu, R. -T.; Long, L.; Guo, C.; Khashab, N. M.; Huang, F.; Sessler, J. L. *J. Am. Chem. Soc.* **2018**, *140*, 2777–2780.

Ji, X.; Wu, R. -T.; Long, L.; Ke, X. -S.; Guo, C.; Ghang, Y. -J.; Lynch, V. M.; Huang, F.; Sessler, J. L. *Adv. Mater.* **2018**, *30*, 1705480.

Yang, L.; Tan, X.; Wang, Z.; Zhang, X. *Chem. Rev.* **2015**, *115*, 7196–7239.

Takashima, Y.; Harada, A. *J. Incl. Phenom. Macrocycl. Chem*. **2017**, *88*, 85–104.

Gyarmati, B.; Szilágyi, B. Á.; Szilágyi, A. *Eur. Polym. J.* **2017**, *93*, 642–669.

Sessler, J. L.; Andrievsky, A.; Gale, P. A.; Lynch, V. M. *Angew. Chem. Int. Ed.* **1996**, *35*, 2782–2785.

Ashton, P. P.; Parsons, I. W.; Raymo, F. M.; Stoddart, J. F.; White, A. J. P.; Williams, D. J.; Wolf, R. *Angew. Chem. Int. Ed.* **1998**, *37*, 1913–1916.

Cao, D.; Wang, C.; Giesener, M. A.; Liu, Z.; Stoddart, J. F. *Chem. Commun.* **2012**, *48*, 6791−6793.

Rotzler J.; Mayor, M. *Chem. Soc. Rev.* **2013**, *42*, 44−62.

Erbas-Cakmak, S.; Leigh, D. A.; McTernan, C. T.; Nussbaumer, A. L. *Chem*. *Rev*. **2015**, *115*, 10081–10206.

Bruns, C. J.; Stoddart, J. F. *Acc. Chem. Res.* **2014**, *47*, 2186–2199.

Kim, D. S.; Chang, J.; Leem, S.; Park, J. S.; Thordarson, P.; Sessler, J. L. *J. Am*. *Chem*. *Soc.*, **2015**, *137*, 16038–16042.

Ji, X.; Wang, H.; Li, Y.; Xia, D.; Li, H.; Tang, G.; Sessler, J. L.; Huang, F. *Chem. Sci*. **2016**, *7*, 6006–6014.

Walter, S. M.; Kniep, F.; Herdtweck, E.; Huber S. M. *Angew. Chem. Int. Ed.* **2011**, *50*, 7187–7191.

Ashton, P. R.; Ballardini, R.; Balzani, V.; Bělohradský, M.; Gandolfi, M. T.; Philp, D.; Prodi, L.; Raymo, F. M.; Reddington, M. V.; Spencer, N.; Stoddart, J. F.; Venturi, M.; Williams, D. J. *J. Am. Chem. Soc.* **1996**, *118*, 4931–4951.

Rose, N. G. W.; Blaskovich, M. A.; Wong, A.; Lajoie, G. A. *Tetrahedron* **2001**, *57*, 1497–1507.

Choony, N.; James, L.; Rabun, C. *Synthetic Commun.* **2001**, *41*, 2539–2543.

Barnes, J. C.; Juríček, M.; Vermeulen, N. A.; Dale, E. J.; Stoddart, J. F. *J. Org. Chem*. **2013**, *78*, 11962–11969.

Luo, Y.; Blaskovich, M. A.; Lajoie, G. A *J. Org. Chem*. **1999**, *64*, 6106–6111.

Shang, J.; Rambo, B. M.; Hao, X.; Xiang, J.-F.; Gong, H.-Y.; Sessler, J. L. *Chem. Sci*. **2016**, *7*, 4148–4157.

Zhao, D.; Moore, J. S. *Org. Biomol. Chem*. **2003** , *1*, 3471–3491.

Mahadevi, A. S.; Sastry, G. N. *Chem. Rev.* **2016***, 116,* 2775−2825.

Wackerly, J. W.; Moore, J. S. *Macromolecules* **2006**, *39*, 7269–7276.

Schmidt, R.; Stolte, M.; Grüne, M.; Würthner, F. *Macromolecules* **2011**, *44,* 3766–3776.

Martin, R. B. *Chem*. *Rev*. **1996**, *96*, 3043–3064.

Xu, J.; Fogleman, E. A.; Craig, S. L. *Macromolecules* **2004**, *37,* 1863–1870.

Zhang, H.; Lee, J.; Lammer, A. D. Chi, X.; Brewster, J. T.; Lynch, V. M.; Li, H.; Zhang, Z.; Sessler, J. L. *J. Am. Chem. Soc*. **2016**, *138*, 4573–4579.

Tang, F.; Cao, R.; Gong, H. -Y.; *Tetrahedron Lett*. **2015**, *56*, 820–823.

Stoddart, J. F. *Chem. Soc. Rev.* **2009**, *38*, 1802–1820.

Balzani, V.; Gómez-López, M.; Stoddart, J. F. *Acc. Chem. Res.* **1998**, *31*, 405–414.

Albelda, M. T.; Frias, J. C.; Garcia-Espana, E.; Schneider, H. J. *Chem*. *Soc*. *Rev*. **2012**, *41*, 3859−3877.

Busschaert, N.; Caltagirone, C.; Van Rossom, W.; Gale, P. A. *Chem*. *Rev*. **2015**, *115*, 8038−8155.

Okesola, B. O.; Smith, D. K. *Chem*. *Soc*. *Rev*. **2016**, *45*, 4226−4251.

Aydogan, A.; Coady, D. J.; Kim, S. K.; Akar, A.; Bielawski, C. W.; Marquez, M.; Sessler, J. L. *Angew*. *Chem*. *Int*. *Ed.* **2008**, *120*, 9794−9798.

Liu, G.; You, S.; Ma, M.; Huang, H.; Ren, N. *Environ*. *Sci*. *Technol*. **2016**, *50*, 11218−11225.

Wang, X.; Lü, S.; Gao, C.; Feng, C.; Xu, X.; Bai, X.; Gao, N.; Yang, J.; Liu, M.; Wu, L. *ACS Sustainable Chem*. *Eng*. **2016**, *4*, 2068−2079.

Jiao, S.; Jin, J.; Wang, L. *Sens*. *Actuators*, *B* **2015**, *208*, 36−42.

Zhang, Y.; Su, Z.; Li, B.; Zhang, L.; Fan, D.; Ma, H. *ACS Appl*. *Mater*. *Interfaces* **2016**, *8*, 12344−12351.

Fowler, C. J.; Haverlock, T. J.; Moyer, B. A.; Shriver, J. A.; Gross, D. E.; Marquez, M.; Sessler, J. L.; Hossain, M. A.; Bowman-James, K. *J. Am*. *Chem*. *Soc*. **2008**, *130*, 14386−14387.

Kim, S. K.; Lee, J.; Williams, N. J.; Lynch, V. M.; Hay, B. P.; Moyer, B. A.; Sessler, J. L. *J. Am*. *Chem*. *Soc*. **2014**, *136*, 15079−15085.

Hartle, M. D.; Hansen, R. J.; Tresca, B. W.; Prakel, S. S.; Zakharov, L. N.; Haley, M. M.; Pluth, M. D.; Johnson, D. W. *Angew*. *Chem*. *Int*. *Ed*. **2016**, *55*, 11480−11484.

Guha, S.; Saha, S. *J. Am*. *Chem*. *Soc*. **2010**, *132*, 17674−17677.

Pan, B.; Xu, J.; Wu, B.; Li, Z.; Liu, X. *Environ*. *Sci*. *Technol*. **2013**, *47*, 9347−9354.

Hai, F. I.; Yamamoto, K.; Fukushi, K. *Crit*. *Rev*. *Environ*. *Sci*. *Technol*. **2007**, *37*, 315−377.

Kim, H.; Watthanaphanit, A.; Saito, N. *ACS Sustainable Chem*. *Eng*. **2017**, *5*, 5842−5851.

Appel, E. A.; Biedermann, F.; Hoogland, D.; Del Barrio, J.; Driscoll, M. D.; Hay, S.; Wales, D. J.; Scherman, O. A. *J. Am. Chem. Soc.* **2017**, *139*, 12985−12993.

Appel, E. A.; Loh, X. J.; Jones, S. T.; Biedermann, F.; Dreiss, C. A.; Scherman, O. A. *J. Am. Chem. Soc.* **2012**, *134*, 11767−11773.

Chen, H.; Ma, X.; Wu, S.; Tian, H. *Angew. Chem. Int. Ed.* **2014**, *53*, 14149−14152.

Liu, J.; Tan, C. S.; Yu, Z.; Lan, Y.; Abell, C.; Scherman, O. A. *Adv. Mater.* **2017**, *29*, 1604951.

Zheng, W.; Chen, L. J.; Yang, G.; Sun, B.; Wang, X.; Jiang, B.; Yin, G. Q.; Zhang, L.; Li, X.; Liu, M.; Chen, G.; Yang, H. B. *J. Am. Chem. Soc.* **2016**, *138*, 4927−4937.

He, X.; Fan, J.; Wooley, K. L. *Chem. -Asian J.* **2016**, *11*, 437−447.

Zheng, W.; Yang, G.; Shao, N.; Chen, L. J.; Ou, B.; Jiang, S. T.; Chen, G.; Yang, H. B. *J. Am. Chem. Soc.* **2017**, *139*, 13811−13820.

Fan, J.; Li, R.; Wang, H.; He, X.; Nguyen, T. P.; Letteri, R. A.; Zou, J.; Wooley, K. L. *Org. Biomol. Chem.* **2017**, *15*, 5145−5154.

Plank, T.N.; Skala, L. P.; Davis, J. T. *Chem. Commun.* **2017**, *53*, 6253−6238.

Kim, H. J.; Lee, J. H.; Lee, M. *Angew. Chem. Int. Ed.* **2005**, *44*, 5810−5814.

Shen, J. -S.; Li, D.-H.; Cai, Q. -G.; Jiang, Y. -B. *J. Mater. Chem.* **2009**, *19*, 6219.

Becker, T.; Yong Goh, C.; Jones, F.; McIldowie, M. J.; Mocerino, M.; Ogden, M. I. *Chem. Commun.* **2008**, 3900−3902.

Shen, J. S.; Cai, Q. G.; Jiang, Y. B.; Zhang, H. W. *Chem. Commun.* **2010**, *46*, 6786−6788.

Ji, X.; Wu, R. -T.; Long, L.; Guo, C.; Khashab, N. M.; Huang, F.; Sessler, J. L. *J. Am. Chem. Soc.* **2018**, *140*, 2777–2780.

Gong, H. Y.; Rambo, B. M.; Karnas, E.; Lynch, V. M.; Sessler, J. L. *Nat. Chem.* **2010**, *2*, 406−409.

Cheng, H. K.; Sahoo, N. G.; Tan, Y. P.; Pan, Y.; Bao, H.; Li,L.; Chan, S. H.; Zhao, J. *ACS Appl. Mater. Interfaces* **2012**, *4*, 2387−2394.

Salavagione, H. J.; Gómez, M. A.; Martínez, G. *Macromolecules* **2009**, *42*, 6331−6334.

Takashima, Y.; Hatanaka, S.; Otsubo, M.; Nakahata, M.; Kakuta, T.; Hashidzume, A.; Yamaguchi, H.; Harada, A. *Nat. Commun.* **2012**, *3*, 1270.

Wu, Z. -S.; Tan, Y. -Z.; Zheng, S.; Wang, S.; Parvez, K.; Qin, J.; Shi, X.; Sun, C.; Bao, X.; Feng, X.; Müllen, K. *J. Am. Chem. Soc.* **2017**, *139*, 4506–4512.

Shi, Y.; Wang, M.; Ma, C.; Wang, Y.; Li, X.; Yu, G. *Nano Lett.* **2015**, *15*, 6276−6281.

Zhang, J.; Xu, D.; Guo, J.; Sun, Z.; Qian, W.; Zhang, Y.; Yan, F. *Macromol*. *Rapid Commun*. **2016**, *37*, 1194−119.

Sawada, J.; Aoki, D.; Uchida, S.; Otsuka, H.; Takata, T. *ACS Macro Lett*. **2015**, *4*, 598−601.

Ali, M.; Dutta, P.; Pandey, S. *J. Phys*. *Chem*. *B* **2010**, *114*, 15042−15051.

Sikorska, E.; Khmelinskii, I. V.; Koput, J.; Sikorski, M. *J. Mol*. *Struct*.: *THEOCHEM* **2004**, *676*, 155−160.

Diaz, S. A.; Giordano, L.; Azcarate, J. C.; Jovin, T. M.; Jares-Erijman, E. A. *J. Am*. *Chem*. *Soc*. **2013**, *135*, 3208−3217.

Choi, M. G.; Hwang, J.; Eor, S.; Chang, S. K. *Org*. *Lett*. **2010**, *12*, 5624−5627.

Kresse, G.; Hafner, J. *Phys. Rev. B* **1993**, *47*, 558.

Kresse, G.; Furthmüller, J. *Comput. Mat. Sci.* **1996**, *6*, 15.

Kresse, G.; Furthmüller, J. *Phys. Rev. B* **1996**, *54*, 11169.

Marcus, Y.; Hefter, G. *Chem*. *Rev*. **2006**, *106*, 4585−4621.

Xing, H.; Li, Z.; Wu, Z.; Huang, F. *Macromol*. *Rapid Commun*. **2018**, *39*, 1700361.

Erevelles, S.; Fukawa, N.; Swayne, L. *J. Bus. Res.* **2016**, *69*, 897–904.

Li, M.; Zheng, X.; Zhuang, G. *J. Bus. Res.* **2017**, *78*, 268–276.

Meruga, J. M.; Fountain, C.; Kellar, J.; Crawford, G.; Baride, A.; May, P. S.; Cross, W.; Hoover, R.; *Int. J. Comput. Appl.* **2015**, *37*, 17–27.

R. Won, *Nat. Photonics* **2012**, *6*, 801.

Graydon, O. *Nat. Photonics* **2013**, *7*, 343.

Park, D. H.; Han, C. J.; Shul, Y. G.; Choy, J. H.; *Sci. Rep.* **2014**, *4*, 4879.

Ji, X.; Wu, R. -T.; Long, L.; Ke, X. -S.; Guo, C.; Ghang, Y. -J.; Lynch, V. M.; Huang, F.; Sessler, J. L. *Adv. Mater*. **2018**, *30*, 1705480.

Appel, E. A.; del Barrio, J.; Loh, X. J.; Scherman, O. A.; *Chem. Soc. Rev.* **2012**, *41*, 6195–6214.

Qi, Z.; Schalley, C. A.; *Acc. Chem. Res.* **2014**, *47*, 2222–2233.

Ni, M.; Zhang, N.; Xia, W.; Wu, X.; Yao, C.; Liu, X.; Hu, X. -Y.; Lin, C.; Wang, L. *J. Am. Chem. Soc.* **2016**, *138*, 6643–6649.

Zheng, W.; Chen, L. -J.; Yang, G.; Sun, B.; Wang, X.; Jiang, B.; Yin, G. -Q.; Zhang, L.; Li, X.; Liu, M.; Chen, G.; Yang, H. -B.; *J. Am. Chem. Soc.* **2016**, *138*, 4927–4937.

Liu, J.; Sun, Y. -Q.; Huo, Y.; Zhang, H.; Wang, L.; Zhang, P.; Song, D.; Shi, Y.; Guo, W. *J. Am. Chem. Soc.* **2014**, *136*, 574–577.

Mendive-Tapia, L.; Subiros-Funosas, R.; Zhao, C.; Albericio, F.; Read, N. D.; Lavilla, R.; Vendrell, M. *Nat. Protoc.* **2017**, *12*, 1588–1619.

Beija, M.; Afonso, C. A.; Martinho, J. M. *Chem. Soc. Rev.* **2009**, *38*, 2410–2433.

Chen, X.; Pradhan, T.; Wang, F.; Kim, J. S.; Yoon, J. *Chem. Rev.* **2012**, *112*, 1910–1956.

Busschaert, N.; Caltagirone, C.; Van Rossom, W.; Gale, P. A. *Chem. Rev.* **2015**, *115*, 8038–8155.

Gale, P. A.; Davis, J. T.; Quesada, R. *Chem. Soc. Rev.* **2017**, *46*, 2497–2519.

Harada, A.; Kobayashi, R.; Takashima, Y.; Hashidzume, A.; Yamaguchi, H. *Nat. Chem.* **2011**, *3*, 34–37.

Nakahata, M.; Takashima, Y.; Yamaguchi, H.; Harada, A. *Nat. Commun.* **2011**, *2*, 511.

Jung, H. S.; Kwon, P. S.; Lee, J. W.; Kim, J. I.; Hong, C. S.;. Kim, J. W; Yan, S.; Lee, J. Y.; Lee, J. H.; Joo, T.; Kim, J. S.; *J. Am. Chem. Soc.* **2009**, *131*, 2008–2012.

Suzuki, D.; Oda, S.; Kawano, Y. *Nat. Photonics* **2016**, *10*, 809–813.

Gao, W.; Emaminejad, S.; Nyein, H. Y. Y.; Challa, S.; Chen, K.; Peck, A.; Fahad, H. M.; Ota, H.; Shiraki, H.; Kiriya, D.; Lien, D. -H.; Brooks, G. A.; Davis, R. W.; Javey, A. *Nature* **2016**, *529*, 509–514.

Connors, K. A. Binding Constants, Wiley: New York, 1987.

Corbin, P. S. Ph.D. Dissertation, University of Illinois at Urbana-Champaign, Urbana, IL, 1999.

Ashton, P. R.; Ballardini, R.; Balzani, V.; Belohradsky, M.; Gandolfi, M. T.; Philp, D.; Prodi, L.; Raymo, F. M.; Reddington, M. V.; Spencer, N.; Stoddart, J. F.; Venturi, M.; Williams, D. J. *J. Am. Chem. Soc.* **1996**, *118*, 4931–4951.

Hoshino, T.; Shirota, N.; Asakawa, A. Compound Having Fluorescent Functional Group and Method for Producing Polymer of The Same. Patent WO2009011427A1, 2009.

S, Z.; Q, Z.; B, Y. Near Infrared BODIPY (Boron Dipyrromethene Compounds) Hydroxyl Radical Probes and Synthesis Method and Usage Thereof. Patent CN103342720A, 2013.

L. Wang, M. Sibrian-Vazquez, J. O. Escobedo, J. Wang, R. G. Moore, R. M. Strongin, *Chem. Commun.* **2015**, *51*, 1697–1700.

Hu, B.; D. M. Henn, D. M.; Wright, R. A. E.; Zhao, B. *Langmuir* **2014**, *30*, 11212−11224.

Yu, K. -K.; Li, K.; Hou, J. -T.; Yang, J.; Xie, Y. -M.; Yu, X. -Q. *Polym. Chem.* **2014**, *5*, 5804–5812.

Wojtecki, R. J.; Meador, M. A.; Rowan, S. J.; *Nat. Mater.* **2010**, *10*, 14–17.

Liu, J.; Tan, C. S. Y.; Yu, Z.; Lan, Y.; Abell, C.; Scherman, O. A. *Adv. Mater.* **2017**, *29*, 1604951.

Takashima, Y.; Hatanaka, S.; Otsubo, M.; Nakahata, M.; Kakuta, T.; Hashidzume, A.; Yamaguchi, H.; Harada, A.; *Nat. Commun.* **2012**, *3*, 1270.

Wu, Z. -S.; Tan, Y. -Z.; Zheng, S.; Wang, S.; Parvez, K.; Qin, J.; Shi, X.; Sun, C.; Bao, X.; Feng, X.; Müllen, K. *J. Am. Chem. Soc.* **2017**, *139*, 4506–4512.

Shi, Y.; Wang, M.; Ma, C.; Wang, Y.; Li, X.; Yu, G. *Nano Lett.* **2015**, *15*, 6276−6281.

Zhang, J.; Xu, D.; Guo, J.; Sun, Z.; Qian, W.; Zhang, Y.; Yan, F. *Macromol. Rapid Commun.* **2016**, *37*, 1194−119.

Caballero, A.; Díez-Barra, E.; Jalón, F. A.; Merino, S.; Tejeda, J. *J. Organomet. Chem.* **2001**, *617–618*, 395–398.

Liu, J.; Tan, C. S. Y.; Yu, Z.; Lan, Y.; Abell, C.; Scherman, O. A. *Adv. Mater.* **2017**, *29*, 1604951.

Liu, J.; Tan, C. S. Y.; Yu, Z.; Li, N.; Abell, C.; Scherman, O. A. *Adv. Mater.* **2017**, *29*, 1605325.

Lehmann, U.; Henze, O.; Schlüter, A. D. *Chem. Eur. J.* **1999**, *5*, 854–859.

CrystalClear, version 1.40; Rigaku Americas Corporation, The Woodlands, TX, 2008.

CrysAlicPro Software System, version 1.171.38.43f; Agilent Technologies UK Ltd.: Oxford, UK, 2013; SuperNova CCD System.

Sheldrick. G. M. *Acta Cryst.* **2015**, *A71*, 3–8.

Sheldrick, G. M. *Acta Cryst.* **2015**, *C71*, 9–18.

Spek, A. L. *Acta Cryst.* **2009**, *D65*, 148–155.

Farrugia, L. J. *J. Appl. Cryst.* **1999**, *32*. 837–838.

Tables 4.2.6.8 and 6.1.1.4, A. In *International Tables for X-ray Crystallography*, Vol. C, Wilson, J. C., Ed.; Kluwer Academic Press: Boston, 1992.

Sheldrick, G. M. SHELXTL/PC, version 5.03; Siemens Analytical X-ray Instruments, Inc.: Madison, Wisconsin, USA, 1994.

Altomare, A.; Burla, M. C.; Caliandro, M.; Camalli, M.; Carrozzini, B.; Cascarano, G. L.; De Caro, L.; Giacovazzo, C.; Polidori, G.; Spagna, R.; *J. Appl. Cryst*. **2005**, *38*, 381–388.

Sheldrick, G. M. *Acta Cryst*. **2008**, *A64*, 112–122.

Spek, A. L. PLATON, A Multipurpose Crystallographic Tool, Utrecht University, The Netherlands, 1998.

Palatinus, L.; Chaupuis, G.; *J. Appl. Cryst*. **2007**, *40*, 786–790.